CHEMICAL AND STRUCTURAL CHARACTERIZATION OF BORON CARBIDE POWDERS AND CERAMICS

by

KANAK ANANT KUWELKAR

A dissertation submitted to the

Graduate School – New Brunswick

Rutgers, The State University of New Jersey

In partial fulfillment of the requirements

For the degree of

Doctor of Philosophy

Graduate Program in Materials Science and Engineering

Written under the direction of

Professor Richard A. Haber

And approved by

_____

_____

_____

_____

_____

_____

New Brunswick, New Jersey

OCTOBER, 2016

ABSTRACT OF THE DISSERTATION

Chemical and Structural Characterization of Boron Carbide Powders and Ceramics

By Kanak Anant Kuwelkar

Dissertation Director:

Richard A. Haber. PhD

Boron carbide is the material of choice for lightweight armor applications due to its extreme hardness, high Young's modulus and low specific weight. The homogeneity range in boron carbide extends from ~9 to ~20 at% carbon with the solubility limits not uniquely defined in literature. Over this homogeneity range, the exact lattice positions of boron and carbon atoms have not been unambiguously established, and this topic has been the consideration of significant debate over the last 60 years. The atomic configuration and positions of the boron and carbon atoms play a key role in the crystal structure of the boron carbide phases. Depending on the atomic structure, boron carbide exhibits different mechanical properties which may alter its ballistic performance under extreme dynamic conditions. This work focusses on refinement and development of analytical and chemical methods for an accurate determination of the boron carbide stoichiometry. These methods were then utilized to link structural changes of boron carbide across the solubility range to variations in mechanical properties.

After an extensive assessment of the currently employed characterization techniques, it was discerned that the largest source of uncertainty in the determination of the boron carbide stoichiometry was found to arise from the method utilized to evaluate

the free carbon concentration. To this end, a modified spiking technique was introduced for free carbon determination where curve fitting techniques were employed to model the asymmetry of the 002 free carbon diffraction peak based on the amorphous, disordered and graphitic nature of carbon. A relationship was then established between the relative intensities of the carbon and boron carbide peaks to the percentage of added carbon and the free-carbon content was obtained by graphical extrapolation.

Samples with varying chemistry and high purity were synthesized across the solubility range by hot pressing mixtures of amorphous boron and boron carbide. Vibrational mode frequencies and lattice parameter measurements from Rietveld refinement were correlated to the respective B:C ratios calculated using the developed characterization techniques. An expansion of the unit cell and change in slope in the lattice parameter-stoichiometry relationship were observed at more boron rich stoichiometries. These observations were justified through the proposal of a simplified structural model considering preferential substitution of boron atoms for carbon atoms in the icosahedra from 20 at% to 13.3 at% carbon, followed by formation of B-B bonds from 13.3 at % C to ~9 at% C. Hardness measurements uncovered decreased hardness values in boron rich boron carbide which was attributed to the formation of weaker unit cells. Load induced amorphization was also detected in all the indented materials.

Finally, experimental observations have shown that failure in boron carbide may be governed by a mechanism other than amorphization and synthesizing boron carbide with a modified microstructure at stoichiometries close to B_4C may be the way forward to attain improved ballistic performance.

ACKNOWLEDGEMENTS

I am very thankful to everyone who has helped and guided me throughout my time at Rutgers University. In particular, my thesis advisor Dr. Haber for taking me in from chemical engineering and giving me the opportunity to work in the material science and engineering department. Thank you Rich for all the help through the years, not just with my research, but everything else. A special thanks to Dr. Domnich for mentoring me throughout my PhD. This work would not have been possible without your invaluable advice, guidance and countless hours spent answering all my questions. It has been a joy working with you. Equally important is Dr. Rafaniello for the direction given to me with regards to my research and professional development.

I want to acknowledge Dr. LaSalvia and Dr. Behler for help with hot pressing at the Army Research Laboratory (ARL). I would also like to recognize my committee members, Dr. Matthewson and Dr. Chhowalla. I am also grateful for financial support from the Army Research Laboratory and National Science Foundation (NSF) which enabled me to complete this dissertation.

I would also like to thank Michelle and Laura, without whom Haber group would not function and my colleagues Metin, Azmi, Zeynep, Fatih, Minh, Fabio, Sukhanya, Tyler, Vince, Mustafa, Bruce, Anthony and Chawon. It has been fun working with you guys. It has also been an absolute pleasure to collaborate with Jamie and Kelvin at Johns Hopkins University.

Finally, I would like to thank my parents for the tremendous support given to me and for the constant words of encouragement when I have needed them the most. Without you, this would never have been possible and I hope I have made you proud.

TABLE OF CONTENTS

LIST OF TABLES

LIST OF FIGURES

1 Introduction and Literature Review of Boron Carbide

1.1 History of Boron Carbide

Boron Carbide was first discovered in the late part of the 19th century as a by-product of reactions with metal borides. Initially non-stoichiometric boron carbide (B_3C and B_6C) was synthesized by Joly and Moissan in the last decade of the 19th century[1]. In 1934, Ridgway suggested that boron carbide had a stable stoichiometry of B_4C[2]. Following Ridgway's identification of "stoichiometric" boron carbide, Russian scientists proposed different stoichiometric formulae for boron carbide[1, 3, 4, 5], but none of these formulae have been confirmed by other authors. More recently, a number of different stoichiometries have been proposed as the stable boron carbide phase. It is accepted that single phase carbon has a solubility range varying from ~9 at% to ~20 at% carbon[1, 6]. The most important properties of boron carbide are its high melting point, low specific weight, chemical inertness and neutron absorption capability. These properties permit boron carbide to be used in the armor, abrasives and nuclear industries.

1.2 Crystal Structure and Phase Diagram

The crystallographic structure of boron carbide consists of a 12-atom icosahedra located at the vertices of the rhombohedral unit cell with an $R\bar{3}m$ space group and a 3-atom chain that connects the icosahedra along the (111) direction (Figure 1). Due to similarities and mutual substitutions between boron and carbon atoms, it is widely accepted that the homogeneity range in boron carbide extends from ~8 at% to ~20 at% carbon[7, 8, 9, 10]. But Konovalikhin et al. have also reported synthesis of a single crystal with a carbon concentration of ~24 at%[8]. Over the boron carbide homogeneity range, the exact positions

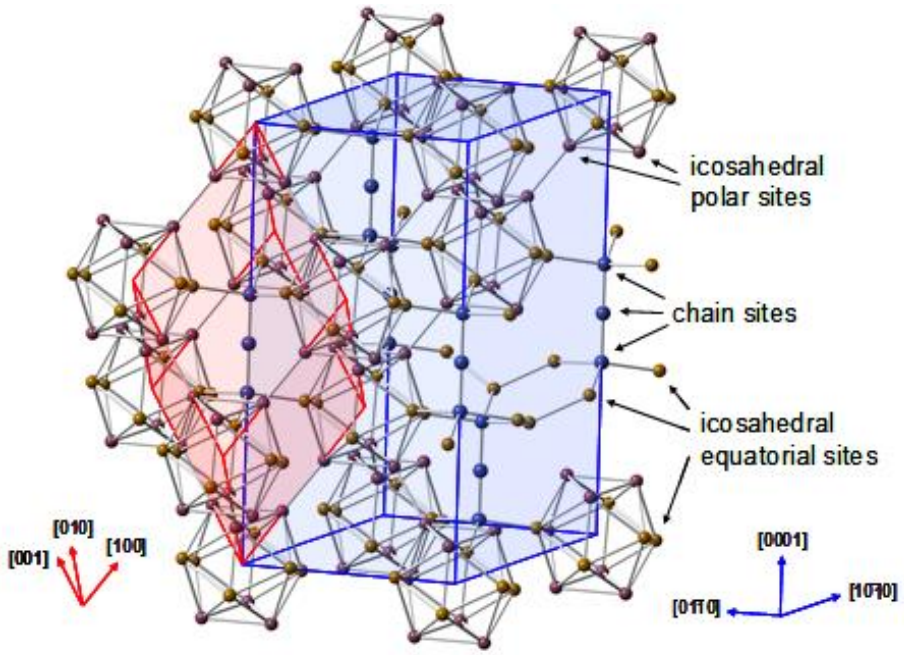

Figure 1. Boron carbide with 12 atom icosahedra located at the vertices of a rhombohedral and hexagonal lattice of trigonal symmetry and 3-atom linear chain linking the icosahedra[6].

of boron and carbon atoms in the unit cell have not been unambiguously established and a number of theories exist that consider preferential boron substitutions for carbon in the icosahedra, intericosahedral chains, or alternatively, formation of vacancies in the chain center position. An example of possible atomic configurations that would help accommodate the structural variations across the solubility range is shown in (Figure 2)[11, 12]. In the literature, these different atomic configurations of boron carbide are sometimes referred to as "polytypes". Based on the solubility range of boron carbide, multiple atomic configurations have been proposed over the years. Because of the fourfold coordination, carbon is generally preferred at the end of the 3 atom chain[13]. Paramagnetic defects have been observed in boron carbide due to the presence of small amount of carbon atoms present at the center of the chains[13, 14]. The results by Yakel et al. revealed that at "stoichiometric" compositions, the structural configurations could be either a $B_{11}C$, B_{12} or

$B_{10}C_2$ icosahedra and C-B-C intericosahedral chain[15]. Following the same work, at 13.3 at% carbon, substitution of the boron atoms for carbon atoms occur in the icosahedra resulting in a B_{12} (C-B-C) structure. Beyond 13.3 at%, the C-B-C chains would be replaced by B_4 groups which would result in an increase in the angle of the unit cell with minimal effect on the cell edge. Other authors have proposed that at 20 at% carbon, the structural configuration consists of C-C-C chains and B_{12} clusters[16] or C-B-C chains and $B_{11}C$ clusters[17, 18]. Boron carbide at 13.3 at% carbon was described as having a configuration with either a B_{12} icosahedra with a C-B-C chain or $B_{11}C$ icosahedra and with a C-B-B chain.

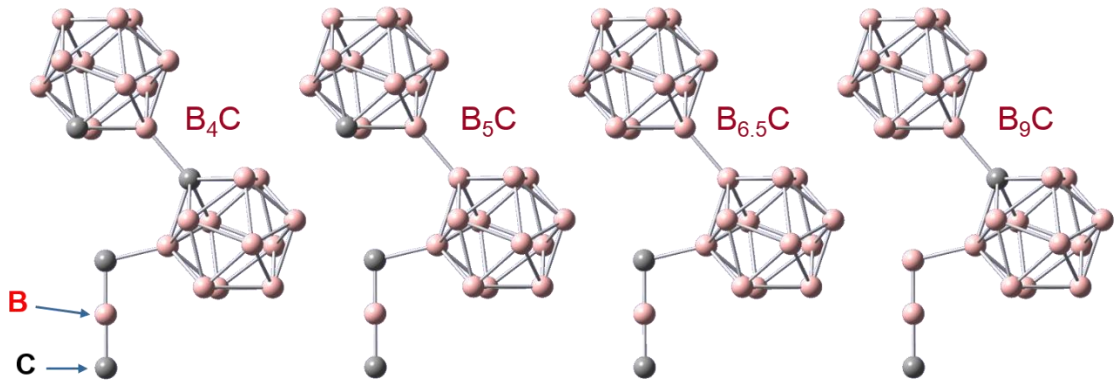

Figure 2. Possible structural units of boron carbide across homogeneity range.

Due to the similarities in the electronic and nuclear scattering cross sections of boron and carbon, the characterization techniques cannot easily distinguish between these two atoms. Based on the study of the free energy as a function of the carbon concentration, it was concluded that entropic and energetic considerations favor replacement of the carbon atoms with boron atoms within the interisocahedral chains, in the 20 – 13.3 at% carbon range. At low carbon concentrations, below 13.3 at%, the boron substitution for carbon occurs within the icosahedra[19]. Structural refinement using X-ray diffraction (XRD) by

Will et al. depicted B_{12} units which are joined to C-B-C chains and B-B bonds leading to the $B_{13}C_2$ formula with 15 atoms per unit cell[17, 18]. The structural model proposed by Larson[20] is in alignment with that of Yakel[15]. At lower carbon concentrations below 13.3 at% carbon, 1/6 of the carbon atoms in the icosahedra are replaced by boron atoms without any evidence of interstitial atoms. Matkovich proposed that the wide homogeneity range could be a result of three possible mechanisms: 1) B and C substitution at the atomic sites; 2) deficient occupancy of some of the atomic sites; 3) occupancy in addition to the 15 established sites[9, 10]. Morosin et al. performed single crystal X-ray diffraction on several boron carbide specimens[21]. Based on the results from least square refinement and the assessment of the electron density maps, it was concluded that for carbon rich boron carbides, the carbon is located in the C-B-C chain and in the icosahedra. The icosahedral boron is distributed in a statistically disordered manner and is predominantly present on either of the two crystallographic boron sites. This result was in accordance with energy band calculations where the $B_{11}C$(C-B-C) structure seemed to be the most energetically preferred. It was also in agreement with the results from other authors. The $B_{11}C$(C-B-C) configuration is widely accepted as the structure for boron carbide at the "stoichiometric" composition[7, 18, 21, 22, 23]. Aselage and Emin proposed an alternative model of the boron carbide solid solution; a) the saturated carbon composition near the carbon rich limit close to 20 at% has a $B_{11}C$ icosahedra and a C-B-C intericosahedral chain; b) between B_4C and $B_{13}C_2$, substitution of carbon by boron occurs primarily in the chains and c) beyond $B_{13}C_2$, boron rich boron carbide is formed by replacement of some carbon atoms in the $B_{11}C$ icosahedra by boron atoms to B_{12} icosahedra[24, 25]. An increase in the thermal factors of the chain disappearance in the Raman band linked to the chain with the increase in the B:C

ratio was provided as direct evidence to support this structural model. But questions are raised regarding the validity of this structural model, due to the varied interpretation of the results.

Werheit et al. proposed that boron carbide structure consists of distorted B_{12} or $B_{11}C$ icosahedra and C-B-C, C-B-B, B-Va-B and C-C-C chains[26]. From IR absorption spectra and phonon oscillator strength analysis, "stoichiometric" boron carbide was deemed to consist of $B_{11}C$ icosahedra (100%), C-B-C (81%) and B-B-C chains (19%)[26, 27]. At $B_{13}C_2$, the $B_{11}C$ structural units are replaced by B_{12} icosahedra and concentration of the structural elements comprised of B_{12} icosahedra (42%), $B_{11}C$ icosahedra (58%), C-B-C (62%), C-B-B (19%) and B-Va-B (19%). Beyond the critical 13.3 at% carbon concentration, an increase in the B-B-C chains is observed with a further increase in the concentration of the B_{12} icosahedra. Saal et al. used an ab initio approach to predict the crystal structure of boron carbide across the solubility range to develop a better understanding of the disordering mechanisms present across the single phase regime[28]. At the carbon rich solubility limit, theoretical calculations based on the enthalpy of formation and infrared mode calculations pointed towards the $B_{11}C$ (C-B-C) structure to be the stable atomic configuration. Preferential substitution of the boron atoms occur in the icosahedra towards 13.3 at% resulting in B_{12} (C-B-C) structures. At carbon concentrations beyond 13.3 at%, boron atoms replace the carbon atoms of the 3 atom chain which is coupled by simultaneous removal of the central boron atom resulting in the formation of a B_{12} (B-Va-C) type structure. Based on the enthalpy of formation, this structure is the preferred atomic configuration among the different ordered structures. Further validation of the proposed structural model was also conducted by investigating the vibrational properties through ab

initio phonon calculations. The shift in the mode from 13.3 to 20 at% was precisely reproduced using the proposed structural model[28].

Multiple phase diagrams of boron carbide have been proposed and the solubility range of carbon in boron carbide is a much disputed issue. One of the first B-C phase diagrams was published by Meerson et al.[3] (Figure 3). The results included the presence of a carbon rich BC_2 and boron rich $B_{12}C$ phase in addition to $B_{13}C_2$ and B_4C over a wide homogeneity range. It was concluded that the boron carbide that was formed, did so in accordance to the peritectic reaction L+B → B_4C at 2250°C. A eutectic reaction L→ B_4C + Graphite at 2150°C and 30.2 wt% carbon was also reported[3, 29]. Based on the phase diagram by Dolloff, rhombohedral $B_{13}C_3$ had a wide solubility range above 1800°C[30] (Figure 4). Clark et al. pointed out that boron carbide could exist from $B_{4.67}$ to B_4C due to the interstitial substitution of boron in the boron carbide holes[31]. Different Russian authors showed that the formation of various boron carbide solid solutions occurred by substitution with covalent bonding[5]. In the phase diagram advocated by Elliott, the carbon solubility limits of the boron carbide phase ranged from 9 at% to 20 at% from room temperature to 2450°C. The melting of the carbide phase occurs congruently at 18.5 at% carbon and 2450°C[29]. The eutectic reaction occurs at 29 at% carbon and 2375°C. Various other phase diagrams have been presented in the literature[32, 33, 34, 35]. A large number of boron carbide phases have been reported over the years. B_6C, BC, B_2C_2, B_3C B_7C, $B_{12}C$, $B_{50}C_2$, $B_{12}C_3$ and $B_{13}C_2$ are only a few of the reported phases that have been published[2, 4, 8, 32, 36, 37, 38]. B_nC solid solutions has also been proposed with n ranging from 2.57 - 24[8, 10, 29, 34, 39, 40]. Hence there is disagreement among the boron carbide community as to the actual carbon limits for boron carbide.

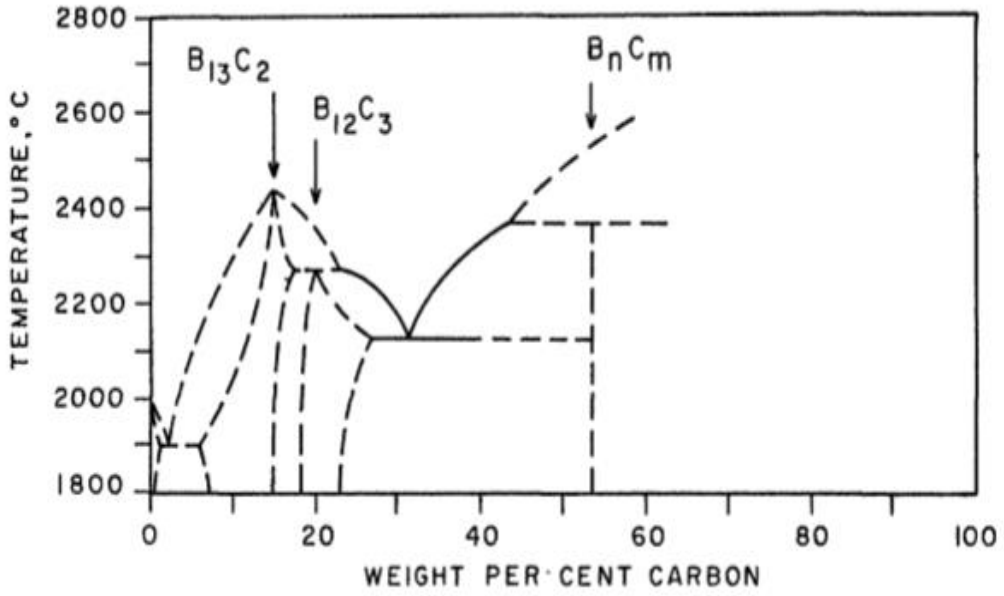

Figure 3. Boron-Carbon phase diagram proposed by Meerson et al.[4]

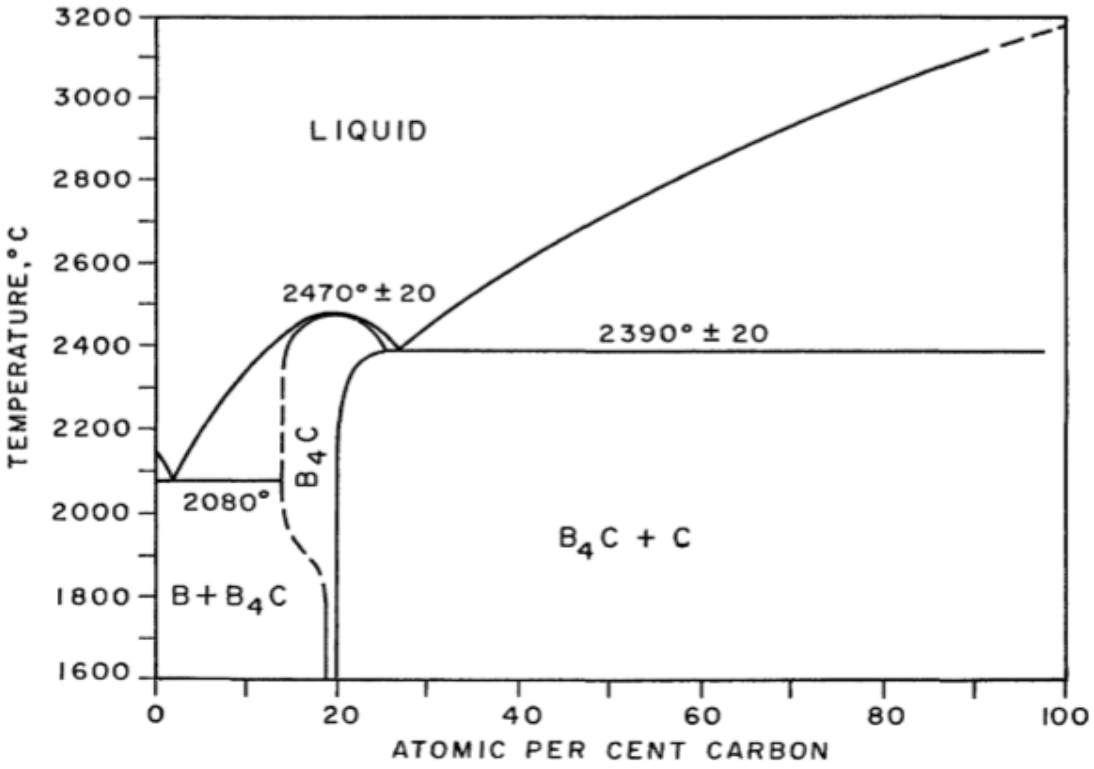

Figure 4. Boron-Carbon phase diagram proposed by Dolloff[30].

Beauvy et al. studied the stoichiometry of boron carbide by synthesizing a large number of carbon rich boron carbide using two different processes; 1) arc melting of mixed B_2O_3 and carbon; 2) magnesothermal reaction of boron oxide, carbon and magnesium[8]. The samples were then characterized using chemical analysis and XRD. From the results of these analyzes, the limiting composition of boron carbide on the carbon rich side was estimated at $B_{3.63 \pm 0.18}C$ or 21.6 ± 0.8 at% carbon. The compositions of the magnesothermal reaction products were at this limit and the stability was not affected by the high sintering temperature. The products from arc melting however, gave more varied results in the range of 21.15 - 19.1 at% carbon. The key points from the phase diagram proposed by Beauvy suggest that the eutectic (E) was not detected in boron carbide less than 24.3 at% carbon at high temperatures (Figure 5). The free carbon that typically occurs in boron carbide beyond the limiting composition is a result of solid state phase transformations taking place during cooling. Single phase boron carbide melted congruently at 2450°C and 18.4 at% carbon which agreed with the results from Elliott et al.[8, 29]. Thevenot investigated the phase diagram by synthesizing samples by hot pressing and melting. The samples were then characterized with electron probe microanalysis and XRD. The results from these analyses showed that the solubility of carbon in boron carbide extends from 9 – 20 at% carbon (Figure 6)[7]. More recently a new phase diagram was proposed by Schwetz et al.[9]. Samples with different synthesis techniques were prepared for analysis. Electron probe microanalysis was used to determine the total carbon, and these results were compared to the results using chemical analysis. The total boron, oxygen, nitrogen and metals were

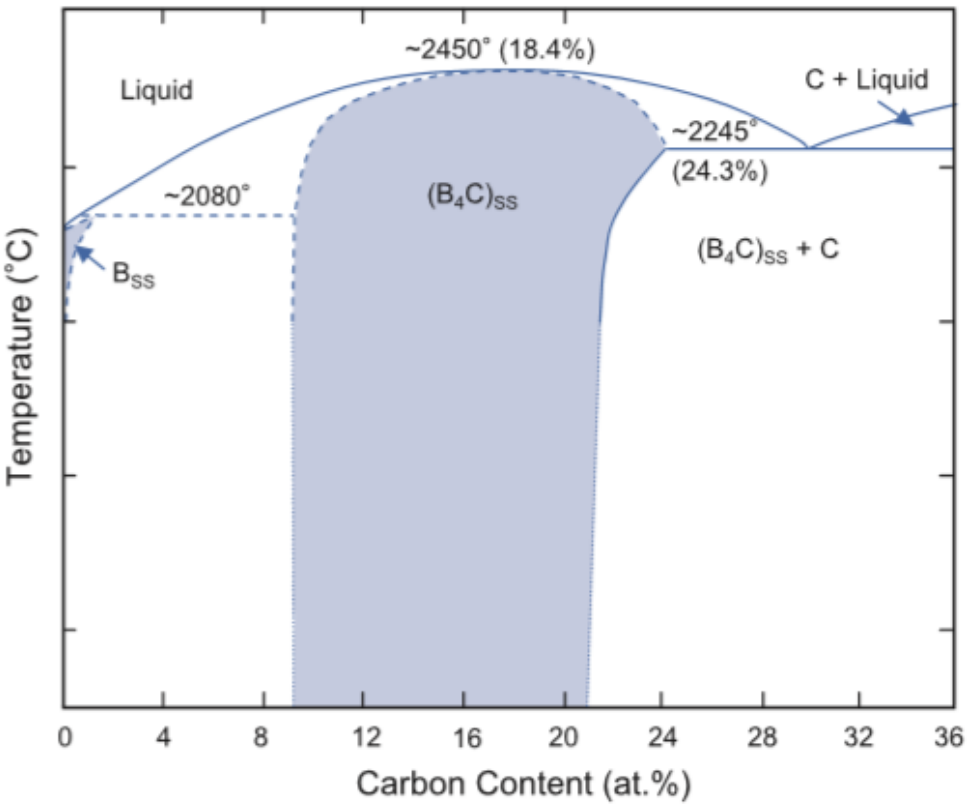

Figure 5. Boron-Carbon phase diagram proposed by Beauvy[8].

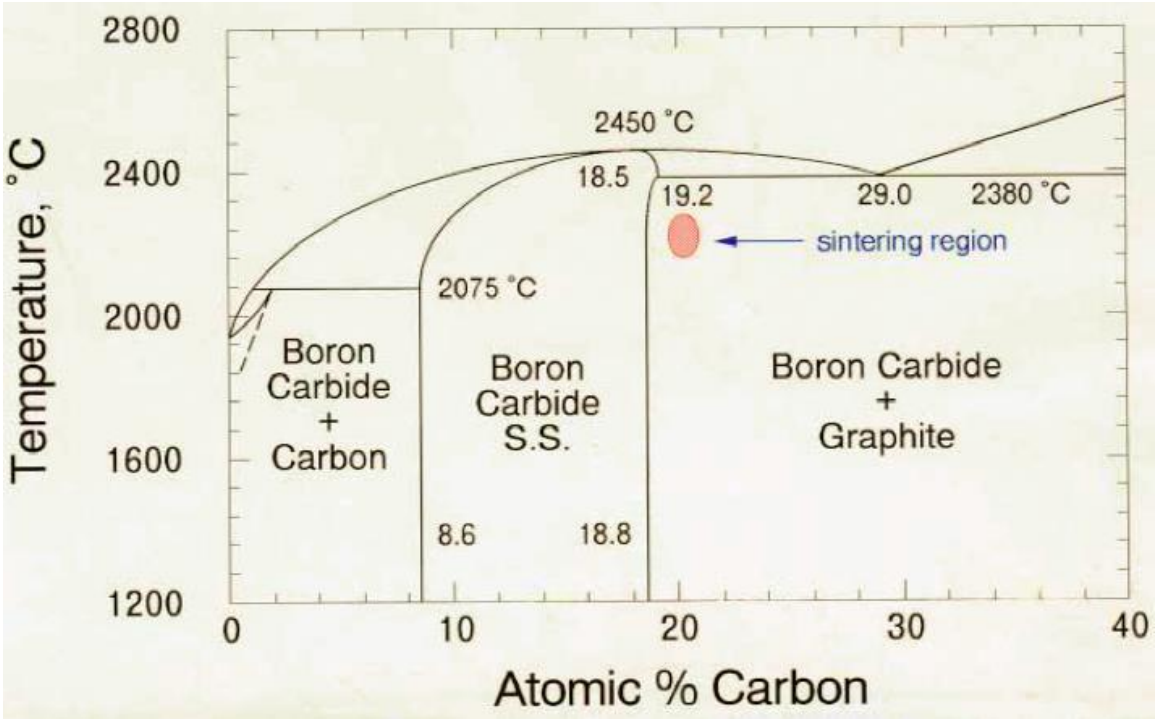

Figure 6. Boron-Carbon phase diagram proposed by Schwetz[9].

determined using various other chemical techniques. The results from these analyses revealed that the rhombohedral boron carbide phase could only accommodate 19.2 at% carbon at the eutectic temperature of 2380°C. At room temperature, the limit of the boron carbide homogeneity range on the carbon rich side was established at 18.8 at%. These results indicate that the stoichiometry of the boron carbide on the carbon rich side is $B_{4.3}C$ irrespective of the starting synthesis method[9]. Hence, it is very evident that there is large disagreement in the boron carbide community about the true solubility limits and this thesis will aim at trying to rectify some of the underlying questions relating to these results.

1.3 Synthesis of Boron Carbide

1.3.1 Carbothermal Reduction

Carbothermal reduction is a highly economical method to produce boron carbide with commercially available raw materials. The source of boron is typically boron oxide or boric acid with petroleum coke or coal providing the source of carbon. Carbothermal reduction is highly endothermic (ΔH = 1812 kJ/mol) and follows the reaction:

$$2\ B_2O_3 + 7\ C \rightarrow B_4C + 6\ CO \quad (1)$$

This process takes place with boron oxide undergoing reduction in the first stage followed by the reaction of the pure boron with carbon to form boron carbide.

$$B_2O_3 + 3\ CO \rightarrow 2\ B + 3\ CO2 \quad (2)$$

$$4\ B + C \rightarrow B_4C \quad (3)$$

The difficulties typically encountered in boron carbide arise from the fact that for each kg of boron carbide about 3 kg more carbon monoxide is produced as compared to any other carbide. Hence boric acid could also be used as a source of boron. If boric acid is used as a starting material for the boron source then the equations proceed as follows:

$4\ H_3BO_3 \rightarrow 2\ B_2O_3 + 6\ H_2O$ (4)

$B_2O_3 + 3\ CO \rightarrow 2\ B + 3\ CO2$ (5)

$4\ B + C \rightarrow B_4C$ (6)

In addition to the above equations other secondary reactions also occur which influence the product due to the water vapor. Hence the effect of the volatility of water vapor needs to be taken into consideration during the production of boron carbide.

1.3.1.1 Arc Furnace Process

The arc furnace process for the synthesis of boron carbide has been patented by Vogt et al.[41]. In this method, boric acid and carbon are melted and the melt is then crushed and mixed with the same amount of boric acid. The mixture is then effectively melted again by heating it in an electric arc furnace to the melting point. There is heavy loss of boron due to the formation and evaporation of oxides. The localized regions near the electrodes reach extremely high temperatures. A typical furnace run could take between 18 - 20 hrs. The mixture in the furnace will usually be of sufficient depth to minimize the spitting out of molten globules[42]. The final product consists of an ingot with several areas consisting of reacted and unreacted material. Generally the material closer to the electrode consists of fully reacted boron carbide. The material then undergoes various crushing and grinding operations.

1.3.1.2 Acheson Type Process

Acheson furnaces use electrical resistance heating to produce silicon carbide and boron carbide. The yield of the product is highly dependent on the length of the furnace and rate of power input. Most Acheson furnaces are shaped like a trough with graphite electrodes situated on each end of the furnace. At the beginning of each run the trough is

filled with the partially reacted mix followed by installation of the graphite core. After this the furnace is again mixed with a new mix containing the carbon and boron source for the formation of the boron carbide. During the heating process boron oxide melts and forms a glassy layer on the surface of the mix. Bubbles are formed due to the gases which causes the mix to spurt out, thus decreasing the efficiency of the procedure. After completion of the reaction the boron carbide collects around the graphite rod in the center and the reacted boron carbide is then typically separated from the unreacted boron carbide manually[43].

1.3.2 Magnesothermal Reduction

Boron carbide can also be produced by the addition of magnesium to boron oxide in the presence of a carbon source. This synthesis method of boron carbide takes place by the following method:

$$2\ B_2O_3 + C + Mg \rightarrow 2\ B_4C + 6\ MgO \quad (7)$$

The mechanism for this reaction can be explained by the following two reactions:

$$2\ B_2O_3 + 6\ Mg \rightarrow 4\ B + 6\ MgO \quad (8)$$

$$4\ B + C \rightarrow B_4C \quad (9)$$

One drawback with this method is that the final product of boron carbide contains magnesium oxide and magnesium borides as impurities. The final particle size of the product is controlled by the preliminary reactants used. This process is commercially unviable due to the high cost of the magnesium[43].

1.3.3 Chemical Vapor Deposition

Chemical vapor deposition (CVD) is a very common technique used in laboratories for the synthesis of boron carbide. This method allows significant control of the microstructure and the stoichiometry of boron carbide due to the carbon source used and

the mass transfer and surface kinetics[44]. Various techniques have been developed for the formation of boron carbide films such as plasma enhanced CVD, hot filament CVD, laser CVD etc.

1.4 Physical Properties of Boron Carbide

1.4.1 Density

The theoretical density of boron carbide (B_4C) at 20°C is 2.52 g/cm^3. The density follows a linear relationship with the carbon content and increases with the increase in the carbon content according to the following equation[7].

Density (d), g/cm^3 = 2.4224 + 0.00489 C at% ,(r=0.998), where 8.8 at% $\leq$ C $\leq$ 20 at%.

The density of $B_{13}C_2$ was measured as 2.488 g/cm^3 and $B_{10.4}C$ as 2.465 g/cm^3.

1.4.2 Coefficient of Thermal Expansion

The ratio of the degree of expansion to the change in the temperature of the material is called the coefficient of thermal expansion.

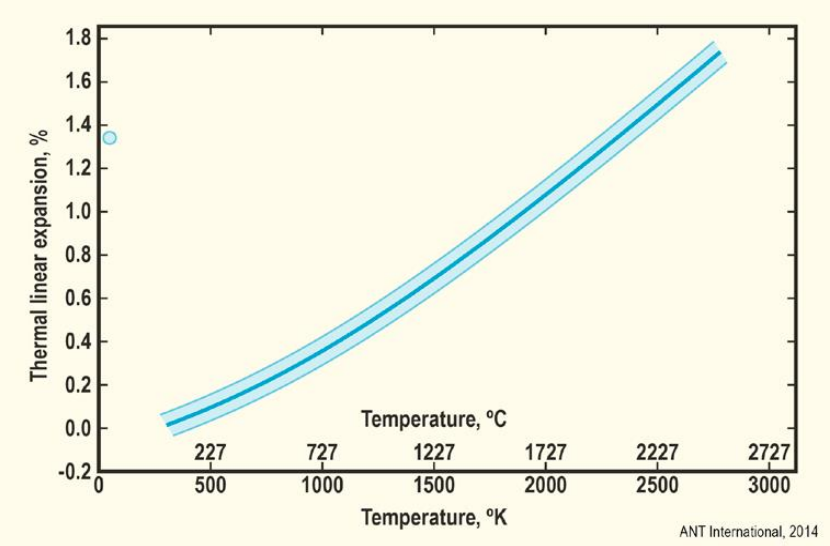

Figure 7. Variation of the thermal expansion coefficient of boron carbide with temperature.

The coefficient of thermal expansion varies with the change in the temperature (Figure 7) according to the equation:

$\alpha = (3.016 \times 10^{-6}) + (4.30 \times 10^{-9})\,T - (9.18 \times 10^{-13})\,T^2$ where T is in °C (10)

$\alpha = 5.79 \times 10^{-6}\ K^{-1}$ (300°K to 1970°K) (11)

$\alpha = 4\text{-}8 \times 10^{-6}\ K^{-1}$ (25°C to 800°C) (12)

1.4.3 Thermal Capacity

Thermal capacity or the specific heat is the ratio of the heat added to an object to the change in the temperature due to the heat added. The variation of the thermal capacity of boron carbide with the temperature is determined by the equation below:

$Cp\ (J/g) = 1.714 + 39.8 \times 10^{-5} - 97 \times 10^{3}T^{-2} + 488 + 10^{10}\ T^{-2} \exp(-33 \times 10^{3}/T)$ where T is in Kelvin.

1.5 Neutron Absorbing Capability

Boron carbide is a neutron absorber and can be used to control the reactivity of nuclear reactors due to the nuclear reactions that take place between B^{10} and n^{1} [45].

$B^{10} + n^{1} \longrightarrow Li^{7}\ (0.84\ MeV) + He^{4}\ (1.47\ MeV) + \gamma\ (0.48\ MeV)\ 94\%$ [45] (13)

$B^{10} + n^{1} \longrightarrow Li^{7}\ (1.02\ MeV) + He^{4}\ (1.78\ MeV)\ 6\%$ [45] (14)

Boron has a high neutron capture cross section. The isotope of boron with atomic mass of 10, is generally found in natural boron at 18.8% and in boron carbide at 14.7%. It provides an absorption cross section for thermal neutrons of 4000 barns[46]. Boron carbide at “stoichiometric” composition exhibits a capture cross section of 600 barns. Secondary gamma radiation for boron is low as compared to other rare earth elements. Boron carbide is thus extensively used in nuclear reactors because of its high melting point and good chemical and physical stability as compared to other elements like cadmium. Moreover the

use of boron carbide is more economical for use in neutron protection as compared to other rare and expensive elements like gadolinium, europium, samarium and dysprosium[46]. Boron carbide is also utilized with natural isotope distributions as considerable quantities of He can be trapped in the boron carbide lattice as most of the boron atoms are the B^{11} isotope.

1.6 Mechanical Properties

Boron carbide is an extremely hard ceramic and only diamond and boron nitride are harder at room temperature. Most other carbides and borides have much lower hardness values as compared to boron carbide as shown in Table 1[46]. The hardness of boron carbide surpasses them at temperatures exceeding 1100°C[47, 48]. This high hardness and low density of boron carbide enable it to be used in a variety of applications. Hardness measurements in boron carbide are difficult due to the inhomogeneity and the presence of free carbon. The results of the hardness values for boron carbide are also scattered due to different sample preparation techniques and measurement conditions[7]. Typically, Knoop hardness is used as a reference for boron carbide and varies linearly with the carbon content[1].

Table 1. Knoop hardness values of carbides and borides at 100 g load[46].

Material	Hardness (kg/mm^2)	Material	Hardness (kg/mm^2)
B_4C	2900 - 3100	TiB_2	2500 - 2600
SiC	2300 - 2600	B	2400 - 2500
TiC	2100 - 2200	BeB_2	2100 - 2300
WC	2050 - 2150	ZrB_2	1800 - 1900
ZrC	2000 - 2100	CaB_4	1600 - 1700

After polishing, the Knoop hardness was estimated at 2910 ± 90 kg/mm^2 for 10.6 at% carbon[1]. With the increase in the carbon content to 20 at% carbon, the Knoop hardness value increases to 3770 ± 90 kg/mm^2 [1]. Variations in the mechanical properties of boron carbide can be traced back to microstructural variations in the carbon content, grain size, inhomogeneity and residual porosity[45]. The yield strength of boron carbide is directly related to the hardness. Values of the yield strength σ have been reported to be in the 300-370 MPa range. An overview of the mechanical properties of boron carbide are detailed in Table 2[49].

Table 2. Mechanical Properties of Boron Carbide[49].

Mechanical Properties	
Hardness – Knoop (kgf/mm^2)	1400 - 3400
Hardness – Vickers (kgf/mm^2)	2800 - 3500
Compressive strength (MPa)	3200
Tensile Modulus (GPa)	440 - 470

The strength and hardness of boron carbide decreases with the increase in the porosity and grain size by the Hall-Petch relation[1, 50, 51, 52]. Based on this relation, yield strength increases with the decrease in the grain size. When the grain size is decreased, the ratio of the grain boundaries to the grain increases, resulting in more frequent dislocations occurring at the grain boundaries. The Hall-Petch equation is denoted as follows:

$$\sigma_Y = \sigma_0 + \frac{K_Y}{D^{0.5}} \quad (15)$$

where σ_Y is the yield stress, σ_0 is the friction stress, k_Y is the material property strengthening coefficient and d is the diameter of the grains. This dependence of the hardness and the

fracture toughness to the grain size was observed by Hyukjae et al. in pressureless sintered boron carbide[53].

Conflicting reports have been published as to the effect of the stoichiometry on the mechanical properties. There is no clear indication about the effect of stoichiometry on hardness[46, 54, 55]. Kieffer et al.[54] proposed that hardness values increase in the $B_{4+x}C$ direction. Niihara et al. prepared 1-3 mm thick boron carbide plates by chemical vapor deposition and performed hardness measurements using a Vickers indenter at a load of 0.98 N[56]. The maximum hardness and fracture toughness was observed at "stoichiometric" compositions. The hardness values decrease with the increase in the B/C ratio at temperatures ranging from 1400°C to 1900°C as shown in Figure 8[56].

Consolidated boron carbide tiles were prepared by Ceradyne Inc. by hot pressing mixtures of amorphous boron and boron carbide[57]. Hardness measurements were then performed using a Knoop indenter at a load of 0.3 kg[57]. The report published by Ceradyne Inc. suggested that the hardness values followed an opposite trend to the Niihara data as

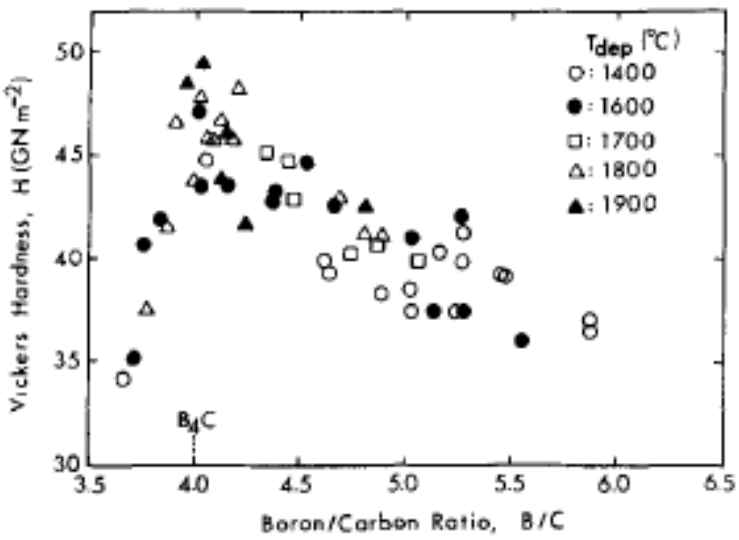

Figure 8. Variation of the Vickers hardness as a function of the B/C ratio at different temperatures and load of 0.98 N[56].

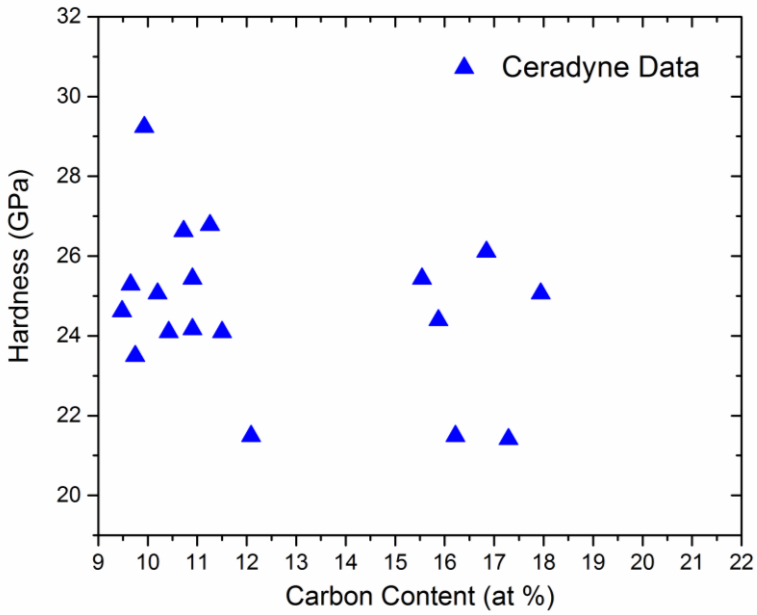

Figure 9. Effect of stoichiometry on the hardness of hot pressed boron carbide at a load of 0.3 Kg[57].

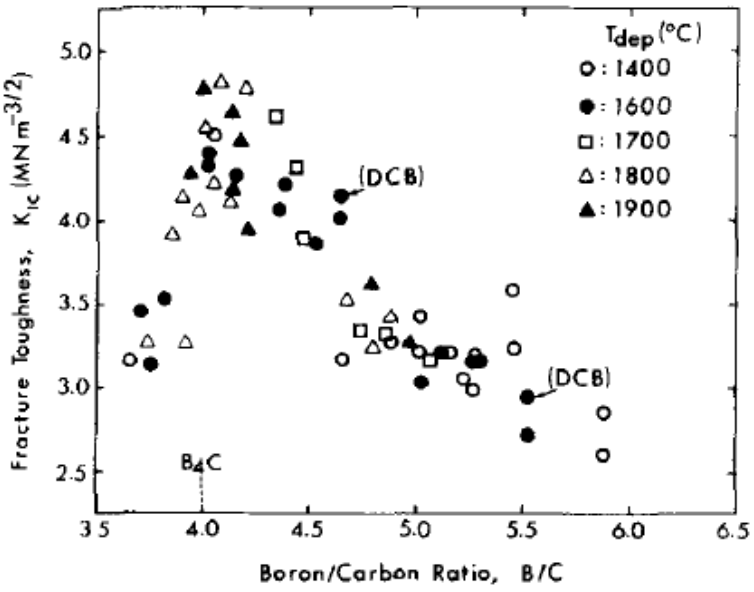

Figure 10. Variation of the fracture toughness (K_{IC}) as a function of the B/C ratio[56].

seen in Figure 9[56, 57]. The maximum Knoop hardness was obtained at stoichiometries close to $B_{13}C_2$ or $B_{6.5}C$ suggesting that the hardness increases with the increase in the B/C ratio. Boron carbide has a very low fracture toughness (K_{IC}) and values extend from 3 - 4 MPa

$m^{1/2}$. The fracture toughness remains relatively constant at higher temperatures. Figure 10 shows the variation of K_{IC} with the B/C ratio for chemically vapor deposited boron carbide[56]. Maximum fracture toughness values were observed at "stoichiometric" compositions similar to the hardness results. At elevated temperatures, wear resistance and coefficient of friction decreases due to the formation of boron oxide and boric acid on the surface of the boron carbide[46]. The fracture toughness remains relatively constant at higher temperatures.

1.7 Elastic Properties

Boron carbide with its rhombohedral symmetry has anisotropic elastic properties. Based on $B_{5.6}C$ single crystal data using resonant ultrasound spectroscopy, the Young's Modulus (E) has values ranging from 523 GPa on c = [0001] to 63 GPa in the orthogonal direction, thus having an anisotropy ratio of 8.1[6, 58]. The Young's Modulus was determined to be independent of the orientation along the (111) plane, but variations existed on the prismatic and basal planes[6, 58] (Figure 11). The Young's Modulus was estimated at 470 GPa for isotropic determination. The maximum Young's Modulus aligned with the [111]

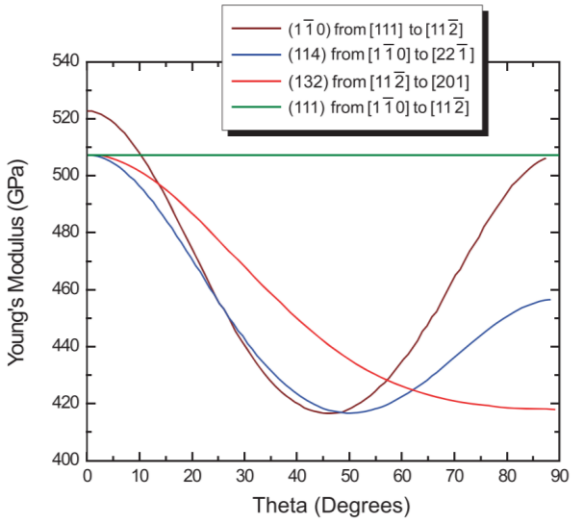

Figure 11. Young's modulus dependence on the orientation for a $B_{5.6}C$ single crystal[6, 58].

direction indicates higher stiffness of the crystal along the chain axis. Table 3 shows the elastic anisotropic factors of the $B_{5.6}C$ single crystal which signify substantial anisotropic elasticity[58]. Comparing the Poisson's ratio of this crystal with other solids, it is evident that the bonding in boron carbide is dependent on the orientation as depicted in Table 4[58].

Table 3. Effect of anisotropy on the elastic properties of boron carbide[58].

Anisotropy Factors	c_{33}/c_{11}	c_{13}/c_{12}	$2c_{44}/(c_{11}-c_{12})$
$B_{5.6}C$	0.98	0.49	0.8

Table 4. Poisson's ratio of boron carbide and other solids[58].

Poisson's Ratio	$B_{5.6}C$	Ti	Zr
$\nu_{31} = - s_{13}/s_{33}$	0.0940	0.265	0.300
$\nu_{12} = - s_{12}/s_{11}$	0.2297	0.486	0.396
$\nu_{13} = - s_{13}/s_{11}$	0.0912	0.188	0.238

The elastic properties of boron carbide depend on the B:C ratio and decreases with the increase in the boron content[1, 51] as evidenced by Table 5 . The Bulk Modulus (K) and Shear Modulus (G) are approximated at 243 GPa and 197 GPa[1]. The Poisson's ratio of boron carbide is low and can be estimated at 0.18[1]. Gieske et al. produced high quality hot pressed boron carbide samples free from secondary phases for elastic property investigations[59]. The absence of secondary phases, eliminated any inconsistencies in the elastic properties data. Carbon rich areas which were typically seen during hot pressing due to the contact of the sample with the die were ground off. Ultrasonic techniques were used in the elastic property measurements. Experimental results revealed that the elastic moduli decreases with the decrease in the carbon concentration (Figure 12)[59]. The maximum value of the Young's Modulus was obtained at a carbon concentration close to

20 at%. A distinct feature of the data is observed at a carbon concentration of ~13.3 at%. A kink is observed at this carbon concentration in the Elastic, Bulk and Shear moduli curves. This kink in the curve is similar to the kink seen in the correlation of the lattice parameters and the carbon content. This is indicative of the distinct mechanism of substitution of the boron atoms in the 12 atom icosahedra and the chain units. Longitudinal and shear velocities also decrease when the carbon content drops below 13.3 at%[59]. At carbon concentrations below 13.3 at%, boron carbide become highly compressible. Manghnani et al.[60] found that a linear relationship existed between the elastic moduli and the pressure up to 21 GPa. The Bulk moduli results obtained by Manghnani et al. were consistent with the values reported by Nelmes et al.[61].

Table 5. Dependence of the Elastic Moduli and the Poisson's ratio on the stoichiometry[6].

Stoichiometry	at% Carbon	Bulk Modulus		Young's Modulus [GPa] exp	Shear Modulus [GPa] exp	Poisson's Ratio [GPa] exp
		Exp	Cal			
B_4C	20	247e	246e	472c	200c	0.18c
		235e	234g	462e	197e	0.17e
		199d	248h	448b	188a	0.21b
			239i	441a		
			220d			
$B_{4.5}C$	18.2	237c		463c	197c	0.17c
$B_{5.6}C$	15.2	236c		462c	197c	0.17c
		237f		460r	195f	0.18f
$B_{6.5}C$	13.3	231c	217g	446c	189c	0.18c
			227i			
$B_{7.7}C$	11.5	178c		352c	150c	0.17c
B_9C	10	183c		319c	150c	0.21c
		130c		348c	132c	0.16c

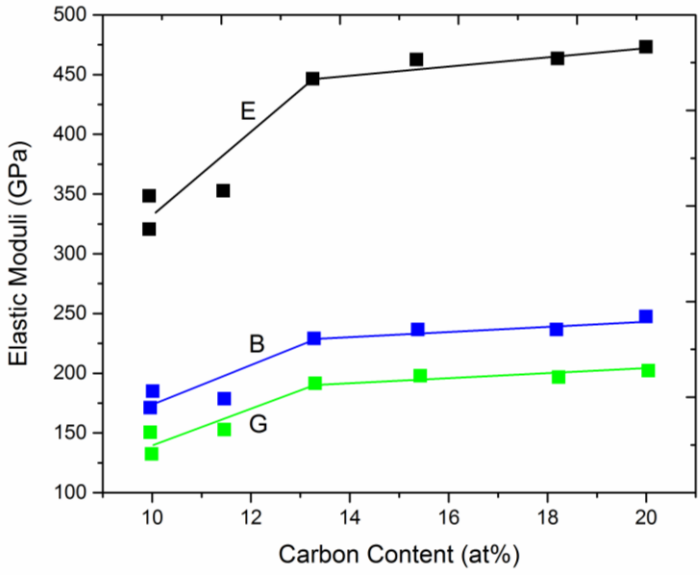

Figure 12. Dependence of the elastic moduli on the carbon concentration.

1.8 Chemical Properties

Boron carbide is a stable compound and is not attacked by cold chemical reagents but by hot oxidizing agents. Molten alkali can decompose boron carbide to form borates. It can readily react with metal and metal oxides at temperatures exceeding 1000°C to form carbides and borides[62]. Etching with hydrogen is a slow process and takes place at 1200°C, but it withstands metallic sodium at 500°C[23]. Carbon can be dissolved in boron carbide at the B_4C-C eutectic temperature of 2400°C[23, 30]. Fine boron carbide powders form B_2O_3 and H_3BO_3 at the surface due to the presence of oxygen and moisture in the air. Water vapor reacts with boron carbide at temperatures as low as 250°C[63]. During hot pressing, oxidation of boron carbide starts at 600°C and forms a thin layer of B_2O_3 on the surface[62]. The reaction that occurs during the oxidation process is as follows:

$$B_4C + 4O_2 = 2B_2O_3 + CO_2 \quad (16)$$

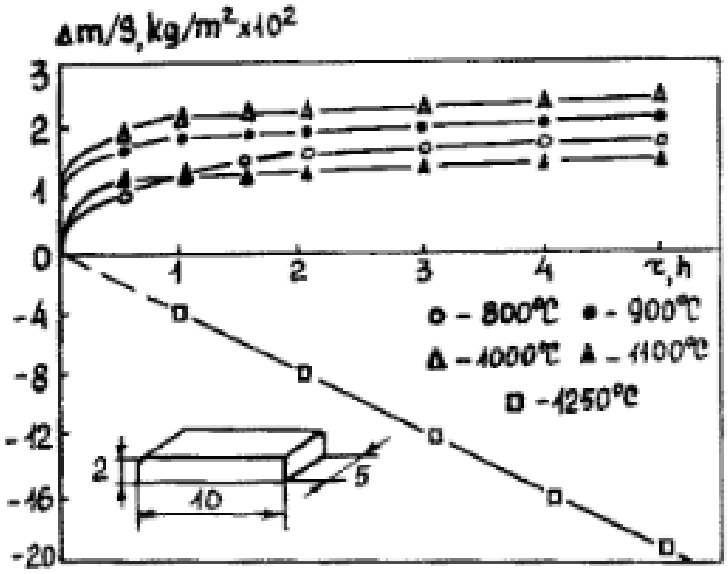

Figure 13. Kinetic curves for the oxidation of boron carbide[62].

From Figure 13, it is evident that there is a weight gain in the samples up to 1100°C and from 1200°C there is a loss in the weight of the sample indicating that the boron oxide formed on the surface of the boron carbide vaporizes at temperatures up to 1100°C. Above this temperature the oxidation is dependent on the rate of the reaction. The glassy B_2O_3 layer formed cracks during cooling[62]. High temperature oxidation studies were also conducted by Steinbruck et al[64]. Multiple boron carbide specimens were investigated under different atmospheres at temperatures ranging from 800°C to 1600°C. In these measurements, change in the mass was not measured, but the release rates of the gaseous reaction products were considered. The oxidation kinetics of boron carbide in steam were the result of two processes; 1) formation of liquid B_2O_3 which acts as a diffusion barrier for the raw materials and products. This process is dependent on the temperature and follows parabolic kinetics; 2) the second process involves evaporation of the B_2O_3 and the concurrent products with steam and is highly dependent on the temperature and surrounding conditions and follows linear kinetics[64]. Figure 14 shows the oxidation

behavior of boron carbide in dry air[64]. At lower temperatures, the rate of weight change remains relatively constant. With the increase in the temperature, a linear weight gain is observed which is due to the formation of a glassy layer of boron oxide on the surface of the boron carbide particles. Conversely, in an air-water system, at temperatures ranging from 200-340°C, the weight change remains constant as seen in Figure 15[64]. With a further increase in temperature to 600°C, weight loss is observed. This weight loss is because of the formation of a gaseous molecule of boric acid from the reaction of boron oxide and water vapor. At 700°C, weight gain occurs followed by a subsequent weight loss. The weight gain is due to the boron oxide formation. Once the maximum weight gain has been achieved, the boric acid formation supersedes the boron oxide formation resulting in a weight loss of the resultant oxidized material.

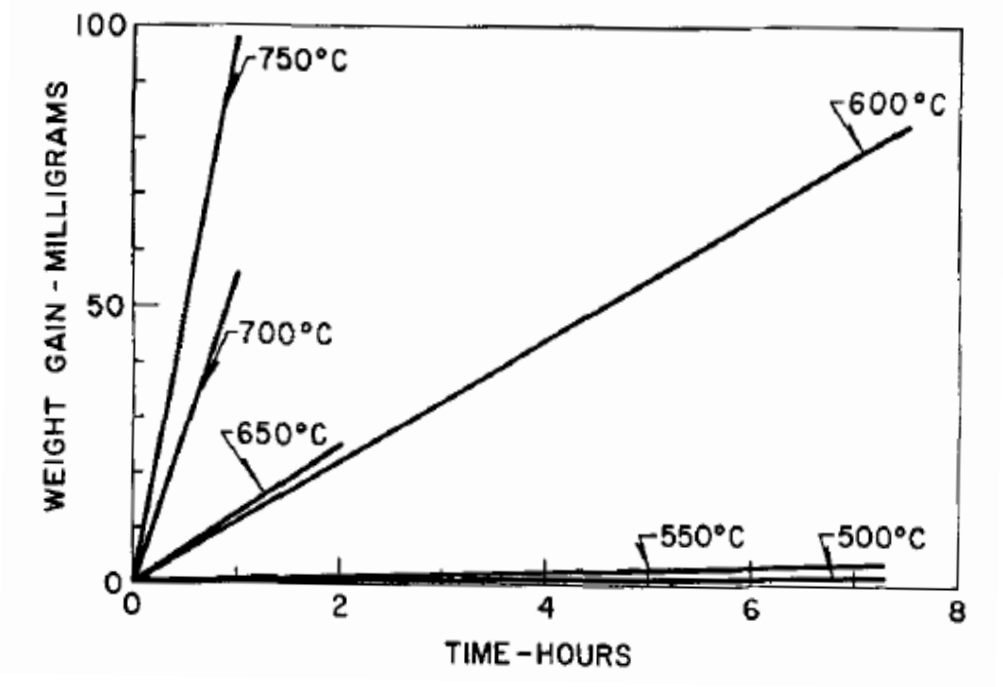

Figure 14. Oxidation of boron carbide in dry air[64].

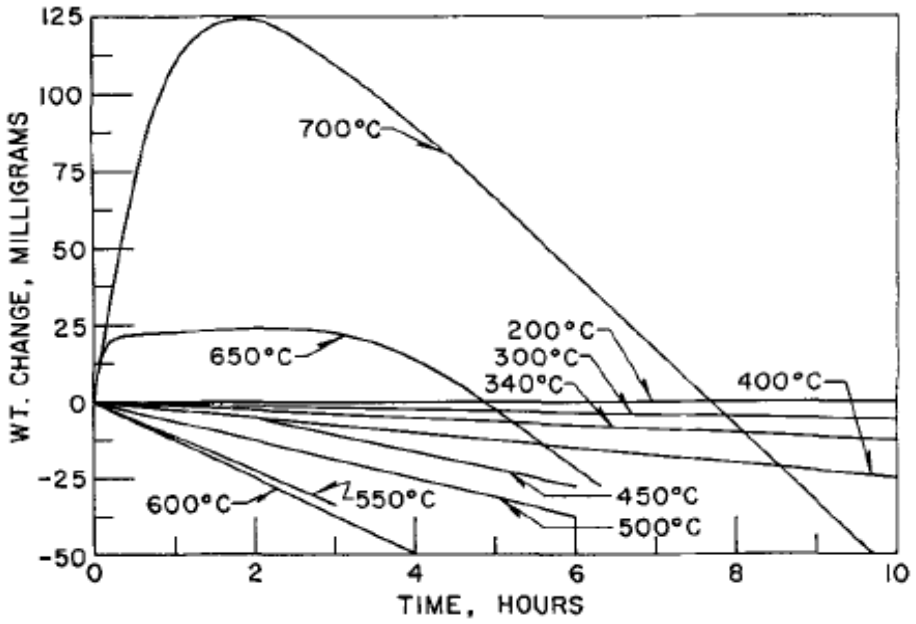

Figure 15. Oxidation of boron carbide in an air-water system[64].

1.9 Microstructural Response to Dynamic Loading

The low density and high hardness of boron carbide make it a prime candidate for armor applications. Understanding the physical process of armor penetration is important to obtain a clearer picture of development of the material system in armor applications. This is shown in Figure 16. Initially when the projectile strikes the plate, the tip of the projectile is destroyed initiating an axial crack in the ceramic. The ceramic then erodes the projectile which causes it to be turned into rubble from coalescing cracks in the fracture conoid. Almost half of the projectile mass and the initial projectile energy is transferred to the eroded projectile material. Generally, erosion is caused because the stress levels on the projectile are greater than the strength of the material of the projectile. The projectile yields and starts to flow perpendicular to the impact. This process of erosion of the projectile will continue until the stress levels achieved fall below the yield strength of the projectile. Soon

this erosion of the projectile stops. The total energy of the system is 60% of the original energy and this is then absorbed by the backup plate. This occurs due to the loss in the mass of the projectile. Hence boron carbide is a good candidate for armor applications as it can potentially withstand longer dwell times and erode the projectile as a result of its high hardness[49, 65, 66].

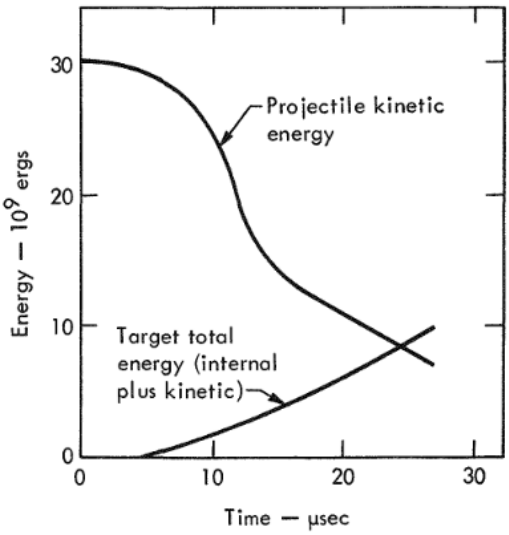

Figure 16. Energy vs time curve for an impact at 2800 ft/sec of a sharp projectile[65].

Boron carbide, inspite of its high hardness shows anomalous fracture behavior at stresses approaching the Hugoniot Elastic Limit (HEL). This is due to its low density, low fracture toughness and the activation of an unidentified damage mechanism at high strain rates and pressures[67]. There is an abrupt drop in the shear strength at loading pressures of 20 GPa. One of the reasons for the drop in the strength could be due to the change in the fragmentation behavior. Literature on the shock response of boron carbide suggests that localized softening or melting occurs under shock wave loading and release. When the HEL is breached, boron carbide deforms plastically and experiences brittle failure (Figure 17)[49, 68]. From the shock compression data (Figure 18) reported by different authors[65, 69, 70, 71, 72, 73, 74, 75, 76], phase transformations might be occurring under loading. High resolution

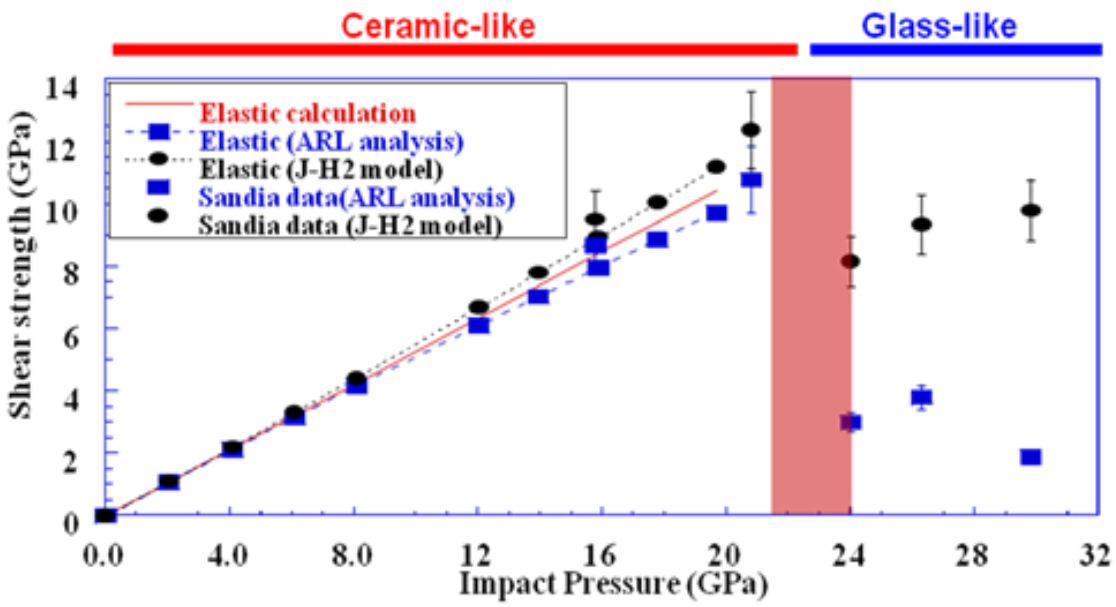

Figure 17. Ballistic impact data from independent experiments conducted at the Army Research Laboratory and Sandia National Laboratory depicting the drastic decrease in the shear strength of boron carbide above the HEL of 20 GPa[49, 68].

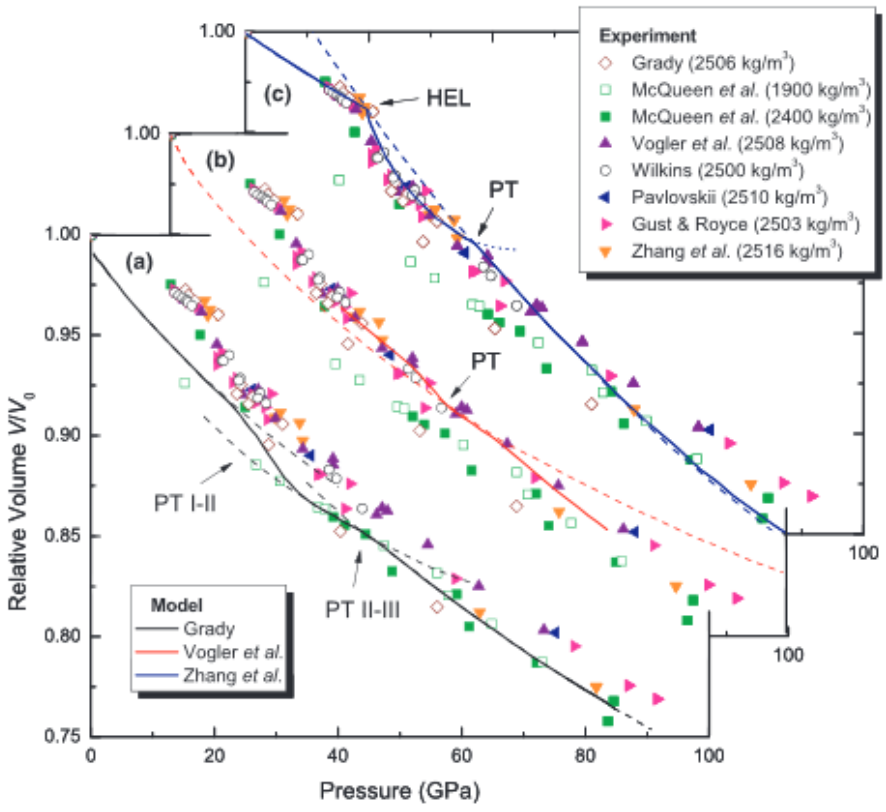

Figure 18. Shock compression data of boron carbide[6].

electron microscopy (HREM) was used to identify the damage mechanism in hot pressed boron carbide (Figure 19)[67]. Armor piercing rounds at velocities from 750 – 1000 m/s were used for ballistic testing with impact pressures varying from 19 to 25 GPa causing complex loading states. HREM showed the damage zones exhibited a loss of lattice fringes indicating the occurrence amorphization. Due to the planarity of the amorphous bands, the amorphous zones align along particular crystallographic planes. Based on low magnification HREM observations the overall orientation of these bands was parallel to the (113) and $(2\bar{1}3)$ planes.

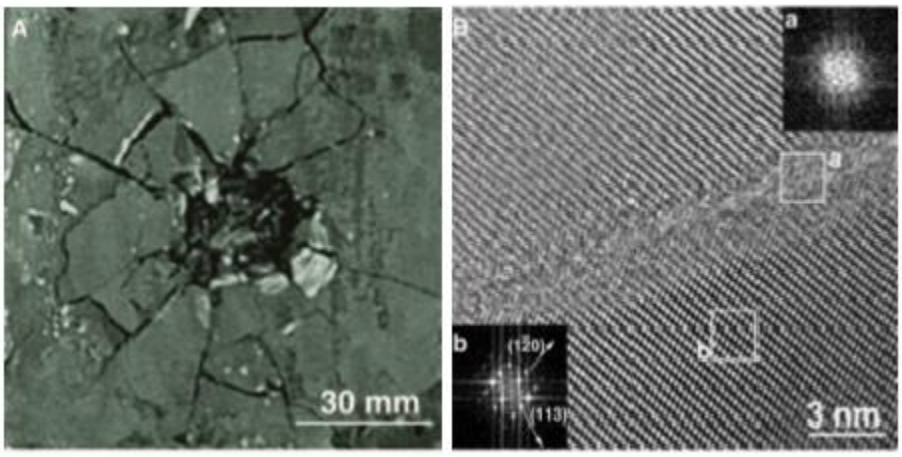

Figure 19. Left : Ballistically impacted boron carbide. Right : HR TEM of a fragment showing the loss of lattice fringes in the band indicating localized amorphization[67].

In addition to contact loading, indentation and scratch tests also caused amorphization. Nanoindentation provides hardness or elastic moduli information of the material that is being investigated and also gives an understanding of the variation of these properties with the depth of penetration of the indenter based on load displacement curves[77, 78]. Nanoindentation is a powerful tool that has direct relevance to realistic loading conditions while reaching pressures in the range of 40 – 45 GPa. In nanoindentation, typically a spherical or Berkovich diamond indenter is utilized resulting in deviatoric

stresses at the contact area. Nanoidentation studies conducted on (0001) and $(10\bar{1}1)$ faces of a $B_{4.3}C$ single crystal showed changes in the Raman spectra of the indented areas suggesting that structural changes, such as stress-induced amorphization occur in boron carbide under static contact loading (Figure 20)[79]. High and low temperature Raman spectroscopy of pressure induced amorphous boron carbide demonstrated that amorphization of B_4C was associated with the breaking of the C-B-C chain[80]. The absence of the boron phases in the Raman spectra of the pressure induced boron carbide indicated that the $B_{11}C$ icosahedra of boron carbide remained intact during loading.

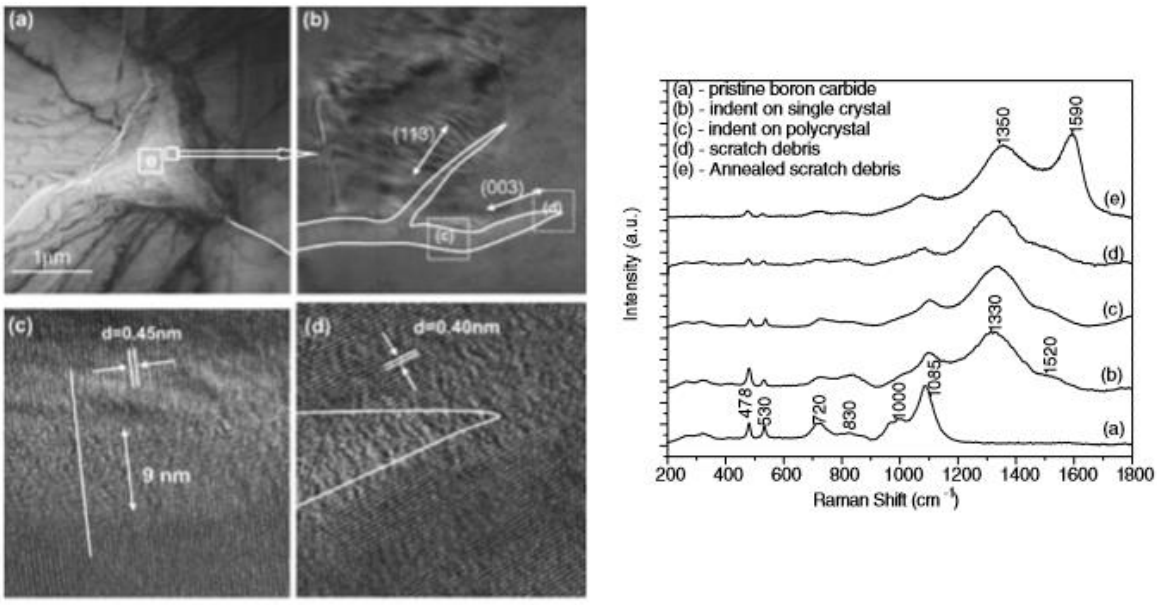

Figure 20. Left : (a) Plan view of TEM micrograph of a 100 mN Berkovich indent, (b) Magnified image showing amorphous bands along the (113) and (003) directions, (c) and (d) HR lattice images on (a) and (b). Right : Raman spectra of a (a) Pristine single crystal $B_{4.3}C$, (b) Indented single crystal, (c) Indented hot-pressed polycrystalline material, (d) Scratch debris of a single crystal and (e) Annealed scratch debris in air by using an argon ion laser with excitation wavelength of 514.4 nm[79].

HRTEM on scratch debris of single crystal and polycrystalline boron carbide showed the formation of nanocrystals and nanoscale lattice distortion[77]. Random grain

distribution was observed which could either be due to the breakage of lattice bonds or a result of solid-state phase transformation occurring under high contact pressures[77].

The effect of the stoichiometry on the mechanical properties of icosahedral boron carbide under loading was studied theoretically by Taylor et al. using density functional theory and quantum molecular dynamic simulations[81]. Placement of carbon atoms in the icosahedra resulted in monoclinic distortion of the structure which reduced the crystal symmetry. B_{12}(C-B-C) showed a reduction in the final stiffness results. All materials exhibited softening of the C_{44} modulus regardless of the final stoichiometry.

1.10 Electrical and Optical Properties

Boron carbide is a p-type semiconductor with a much smaller band gap as compared to other semiconductor ceramics. Due to the wide compositional range of boron carbide, varying band gaps have been reported by a number of authors over the years[6, 26].

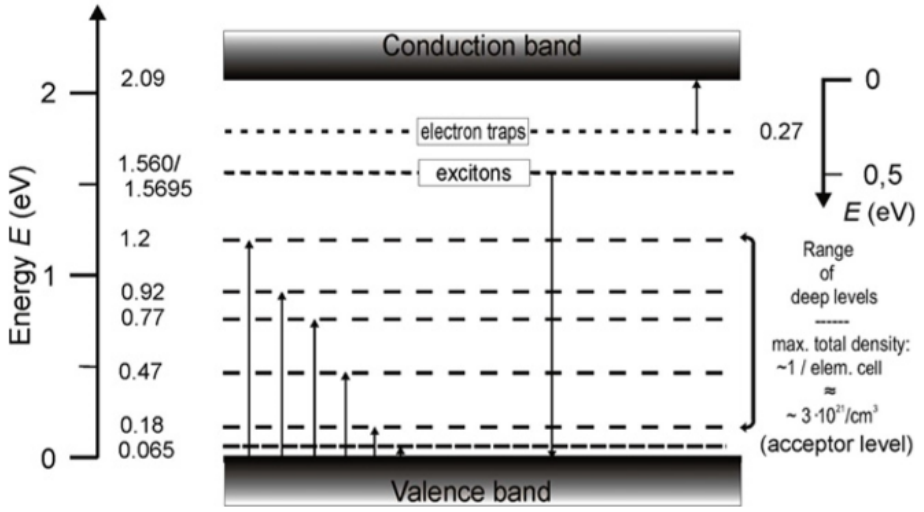

Figure 21. Energy band scheme of boron carbide[26]

Values ranging from 0.8 eV to 2.09 eV have been reported based on experimental data (Figure 21)[26, 82, 83, 84]. Based on electronic band structure calculations stoichiometric B_4C was confirmed to be a semiconductor[6, 85].

It was suggested that this semiconducting nature of boron carbide is due to the structural disorder that exists across the homogeneity range. According to Werheit, this semiconductor behavior could be attributed to the role of Jahn-Teller distortion of the 12 boron atom icosahedra causing a separation of occupied and unoccupied electronic states. Valence electron deficiencies in boron rich compounds enabled them to be characterized as metallic in nature. The energy band scheme based on the optical absorption, luminescence, XRS and transport properties as shown in Figure 21[26].

2 Goal of Thesis

Boron Carbide has a wide compositional range, varying from ~9 at% to ~20 at% carbon and the stoichiometric formula of boron carbide is a much disputed area. Understanding the "true" carbon limits of boron carbide at room temperature and refinement of the analytical methods for the determination of the boron carbide stoichiometry is of primary importance as dynamic response of boron carbide varies with stoichiometry[57]. Furthermore, using these developed techniques to investigate the variation in the structural properties of boron carbide across the compositional range would provide insight regarding the variability of the atomic configurations at different B:C ratios. Additionally, understanding how the presence of a particular polytype affects the mechanical properties would shed some light on the preferred composition and purity of boron carbide required for extreme dynamic environments. This goal will be achieved by examining and then refining existing characterization techniques with the aid of X-ray diffraction (XRD), chemical analyses and Raman spectroscopy. The results from the structural and mechanical characterization could then be applied to boron carbide ceramics to understand and control dynamic failure processes in order to improve performance.

3 Assessment of Current Analytical Techniques for Determination of the Boron Carbide Stoichiometry

3.1 Introduction

The first objective of this thesis is to assess the current analytical and chemical techniques used for the characterization of boron carbide and to evaluate the possible sources of error associated with the reported stoichiometry. This work on boron carbide will be performed by characterizing commercial boron carbide samples with the focus on understanding purity and stoichiometric variations. For this task, the comparative analysis of boron carbide produced by H.C. Starck (Germany), Ceradyne Inc. (Germany), Superior Graphite (US), UK Abrasives (US) and Vajrabor (India) will be performed by means of X-ray diffraction, Raman spectroscopy and chemical methods.

X-ray diffraction (XRD) will be performed on these commercial samples to determine the typical primary and secondary phases present. Different Powder Diffraction Files (PDF) will be examined for phase identification. The stoichiometry from these PDF cards will be compared to the stoichiometric results obtained using lattice parameter measurements and chemical analysis. A major problem with the existing International Crystal Structure Database (ICSD) is the lack of accuracy of the different PDF cards for boron carbide. This is due to inconsistencies in the boron carbide chemistry of the PDF cards and the corresponding line positions and unit cell data. Quantitative analysis on the samples will be performed using Rietveld Refinement[86]. The peak fitting functions which include the Gaussian, Lorentzian, Pseudo-Voight and Pearson VII functions will be extensively examined to determine the appropriate function required to provide accurate quantitative analysis. X-ray fluorescence (XRF) scans will help identify the metallic

impurities present which would further aid in determining the trace phases present that cannot be easily identified using XRD. The total boron present in the boron carbide samples will be evaluated using boron titration. LECO CS230 will be used to obtain the total carbon present and the total oxygen and nitrogen present will be determined using LECO TC600. The data from these analyses will then be used to calculate the final stoichiometry of the boron carbide samples. An assumption made during the determination of the final stoichiometry is that the total oxygen and nitrogen present in the resulting samples are present either as boron oxide or boron nitride. The assumptions made here portrays the existing thought process of most authors with regards to the determination of the stoichiometry. Little importance is given to the soluble boron and boric acid measurements which can affect the boron available for boron carbide, which in turn further alters the B:C ratio. Hence, in addition to the chemical analyses performed at Rutgers, samples will also be sent to an external analytical company (Washington Mills, USA) for the determination of the soluble boron content and the boric acid present.

The lattice parameters of these samples will be measured by applying the Rietveld Refinement procedure to the XRD data. Initially, the lattice constant-stoichiometry relationship developed by Aselage et al.[13] would serve as a basis to measure the bound carbon concentration. Owing to the scatter of this data, multiple fits will be evaluated to assess the effect of the fit on the stoichiometric results. A further detailed analysis on other lattice constant-stoichiometry relationships will be thoroughly evaluated in **Section 5**. A comparative study on the stoichiometric results from the unit cell constants and chemical analysis will be conducted. After the completion of this comparative study, comments will

be made about the possible sources of error associated with the chemical analysis and lattice parameter-stoichiometry calibration curves.

Following a detailed analysis of the commercial powders mentioned above, boron carbide samples with varying particle sizes from Vajrabor (India) will be investigated to determine the effect of washing and particle size on the final stoichiometry. The powders will be exposed to atmospheric air for a period of 2-3 weeks. Following the exposure period, these powders would then be characterized using the different analytical and chemical characterization techniques mentioned earlier. The next step would involve washing the powders to eliminate any surface oxides and boric acid which may have accumulated on the surface of the particles as a result of prolonged atmospheric exposure. This step will be followed by determination of the stoichiometry and comparison of these results to those obtained prior to washing. Furthermore, assessing the particle size distribution would aid in comprehending the effect of particle size on the O/N accumulation levels and more importantly, the resultant stoichiometry.

Raman spectroscopy will be performed to help complement the chemical and structural results obtained using x-ray diffraction and chemical analysis on a microscopic level. The Raman spectra will be acquired from randomly selected areas in order to obtain statistically significant results. Data analysis will be performed using the curve fitting algorithms available in the Renishaw Wire software package. Statistical analysis will be conducted on the Raman spectra, taking into consideration the peak center, width, height, area, low edge and high edge, in order to obtain the most representative spectrum for each of the powders. To alleviate possible atomic and microstructural variations across the surface of each sample, curve fitting procedure will be applied to all data and the results

will be treated statistically assuming normal distributions. It is essential to note whether the carbon concentrations obtained by Raman measurements are commensurate with those obtained from the XRD data, which could suggest that Raman spectra could also be used for evaluation of the boron carbide stoichiometry.

Finally, more commercial powders will be acquired from various boron carbide manufacturers to help understand the commercial variability in powders and ceramics. The results from XRD, chemical analysis and Raman spectroscopy will be tabulated to form a database which will serve as a basis for any future work done in this area.

3.2 Experimental Procedure

3.2.1 X-ray Diffraction (XRD) and Rietveld Refinement

X-ray diffraction was performed using a single crystal silicon wafer. The powder was dispersed on the wafer surface using methanol and flattened with a glass slide to ensure the specimen remained within the cavity of the holder to prevent sample displacement errors. Utilizing a silicon wafer over a bulk holder is advantageous as a result of reduced peak asymmetry, which typically occurs in materials with low atomic numbers because of reduced absorption of x-rays. The zero background holder is also preferred over a bulk holder because of the low background of the monocrystal holder and ability to use considerably smaller quantities of samples[87]. For high quality data and Rietveld refinement, it is essential that the powder diffraction data were collected appropriately. Various factors were considered prior to data collection such as diffractometer geometry, quality of alignment of the instrument, suitable radiation, wavelength, sample preparation, thickness, slit sizes and counting time[88]. For high resolution and for easy deconvolution of the complex diffraction pattern of boron carbide, care was taken to achieve the optimal

conditions for the XRD scans. The XRD scans were then taken using a Panalytical X'Pert system (Figure 22) with a Cu x-ray source at 45 kV and 40 mA over a continuous scan range of 10° to 90° 2θ; at a virtual step size of 0.0131° and counting time of 198.645 seconds. In the incident beam path, an anti-scatter slit of 1° and divergent slit of 1/2° were used. The diffracted beam path had an anti-scatter slit of 9.1 mm. The sample was rotated at a speed of 4 seconds per rotation in order to randomize particle orientation. Similar conditions will be used throughout this thesis. Minor deviations in the standard sample preparation techniques will be discussed in the appropriate section.

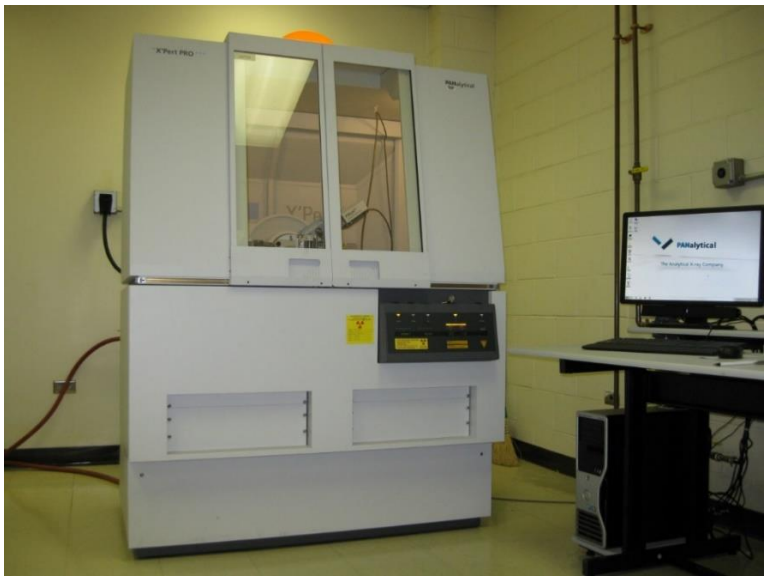

Figure 22. Panalytical X'Pert powder X-ray Diffractometer.

Phase analysis was conducted using MDI Jade version 9.0 software followed by quantitative analysis by whole pattern fitting and Rietveld refinement. An accurate description of the peak shape was critical to the results from Rietveld refinement[88]. Before structural or profile refinement is conducted, the positions of the observed and calculated peaks should agree. This was controlled by refining the global parameters. These include, the zero offset and 2θ correction which account for errors due to sample displacement

caused during sample preparation. Alternatively, NIST line position standards were also used during sample preparation specifically on those specimens whose lattice parameters were to be determined. The initial assumption made pertaining to the structural model is important and should not deviate significantly from the observed models. The shapes of the peaks observed are dependent on the sample and instrument. From the numerous analytical peak-shape functions, the Pseudo-Voigt approximation was used for refinement in this thesis. Atomic scattering factor (f), Lorentz polarization absorption factor (LPA), Multiplicity (P), Structure factor (F) and Temperature factor (B) are the main contributors to the peak intensity of the x-ray diffraction patterns and the parameters that were considered during Rietveld refinement. Variation of the intensity is given by the equation developed by Hugo Rietveld shown below[89, 90]:

$$I = [F^2(f,h,k,l)]\,[LPA\,(\theta,\mu)]\,[P]\left[e^{-B(sin\emptyset/\lambda)^2}\right] \quad (17)$$

The Pseudo-Voigt function was used to fit the peak shape during refinement[89, 90, 91] and is given as:

$$P(t) = \eta\, L(t,\Gamma) + (1-\eta)G(t,\sigma) \quad (18)$$

The Pseudo-Voigt function, which is a convolution of the Gaussian and Lorentzian functions was used to fit the peaks. Mixing parameter (η), standard deviation (σ) and position ($t=2\theta-2\theta_0$) are the variables considered in the Pseudo-Voigt function[89, 90]. Once the appropriate structural model and peak profile was chosen, Rietveld refinement was performed. While the refinement is being carried out, it should constantly monitored due to the high probability of false minima occurring during refinement of powder diffraction data. Lattice parameters were calculated using a hybrid whole pattern fit/least squares refinement. Lattice parameters had an average precision of +/- 0.0003 angstroms using this

method. The difference between the calculated and observed patterns was defined in terms of the residual error or R value obtained. During Rietveld refinement, it was ensured that the R values were between 3-5% to attain significant agreement between the calculated and observed XRD patterns. In the case of consolidated boron carbide ceramics, sample preparation was done using a dense sample holder which consisted of a cavity within which the dense ceramic was placed using putty. During sample preparation, it is imperative to align the dense ceramic with the holder to prevent errors due to specimen displacement.

3.2.2 X-ray Fluorescence (XRF)

The X-ray fluorescence (XRF) scans were taken using a QuanX X-Ray fluorescence spectrometer (Figure 23) with an excitation voltage of 20KV, live time of 100 sec and a Paladium filter. XRF scans were taken under vacuum rather than in argon atmosphere to ensure minimal contamination in the resultant XRF spectra. The scans were run at a low, medium and high atomic number to detect the full range of mainly metallic impurities present in most commercial and Rutgers University boron carbide powders. The typical XRF sample holder consists of two parts; a double open-ended cup and snap ring as shown in Figure 23. An Ultralene polymer film is placed over the ring and held taught to remove any wrinkles. The ring is then placed on top of the film and snapped into place

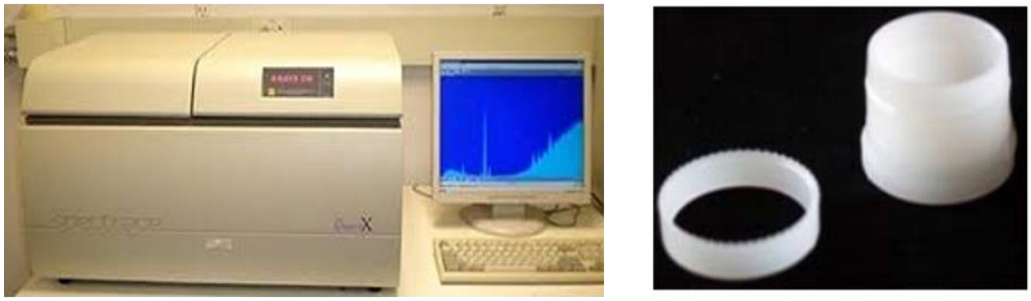

Figure 23. Left: Quanx X-ray Fluroscence Spectrometer. Right: Sample holder used for XRF measurements.

ensuring no tears are present in the film. The powder or dense material is added into the cup and a second film and snap ring are put onto the top of the cup to prevent any spillage incase the powder is to be analyzed. XRF spectra were analyzed using KLM markers which superimpose the screen lines corresponding to the expected position of the emission lines for each element.

3.2.3 Raman Analysis

Vibrational properties were probed by Raman Spectroscopy. Raman spectroscopy analysis was performed using a Renishaw InVia® unit (Figure 24) equipped with a 633 nm wavelength laser and a 1200/mm diffraction grating. 20x to 100x objective lenses were used which permitted the laser beam to be focused onto a 4 μm^2 to 1 μm^2 area on the sample surface. On each sample, spectra were acquired from several selected areas in order to obtain statistically significant results. Data analysis was then performed using curve fitting algorithms available in the Renishaw Wire software package. Statistical analysis was also conducted on the Raman spectra, taking into consideration the peak center, width, height, area, low edge and high edge to obtain the most representative spectrum for each of the powders.

Figure 24. Renishaw InVia Reflex Raman Microscope.

3.2.4 Chemical Analysis

3.2.4.1 Boron Titration

Boron titration was performed using a Metrohm Titrando 907 with multiple dosing units for mannitol, acid and base solutions (Figure 25). The Tiamo software enables the detection of multiple inflection points accurately. The total boron content in the powder was determined according to ASTM C791-04[92]. This method involves fusing a mixture of boron carbide powder and alkaline reagent. The resultant melt was dissolved in water, filtered to remove the insoluble residue, acidified and heated to remove the carbon dioxide. The boron was then measured after titration with sodium hydroxide. First, 2 g of Na_2CO_3 were added to a 30 ml platinum crucible along with 0.13 to 0.15 g of boron carbide powder. 100 mg of potassium nitrate were then added to the crucible and thoroughly mixed with the help of a short length of wire. An additional 2 g of Na_2CO_3 were added to completely cover the above mixture. The crucible was then placed in a muffle furnace and heated to 600°C at 10°C/ min. Once this temperature was attained, the crucible was further

Figure 25. Metrohm Titrando 907 used for boron titration.

heated to 1000°C at 3°C/min and held at this temperature for 20 min. The crucible was removed from the furnace and placed in a boron free beaker on cooling. Nitric acid (3.5 N) was added along the rim of the crucible to dissolve the melt. The beaker was filled with distilled water up to the level of the crucible, covered with parafilm and allowed to sit overnight for complete dissolution of the melt. After the fused residue had completely dissolved in the melt, the solution was boiled gently for 15 min to remove carbon dioxide. Nitric acid was added to attain a pH of 3 ± 0.1 in the solution. This solution was titrated with 0.25 N NaOH to find the first potentiometric end point. Then, 20 g of mannitol was added and after the mannitol had completely dissolved, the solution was titrated again with 0.25 N NaOH to determine the second potentiometric end point. Based on these results, weight of the boron carbide initially added, normality of the NaOH and reagent blanks, the total boron was calculated using the relationship detailed below:

$$\text{Boron, weight \%} = \frac{(T_S - R)NA}{W_S} \text{ X } 100 \quad (19)$$

where T_s is the ml of NaOH used in the titration of the sample, R is the reagent blank, N is the normality of the NaOH solution, A is the atomic weight of the boron computed for the sample based upon the measured isotopic composition and W_S is the sample weight (mg). Soluble boron was determined by Washington Mills using ASTM C791-12[92].

3.2.4.2 Total Carbon Analysis

The total carbon was determined using combustion techniques with a LECO CS230 instrument (Figure 26). This method evaluates the total carbon content in the specimen by oxidation of the sample followed by infrared detection[93]. In this method, the blank was first determined by adding one scoop of LECOCELL II (502-294) and Iron chips (502-231) into a preheated crucible followed by combustion in the instrument furnace and infrared

analysis of the resultant gases. A total of 4 blanks were run and this was then followed by running 3 standard samples. The standards were run by adding one scoop of LECOCELL II (502-294), Iron chips (502-231) and 0.25 g of LECO (501-123) into a preheated crucible followed by analysis in a similar manner to the blanks. The blanks and standards were run to calibrate the system to ensure accurate results of unknown powders.

Figure 26. LECO C/S 230 (Carbon/Sulphur Analyzer).

Following calibration of the instrument, the carbon content of the powders were determined by adding one scoop of LECOCELL II (502-294), Iron chips (502-231) and 0.08 g of boron carbide into a preheated crucible. These chips serve as accelerators to enhance the oxidation of the sample. Internally, the sample was oxidized to carbon dioxide which absorbs IR energy at a particular wavelength within the IR spectrum. The total carbon was then measured as a function of the reduction at that energy level. A total of 5 readings for each boron carbide sample were run in order to obtain statistically significant results.

3.2.4.3 Total Oxygen and Nitrogen Analysis

Similarly, LECO TC600 instrument was used to determine total oxygen and nitrogen present by combustion (Figure 27). Oxygen analysis was performed when the oxygen in the sample reacted with the carbon crucible resulting in the formation of carbon monoxide and carbon dioxide. The oxygen was then detected by IR detection of CO and CO_2 in the IR cell[94]. Nitrogen values were obtained by measuring the change in the thermal conductivity of the gas before and after combustion[94]. The boron carbide blank required a Nickel capsule (LECO: 502-822) and graphite crucible containing 0.45 g Nibble Nickel (LECO: 501-598) and 0.05 g graphite powder (LECO 502-822). Typically 4 blanks are used for analysis followed by calibration standards.

Figure 27. LECO TC 600 (Oxygen/Nitrogen Analyzer).

Three oxygen standards were run using 0.14 g (LECO: 502-399) according to the procedure detailed above. In addition to the oxygen standards, three runs of 0.5 g of nitrogen standards (LECO: 502-102) were also run to complete the calibration of the instrument. The next step involved running the unknown boron carbide samples in a similar manner to the blanks and standards. Boron carbide powder was weighed (~0.1 g) and placed in the nickel capsule followed by analysis using the LECO software. The final

results of the oxygen and nitrogen were obtained as a weight percentage. A total of 5 readings were taken for each boron carbide sample to attain statistically significant results.

3.2.5 Powder Cleaning

The cleaning procedure entailed mixing the powder (10 - 15 g) with hydrochrolic acid (3.5 pH) in an ultrasonicator for 15 minutes and heating the solution at 150°C. After the powder settled to the bottom, the excess acid was decanted. This residue was washed twice with distilled water and the excess water was decanted each time after the powder settled to the bottom of the beaker. The remaining slurry was then washed with ethanol and the excess ethanol was decanted in a similar manner to the hydrochloric acid and distilled water. The beaker was placed in a drying oven at 100°C to allow for evaporation of the moisture and residual alcohol. After the powder was dried, analysis was conducted to determine the stoichiometry of the powder after washing.

3.2.6 Particle Size Analysis

Particle size analysis was conducted using a Malvern Mastersizer 2000 with the Hydro 2000S cell (Figure 28). This instrument uses a laser diffraction technique to measure the size of the particles. The sample was analyzed by dispersing the powder in a solvent. The solvent used in the particle size analysis for boron carbide powders was deionized water. This solution was fed to the Hydro S dispersion cell after ultrasonication for 45 – 50 seconds. Ultrasonication is primarily done to break up aggregates that have agglomerated due to cohesion. This would prevent a typical bimodal distribution due to agglomeration.

Figure 28. Malvern Mastersizer 2000 Light Scattering Particle Sizer.

3.3 Results and Discussion

3.3.1 Phase Identification and Quantitative Analysis

Phase identification and quantitative analysis were performed on commercial boron carbide samples produced by H.C. Starck (Germany), Ceradyne Inc. (Germany), Superior Graphite (US), ESK (Germany) and Vajrabor (India). Phase identification on the samples revealed a major and minor phase of boron carbide and carbon respectively. Multiple Powder Diffraction Files (PDF), each with a varying B:C ratio were used to match the boron carbide phase. PDF cards are basically datasets of diffraction patterns and properties of elements and compounds. The database employed for the PDF cards was the International Crystal Structure Database (ICSD). This information was used for a basic estimation of the boron carbide stoichiometry. Based on the fit with the experimental data, it was established that the stoichiometry of the major boron carbide phase was ~B_4C (97-065-4971). Table 6 presents the theoretical 2Θ positions, relative intensities, d-spacing and indexing of boron carbide as established by Clark et al.[31]. Other PDF cards $B_{0.8}C_{0.2}$ (97-008-1961), $B_{6.5}C$ (97-000-0446) and B_4C (97-002-9093) showed deviations from the experimental 2θ positions. Exclusively using PDF cards to calculate the stoichiometry of

Table 6. Indexing, theoretical reflections and relative intensities of boron carbide[31].

2-Theta (Deg)	d(Å)	I(f)	(h k l)	Theta (Deg)	1/(2d)	2pi/d n^2
19.701	4.5027	5.3	(1 0 1)	9.85	0.111	1.3954
21.983	4.0400	17.3	(0 0 3)	10.992	0.1238	1.5552
23.476	3.7865	83.9	(0 1 2)	11.738	0.132	1.6594
31.937	2.8000	15.7	(1 1 0)	15.968	0.1786	2.244
34.886	2.5697	49.6	(1 0 4)	17.443	0.1946	2.4451
37.805	2.3778	100	(0 2 1)	18.903	0.2103	2.6425
39.111	2.3013	8.7	(1 1 3)	19.555	0.2173	2.7303
40.016	2.2513	<1	(2 0 2)	20.008	0.2221	2.7909
41.619	2.1683	<1	(0 1 5)	20.809	0.2306	2.8978
44.833	2.0200	0.2	(0 0 6)	22.416	0.2475	3.1105
48.016	1.8932	0.1	(0 2 4)	24.008	0.2641	3.3187
50.302	1.8124	6.7	(2 1 1)	25.151	0.2759	3.4667
52.084	1.7545	0.1	(1 2 2)	26.042	0.285	3.5811
53.401	1.7143	11.8	(2 0 5)	26.700	0.2917	3.6651
56.096	1.6382	0.6	(1 1 6)	28.048	0.3052	3.8354
56.379	1.6306	2.9	(1 0 7)	28.19	0.3066	3.8532
56.914	1.6166	0.5	(3 0 0)	28.457	0.3093	3.8867
58.831	1.5684	1.1	(2 1 4)	29.416	0.3188	4.0062
61.758	1.5009	9.5	(0 3 3)	30.879	0.3331	4.1863
63.586	1.4621	15.7	(1 2 5)	31.793	0.342	4.2975
64.373	1.4461	15.6	(0 1 8)	32.186	0.3458	4.345
66.276	1.4091	3.6	(0 2 7)	33.138	0.3548	4.459
66.763	1.4000	15.3	(2 2 0)	33.381	0.3571	4.488
69.780	1.3467	0.5	(0 0 9)	34.890	0.3713	4.6657
70.366	1.3369	10.8	(1 3 1)	35.183	0.374	4.6999
71.226	1.3228	10.3	(2 2 3)	35.613	0.378	4.7498
71.834	1.3131	11.9	(3 1 2)	35.917	0.3808	4.7849
73.671	1.2848	3.4	(2 0 8)	36.836	0.3892	4.8902
75.222	1.2622	5.7	(0 3 6)	37.611	0.3961	4.9781
75.466	1.2587	9.9	(2 1 7)	37.733	0.3972	4.9918
77.595	1.2294	0.2	(1 3 4)	38.797	0.4067	5.1108
78.798	1.2136	2.4	(1 1 9)	39.399	0.412	5.1773
79.360	1.2064	2.3	(4 0 1)	39.68	0.4145	5.2081
80.770	1.1889	5.2	(0 4 2)	40.385	0.4206	5.285
81.830	1.1761	1.8	(3 1 5)	40.915	0.4251	5.3422
81.855	1.1758	1.3	(1 0 10)	40.927	0.4252	5.3436
82.543	1.1678	4.6	(1 2 8)	41.271	0.4282	5.3805
84.047	1.1507	2.9	(2 2 6)	42.024	0.4345	5.4605
86.362	1.1257	0.9	(4 0 4)	43.181	0.4442	5.5818
88.093	1.1080	<1	(3 2 1)	44.047	0.4513	5.671
89.482	1.0943	1.1	(2 3 2)	44.741	0.4569	5.7416

unknown samples proves unreliable due to the lack of agreement in the stoichiometries and line positions reported in the PDF cards. This is a direct consequence of inaccuracies with regards to the chemical techniques previously employed and the assumption that boron carbide only existed at a stoichiometry of B_4C or $B_{6.5}C$. Hence using certain PDF cards to ascertain the stoichiometry leads to uncertainty in the results. The secondary phases present in the powders differed in terms of the type of carbon present. Differences in the nature of the carbon identified by XRD can be gleaned from the peak positions, FWHM and asymmetric nature of the 002 carbon peaks as will be discussed in **Section 4.** The absence of additional secondary phases of boric acid in certain powders were a result of the dispersion of the powder in methanol during XRD sample preparation. This can be rationalized from the reaction of the boron oxide with methanol resulting in a $B\text{-}OCH_3$ species which was washed away. However, in certain commercial powders, boron oxide and boric acid diffraction peaks are observed as in these cases boric acid is present in large quantities and hence is not completely washed away. Nonetheless, the boron oxide and boric acid amounts were considered based on the oxygen values obtained from chemical analysis as will be discussed in **Section 3.3.3**.

Figure 29 shows the phase identification of the XRD patterns in boron carbide samples manufactured by Ceradyne Inc. The typical primary and secondary phases present include boron carbide and carbon. Boric acid is also observed in the ATD-2012-6-20 and ATD-2012-6-58 samples which could potentially be attributed to the presence of residual reactants during synthesis of the boron carbide. Alternatively, in submicron boron carbide powders, prolonged exposure to the atmosphere may cause the residual amorphous boron to be converted to boron oxide and subsequently boric acid on contact with moisture from

the air. Moreover, the absence of significant quantities of metallic impurities provide insight regarding the purity of boron carbide samples manufactured by Ceradyne Inc. Powders manufactured by H.C. Starck on the other hand show considerably lower quantities of carbon, although impurities such as tungsten carbide are observed in trace amounts specifically in the ST-HD05 powder (Figure 30). Generally, in commercial powders grinding media is used to obtain a uniform particle size distribution. But, as a result of the high hardness of boron carbide, the ceramic media employed will inevitably lead to contamination in the resultant powder. Powders manufactured by Vajrabor are similar in terms of the primary and secondary phases to the Ceradyne samples (Figure 31). No evidence of impurities were observed within the detection limits of XRD. This could indicate that the manufacturing techniques utilized by these companies were similar in terms of the raw materials used and synthesis methods employed. Powders synthesized by ESK (ED-102) were analogous to the Ceradyne and Vajrabor samples as evidenced by Figure 32 (Top).

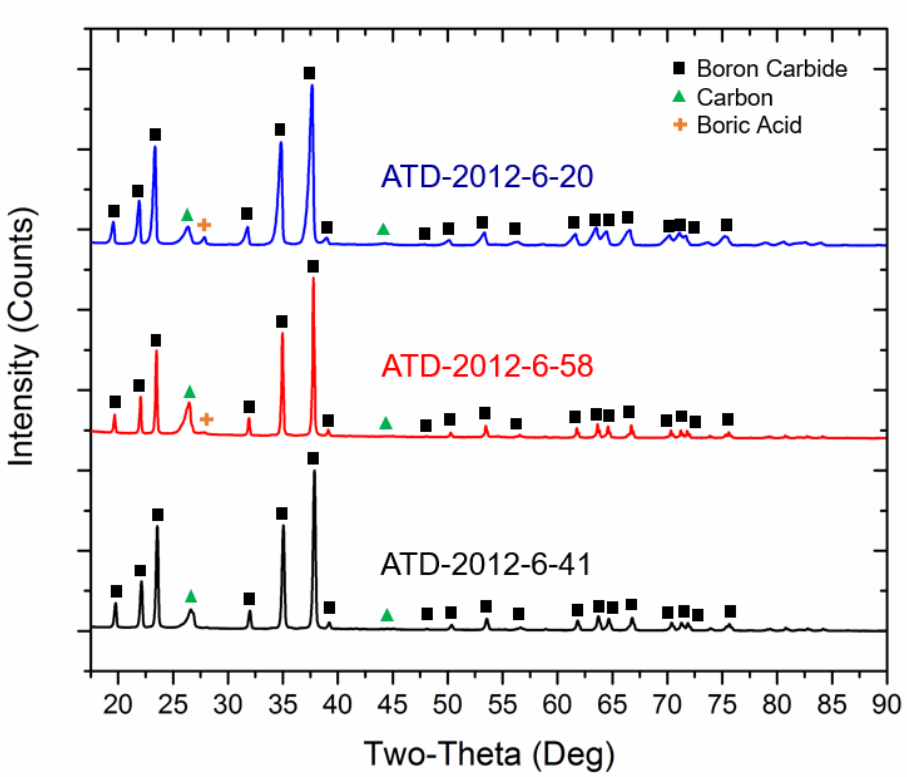

Figure 29. Phase identification of boron carbide samples produced by Ceradyne Inc.

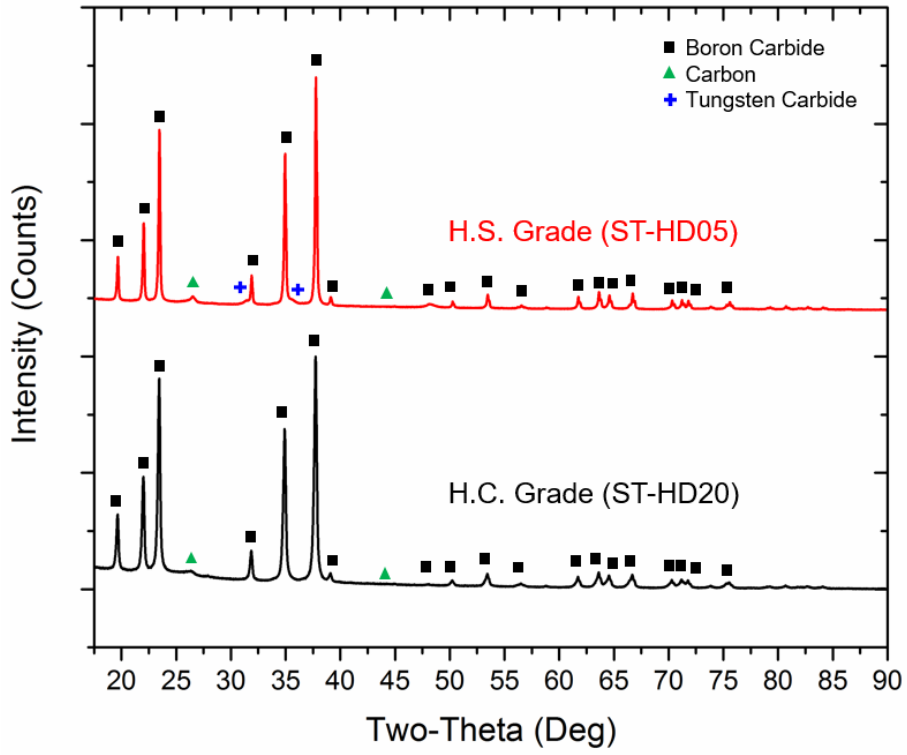

Figure 30. Phase identification of boron carbide samples produced by H.C.Starck.

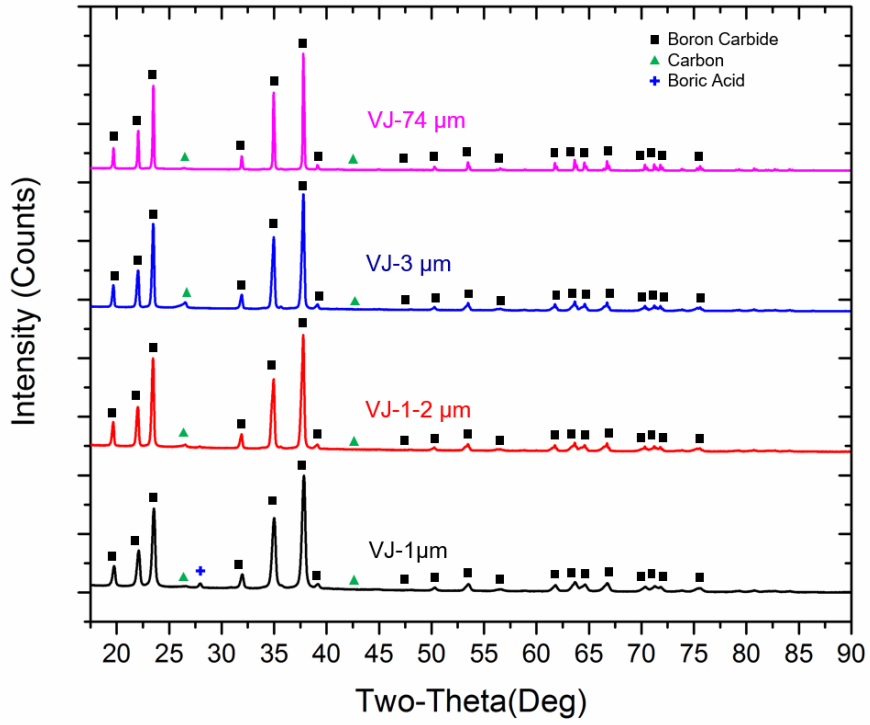

Figure 31. Phase identification of boron carbide samples produced by Vajrabor.

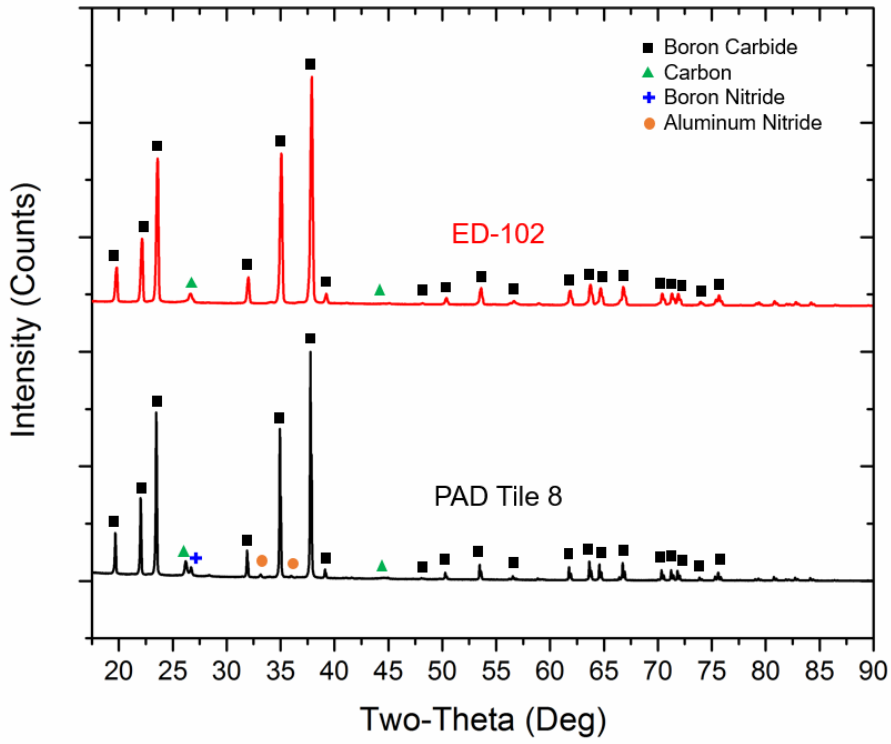

Figure 32. Top: Phase identification of boron carbide samples produced by ESK
Bottom: Phase identification of boron carbide samples produced by Coorstek.

Table 7. Summary of the results of phase identification of selected powders by X-ray diffraction.

Sample #	Sample Company	Phase Analysis					
		B_xC	Carbon	Boric Acid	Tungsten Carbide	Aluminum Nitride	Boron Nitirde
ATD-2011-8-20	Ceradyne Inc.	94.5	5.1	0.4	-	-	-
ATD-2011-8-58	Ceradyne Inc.	94.4	5.5	0.1	-	-	-
ATD-2012-6-41	Ceradyne Inc.	96.9	3.1	-	-	-	-
ST-HD05	H.C. Starck	98.8	1.1	-	0.1	-	-
ST-HD20	H.C. Starck	99.4	0.6	-	-	-	-
VJ-1µm	Vajrabor	99.7	0.1	0.2	-	-	-
VJ-1-2 µm	Vajrabor	99.6	0.3	0.1	-	-	-
VJ-3 µm	Vajrabor	99.5	0.5	-	-	-	-
VJ-74 µm	Vajrabor	99.9	0.1	-	-	-	-
Tile 8	CoorsTek	98.0	1.1	-	-	0.3	0.6
ED-102	ESK	99.5	0.5	-	-	-	-
SG-010813	Superior Graphite	97.3	2.7	-	-	-	-

Boron carbide has a low sinterability due to the strong and stable covalent bonding between atoms[95]. Densification of undoped B_4C is non-uniform and results in large porosity. On addition of sintering aids, uniform densification is observed as well as decrease in porosity. Consolidated commercial boron carbide ceramics characteristically shows the presence of multiple secondary phases. Tile 8 manufactured by CoorsTek (Figure 32, Bottom) is a prime example of a commercial boron carbide armor material where sintering aids have been added to improve the densification behavior in addition to enhancement of mechanical properties. In addition to the boron carbide matrix in Tile 8,

secondary phases of carbon, aluminum nitride and boron nitride were observed in the XRD pattern. The secondary phases were typically present as nano-precipitates within boron carbide grains as well as along grain boundaries. An important point to note about Tile 8 is the fact that it was used as a baseline tile within the Materials in Extreme Dynamic Environments (MEDE) program which is a collaborative research alliance between Rutgers University, U.S. Army Research Laboratory, Johns Hopkins University and California Institute of Technology. Specific observations regarding the tile will be discussed throughout this thesis dissertation.

Quantitative analysis of the commercial powders and dense ceramics was performed using whole pattern fitting and refinement. To attain good agreement between the observed and calculated diffraction patterns, Rietveld refinement was conducted accounting for sample displacement, peak intensity and other parameters detailed in **Section 3.2.1**. The results from these analyses are shown in Table 7. Significantly higher levels of carbon were noticed in powders manufactured by Ceradyne and Superior Graphite probably owing to the incomplete reaction of the boron and carbon source. Another possibility for the high carbon levels could be attributed to the addition of carbon to boron carbide to serve as sintering aids during consolidation of the synthesized powders. Powders manufactured by H.C. Starck, ESK and Vajrabor show free carbon values in the 0.5 – 1.1% range. Although Rietveld refinement serves as a useful tool for quantitative analysis, the accuracy of the free carbon results are questionable because of the existence of varying forms of carbon which cannot be accurately quantified using this method. Further examinations of methods used to determine the free carbon concentrations will be discussed in **Section 4**.

3.3.2 Impurity Detection

Initial elemental results from x-ray fluorescence gives an insight into the possible trace phases present in the commercial powders which are not possible to detect using x-ray diffraction. The trace elements present in the commercial samples were then determined by x-ray fluorescence based on their respective atomic number. The x-ray fluorescence spectra were acquired at low, mid and high atomic numbers (Za) and analyzed using KLM markers. Examples of peak locations for the identified elements in the ED-102 sample manufactured by ESK are shown in Figure 33, Figure 34 and Figure 35. For XRF analysis, only particular samples were chosen from each company as a representation of the entire range of powders manufactured by the company. These impurities were present in such low quantities that their presence did not significantly affect the stoichiomertry of boron carbide. Identification of these impurities provides insight into the synthesis methods used and the grinding media typically employed during processing. The most common contaminants evaluated in commercial powders were found to be Calcium, Titanium, Nickel, Iron, Copper and Zirconium.

Table 8. Impurities detected using X-ray fluorescence of selected commercial boron carbide samples.

Sample	Company	Impurities Present
SG-010813	Superior Graphite	Ca, Ti, Fe, Ni, Cu, Zr
ATD-2012-6-41	Ceradyne Inc.	Ca, Ti, Cr, Fe, Ni, Cu, Zr, W
ST-HD20	H.C. Starck	Ca, Ti, Cr, Mn, Fe, Ni, Cu, Zr, W, Ta
ED-102	ESK	Ca, Ti, Mn, Fe, Ni, Zr
VJ-3 µm	Vajrabor	Fe, Ca, Ni, Cu, Zr, W
Tile 8	CoorsTek	Fe, Ti, Cr, Ni, Al,

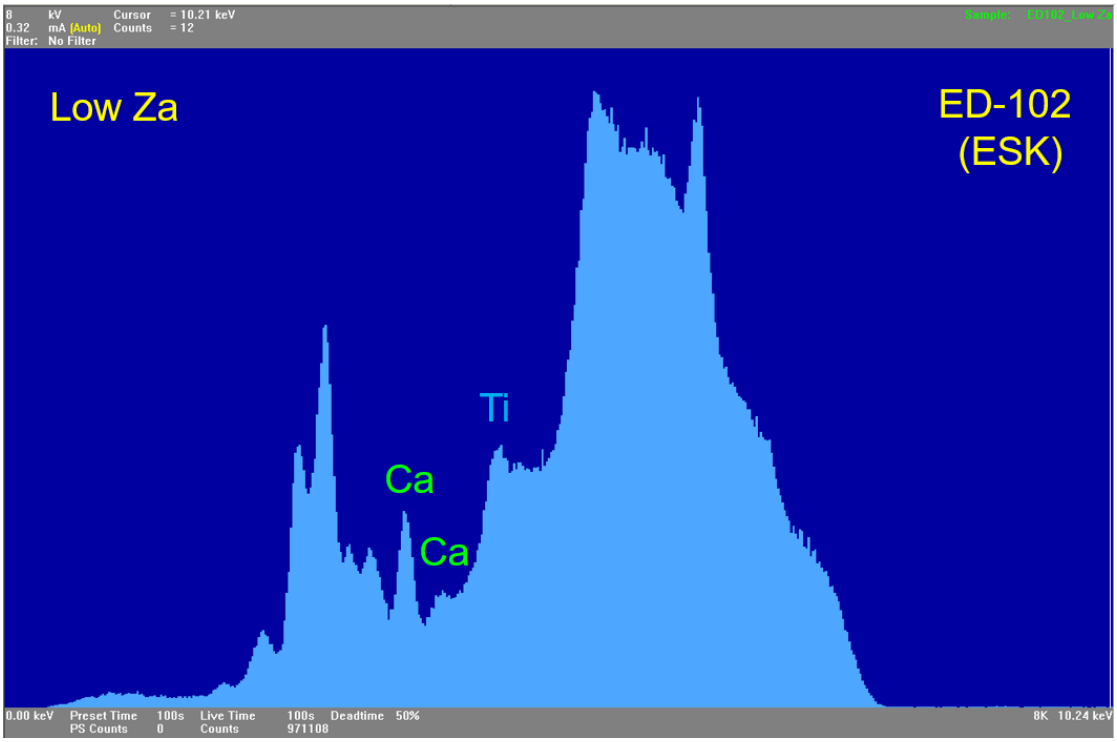

Figure 33. XRF spectra at low Za for boron carbide powders manufactured by ESK.

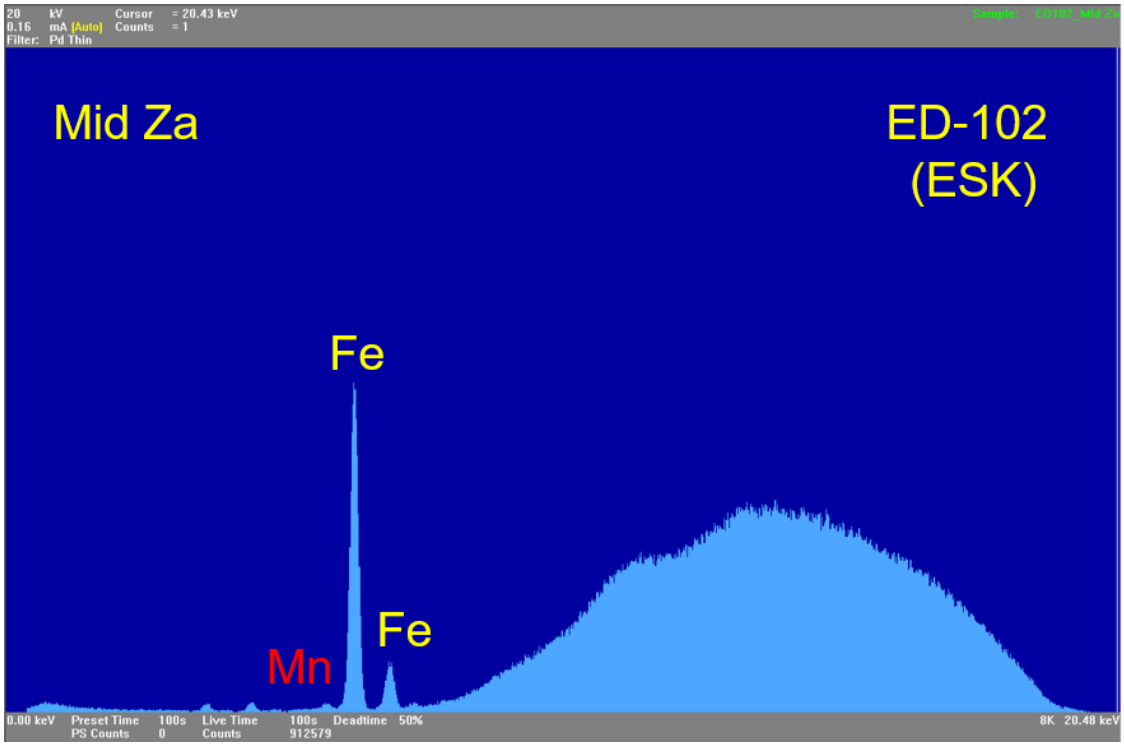

Figure 34. XRF spectra at mid Za for boron carbide powders manufactured by ESK.

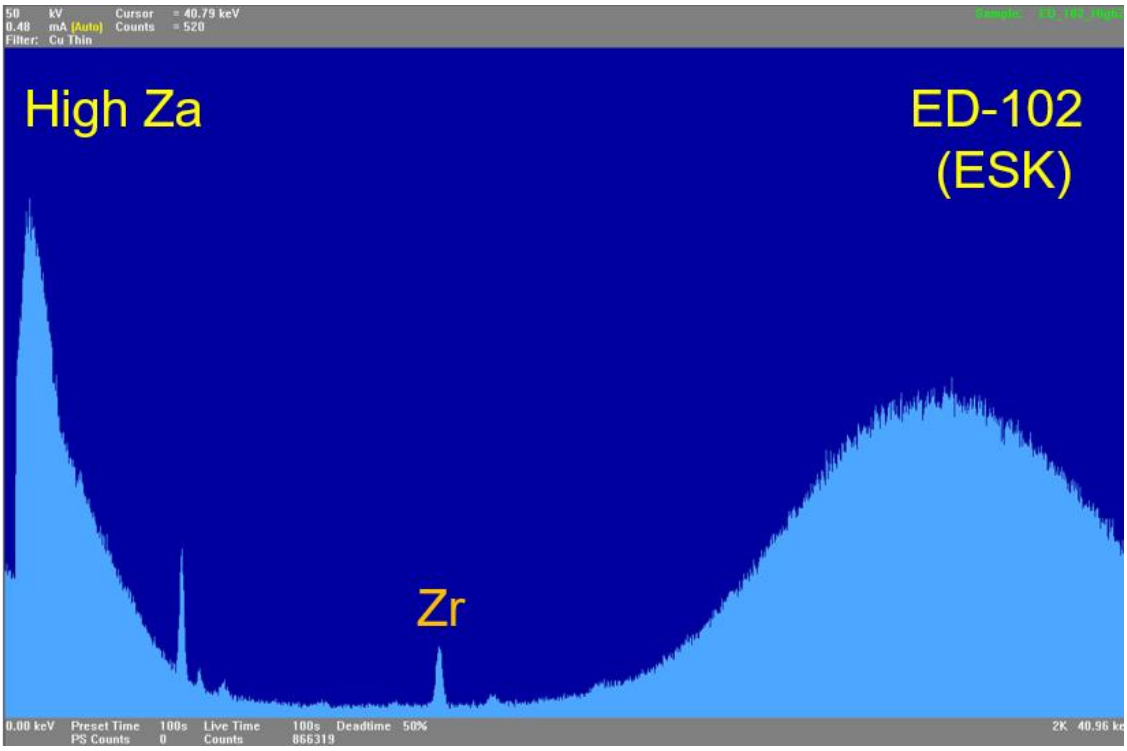

Figure 35. XRF spectra at high Za for boron carbide powders manufactured by ESK.

3.3.3 Stoichiometric Measurements

The stoichiometry of the commercial samples was determined based on the x-ray diffraction and chemical analysis results. The stoichiometry was evaluated based on specific assumptions made during calculations. Total boron present was assumed to be bound to boron carbide, boron oxide and boron nitride. The total carbon in boron carbide was assumed to consist of free carbon and carbon bound to boron carbide. The total nitrogen and oxygen present were assumed to be in the form of boron nitride and boron oxide respectively. Titration and combustion methods were used for elemental analysis following which stoichiometric measurements were conducted on selected boron carbide powders, namely ATD-2012-6-41, ST-HD20 and SG-01081. The results from the chemical

analysis are shown in Table 9 and the steps involved in the determination of the final stoichiometry are detailed below.

Table 9. Chemical analysis of select commercial boron carbide samples.

Sample #	Total Boron (Titration) (wt%)	Total Carbon (LECO) (wt%)	Total Oxygen (LECO) (wt%)	Total Nitrogen (LECO) (wt%)
SG-010813	76.21 ± 0.05	22.33 ± 0.25	1.37 ± 0.03	0.10 ± 0.01
ST-HD20	75.82 ± 0.05	22.38 ± 0.18	1.60 ± 0.01	0.20 ± 0.01
ATD-2012-6-41	77.41 ± 0.28	20.93 ± 0.25	1.07 ± 0.02	0.59 ± 0.01

Based on the calculations of the stoichiometry (see steps involved in the determination of the boron carbide stoichiometry), the stoichiometries of ST-HD20, ATD-2012-6-41 and SG-010813 were estimated at $B_{3.81}C$, $B_{4.72}C$ and $B_{4.27}C$ respectively. Most commercial powders are typically made at stoichiometries close to ~B_4C due to the improved properties at this stoichiometry. From the stoichiometric calculations, it is discernable that the experimental error associated with the free carbon content was the highest. The methods used to determine the boron, oxygen and nitrogen values have lower experimental errors. Moreover, the accuracy of these methods is high as compared to the techniques used to determine the free carbon concentration. The different techniques employed to determine the free carbon concentration will be detailed in **Section 4**. The powders used for analysis were washed before the stoichiometry was determined to minimize the impact of surface oxygen on the analysis. A further detailed analysis on the effect of powder cleaning will also be discussed in **Section 3.3.4**.

Steps involved in the Determination of the Boron Carbide

Stoichiometry

1) SG-010813 (Superior Graphite)

1) Total Carbon (LECO) = 22.33 ± 0.25
Moles of Total Carbon = 1.86 ± 0.02

2) Total Boron (LECO) = 76.21 ± 0.05
Moles of Total Boron = 7.05 ± 0.005

3) Total Oxygen (LECO) = 1.37 ± 0.03
Moles of Oxygen = 0.09 ± 0.002

4) Total Nitrogen (LECO) = 0.1 ± 0.01
Moles of Nitrogen = 0.01 ± 0.000

5) Free Carbon (XRD) = 2.72 ± 0.16
Moles of free Carbon = 0.23 ± 0.01

Moles of Boron in Boron Carbide = [Moles of Total Boron] − [Moles of Boron in Boron Oxide] − [Moles of Boron in Boron Nitride]

= (7.05 ± 0.005) − (0.06 ± 0.001) − (0.01 ± 0.000)

= 6.99

Moles of Carbon in Boron Carbide = Moles of Total Carbon − Moles of Free Carbon

= (1.86 ± 0.02) − (0.23 ± 0.01)

= 1.64 ± 0.03

Stiochiometry of BxC = $\frac{\text{Moles of Boron in Boron carbide}}{\text{Moles of Carbon in Boron carbide}}$

Stiochiometry of BxC = $B_{4.27 \pm 0.06}C$

The bound carbon content based on chemical analysis is thus 18.98 at%.

2) ST-HD20 (H.C. Starck)

1) Total Carbon (LECO) = 22.39 ± 0.18
Moles of Total Carbon = 1.86 ± 0.01

2) Total Boron (LECO) = 75.82 ± 0.05
Moles of Total Boron = 7.01 ± 0.004

3) Total Oxygen (LECO) = 1.60 ± 0.01
Moles of Oxygen = 0.10 ± 0.000

4) Total Nitrogen (LECO) = 0.20 ± 0.005
Moles of Nitrogen = 0.01 ± 0.000

5) Free Carbon (XRD) = 0.55 ± 0.05
Moles of free Carbon = 0.05 ± 0.004

Moles of Boron in Boron Carbide = [Moles of Total Boron] − [Moles of Boron in Boron Oxide] − [Moles of Boron in Boron Nitride]

= (7.01 ± 0.004) − (0.07 ± 0.000) − (0.01 ± 0.000)

= 6.93

Moles of Carbon in Boron Carbide = Moles of Total Carbon − Moles of Free Carbon

= (1.86 ± 0.01) − (0.05 ± 0.004)

= 1.81 ± 0.03

Stiochiometry of BxC = $\frac{\text{Moles of Boron in Boron carbide}}{\text{Moles of Carbon in Boron carbide}}$

Stiochiometry of BxC = $B_{\mathbf{3.81} \pm 0.03}C$

The bound carbon content based on chemical analysis is thus 20.8 at%

3) ATD-2012-6-41 (Ceradyne)

1) Total Carbon (LECO) = 20.93 ± 0.25
Moles of Total Carbon = 1.74 ± 0.02

2) Total Boron (LECO) = 77.41 ± 0.28
Moles of Total Boron = 7.16 ± 0.03

3) Total Oxygen (LECO) = 1.07 ± 0.02
Moles of Oxygen = 0.07 ± 0.001

4) Total Nitrogen (LECO) = 0.59 ± 0.01
Moles of Nitrogen = 0.04 ± 0.001

5) Free Carbon (XRD) = 2.96 ± 0.18
Moles of free Carbon = 0.25 ± 0.02

Moles of Boron in Boron Carbide = [Moles of Total Boron] − [Moles of Boron in Boron Oxide] − [Moles of Boron in Boron Nitride]

= (7.16 ± 0.03) − (0.04 ± 0.000) − (0.04 ± 0.001)

= 7.10

Moles of Carbon in Boron Carbide = Moles of Total Carbon − Moles of Free Carbon

= (1.74 ± 0.02) − (0.25 ± 0.02)

= 1.50 ± 0.03

Stiochiometry of BxC = $\frac{\text{Moles of Boron in Boron carbide}}{\text{Moles of Carbon in Boron carbide}}$

Stiochiometry of BxC = $B_{\mathbf{4.72} \pm 0.08}C$

The bound carbon content based on chemical analysis is thus 17.48 at%

Table 10. Soluble boron values determined by titration analysis.

Powder Company	Soluble or Free Boron (Titration) (wt%)
SG-010813	3.10
ST-HD20	5.48
ATD-2012-6-41	0.93

Another factor which affects the stoichiometry of boron carbide is the soluble boron content. Previous work done in this area, namely analysis by Schwetz et al. [9] disregard the soluble boron content which may give an incorrect evaluation of the final B:C ratio. As a result of the limited equipment capability at Rutgers University, selected powders were analyzed externally at Washington Mills (USA). The soluble boron content in the ST-HD20 and SG-010813 powder showed large quantities of elemental boron which were not observed using XRD (Table 10). Increased quantities of soluble boron lead to a decrease in the boron content available for boron carbide, which in turn reduces the stoichiometric value. Table 11 shows the modified values of the stoichiometry considering the soluble boron contents.

Table 11. Comparison of the stoichiometry of the boron carbide powders assuming the absence and presence of soluble boron.

Powder Company	Stoichiometry	
	Without Soluble Boron	With Soluble Boron
SG-010813	4.27 ± 0.05	3.92 ± 0.05
ST-HD20	3.81 ± 0.04	3.60 ± 0.05
ATD-2012-6-41	4.72 ± 0.07	4.58 ± 0.08

3.3.4 Effect of Powder Cleaning on the Stoichiometry

Washing powders before analysis is of prime importance particularly in powders in the micron-submicron regime. To study the effect of powder cleaning on the stoichiometry, 4 powders manufactured by Vajrabor (India) were considered. Particle size analysis on the powders resulted in mean particle values of 1 µm, 1-2 µm, 3 µm and 74 µm. These powders had a diverse particle size distribution and effectively served as a suitable basis to examine particle size effect on the oxygen/nitrogen content and stoichiometry. Chemical analysis on the unwashed Vajrabor samples (Table 12) showed higher values of oxygen and nitrogen and low amounts of free carbon. In particular, the 1 µm powder had significantly higher oxygen and nitrogen contents. On prolonged exposure to the atmosphere, boron carbide powders in the micron-submicron regime amass oxygen/nitrogen from atmospheric air. Oxide layers are typically formed on the surface of the powders owing to their increased surface area and decreased particle size. Furthermore, boron oxide present in the material may react with the atmospheric moisture forming boric acid. These factors affect analysis and provide a false estimation of the boron carbide stoichiometry. The effect of increased oxygen/nitrogen contents gradually decreased with the increase in the particle size and decrease in the surface area of the powders. Results from chemical analysis on the cleaned powders are detailed in Table 13. The washing procedure entails removal of the surface oxides, boron oxide and boric acid, accumulated on the surface of the boron carbide particles over time. Post washing, a drastic drop in the oxygen and nitrogen values was seen in the 1 µm and 1-2 µm powders. With the reduction in the oxygen/nitrogen values, understandably the total boron, carbon and free carbon quantities increased. The results from the 3 µm and 74 µm powders deviated marginally before and after powder cleaning

because of its higher particle size and reduced surface area which prevented increased accumulation of oxygen/nitrogen. The B:C ratio of the 3 µm and 74 µm powders remained at similar levels as a result of consistent oxygen/nitrogen amounts. But, the final stoichiometry of low particle size powders deviated by ~5-7%. For a true estimation of the chemistry of boron carbide, powders should be cleaned before analysis and stored in temperature and humidity controlled dryboxes to prevent oxygen/nitrogen buildup.

Table 12. Summary of the chemical composition and stoichiometry of unwashed Vajrabor samples with variable particle sizes.

Sample #	B (wt%)	C (wt%)	O (wt%)	N (wt%)	Free Carbon	Stoichiometry
VJ-1 µm	70.94	17.83	5.07	6.16	0.10	$B_{4.0}C$
VJ-1-2 µm	77.90	18.25	2.03	1.82	0.30	$B_{4.6}C$
VJ-3 µm	80.01	18.94	0.16	0.89	0.49	$B_{4.7}C$
VJ-74 µm	78.91	20.80	0.14	0.14	0.10	$B_{4.2}C$

Table 13. Summary of the chemical composition and stoichiometry of washed Vajrabor samples with variable particle sizes.

Sample #	B (wt%)	C (wt%)	O (wt%)	N (wt%)	Free Carbon	Stoichiometry
VJ-1 µm	78.62	19.98	0.83	0.57	0.40	$B_{4.3}C$
VJ-1-2 µm	80.57	18.87	0.43	0.12	0.20	$B_{4.8}C$
VJ-3 µm	80.31	19.34	0.19	0.15	0.40	$B_{4.7}C$
VJ-74 µm	78.97	20.80	0.08	0.15	0.10	$B_{4.2}C$

3.3.5 Lattice Parameter Measurements

Lattice parameter-stoichiometry relationships were used to determine the bound carbon concentration of boron carbide, the results of which were compared to those calculated from chemical analysis. Evaluating the carbon concentration from the lattice parameters, provides a convenient and non-destructive method in obtaining the stoichiometry of boron carbide. Over the years, a number of conflicting and sometimes contradictory reports have been published that detail the lattice parameter dependence on the carbon concentration in boron carbide. These reports have been found to exhibit large scatter[13, 15, 33, 96, 97, 98, 99]. The scatter in the data is presumably a consequence of large discrepancies in chemical analysis. Additional factors contributing to the unreliable data could be inconsistencies in experimental techniques i.e. wavelength choice, mis-indexed powder lines and incorrect centering of the specimen in the diffractometers. The most consistent work on the lattice parameter dependence on the stoichiometry was done by Bouchacourt et al. [33], Aselage et al. [13] and Gosset et al.[96]. In this sub-section, only the results from Aselage et al.[13] will be reviewed. A further detailed investigation of other lattice parameter carbon concentration relationships will be discussed in **Section 5**. Based on the Aselage data (Table 14), the lattice parameters increase with the decrease in the carbon content. The large range of lattice parameters reported near 20 at% carbon exemplify the difficulty associated with analysis of the stoichiometry and lattice parameters near the carbon rich solubility limit. With further boron addition, the *c* lattice parameter levels out at ~13 at% carbon and remains constant towards the boron rich solubility limit. This abrupt break in the slope around 13.3 at% carbon (corresponding to $B_{13}C_2$) denotes the change in the mechanism of substitution of boron and carbon atoms either side of $B_{13}C_2$. Due to the scatter in the

Aselage et al. data, the lattice constant-stoichiometry relationship it can be fitted using different linear fits (Figure 36). Depending on the type of fit used, the stoichiometric results can differ significantly. The lattice parameters of three representative boron carbide powders were determined and overlaid on the Aselage et al. data as seen in Figure 36. The corresponding carbon concentration from the lattice parameters are reported in Table 14. The largest deviations in the results were seen in the stoichiometric values using the c lattice parameter. This was primarily related to the change in the slope at 13.3 at% carbon. Although the change in the slope at ~13 at% carbon has been previously established, a linear dependence of the c lattice parameter on the carbon concentration across the entire solubility range can also be assumed which would drastically alter the results. As the stoichiometry of the sample is dependent on the fit used, minimizing the scatter in the lattice parameter data would effectively lead to improved results for the B:C ratio.

Table 14. Summary of hexagonal lattice parameters and corresponding carbon concentration as determined by Aselage et al.[13].

a(Å)	c(Å)	Carbon Concentration (at%)
5.5991	12.0740	20.2
5.5980	12.0707	19.4
5.5995	12.0707	19.2
5.5993	12.0655	19.6
5.6030	12.0802	19.6
5.6030	12.0909	18.8
5.6032	12.0909	18.7
5.6071	12.1032	17.4
5.6152	12.1411	16
5.6244	12.1727	12.8
5.6286	12.1748	12.3
5.6344	12.1793	10.4
5.6438	12.1750	9.3
5.6440	12.1730	8.1

Variations in the estimated carbon concentrations existed depending on whether *a* or *c* lattice parameters were considered. In certain cases, as in the ATD-2012-6-41 powder, the carbon concentrations deviated by ~1 at% carbon. The differences in the carbon content results were attributed to inaccurate lattice parameter data. Additionally, relatively small amounts of impurities substantially alter the lattice parameters and increase the unit cell volume of the boron carbide crystal. Furthermore, particular elemental impurities such as Si or Al, could preferentially alter the lattice parameter results along either the x or y direction. To account for variable sources of error, the stoichiometry of boron carbide powders was determined from the average values of the carbon concentration acquired from the lattice parameters (Table 16). The chemistry of the SG-010813 powder was closer to the "stoichiometric" value of boron carbide as compared to the ST-HD20 and ATD-2012-6-41 powder which were boron rich. On comparing these results with those from chemical analysis, significant deviations were noticed. This is the primary source of the problem with regards to the accuracy of chemical techniques employed as well as the errors

Table 15. Summary of lattice parameters and the corresponding carbon concentration from XRD depending on the fit used for the data.

Powder #	Powder Company	*a*(Å)	*c*(Å)	Carbon Concentration (at%)			
				Fitting 1		Fitting 2	
				Based on *a*	Based on *c*	Based on *a*	Based on *c*
SG-010813	Superior Graphite	5.6006	12.0750	19.4	19.5	19.4	20.1
ST-HD20	H.C.Starck	5.5995	12.0774	19.7	19.3	18.3	19.8
ATD-2012-6-41	Ceradyne Inc.	5.6071	12.0907	17.7	18.6	17.7	18.5

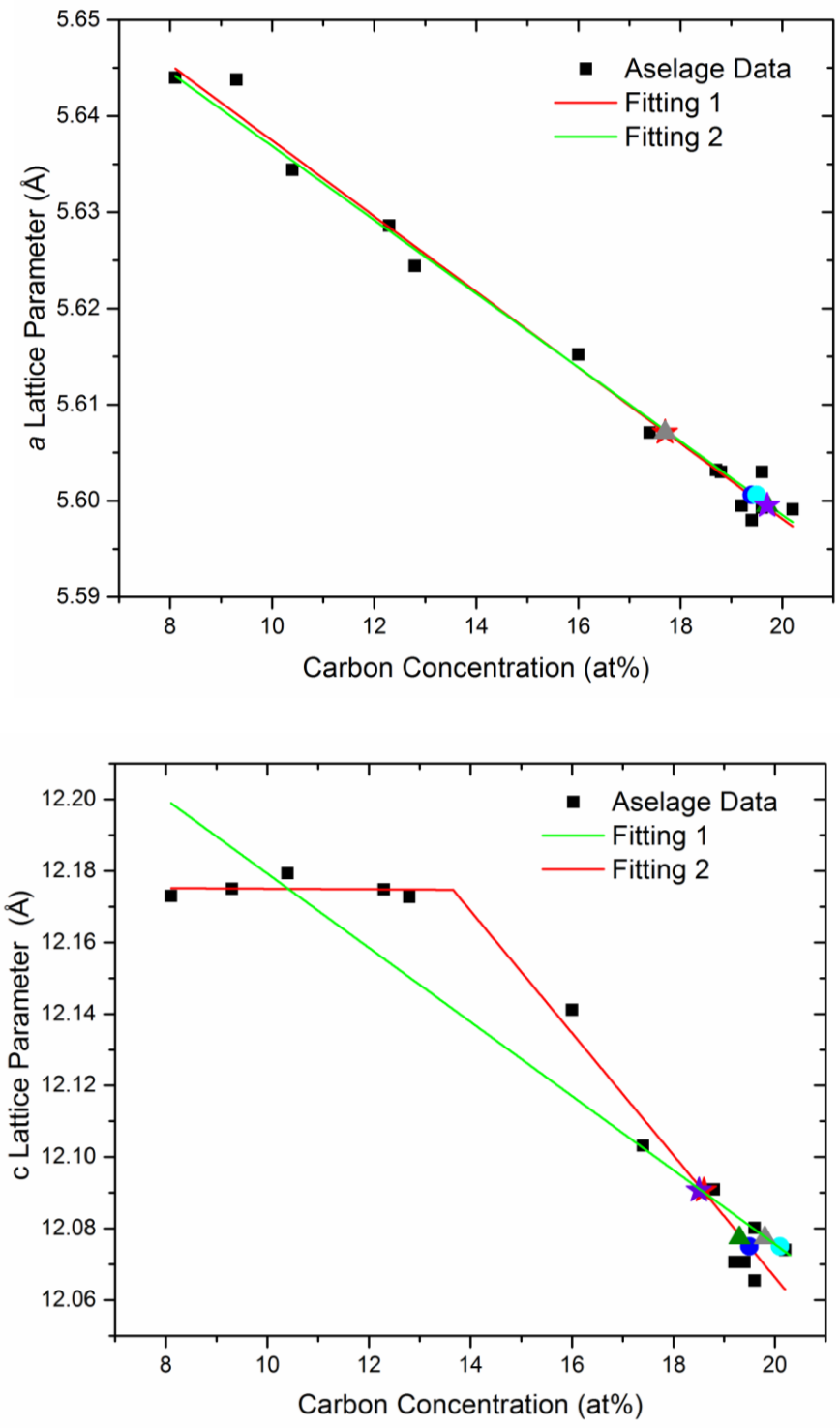

Figure 36. Comparison of the Hexagonal lattice parameters and the corresponding carbon concentration utilizing multiple linear regression fits of the Aselage data[13]. Fit 1, ●: SG-010813 (Superior Graphite), ▲: ST-HD20 (H.C.Starck), ★: ATD-2012-6-41 (Ceradyne Inc.). Fit 2, ●: SG-010813 (Superior Graphite), ▲: ST-HD20 (H.C.Starck), ★: ATD-2012-6-41 (Ceradyne Inc.).

Table 16. Summary of average carbon concentration and the corresponding stoichiometry obtained from lattice parameter – stoichiometry relationships.

Powder #	Powder Company	Average Carbon Concentration (at%)	Chemistry
SG-010813	Superior Graphite	19.4	$B_{4.15}C$
ST-HD20	H.C.Starck	18.8	$B_{4.32}C$
ATD-2012-6-41	Ceradyne Inc.	18.1	$B_{4.52}C$

associated with the lattice parameter-stoichiometry relationship. Previously developed methodologies provide an estimation of the stoichiometry of unknown samples, but these results exhibited large deviations and disagreement depending on the method used to evaluate the final stoichiometry. Therefore, there is a need for the development of improved testing techniques, especially for the free carbon determination as this method provides the largest source of error. Furthermore, the true relationship of the lattice parameters and the carbon concentration needs to be investigated and effectively correlated to the final B:C ratio.

3.3.6 Raman Analysis

The Raman spectra of boron carbides are characterized by a combination of narrow and broad Raman bands extending from 200 to 1200 cm^{-1} (Figure 37). In literature, there are conflicting allocations of the Raman peaks to vibrations of the principal structural elements of boron carbide i.e. icosahedra and three-atom chain[100, 101, 102, 103, 104]. But the general consensus is bands extending from 600 to 1200 cm^{-1} are attributed to vibrations caused in the icosahedral units. The $B_{11}C$ icosahedra experiences anisotropy as a result of

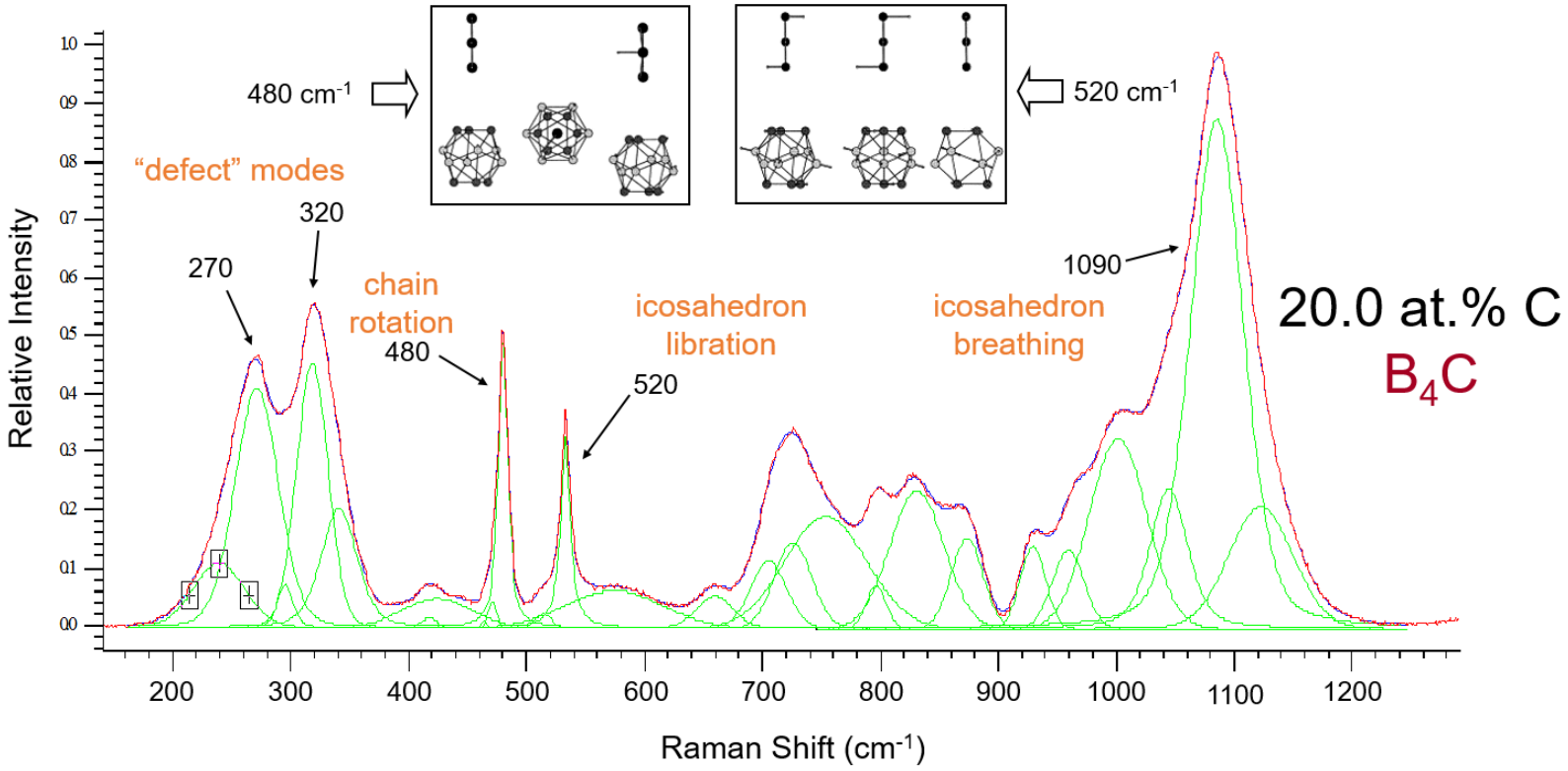

Figure 37. Characteristic Raman spectra from boron carbide powder produced by Ceradyne Inc (red lines). Individual bands used in the curve fitting procedure are shown in green, and the simulated spectrum in blue.

the distribution of carbon atoms between the icosahedral sites. This results in broadening of icosahedral vibrational bands of boron carbides[105]. The narrow peak at ~480 cm^{-1} was assigned to the vibrations of C-B-C chains. As the C-B-C chains bond to the equatorial boron sites (Figure 38), these three-atom chains have similar chain-icosahedral bonding and orientational symmetry. The 520 cm^{-1} band was linked to the icosahedral libration mode. The occurrence of the two broad bands at ~300 cm^{-1} has not been completely understood. Werheit et al. studied carbon isotope and carbon content dependencies of boron carbide using a 1070 nm laser[104, 106, 107, 108]. At these wavelengths, similar bands are observed at 300 cm^{-1} which were attributed to librational modes in C-B-B and C-B-C chains. From first-principle calculations of Vast et al, these features were linked to disorder-activated acoustic phonons[109, 110]. But this may not be the case as similar bands are seen in single crystal and hot pressed boron carbide samples.

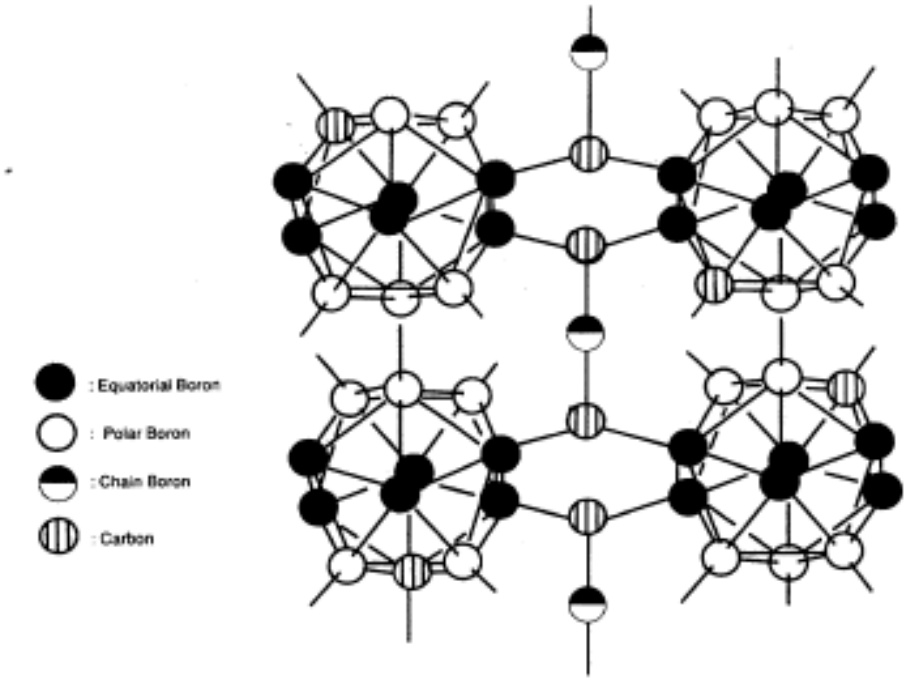

Figure 38. Structure of boron carbide at 20 at% carbon showing C-B-C chains and the $B_{11}C$ icosahedra with the carbon atom at the polar sites[105].

Raman spectra were acquired from different locations on commercial boron carbide samples manufactured by Ceradyne Inc. The Raman spectra from different locations were statistically treated based on the peak center, width, height, area, low edge and high edge to obtain the most representative spectrum for the commercial powders. The results of the peak parameters for the most representative mean peak position of a selected Ceradyne powder is provided in Table 17 and Table 18. Similar analysis was performed on other samples based on peak areas, peak half-widths and peak shapes. Similar observations to the characteristic Raman spectrum in Figure 37 were made in the current study, as evidenced by the representative Raman spectra for commercial boron carbide powders shown in Figure 39. However, due to the presence of free carbon in commercial powders, characteristic D (~1360 cm^{-1}) and G (~1580 cm^{-1}) bands for amorphous/graphitic carbon were observed. The D band arises from breathing vibrations of sixfold aromatic rings in finite graphitic domains[6]. The D band is formed as a result of the formation of an electron-hole pair caused by laser excitation followed by one-phonon emission[6]. The G band is a direct consequence of in-plane stretching vibration of C=C bonds. Depending on the intensity of the D band with respect to G, an inversely proportional relationship exists with the size of the graphite particles as shown below[6, 111, 112]:

$$\frac{I(D)}{I(G)} = \left(\frac{C(\lambda)}{L}\right)^{1/2} \quad L<20\ Å \tag{20}$$

$$\frac{I(D)}{I(G)} = \frac{C(\lambda)}{L} \quad L>20\ Å \tag{21}$$

Here, C(λ) depends on the wavelength of the laser, and L is the diameter of the sp^2 domain.

Table 17. Raman peak positions for selected locations on a commercial boron carbide sample ATD-2012-6-41 produced by Ceradyne Inc.

Location	Peak 1 (cm^{-1})	Peak 2 (cm^{-1})	Peak 3 (cm^{-1})	Peak 4 (cm^{-1})	Peak 5 (cm^{-1})	Peak 6 (cm^{-1})	Peak 7 (cm^{-1})
1	273.8	321.5	470.7	522.6	1060.3	1329.0	1565.1
2	256.4	324.9	471.6	521.8	1063.7	1345.3	1585.0
3	271	324.7	470.6	521.6	1063.1	1319.6	1580.1
4	267.5	316.9	470.4	522.1	1063.9	1312.7	1586.9
5	253.5	321.4	470.9	523.1	1066.8	1338.1	1584.5
6	255.3	327.3	470.8	522.5	1065.8	1329.4	1573.6
7	260.1	314.5	471.7	522.5	1064.7	1332.7	1567.2
8	269.2	315.5	470.0	521.9	1063.4	1324.7	1585.3
9	273.2	309.0	470.9	521.6	1060.7	1334.5	1585.3

Table 18. Summary of Raman peak parameters of the typical boron carbide sample ATD-2012-6-41 produced by Ceradyne Inc.

Peak	Center (cm^{-1})	Height (Counts)	Width (cm^{-1})	Area $(Counts)^2$	Absolute Intensity $(Counts)^2$	Low Edge (cm^{-1})	High Edge (cm^{-1})
1	260.11	-	-	-	0.17	-	-
2	314.55	0.04	23.22	18.84	0.16	288.45	378.54
3	471.76	0.22	11.47	8.61	0.33	460.73	489.63
4	522.58	0.13	11.10	4.79	0.21	511.65	531.92
5	1064.72	-	-	-	0.42	-	-
6	1332.72	0.03	2.80	7.02	0.61	1326.41	1329.43
7	1567.26	0.47	22.86	58.86	0.99	1535.94	1585.51

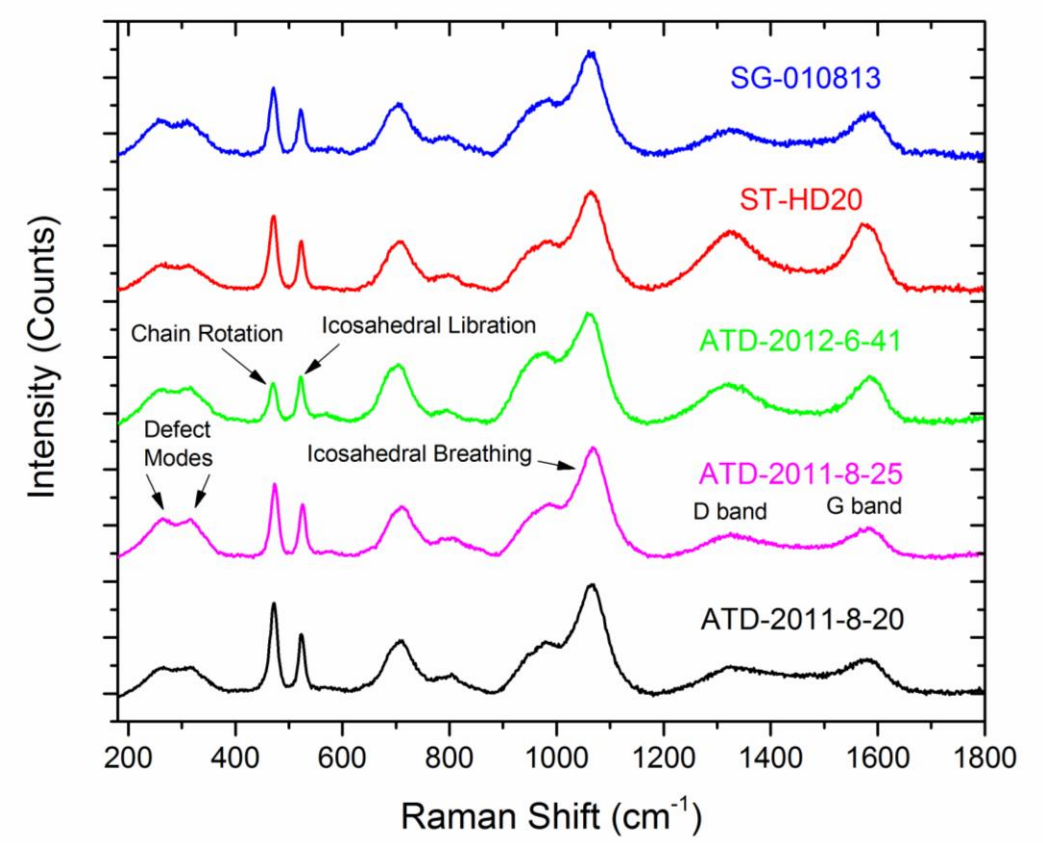

Figure 39. Characteristic Raman spectra of commercial boron carbide powders. The bands below 1200 cm^{-1} originate from vibrations in boron carbide, whereas bands above 1200 cm^{-1} are attributed to amorphous/graphitic carbon.

An alternate explanation for the occurrence of the band near 1580 cm^{-1} was provided by Kuhlmann et al.[101, 113]. It was suggested that the peak near 1580 cm^{-1} was linked to the replacement of C-B-C chains by B-B-C chains because of the activation of the stretching vibrations of boron carbide. As the carbon concentration in boron carbide decreases, downshift of the peak at 530 cm^{-1} was observed (Figure 40). Conversely, the band at 485 cm^{-1} shifts towards higher frequencies with the decrease in the carbon concentration. Based on the results by Domnich et al.[114], the separation between the 485 cm^{-1} and the 530 cm^{-1} Raman bands was used for the determination of the boron carbide stoichiometry of the three commercial powders manufactured by Ceradyne, H.C.Starck

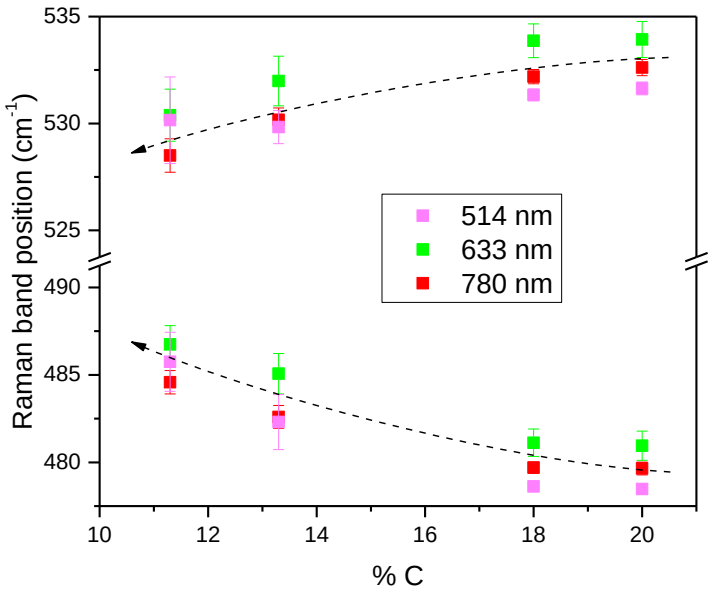

Figure 40. Dependence of the narrow bands centered at 500 cm^{-1} on the carbon concentration (at%)

and Superior Graphite as shown in Table 19. The stoichiometric results from the calibration curves served as another indicator of the disagreement in the stoichiometry of boron carbide using different methodologies. This calibration curve was constructed using minimal data points which contributes to the error in analysis. For a precise determination of the stoichiometry of boron carbide, further data points will need to be investigated to understand the nature of the calibration curve. This curve will be further refined and discussed in **Section 5**.

Table 19. Summary of the stoichiometry of boron carbide from the difference in the peak positions of the Raman bands.

Powder #	Powder Company	Difference between 480 cm^{-1} and 530 cm^{-1} Raman Bands	Carbon Concentration (at%)	Stoichiometry
SG-010813	Superior Graphite	52.5	18.2	$B_{4.5}C$
ST-HD20	H.C.Starck	52.8	18.7	$B_{4.3}C$
ATD-2012-6-41	Ceradyne Inc.	51.2	16.6	$B_{5.0}C$

3.3.7 Database of Commercial Boron Carbide Powders and Ceramics

Additional commercial powders were acquired from different boron carbide manufacturers and the techniques discussed above were employed to evaluate variability in commercial boron carbide powders and consolidated ceramics. These results provided insights into the type of materials manufactured by different companies and the particular stoichiometry of the specimens. This database also serves as a reference point for any information needed regarding powder and ceramic characteristics within the Materials for Extreme Dynamic Environments (MEDE) program (Collaborative program involving John's Hopkins University (JHU), Army Research Laboratory (ARL), California Institute of Technology (CALTECH) and Rutgers University (RU)). Furthermore, depending on the chemical and structural properties of different commercially manufactured ceramics, particular specimens can be chosen as a baseline for impact fragmentation and ballistic tests. Table 20 shows an excerpt from the database that was developed. In addition to the phase identification, lattice parameters and stoichiometric measurements, the XRD patterns and Raman spectra were also provided for different powders in the event future analysis needs to be conducted on these specimens.

Table 20. Summary of developed database detailing commercial powder and ceramic properties.

Sample #	Powder Company	Total carbon from chemical analysis (wt%)	Phase analysis from XRD (wt.%)		Lattice parameters			Carbon content based on *c*/*a* (at.%)	Carbon content based on *a* (at.%)	Carbon content based on *c* (at.%)	Carbon content from Raman analysis (at.%)
			$B_{4-x}C$	C (Graphite)	*a* (Å)	*c* (Å)	*c*/*a* ratio				
ATD-2011-8-58	Ceradyne Inc.	21.3	94.8	5.2	5.6091	12.092	2.1558	20.0	17.2	18.4	17.3
ATD-2011-6-20	Ceradyne Inc.	21.3	95.9	4.1	5.6068	12.0866	2.1557	20.1	17.8	18.8	19.0
UK-Reg	Uk Abrasives	21.8	90.0	10.0	5.5985	12.0661	2.1552	20.2	19.4	20.1	-
VJ-15	Vajrabor	18.6	99.4	0.4	5.619	12.119	2.1568	14.6	18.4	19.4	-
ESK-Proc	ESK	-	99.0	<0.1	5.606	12.096	2.1577	18.0	17.1	18.2	-
BCSF-10	Rutgers University	-	99.8	0.2	5.6035	12.089	2.1574	18.7	18.7	18.6	-
Cer-4-144	Ceradyne Inc.	13.7	99.5	0.5	5.5999	12.0832	2.1578	19.6	19.4	19.0	18.4

3.4 Summary

In this objective, currently used analytical techniques have been examined to assess the inaccuracies associated with the determination of the boron carbide stoichiometry. Current PDF cards cannot be employed exclusively to estimate the final B:C ratio, primarily because of inconsistensies in experimental techniques and earlier misconceptions that boron carbide existed at a stoichiometry of B_4C or $B_{6.5}C$ rather than a wide homogeneity range. Boron carbide powders manufactured commercially and at Rutgers University typically show the presence of a two phase material of boron carbide and free carbon. The stoichiometric measurements indicate the largest error associated with the determination of the B:C ratio, arises from the method employed for free carbon evaluation. Other techniques such as Raman spectroscopy and lattice parameter calibration curves were used in conjunction with chemical analysis to supplement the stoichiometric results. But these results were not commensurate with each other. A comparative study of numerous boron carbide powders and consolidated ceramics was also conducted to ascertain the typical characteristics of commercially available powders and ceramics. Various factors affecting the final stoichiometric results have also been discussed and a better understanding of the analytical and chemical techniques employed to determine the stoichiometry of boron carbide has been gleaned. Based on the observations in this section, the free carbon methodology requires refinement and improved lattice parameter and Raman calibration curves need to be developed. These improved methodologies would provide further insight into the structural and mechanical variations at different stoichiometries.

4 Development of an Improved Methodology for Free Carbon Analysis

4.1 Introduction

In boron carbide powders and ceramics, carbon may be present either as bound to boron or free carbon. Quantitative determination of the free carbon content presents a difficult problem in analytical chemistry of non-metallic hard materials. The free carbon in boron carbide is very difficult to determine due to its low atomic number and similarities in chemical properties to boron carbide. As discussed in the previous section, the experimental uncertainties involved in the determination of the total boron, carbon, oxygen and nitrogen are negligible as compared to the accuracy of the methodology used to evaluate the free carbon content. This objective aims at developing an improved technique for accurate free carbon measurements. Over the years, different methods have been proposed to assess the free carbon levels; combustion methods, wet chemical oxidation, Reitveld refinement and Spiking technique.

The combustion method developed by Alizadeh et al.[115] determine the free carbon by heating the boron carbide at 700°C in air for 30 minutes. The free carbon is then obtained by measuring the weight of the sample before and after heat treatment and subsequent washing to remove B_2O_3. Two major assumptions are made in the combustion method; free carbon and part of the boron carbide are oxidized during the initial heat treatment and washing in hot water removes the oxidized part of the boron carbide i.e. B_2O_3. Certainly, these assumptions may be partially true for certain boron carbide powders. But studying the oxidation behavior of boron carbide undermines the assumptions made by Alizadeh et al. Oxidation of boron carbide in an air water system leads to an initial weight gain due to the formation of boric acid. This is followed by a weight loss as the boron oxide formation

supersedes the boric acid formation. This phenomenon is appropriately evidenced in Figure 15. Hence, the initial oxidation of boron carbide will result in the formation of boron oxide as stated by Alizadeh, but this will also be accompanied by boric acid formation. The next step in the analysis involves washing the oxidized material with hot water to remove boron oxide. But this will leave behind residual boric acid as boric acid is only leached by nitric acid. This means the results of the free carbon finally obtained will be underestimated. The oxidation behavior in literature also suggests that the oxidation of the free carbon, boron carbide and boric acid is highly dependent on the particle size of the powder and would lead to inconsistent data depending on the particle size of the boron carbide powders[63, 64]. The wet chemical oxidation method developed by Schwetz et al.[116] is commonly used in analytical laboratories and research companies across the world. Hence, assessing the pitfalls and inaccuracies of this method becomes very critical. In the wet chemical method, boron carbide is subjected to heat treatment along with a chromic-iodic-sulphuric acid mixture. The CO_2 concentration versus time graph is plotted and the free carbon is obtained by graphical extrapolation. But the wet chemical oxidation method, similarly to the combustion method, is highly dependent on the particle size and morphology of the powder as will be discussed in **Section 4.3.2**.

As mentioned above, due to the similar chemical properties of carbon and boron carbide, it becomes evident that the free carbon has to be determined using a non-destructive x-ray method. Rietveld refinement was used to assess the free carbon concentration, but the accuracy of this method is compromised in the presence of amorphous materials. Another technique known as the Spiking technique[117] proves to be the most promising method. This method was developed by Beauvy[117] in the 1980's and

can be used to determine the free carbon less than 10% in a crystal matrix from the ratio of the intensities of the two diffraction lines corresponding to free carbon and boron carbide. There is a proportionality relationship between this ratio and the quantities of the two components when: (1) the phases are uniformly distributed; (2) grains are randomly oriented; (3) good X-ray diffraction lines are observed[117]. These conditions were fulfilled using the XRD parameters detailed in **Section 3.2.1** which result in XRD scans with significantly high resolution and random particle orientation. In the method developed by Beauvy, boron carbide powders were mixed with various amounts of graphite powder and the resulting specimens of mixed powders were analyzed by XRD to evaluate the ratio of intensities between diffraction lines of graphite (102) and boron carbide (111) as illustrated in Figure 41[117]. A linear relationship exists between the amount of added graphite and the relative intensity of the diffraction lines up to about 4 wt% added graphite. The free carbon concentration is then obtained by graphical extrapolation on the negative y axis. Particle size effect on the free carbon content was also investigated by Beauvy. The major advantage of the Spiking technique is its independence on the particle size of the boron carbide (Figure 42) and its ability to detect small quantities of graphite owing to the penetration of X-rays. But a major drawback with the Spiking technique is that the correct amount of free carbon can only be calculated if it is present as graphite. This condition is normally satisfied in boron carbide owing to the high synthesis temperatures involved which completely crystallize carbon to graphite. These synthesis methods include carbothermal reduction using an electric arc furnace and Acheson type process where boron carbide powders are synthesized at temperatures >2200°C. When other synthesis

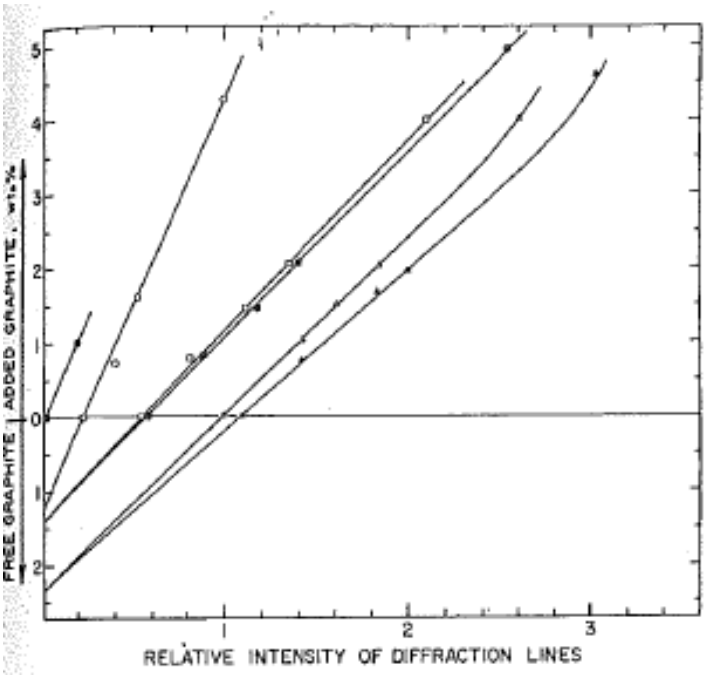

Figure 41. Determination of the free-graphite content in various boron carbide powders by the spiking technique[117].

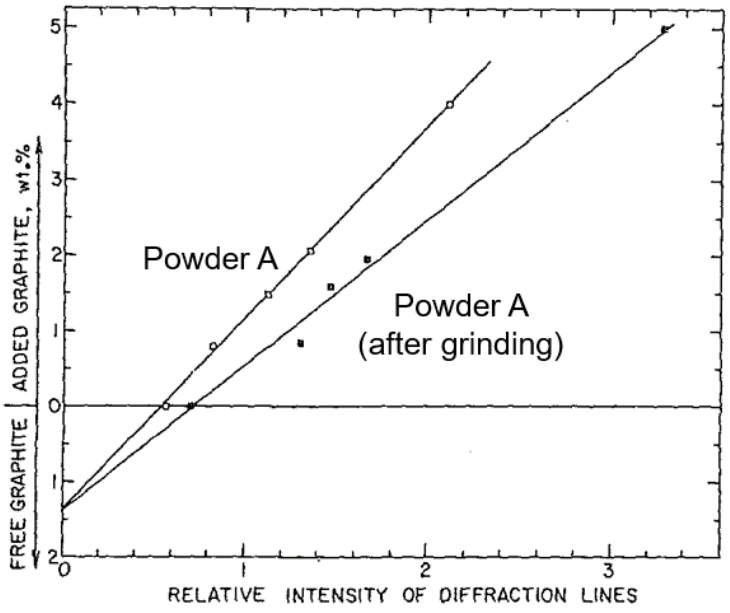

Figure 42. Effect of particle size distribution of boron carbide on the free carbon content calculated using the Spiking technique[117].

methods such as magnesiothermal reduction and rapid carbothermal reduction are used, the temperatures involved are much lower. This may lead to the development of partially crystallized carbon which cannot be correctly evaluated using the Spiking technique developed by Beauvy et al.[117]. In order to address this shortcoming and owing to the promising nature of the Spiking technique, an improved method known as the Modified Spiking technique has been developed in the course of this work to ensure its applicability to different forms of carbon. For this objective, three powders with a wide variability in particle size and free carbon were chosen for analysis i.e. ST-HD20 (H.C.Starck), ATD-2012-6-41 (Ceradyne) and SG-010813 (Superior Graphite). A reference boron carbide powder (ED 102) manufactured by ESK was also used to test the validity of the developed characterization techniques.

4.2 Experimental Procedure

4.2.1 Free Carbon Analysis

Amorphous carbon (Carbon Lampblack, Fisher Scientific) was heat treated in air at varying temperatures to study the effect of temperature on its crystallization behavior. The free carbon analysis on the samples was then conducted using the modified spiking technique. In this method, graphite from Industrial Graphite Sales (USA) ranging from 0.01 g to 0.07 g was added to 2 g of commercial boron carbide powders. A mechanical mixture was then developed using a high energy Spex Sample Prep Mixer/The Mill® (8000M) and run for 30 min (Figure 43) to develop a uniform mixture of the two components. Alumina grinding media was initially utilized to obtain a uniform particle size distribution of the mixture and ensure a homogenous mix of carbon and boron carbide. But,

Figure 43. Spex mill used to develop mechanical mixtures of carbon and boron carbide.

preliminary XRD patterns revealed the presence of alumina contaminants as shown in (Figure 44 and Figure 45). Further, the positions of the alumina peaks overlapped with those of free carbon affecting the intensity of the free carbon peaks and deconvolution of the 100% intensity (002) carbon peak located at 2θ of ~26.6°. The material used as the grinding media should be chosen such that its XRD pattern does not overlap with that of free carbon. Consequently, subsequent mixtures of boron carbide and graphite were mixed using spherical zirconia media. X-ray diffraction was performed on the resultant carbon-boron carbide mixtures using similar sample preparation techniques and conditions discussed in **Section 3.2.1**. A graph with the ratio of the relative intensity of the (021) (2θ = ~37.5°) boron carbide and (002) (2θ = 24.5° - 26.6°) carbon peak was plotted against the percentage of added graphite. The value of the free carbon content in the resultant powder was determined by graphical extrapolation onto the negative y axis. Due to the varying forms of carbon that can be present, evaluation of the "true" intensity of the 002 carbon peak was very challenging. In order to clearly distinguish between the various forms of free carbon that contribute to the intensity of the major 002 carbon peak, the XRD patterns

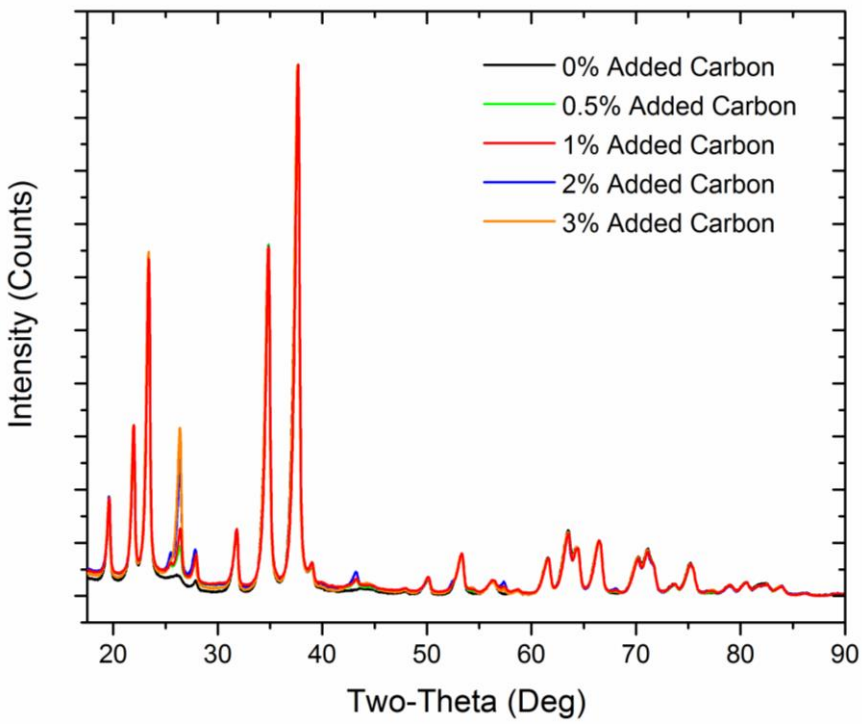

Figure 44. XRD pattern of the ST-HD20 boron carbide powder doped with varying quantities of carbon and mixed with alumina media.

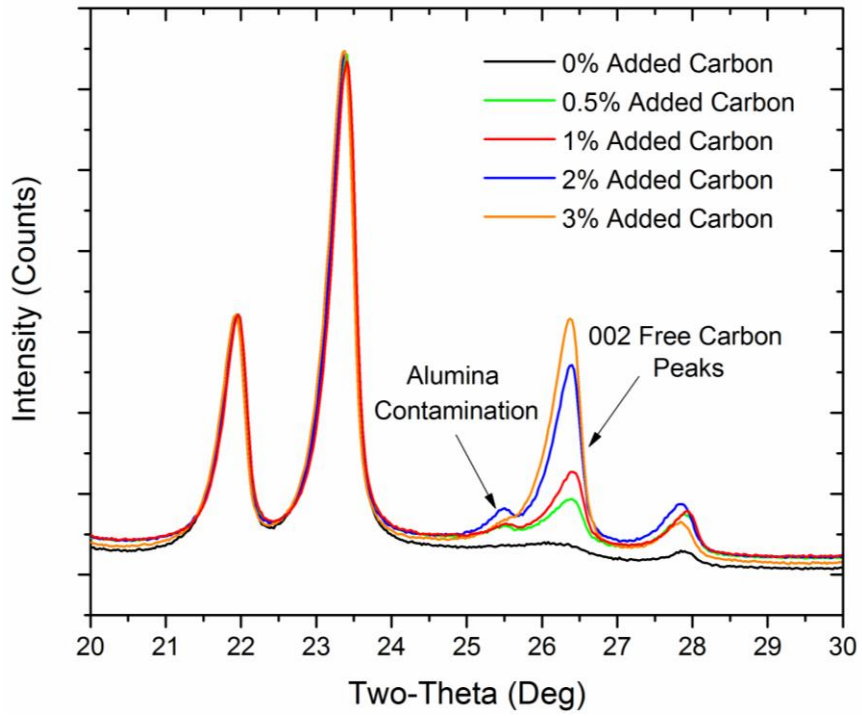

Figure 45. XRD pattern of the ST-HD20 boron carbide powder doped with varying quantities of carbon and mixed with alumina media showing alumina contamination and overlap of the alumina peaks with the 002 carbon peak.

of the commercial powders were curve fitted by accounting for the asymmetry in the peak owing to the presence of amorphous, disordered and graphitic carbon. Curve fitting of the peaks was conducted using the Renishaw Wire software package. Specific details of the curve fitting procedure employed will be extensively discussed in **Section 4.3.1.2.**

4.2.2 Wet Chemical Oxidation

In addition to the modified spiking technique, the free carbon concentration was also evaluated using the wet chemical oxidation method developed by Schwetz et al.[116]. Due to the limited capability at Rutgers University, commercial boron carbide samples were analyzed using the wet chemical method by ESK Ceramics GmbH & Co.KG, Germany. This method involves chemical oxidation of the free carbon in boron carbide with a hot-chromic-sulphuric-iodic solution at 150°C.

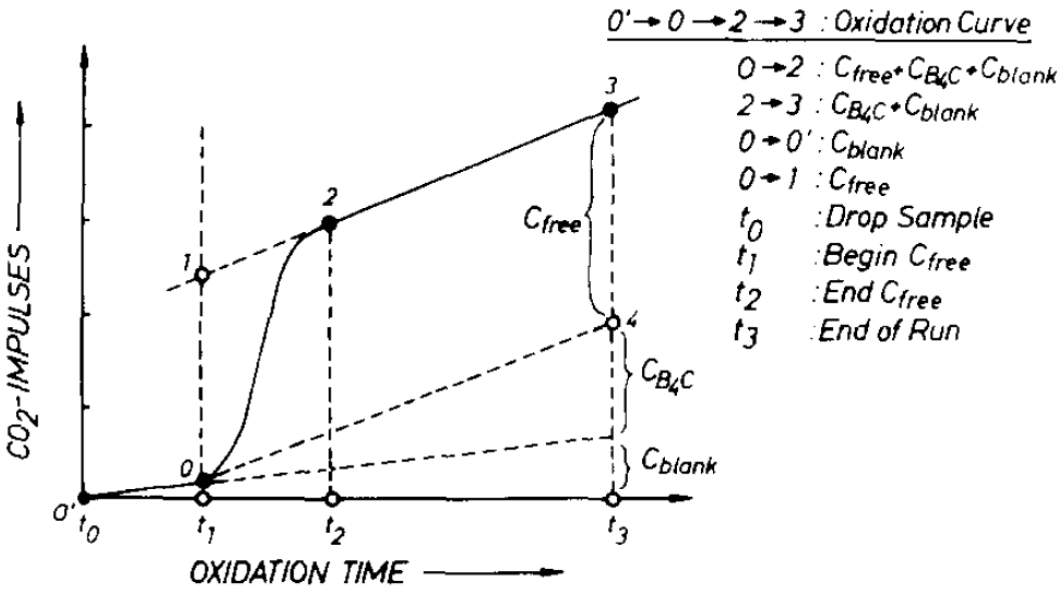

Figure 46. Analysis of free carbon in boron carbide from the CO_2 vs time plot[116].

The apparatus consists of a Coulomat 702 CO_2 analyser, reaction tube, aluminum block and a tube furnace. Once the sample is dropped into the reaction tube, the CO_2 evolved is swept into the electrolytic cell with argon gas which measures the CO_2 by coulometric

titration. The wet chemical method makes use of the rate of oxidation of free carbon and carbon bound to the boron carbide crystal structure as well as the fact that the oxidation rate of bound carbon is not a function of the reaction time. The oxidation of the free and bound carbon in boron carbide is monitored based on the concentration of the carbon dioxide formed. The free carbon concentration is then calculated from the CO_2 concentration vs time plot by graphical extrapolation. The oxidation reaction takes place in two stages as depicted in Figure 46. In the first stage (curve between points 0 and 2), only the free carbon reacts and a small quantity of combined carbon. The second stage (straight line between points 2 and 3) involves the incomplete oxidation of boron carbide[116]. The free carbon concentration is then calculated using the equation below:

$$\frac{\text{Corrected Impulses X 2}}{\text{Sample Weight X 100}} = \%\ \text{Free Carbon} \qquad (22)$$

4.3 Results and Discussion

4.3.1 Modified Spiking Technique

4.3.1.1 Heat Treatment of Amorphous Carbon

Carbon in its primary form can exist as either amorphous, disordered (turbostratic) or graphite. Amorphous carbon and graphite are composed of essentially parallel planes, with each layer consisting of a number of benzene rings[118]. Graphite has a layered structure with an interplanar spacing of 3.35 Å where each layer is systematically oriented about the layer normal[119]. Each carbon atom in a layer is bonded to 3 neighboring carbon atoms at 1.42 Å to form a two dimensional hexagonal net as shown in Figure 47. Half the atoms lie directly over atoms in the previous layer and the other half are over the centers of the hexagons. Amorphous carbon on the other hand consists of stacked layer planes that are

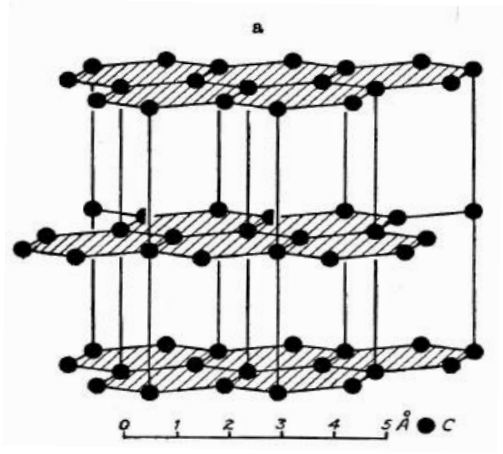

Figure 47. Structure of graphite[119]

randomly oriented about the layer normal. The spacing of the layers is larger than that of graphite and dimensions of the parallel layer groups are called L_c and L_a and have values of the order of 12 Å and 20 Å respectively[119]. Intermediate carbon shows a degree of three dimensional ordering and is referred to as disordered carbon or turbostratic carbon. Turbostratic carbon is regarded as a variant of graphite. Both graphite and turbostratic carbon are stacked up with layers with the main difference being the different ordering degrees. Typical powder diffraction patterns of carbon lampblack and heat treated carbon lampblack are shown in Figure 48. Carbon lampblack typically consists of graphite layers which are parallel to each other, but are randomly oriented about the normal[119]. The XRD pattern of carbon exhibits a high background and weak intensity with a (002) and (hk) peak. This indicated the carbon lampblack is amorphous in nature. The diffraction profile of amorphous carbon shows the occurrence of a highly asymmetric (002) peak at ~24.5° 2θ. Within this asymmetric carbon peak, existence of another band to the left could be present. In the literature, this band is called the ɤ band and is attributed to the presence of saturated structures such as aliphatic side chains[120, 121, 122]. But these bands are typically present in coals and were not considered during curve fitting. As the carbon lampblack was heat

treated to >1800°C, modulations are seen in the reflections which were observed by the splitting of the (hk) peak leading to the formation of (100) and (101) peaks. Some degree of ordering occurs causing carbon to transition from amorphous to disordered carbon (turbostratic carbon) and finally ordered or graphitic carbon. The (002) diffraction peak increases in intensity and becomes narrower revealing an increase in the crystallinity and degree of graphitization of the amorphous carbon. The sharpening of the (002) peak is a result of an increase in the average number of layers. Moreover, there is a shift in the peak position of the (002) diffraction peak from ~24.5° 2θ (amorphous carbon) towards ~26.6° 2θ (graphite). The region between amorphous carbon and graphite consists of disordered graphite (turbostratic carbon) which shows varying degree of ordering. Each of these disordered carbon phases has a particular degrees of graphitization associated with it depending on the degree of order, position of the (002) diffraction line and the FWHM of the peak.

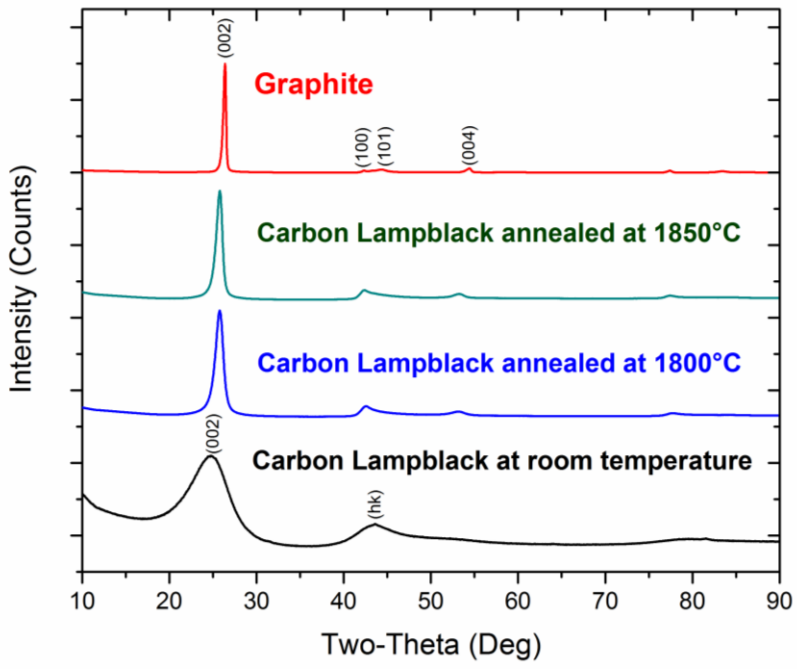

Figure 48. Effect of heat treatment on carbon lampblack on the XRD pattern.

According to Zhao et al., the graphitization process can be broken up into 3 distinct regions; non-graphitization region, near graphitization region and graphitization region which correspond to below 900°C, 1000-1200°C and above 1200°C respectively[120]. Certainly, more thorough investigations have been conducted on the graphitization behavior of carbon black,[119, 123, 124, 125, 126], but this study aims at understanding the differences seen in the type of carbon to ensure the carbon mixed with the boron carbide been subjected to the same level of graphitization as the free carbon in the commercial boron carbide powder. If the free carbon present in the boron carbide powder is not graphite, then the added carbon in the modified spiking technique should be annealed to the same temperature as the synthesized boron carbide to ensure similar levels of ordering and graphitization.

4.3.1.2 Peak Deconvolution and Curve Fitting

Figure 49 (a) depicts the XRD patterns of the ST-HD20 powder with increasing percentages of added carbon. The intensities of XRD peaks are directly proportional to the concentration of the component producing them. The diffraction lines employed while determining the free carbon concentration include the (002) carbon and (021) boron carbide peaks. Figure 49 (b) provides evidence of the proportional increase in the intensity of the (002) carbon peak with the percentage of added carbon. The zirconia media used leads to minor contamination in the resultant mixtures. But these peaks do not interfere with the major peaks of boron carbide and carbon thus preventing alteration of the final results. No other contaminants were observed during phase identification of the mixed powders. As expected, the increase in the percentage of added carbon has no effect on the intensity of the (021) boron carbide peak shown in Figure 49 (c). Similar observations were made in

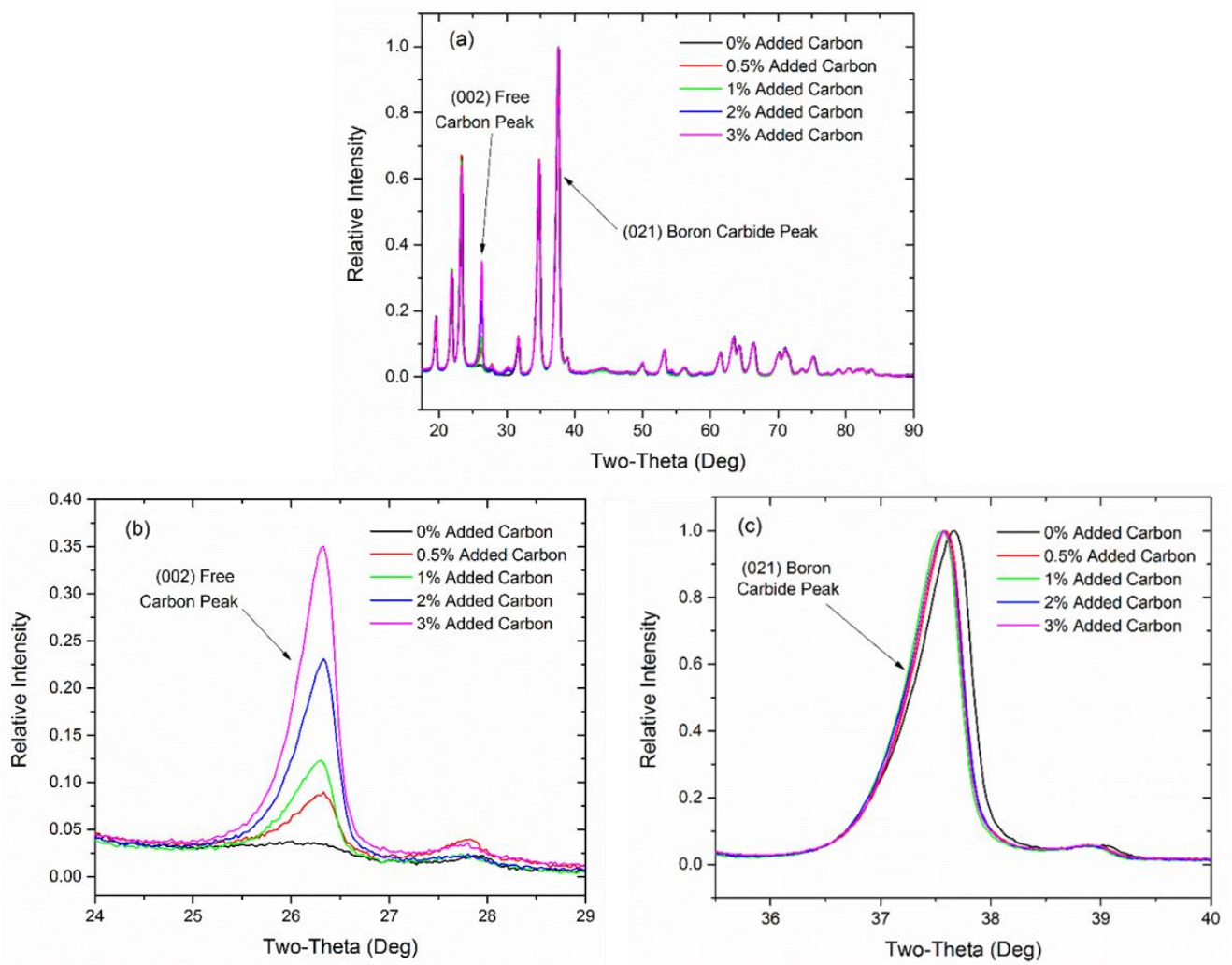

Figure 49. (a) XRD patterns of ST-HD20 boron carbide powder mixed with varying quantities of added carbon. (b) Variation of the intensity of the (002) carbon peak with the increase in the added carbon. (c) Variation in the intensity of the (021) boron carbide peak with the increase in the added carbon.

the SG-010813 and ATD-2012-6-41 boron carbide-carbon mixtures. Characteristically, the accuracy of the method for measuring the diffraction intensities is dependent on the number of counts at the required angles. As the counts obtained in these mixtures range from 250K-500K, the accuracy of quantitative analysis is reduced to 1%[127]. While measuring the intensity of these peaks for free carbon analysis, the integrated peak area is preferred to the maximum intensity as the presence of microstrain or grain size effects in the specimen may lead to significant deviations in the line shape[128]. Diffraction lines can also suffer from peak broadening because of small particle size which will influence the line intensity. The integrated area is estimated by measuring the area enclosed by the peak and the background. Accurate assessment of the peak area is key in reducing the error associated with the determination of the free carbon values and eventually the final B:C ratio. As mentioned earlier, the type of carbon present affects the peak profile of the carbon peaks, particularly the symmetric or asymmetric nature of the (002) carbon diffraction line. To account for the asymmetry in the peak shape of the (002) carbon diffraction peak based on the amorphous, disordered and graphitic nature of carbon, data analysis was conducted using curve fitting algorithms available in the Renishaw Wire software package. This technique is known as the peak separation method and is used to process assymmetrical profiles. Care must be taken to ensure the superimposed profile is close to the original one. Powder Diffraction Files (PDF) were used to ascertain the theoretical peak positions of highly amorphous and graphitic carbon as shown in Table 21.

Table 21. Theoretical peak positions and corresponding d-spacing of the amorphous and graphitic carbon used for curve fitting of the 002 carbon peak in the modified spiking technique.

Type of Carbon	2θ (°)	d-spacing (Å)
Amorphous Carbon	24.266	3.665
Graphitic[129]	26.611	3.347

The region between these two peaks was fitted with disordered carbon peaks with each peak having a particular degree of graphitization. The interlayer spacing $d_{(002)}$ and the corresponding 2θ for these disordered carbon peaks can be calculated from the model proposed by Maire and Mering using the following equation[130, 131, 132]:

$$\text{Degree of Graphitization (\%)} = \frac{d_{(\text{amorphous carbon})} - d_{(002)}}{d_{(\text{amorphous carbon})} - d_{(\text{Graphite})}} \quad (23)$$

Here, $d_{(\text{Amorphous})}$ = Interlayer spacing of amorphous carbon

$d_{(\text{Graphite})}$ = Interlayer spacing of graphite

$d_{(002)}$ = Interlayer spacing of particular graphitized peak.

Table 22 details the degree of graphitization, d-spacing and 2θ values of the curves used to fit the asymmetry of the carbon peak. In total, 25 peaks were used during the curve fitting process. The increments in the peaks used near the graphite peak were decreased to improve the fit near the maximum intensity peak. Initial observations showed that an improved fit near the maximum intensity peak, lead to a decrease in the least squared error during curve fitting. While a finite number of peaks were used during curve fitting, a continuous disorder exists between amorphous and graphitic carbon which can only be

quantified using an appropriate theoretical model, development of which is beyond the scope of the present work.

Table 22. Summary of the correlation between degree of graphitization and the corresponding2θ value.

Degree Of Graphitization %	d-spacing (Å)	2θ (°)
0	3.665	24.27
5	3.649	24.37
10	3.633	24.48
15	3.617	24.59
20	3.601	24.70
25	3.586	24.81
30	3.570	24.92
35	3.554	25.04
40	3.538	25.15
45	3.522	25.27
50	3.506	25.38
55	3.490	25.50
60	3.474	25.62
65	3.458	25.74
70	3.442	25.86
75	3.427	25.98
80	3.411	26.11
82.5	3.403	26.17
85	3.395	26.23
87.5	3.387	26.29
90	3.379	26.36
92.5	3.371	26.42
95	3.363	26.48
97.5	3.355	26.55
100.0	3.347	26.61

The major 002 carbon peak was deconvoluted and curve fitted based on the amorphous, disordered and graphitic nature of carbon. Amorphous carbon and graphitic carbon were fixed at 24.5° 2θ and 26.6° 2θ which are the theoretical positions of amorphous and graphitic carbon respectively. Minimization of the normalized value of the difference between the experimental and derived patterns was paramount during the curve fitting

process. From Figure 50, it is evident that the carbon present in the H.C. Starck powder is predominantly disordered owing to the asymmetric nature of the 002 carbon diffraction peak. In addition to disordered carbon (5-97.5% graphitization), minor quantities of pure graphite and amorphous carbon are also present. Conversely, the 021 boron carbide peak exhibited symmetry and only a single symmetric peak was employed during curve fitting. The experimental and derived patterns in both cases showed good agreement with each other. All the peaks used in the deconvolution process contribute to the total intensity of the derived pattern. This intensity was calculated as a summation of the profiles used to fit the asymmetry of the 002 carbon diffraction profile. The peaks used during the curve fitting process were assigned specific peak positions as depicted in Table 22 and constraints of ± 0.1° were defined to prevent the peaks from deviating significantly from their allocated peak positions. Curve fitting using the Renishaw Wire software was done using the Levenberg-Marquardt method which is typically used to solve nonlinear least square problems[133].

The 002 carbon peak in ATD-2012-6-41 was resolved into predominantly graphitic and partially disordered carbon peaks as illustrated in Figure 51. No presence of amorphous carbon was observed. Furthermore, the disordered carbon peaks with a degree of graphitization ranging from 5-55% were virtually non-existent providing evidence of the dissimilarity in the overall nature of carbon as compared to the ST-HD20 specimen. The major carbon peak in the Ceradyne sample showed the presence of a $K\alpha_2$ peak caused by $K\alpha_2$ radiation which is an artifact of the XRD instrumentation. This peak contributed to the overall intensity of the major carbon diffraction profile and was disregarded while calculating the integrated intensity of the deconvoluted peaks. The curve fitting results

from SG-010813 revealed trace levels of amorphous carbon and a majority of disordered and graphitic carbon peaks (Figure 52). As these powders were manufactured commercially, synthesis methods and temperatures used are not known. But, by linking the disorder in the carbon, positions of the deconvoluted peaks and temperatures required to achieve a particular degree of graphitization, valuable information can be gained regarding the conditions and temperatures employed by different commercial manufacturers in the production of boron carbide. This relationship is beyond the scope of this thesis but this method can be applied to understand typical synthesis temperatures utilized commercially. Although the 002 carbon peak was deconvoluted into multiple peaks, in actuality a continuous and incremental ordering exists between amorphous and graphitic carbon. To test the validity of peak deconvolution, curve fitting and background subtraction (discussed in **Section 4.3.1.3**) techniques developed, pure graphite was obtained from Industrial Graphite Sales. Figure 53 clearly shows the absence of amorphous carbon. Additionally, only graphitic carbon and disordered carbon peaks with a degree of graphitization >90% were observed which was in agreement to the nature of the graphite powder.

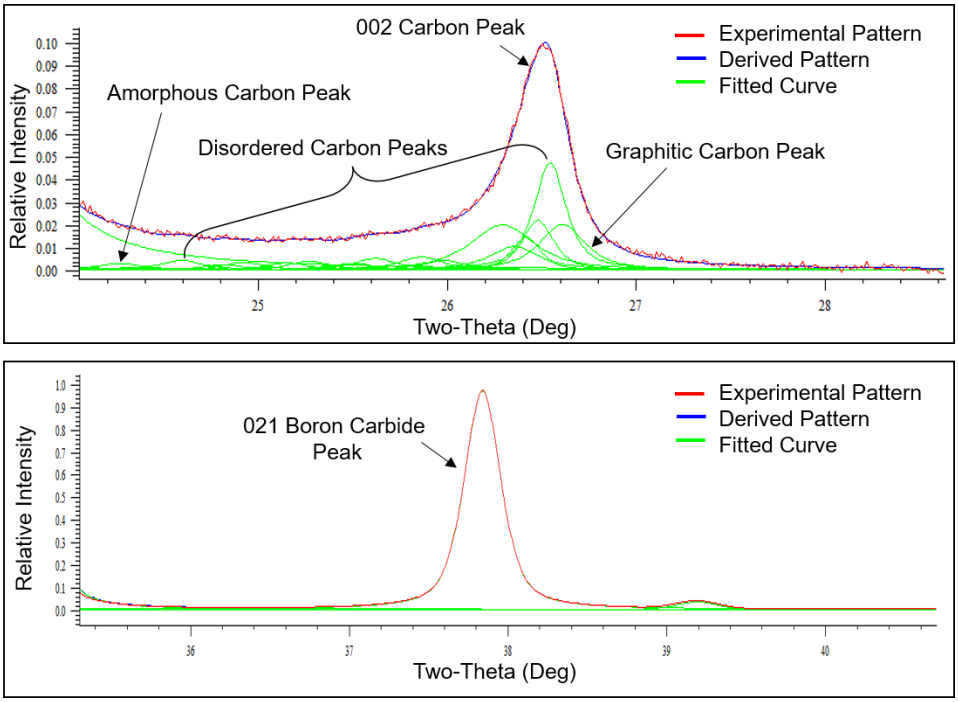

Figure 50. Curve fitting of the 002 carbon and 021 boron carbide peaks of the XRD pattern of the ST-HD20 powder with 0.5% added carbon.

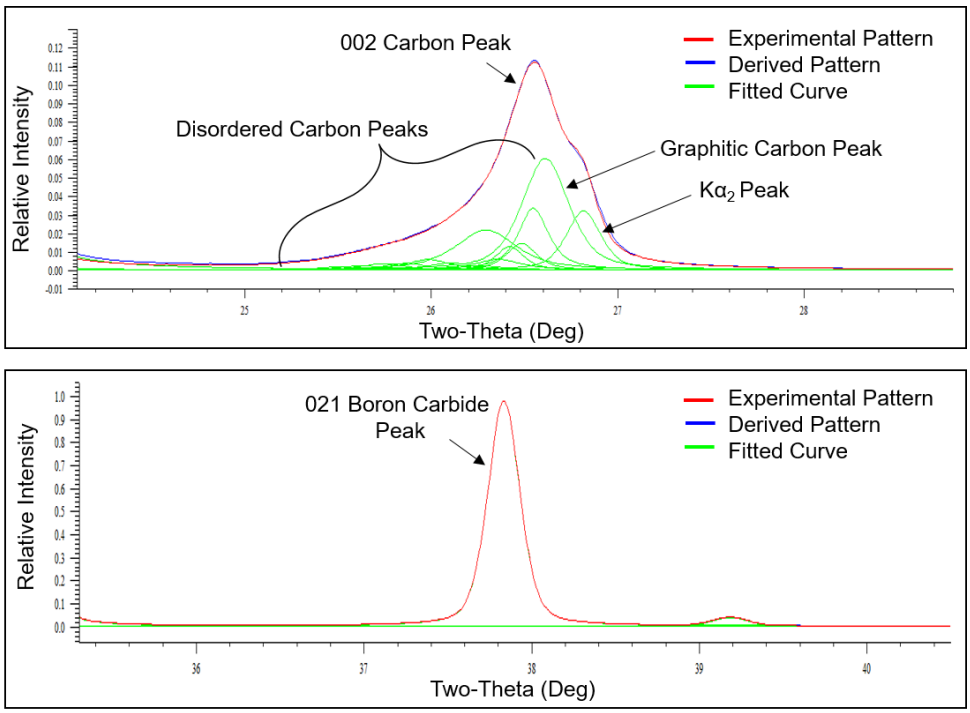

Figure 51. Curve fitting of the 002 carbon and 021 boron carbide peaks of the XRD pattern of the ATD-2012-6-41 powder 0.5% added carbon.

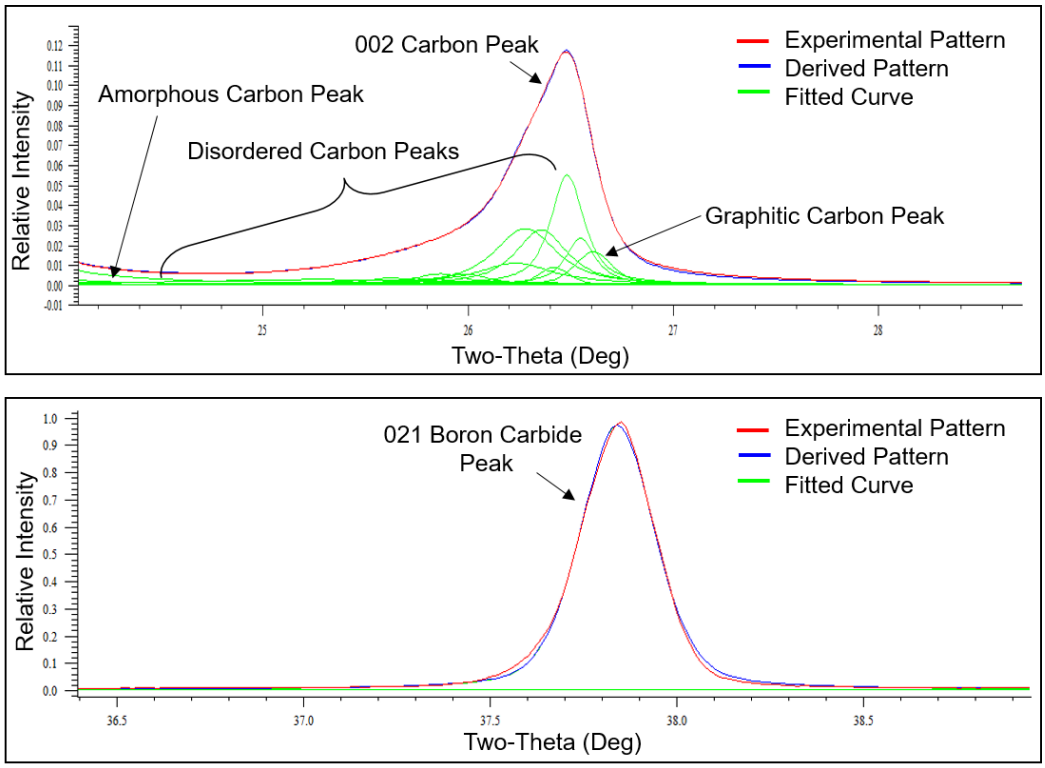

Figure 52. Curve fitting of the 002 carbon and 021 boron carbide peaks of the XRD pattern of the SG-010813 powder 0.5% added carbon.

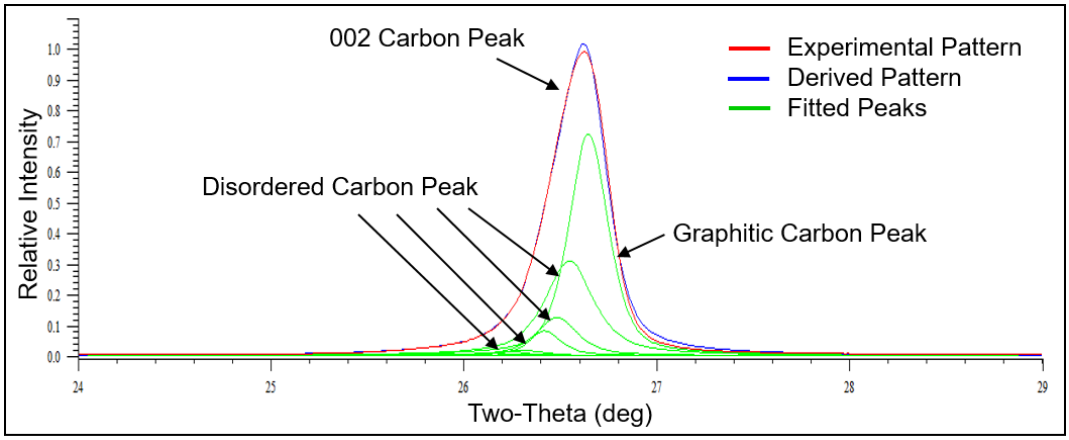

Figure 53. Curve fitting of the 002 carbon peak in pure graphite from Industrial Graphite Sales.

4.3.1.3 Background Subtraction

The level of the background is the most uncertain factor in the calculation of the integrated intensity of the diffraction peaks. The background can either be estimated by linear interpolation between selected points, between peaks, or modelled using an empirical function. For a relatively simple pattern where the peaks can be easily resolved, both methods work well. But for complex patterns like that of boron carbide, which have a large degree of overlap, the estimation of the background becomes critical. Minor variations in the subtraction of the background lead to large differences in the ratio of the relative intensities of carbon and boron carbide and eventually the free carbon values. Hence the approach used for background subtraction becomes vital. Polynomial functions used for background subtraction are empirical in nature [88]. Polynomial functions would work well only if they correctly describe the background, but this is very rarely achieved in complex patterns. After considering these factors, the background was subtracted using linear interpolation. But this method is highly dependent on the user's interpretation of the peak overlap and deconvolution of peaks, and thus requires some level of judgement on the part of the operator. Figure 54 illustrates the background subtraction from an XRD pattern with the use of a cubic spline curve which is the most common methodology for background subtraction in XRD analytical work. Here, two different curves are used for background subtraction. Depending on the user's interpretation of the tail of the 002 carbon peak and its overlap region with neighboring peaks, different integrated peak areas were calculated. This discrepancy directly affected the relative intensity of the carbon and boron carbide peaks which in turn influenced and alter the free carbon results. In lieu of the erraticity in the results, an alternate approach was devised.

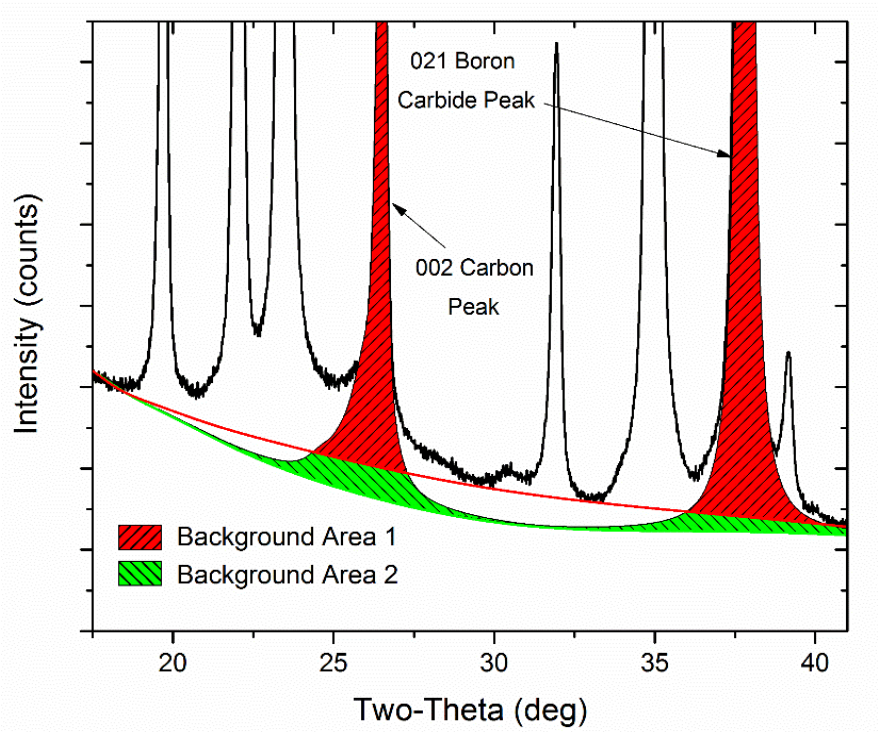

Figure 54.Variation in the integrated intensity/area during background subtraction using a cubic spline curve

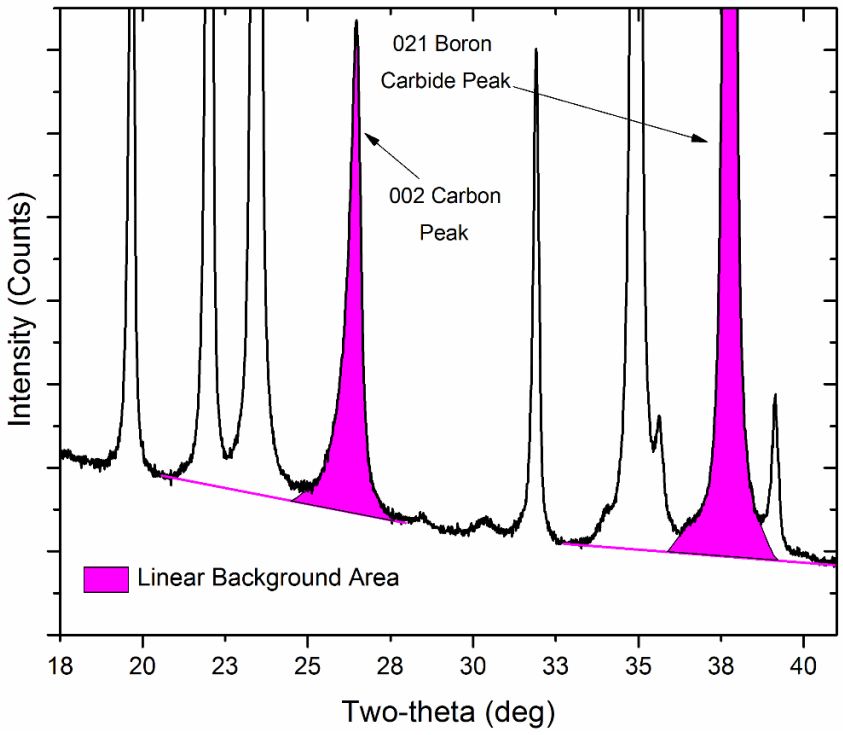

Figure 55. Linear approximation during background removal.

The background curve is approximated to be linear from ~18.5° 2θ to ~ 29.6° 2θ and ~30° 2θ to ~ 43.4° 2θ as depicted in Figure 55. It was assumed that the individual diffraction peaks have a profile of a tailed triangle and each peak has an approximately linear function. This methodology proved to give accurate results and minimized the dependence of background subtraction on the user. A similar approach has been used in literature to model the background of individual peaks[134, 135].

4.3.1.4 Free Carbon Analysis

After curve fitting and background subtraction was completed, the integrated intensity of the 002 carbon peak was calculated as a summation of the deconvoluted peaks based on the amorphous, disordered and graphitic nature of carbon. The graph of the relative intensities of the 002 carbon and 021 boron carbide peaks to the percent of added carbon shows a linear relationship. Through graphical extrapolation of this linear relationship onto the negative y axis, the free carbon content is calculated in the original boron carbide powder as shown in Figure 56, Figure 57 and Figure 58. The free carbon contents of the three powders discussed in this section are provided in Table 23. A total of 3 separate mixtures at each composition were prepared and subsequent curve fitting was conducted to evaluate the standard deviations and the error associated with the modified spiking technique. These standard deviations ranged from ~4% - ~8%.

Table 23. Comparison of the free carbon values of boron carbide powders obtained using the modified spiking technique

Sample #	Sample Company	Free Carbon (wt%)	Standard Deviation
ST-HD20	H.C.Starck	0.96	± 0.04
ATD-2012-6-41	Ceradyne Inc.	2.38	± 0.20
SG-010813	Superior Graphite	1.83	± 0.08

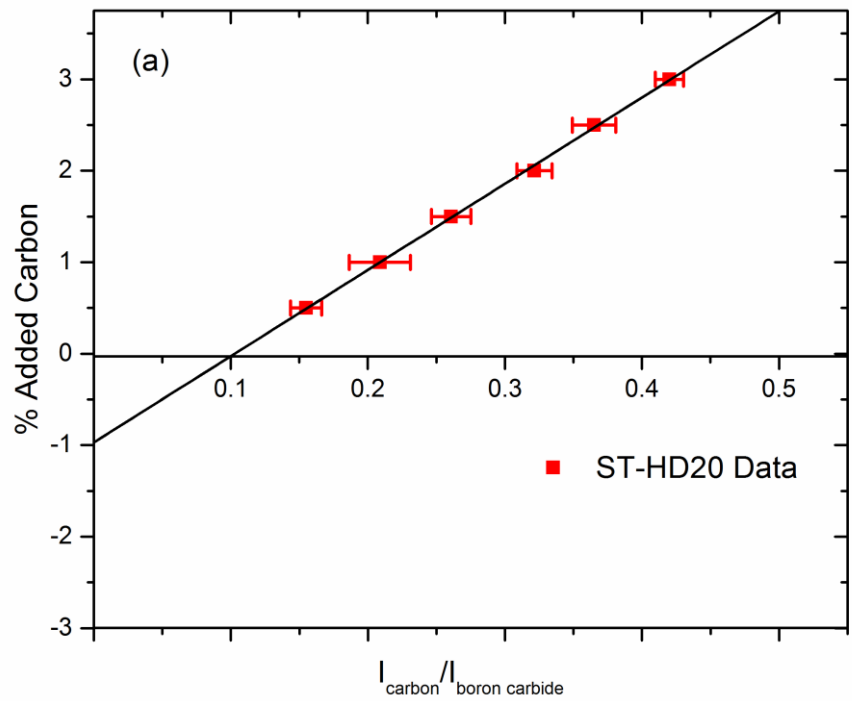

Figure 56. Determination of the free carbon content in the ST-HD20 powder by the modified spiking technique. The free carbon concentration was estimated at 0.96%.

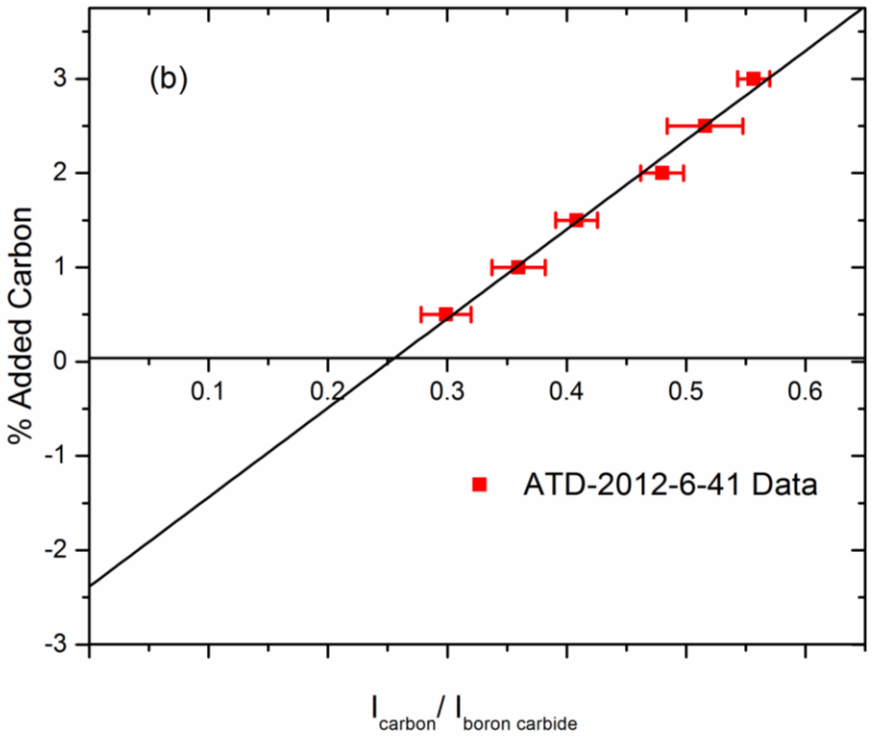

Figure 57. Determination of the free carbon content in the ATD-2012-6-41 powder by the modified spiking technique. The free carbon concentration was estimated at 2.38%.

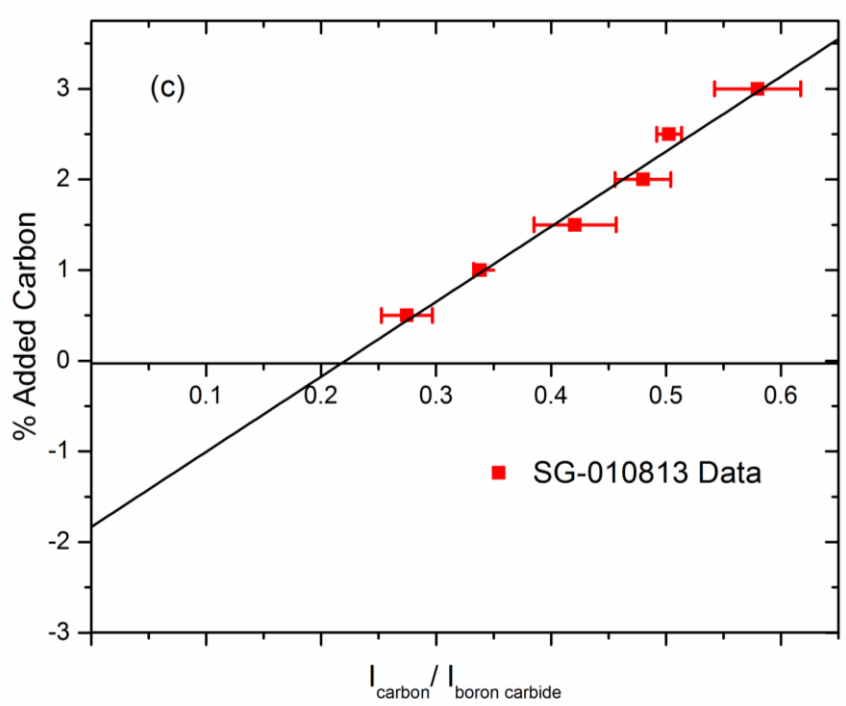

Figure 58. Determination of the free carbon content in the SG-010813 powder by the modified spiking technique. The free carbon concentration was estimated at 1.83%.

4.3.2 Wet Chemical Oxidation

Comparison of the free carbon results using the wet chemical oxidation method and modified spiking technique are shown in Table 24. The carbon values using the wet chemical method in the ST-HD20 powder were almost twice the results obtained from the modified spiking technique. However, visual examination of the XRD pattern of the ST-HD20 powder was inconsistent with the 1.82% free carbon assessment from the wet chemical method. This was immediately evident by evaluating the intensity ratios of the 002 carbon and 021 boron carbide peaks from Figure 59.

Overestimated free carbon values typically occurs in powders with low particle sizes. In a submicron particle size powder, due to the increased surface area and similarity in chemical properties of carbon and boron carbide, oxidation of boron carbide occurs

concurrently with that of free carbon. The wet chemical method is highly dependent on the difference in the rate of oxidation of free carbon and carbon bound to boron carbide. But, in superfine powders, this assumption no longer holds any validity and the free carbon value extrapolated (Figure 46) contains significant levels of CO_2 from oxidized boron carbide, thus overestimating the final results. The results of the wet chemical analysis of ATD-2012-6-41 powder on the other hand differed from the values obtained by the modified spiking technique on the same sample by a factor of ~2. Visual examination of the XRD pattern (Figure 60) and the intensity ratio of the carbon and boron carbide peak profiles proved that the 1.25% assessment by the wet chemical method was not plausible. SEM micrographs revealed the coarse nature of the ATD-2012-6-41 powder with carbonaceous inclusions trapped within the boron carbide grains. These inclusions are not completely oxidized thus leading to an underestimation of the free carbon concentration. XRD detects these inclusions because of the increased penetration depth of the x-rays in light elements. The free carbon in the SG-010813 sample agreed quite well with results from the modified spiking technique as a result of the increased particle size and powder morphology. This imposes limitations on the wet chemical oxidation method as it provided accurate results only in specific cases.

Table 24. Comparison of the free carbon values of boron carbide powders using the modified spiking technique and wet chemical oxidation method.

Sample #	Sample Company	Modified Spiking Technique (wt%)	Wet Chemical Oxidation (wt%)
ST-HD20	H.C.Starck	0.96	1.82
ATD-2012-6-41	Ceradyne Inc.	2.38	1.25
SG-010813	Superior Graphite	1.83	2.01

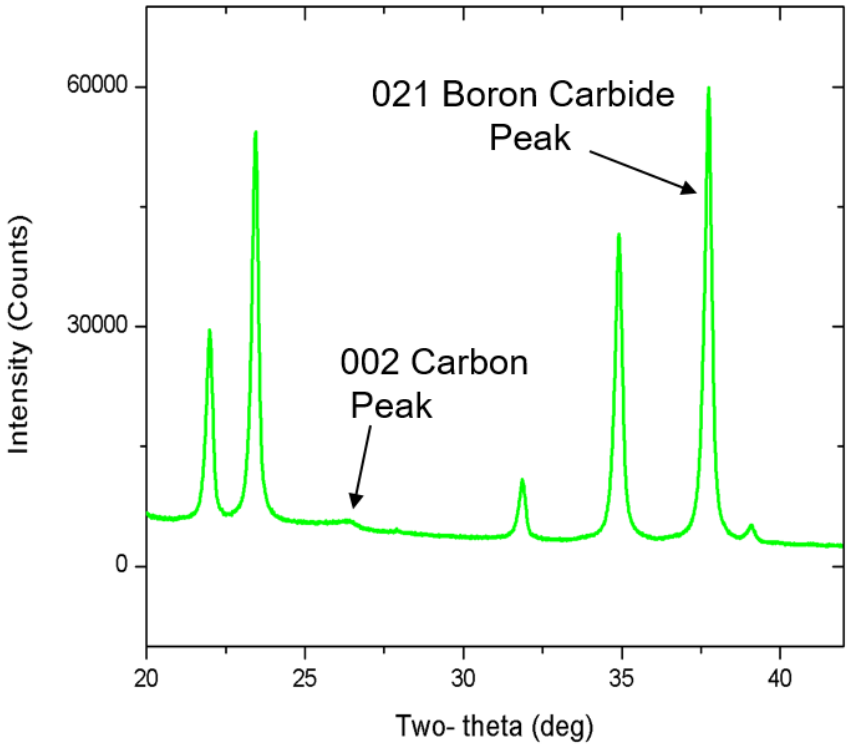

Figure 59. XRD pattern of the ST-HD20 powder manufactured by H.C. Starck.

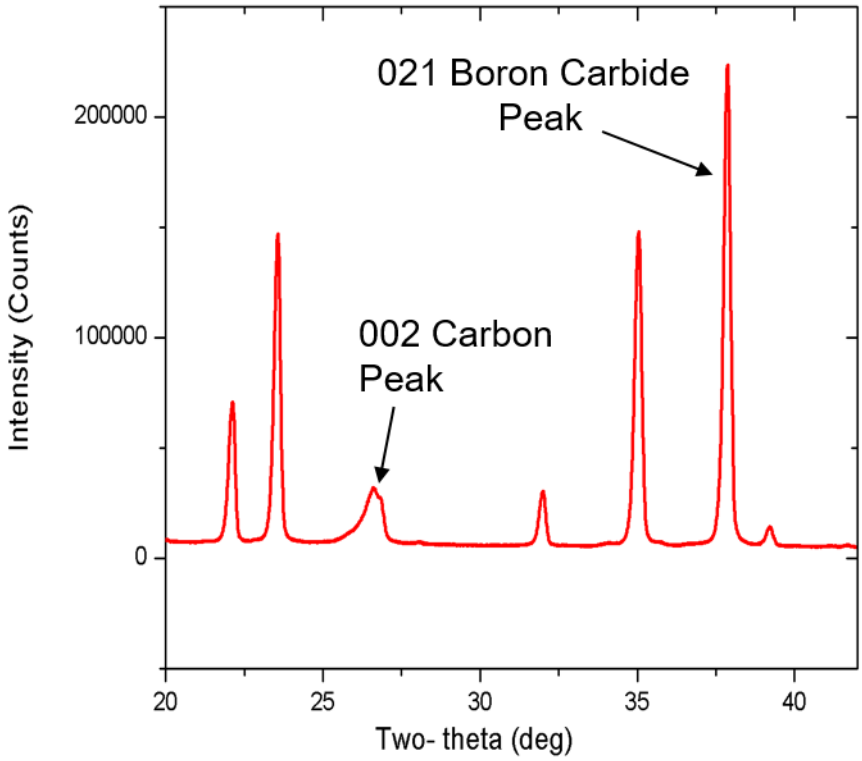

Figure 60. XRD pattern of the ATD-2012-6-41 powder manufactured by Ceradyne Inc.

4.3.3 Stoichiometric Measurements

Utilizing the free carbon results from the modified spiking technique detailed in the preceding sections and the values from the chemical analysis in Table 9, the stoichiometry of the commercial powders was recalculated as shown in Table 25. The accuracy and precision of these values has been increased as a result of an improved method to determine the free carbon concentrations. The ST-HD20 and SG-010813 powders had stoichiometric compositions close to that of B_4C while the ATD-2012-6-41 powder was boron rich. Even though the standard deviations associated with the stoichiometry are comparable to the results obtained in Table 11, the accuracy and precision of these values has been increased as a result of an improved method to determine the free carbon values.

Table 25. Summary of the stoichiometric values using the modified spiking technique and chemical analysis.

Sample #	Sample Company	Stoichiometry
ST-HD20	H.C.Starck	3.88 ± 0.04
ATD-2012-6-41	Ceradyne Inc.	4.62 ± 0.07
SG-010813	Superior Graphite	4.09 ± 0.05

4.3.4 Reference Sample

A reference material (ED-102) manufactured by ESK was obtained from Germany to test the validity of the developed characterization techniques. This powder was extensively characterized by analytical companies and research institutes across the world and was accepted as a European reference material. Good agreement was observed in the

reported and measured values of the reference sample (Table 26 and Table 27. The free carbon concentration using the modified spiking technique was within the expected standard deviation of ± 0.12 reported in the reference sample. Furthermore, the stoichiometric values attained using the developed characterization techniques were commensurate with those reported in the reference sample. These results provided further evidence that the developed characterization techniques were accurate and precise.

Table 26. Methods used and reported values of the European Reference Material (ED-102) produced by ESK.

Parameter	Certified Value (wt%)	Standard Deviation	Method
Total Carbon	21.01	± 0.28	Combustion –Coulometric
Total Oxygen	0.10	± 0.04	Carrier Hot Gas –Infrared Detection
Total Nitrogen	0.21	± 0.03	Carrier Hot Gas –Thermal Conductivity Detection
Total Boron	78.47	± 0.31	Potentiometric
Free Carbon	0.51	± 0.12	Wet Chemical Oxidation
Stoichiometry	4.23	± 0.06	

Table 27. Methods used and measured values of the European Reference Material (ED-102) produced by ESK.

Parameter	Measured Value (wt%)	Standard Deviation	Method
Total Carbon	20.83	± 0.07	Combustion – Infrared Detection
Total Oxygen	0.10	± 0.01	Carrier Hot Gas –Infrared Detection
Total Nitrogen	0.24	± 0.01	Carrier Hot Gas –Thermal Conductivity Detection
Total Boron	78.10	± 0.28	Potentiometric
Free Carbon	0.58	± 0.03	Modified Spiking Technique
Stoichiometry	4.27	± 0.02	

4.4 Summary

In this objective, a novel method to determine the free carbon concentration has been proposed which has shown an increased accuracy and reliability as compared to previously used analytical techniques. The modified spiking technique can be applied to evaluate the free carbon values in boron carbide, irrespective of the nature of the carbon present. This technique is also applicable to boron carbide powders synthesized at low temperatures where the amorphous carbon has not completely crystallized to graphite. This technique overcame the drawbacks of the wet chemical method which depended on powder morphology and particle size. Furthermore, the modified spiking technique can be used to calculate free carbon concentrations as low as 0.1 wt% which is the detection limit of the XRD.

Although specific peaks were employed in the modified spiking technique to account for amorphous, disordered and graphitic carbon, in actuality, a continuous disorder exists from amorphous carbon to graphite. Therefore, the carbon peak can be fitted with an infinite number of disordered carbon peaks to attain the best fit. Ideally, a structural model is required which would describe the level of disorder and integrated intensity. This would not alter the integrated area measurements and free carbon results, but would serve as a theoretical model to predict the free carbon values from experimental observations of the XRD patterns. In the future, the structural model developed by Shi[136] coupled with the results from the modified spiking technique can be employed to not only evaluate the free carbon values but also examine the nature of the disorder present in carbonaceous inclusions.

5 Investigation of the Structural and Mechanical Properties of Boron Carbide Across the Solubility Range

5.1 Introduction

So far, an in-depth understanding of the currently used analytical and chemical techniques has been attainted and a new method to determine the free carbon concentration has been proposed. These techniques have reduced the errors associated with the determination of the boron carbide stoichiometry. This objective aims at investigation of the structural variations in boron carbide across the solubility range through the development of the lattice parameter-stoichiometry calibration curve. This will be achieved through the synthesis of boron carbide samples over a range of controlled stoichiometries. Additionally, the changes in the mechanical properties will also be investigated to evaluate the preferred composition and purity of boron carbide for extreme dynamic conditions.

Due to the structural variations of boron carbide across the solubility range, there is a direct dependence of the hexagonal and rhombohedral lattice parameters on the carbon concentration. However, the exact nature of this relationship is ambiguous and has been the consideration of significant debate over the last 60 years[13, 15, 20, 33, 40, 96, 97, 98, 99, 137]. Identifying the stoichiometry from measured lattice parameters, provides a convenient and nondestructive technique in obtaining the final composition of boron carbide. From XRD, it is possible to get the lattice parameters with an accuracy less than 30 ppm as compared to TEM which is 1000 ppm. A detailed study on the assessment of the characterization techniques for the determination of the boron carbide stoichiometry has underlined the importance of the method used to evaluate the free carbon concentration. The uncertainly involved with the determination of the free carbon is negated by using the lattice parameter

and stoichiometry relationship. Assessing the stoichiometric value accurately is of prime importance, especially since the physical, mechanical, elastic, electronic and optical properties of boron carbide appear to be dependent on the boron to carbon stoichiometry[6, 7, 11, 56, 57, 59, 85, 138]. Further, the microstructural and ballistic response of boron carbide could also be affected by the B:C ratio due to the change in the mechanical properties and elastic properties.

The available literature data on the correlation between the width and height of the unit cell and B:C ratio shows significant scatter (Figure 61) primarily due to the limitations of the previous analytical techniques and a long standing misconception that B_4C was the only stoichiometric composition of boron carbide. Yakel's[15] and Robson's[99] data are reasonably in agreement with each other. But there seems to be a systematic shift of Robson's lattice parameters towards higher values. Furthermore, questions remain regarding the chemical techniques used and the accuracy of their measurements[9,33]. The model developed for the single crystal by Yakel had a chemical composition of nearly 50% more than his measured values for the synthesized bulk specimens. This discrepancy was present at low carbon concentrations. Due to the significant error associated with these samples, ion beam analysis was conducted which only reduced the error by 10%. Additionally, a clear trend between the lattice parameters and carbon content could not be observed due to the wide distribution of data. Higher lattice parameters reported by Allen could be a direct consequence of the presence of impurities[34]. Aselage et al.[13, 98] used three approaches to prepare samples: 1) solid-state reaction; 2) hot pressing; and 3) solution growth from metallic fluxes. Initially, only the results from hot pressing will be discussed. A detailed

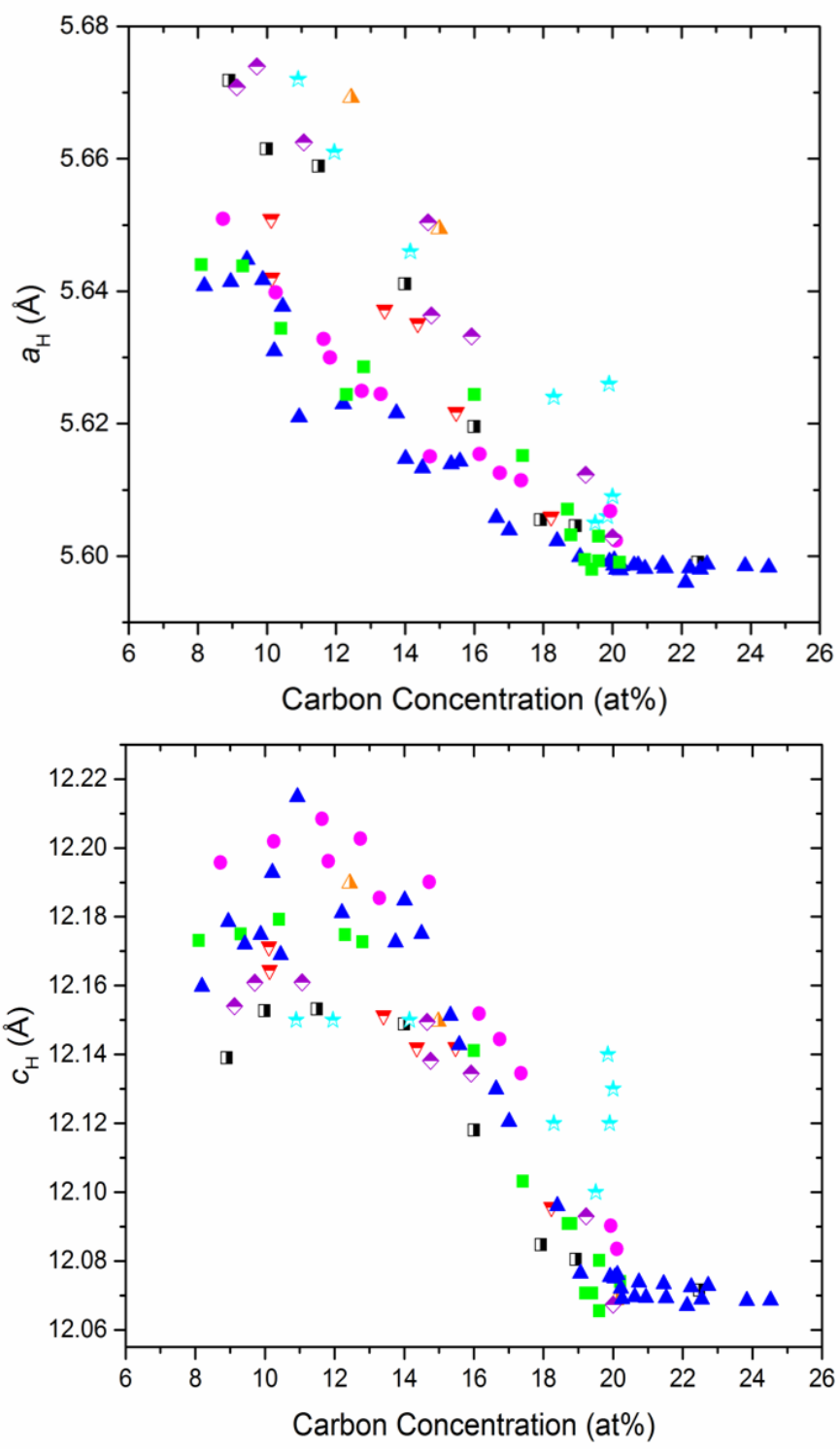

Figure 61. Comparison of the Hexagonal lattice parameters of boron carbide and the carbon concentration as determined by previous authors. □: Yakel[15], ◭: Allen[55], □: Aselage et al.[98] (Hot Pressing), ☆: Bouchacourt et al.[40] (E-beam), ●: Bouchacourt et al. (Hot Pressing), □: Robson[99], ■: Aselage et al.[13] (Solid State Reaction) ▲: Gosset et al.[96] (Hot Pressing).

examination of the results from solid state reaction will be explained later. Aselage et al.[98] used uniaxial hot pressing to prepare consolidated materials from mixtures of boron and high purity graphite. To prevent contamination of boron carbide from the graphite die, a high purity BN liner was used with an inner diameter of 3/8 in or 1/2 in. But this experimental setup will not completely prevent boron carbide from graphite contamination from the grafoil (graphitic sheet present between the die and sample) and die. Contamination of graphite from the die and grafoil leads to the formation of "stoichiometric" boron carbide, rather than boron carbide with the expected B:C ratio. This diffusion of graphite into boron carbide causes a gradient of B:C ratios in the densified material. Thus, the analysis conducted after hot pressing would result in an incorrect assessment of the stoichiometry. An effort was made by Aselage to investigate the graphite contamination from the grafoil using Raman spectroscopy, but this method only served as a semi-quantitative technique to evaluate the carbon concentration in boron carbide. Based on these assessments, 500 μm was removed from the top and bottom of the hot pressed specimen so that the Raman spectra from the surface matched the one taken from the interior of the sample. But the variations seen in the Raman spectra from 20 at% to 13.3 at% are not as significant as compared to those spectra taken beyond 13.3 at% carbon, as will be discussed later in this paper. Consequently, even if specimens differ by a carbon concentration of 1-2%, these subtle variations cannot be deciphered through the changes seen in the Raman spectra. The BN lining that was also used may not have completely isolated the boron and carbon mixture, thus leading to a further gradient in the B:C ratio across the sample. This phenomenon remained unexamined in this paper. Hence questions are raised regarding the homogeneity of the samples used for analysis and the accuracy of

the stated stoichiometry. This work also reported higher lattice constant values, when compared to the other results available in the literature. The high hexagonal lattice parameters could be a consequence of residual strains in the samples which would cause a shift in the XRD peak positions. The densified materials were not crushed prior to analyzing the samples. Crushing serves a dual purpose: 1) relieves the residual strain; and 2) improve the accuracy of chemical analysis by working with finer materials.

A more comprehensive analysis to measure the lattice parameter-carbon concentration relationship was conducted by Bouchacourt et al.[33, 97] using sample preparation techniques similar to the hot pressed samples produced by Aselage[13]. The major difference in the sample preparation involved the absence of BN lining along the inner circumference of the graphite die. The entire crushed hot pressed samples with varying B:C ratios was used for analyses. This approach presents a problem as detailed above: it leads to graphite contamination and the presence of a gradient with varying stoichiometries across the sample size that was more pronounced than in the samples produced by Aselage. The boron and carbon contents were determined using analytical chemistry, quantitative electron microprobe analysis and activation analysis. Based on the reported data, the *a* lattice parameter depends linearly on the carbon concentration, but exhibits an increase in the slope beyond 13.3 at% carbon. The values of the *c* lattice parameter on the other hand decreased towards the boron rich limit after the critical composition of 13.3 at% was achieved. These observations in the trend of the lattice constants from 13.3 – 20 at% carbon were attributed to the increase in the length of the C-B-C chain with the decrease in the carbon concentration and pointed towards the possibility of a substitution phenomenon in the B_{12} icosahedra. From 8 – 13.3 at%, the changes seen in the lattice parameters with the

carbon concentration were interpreted as a result of substitution of the C-B-C chain by the B_4 group. Due to the large scatter associated with these results and the possible inaccuracies with regards to the chemical composition of the resultant samples, the trends seen in the Bouchacourt lattice parameter curves are highly debatable. Additionally, the absolute values of the *c* lattice parameters are higher as compared to the values reported by other researchers. Possible reasons for this could be due to incorrect sample preparation or misalignment of the diffractometer. The absolute errors in the lattice parameters measurements ranged from □a = 0.001 Å and □c = 0.005 Å which translates to an inaccuracy of 0.3 at% and 1.3 at% carbon respectively.

The more widely accepted correlation of the lattice parameters to the bound carbon content was proposed by Aselage et al.[13] where boron carbide samples were made by solid state reaction between amorphous boron and graphite. The *a* lattice parameter increased linearly from 20 at% to the boron rich phase limit of 9 at%. The *c* lattice parameter flattened out at 13.3 at% carbon. The results reported by Aselage differ when compared to Bouchacourt's hot pressed samples. Significant scatter is observed in the lattice parameters and the carbon concentration throughout the solubility range, but especially close to the carbon rich solubility limit. The major reason for this scatter is because of uncertainties associated with the determination of the free carbon concentration which in turn increased the error associated with final stoichiometry. The scatter is responsible for the increased R value during linear regression which affects the fit used to develop an empirical relationship between the lattice parameters and the carbon content. As a result of the increased error in this relationship, the carbon concentration of unknown samples may not be completely accurate. To test the accuracy of the Aselage data, lattice parameters of a

reference sample (ED-102) were measured by XRD and overlaid on to existing curves. The results differed by a carbon concentration of ~0.4% when compared to the calibration curve developed as part of this work. Another possible explanation for the difference in the data, could be due to the presence of surface oxygen, nitrogen, boron oxide and boron nitride. Considering these values is of prime importance, especially in fine powders due the oxygen and nitrogen buildup on the surface of the powders. An initial effort was made by Aselage to remove surface oxides by heating the loose powder at 1900°C under vacuum. Moreover, degradation of the PBN crucibles was also observed which further led to contamination of the boron carbide powder. Although O or N species were not observed using Raman spectroscopy, Raman serves as a semi-quantitative technique and ultimately identifying the oxygen and nitrogen contents using chemical combustion techniques provides a true reflection of the oxygen and nitrogen values. Negating these factors would effectively alter the stoichiometry and shift the lattice parameter curve towards the carbon rich limit. These factors may account for the inconsistencies seen in determining the stoichiometry of the reference sample and would further translate into inaccuracies in unknown samples.

The inherent differences and inaccuracies which accompany the available lattice parameter-stoichiometry relationships have been gleaned in the preceding paragraphs. To improve the existing understanding, a systematic sample preparation and specimen analysis will be discussed to shed some light on the lattice parameter variations across the solubility range. Many questions also remain unanswered regarding the structural and atomic configurations of boron carbide across the solubility range as discussed extensively in **Section 1.2**. The exact occupancy of the carbon and boron atoms is still highly debated and numerous theories exist that consider the preferential substitution of boron atoms for

carbon atoms in the icosahedra, intericosahedral chains or formation of vacancies[13, 15, 20, 21, 28, 33, 107, 139, 140]. Understanding the changes seen in the lattice parameters as a function of the carbon concentration could shed some light regarding the preferred structural model of boron carbide across the solubility range.

Variations in mechanical properties can be traced back to microstructural variations in the carbon content, grain size, inhomogenieties and porosity. However, in this work, only the effect of stoichiometry on the mechanical properties will be investigated to evaluate the preferred composition and purity of boron carbide for extreme dynamic environment applications. The effect of stoichiometry on the hardness of boron carbide has been an area that has not been well documented. Contradictory reports have been published regarding the effect of the B:C ratio on the hardness of boron carbide[56, 57]. Furthermore, linking the results from the structural variations to the change in the hardness as a function of the B:C ratio would help supplement understanding of the specific atomic configurations contributing to an improvement or diminishment in the hardness.

5.2 Experimental Procedure

5.2.1 Sample Preparation

Consolidated boron carbide samples were prepared by hot pressing mixtures of Ultra High Purity amorphous boron (ABCR GmbH &Co. KG, Germany) and boron carbide (H.C. Starck). In the first step of the sample preparation procedure, the boron carbide powder was cleaned to remove surface oxides, excess boron oxide and boric acid that had accumulated due to prolonged exposure to the atmosphere. The washing procedure entailed mixing the powder with hydrochrolic acid (3.5 pH) in an ultrasonicator for 15 minutes and heating the solution at 150°C. The solution was allowed to sit overnight and post the

sedimentation process, excess acid was decanted. The residual powder was then mixed with distilled water and decanted as described above. The mixing, sedimentation and decantation procedures were carried out twice with distilled water and ethanol. After the sample had been cleaned with ethanol, it was placed in a drying oven (Thermolynn Drying Oven) at 100°C.

The stoichiometry of the principal H.C Starck (ST-HD20) boron carbide powder was estimated at $B_{3.88}C$ as calculated in **Section 4.3.3**. Based on this value of the B:C ratio, consolidated boron carbide samples across the compositional range were then prepared by mixing precise amounts of amorphous boron with the washed boron carbide powder, to first eliminate the free carbon in the parent boron carbide and then to attain boron carbide at a particular stoichiometry. Addition of amorphous boron to "stoichiometric" boron

Table 28. Summary of the excess amorphous boron needed during hot pressing to produce boron carbide with an expected stoichiometry of $B_{13}C_2$.

Calculations for Boron Rich Samples	Amount of Powder (g)
Total boron carbide (ST-HD20)	4.00
Total boron required to get $B_{13}C_2$	5.00
Excess boron added to eliminate the free carbon present in the boron carbide (Assumption: Reaction between graphite and excess boron Takes place according to B_4C)	0.15
Excess boron added to get $B_{13}C_2$	2.15
Summation of excess boron and boron carbide (H.C. Starck) added to get $B_{13}C_2$	6.15

carbide would result in the boron entering the boron carbide crystal lattice, thus forming boron rich boron carbide. An example of the specific calculations used to make one such consolidated boron carbide tile are shown in Table 28. An assumption made during calculations was that part of the amorphous boron reacted with the free carbon in the boron carbide to form B_4C. This mixing methodology was used to make boron carbide specimens at variable B:C ratios. Amorphous boron and dried boron carbide powders were mixed in a high energy Spex mill for 10 minutes in the absence of grinding media to prevent any external contamination. Initially, dense boron rich samples with controlled stoichiometries were produced using spark plasma sintering at

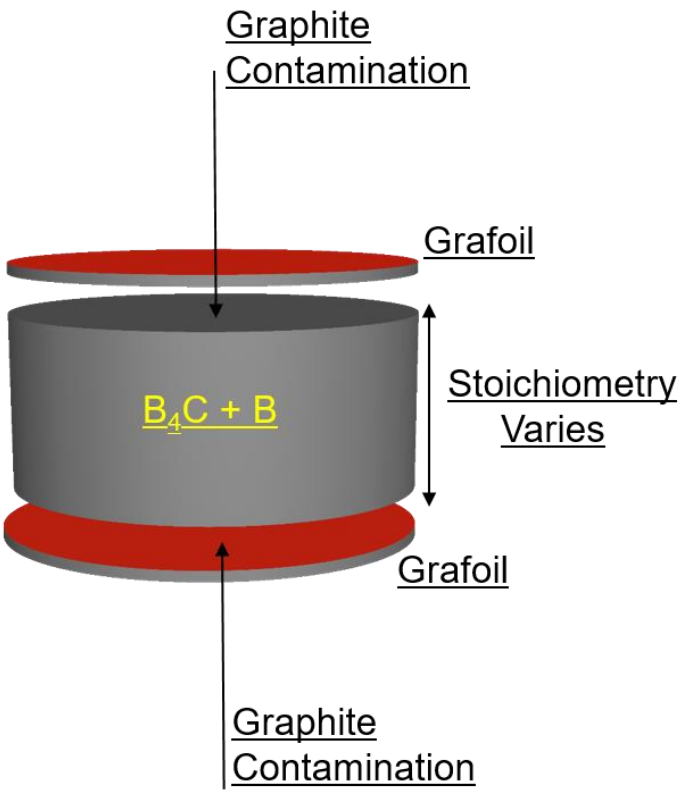

Figure 62. Diffusion barriers in consolidated boron carbide synthesized using spark plasma sintering.

1900 °C for 10 min. But this approach proved unsuccessful based on analysis of densified samples. The boron carbide diffraction pattern showed the presence of asymmetric peaks which indicated possible presence of multiple polytypes of boron carbide within the same sample. Additionally, the stoichiometry of the densified tiles was significantly lower when compared to the expected values. This deviation from the expected results can be explained on the basis of an incomplete reaction during sintering and contamination of graphite from the grafoil and graphite punches as shown in Figure 62. Thermodynamically, stoichiometric boron carbide ($B_{4-x}C$) is the stable phae. During sintering, the amorphous boron reacted with graphite from the die to form stoichiometric boron carbide rather than

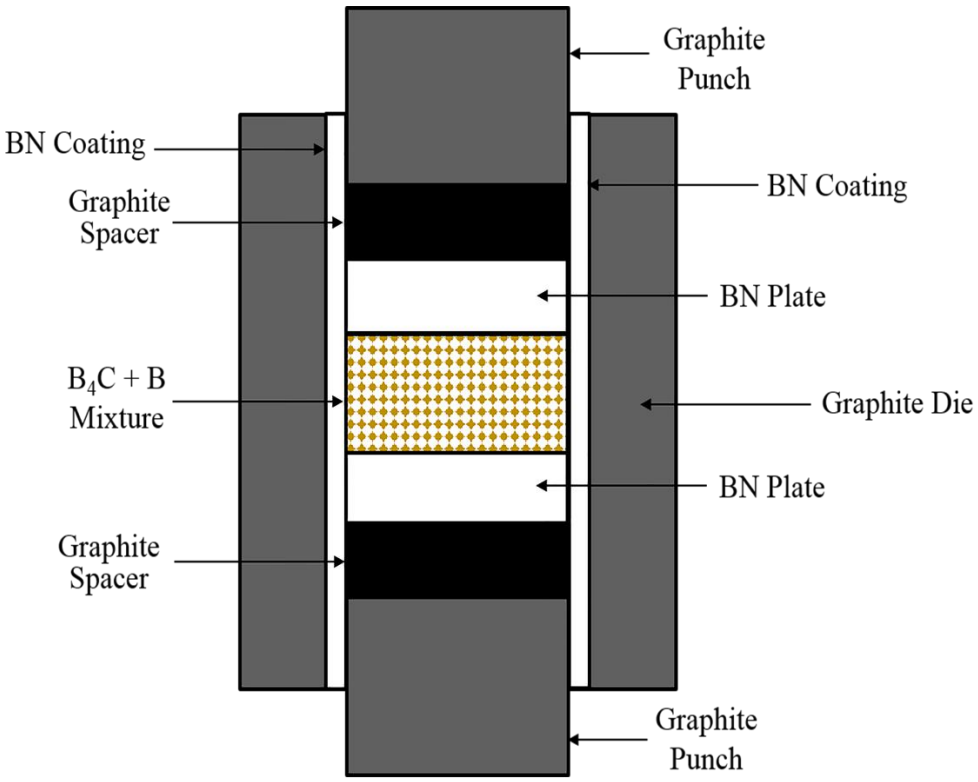

Figure 63. Schematic of the assembly used during hot pressing of the boron carbide and amorphous boron mixtures.

boron carbide at the expected stoichiometry. To overcome the complications associated with spark plasma sintering, an alternate approach was utilized where mixtures of amorphous boron and boron carbide weighing 6 to 6.5 g were isolated with boron nitride plates and a boron nitride coating (ZYP Coating) as shown in Figure 63. Boron nitride plates were preferred as these acted as more effective barriers when compared to BN tape or BN coating. Isolating the mixtures proved to be of particular importance to prevent graphite contamination from the graphite spacers and die. In the absence of the isolation chamber, amorphous boron reacted with graphite resulting in the formation of "stoichiometric" boron carbide and eventually altered the final stoichiometry. This assembly was prepressed at 5000 psi and then hot pressed using an Oxy-gon High Temperature Vacuum Furnace System (Figure 64). The densification cycle employed during hot pressing is detailed in Table 29. Hot pressing was also preferred over spark

Figure 64. Oxy-gon High Temperature Vacuum Furnace System used to hot press mixtures of amorphous boron and boron carbide.

plasma sintering as temperatures in excess of 2000°C could be used which served as a sufficient driving force for producing boron rich boron carbide. Moreover due to the longer hold times and absence of localized hot zones, potentially more homogenous samples were formed. All the hot pressing work was done at the Army Research Laboratory (ARL) in Aberdeen, MD.

Table 29. Summary of the cycle used to hot press mixtures of amorphous boron and boron carbide.

Segment Number	Temperature	Pressure
Segment 1	Ramp: 1000°C at 10°C/min under vacuum	Ramp: 1000 lbf
Segment 2	Dwell: 1000°C for 10 min under vacuum	Ramp: 2000 lbf
Segment 3	Ramp: 2000°C at 10°C/min under argon	Dwelve: 2000 lbf
Segment 4	Dwell: 2000°C for 120 min under argon	Dwelve: 2000 lbf for 120 min
Segment 5	Cool Down	Cool Down: 1000 lbf

5.2.2 Sample Analysis

Characterizing homogenous bodies was a main emphasis in this effort. Despite efforts to isolate carbon intrusion, some amount of carbon diffused from the graphite die due to volatilization of the BN lining. Hence, the core of the samples was analyzed exclusively, as shown in Figure 65 (a). The boron nitride plates adhered to the densified tiles were ground off with coarse polishing pads (125 μm and 70 μm) to minimize boron nitride contamination (Figure 65 (b)). The samples were subsequently sectioned according to the dimensions specified in Figure 65 (c) and XRD analysis was performed on the center of

the cross sectional faces. Figure 66 presents an illustration of the variation of the carbon concentration from XRD results from cut 1 to cut 4 in a densified sample that has an expected carbon content of 14 at%. These results show that the carbon content in cuts 1 and 2 are slightly higher than the expected values. As one moves towards the central core, the carbon concentration approached expected results. Similar analysis on all the prepared boron carbide samples revealed that a gradient existed from the outer rim towards the inner core to ~5 mm towards the center because of graphite infiltration from the die. This phenomenon as discussed earlier was attributed to the volatilization of the boron nitride

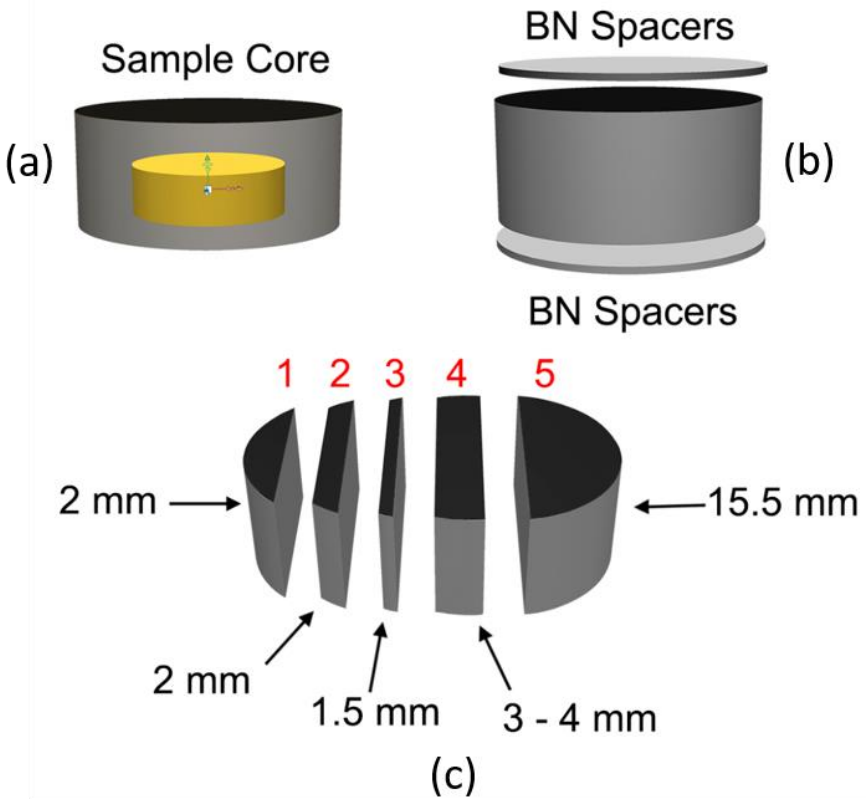

Figure 65. Schematic of the hot pressed boron carbide. (a): Core of the sample used for analysis. (b): Boron nitride spacers ground off with coarse polishing pads. (c): Schematic of the sectioned tile showing the thickness of each cut.

coating which resulted in graphite reacting with the amorphous boron forming "stoichiometric" boron carbide rather than boron carbide with the expected B:C ratio. As cut 3 and cut 4 had B:C ratio's similar to the expected values, these samples were used for subsequent chemical, x-ray diffraction and Raman analysis for the determination of the lattice parameters and the corresponding stoichiometry. Cut 3 was mounted in an epoxy with a Buehler Simpliment 100 mounting machine and the surface of cut 3 facing cut 4 was polished. The polishing procedure employed is detailed in **Section 5.2.3**. After the polishing procedure was completed, Raman spectroscopy was performed to complement x-ray diffraction results. Additionally, hardness measurements were performed to examine the effect of stoichiometry on the hardness as described in **Section 5.2.4.**

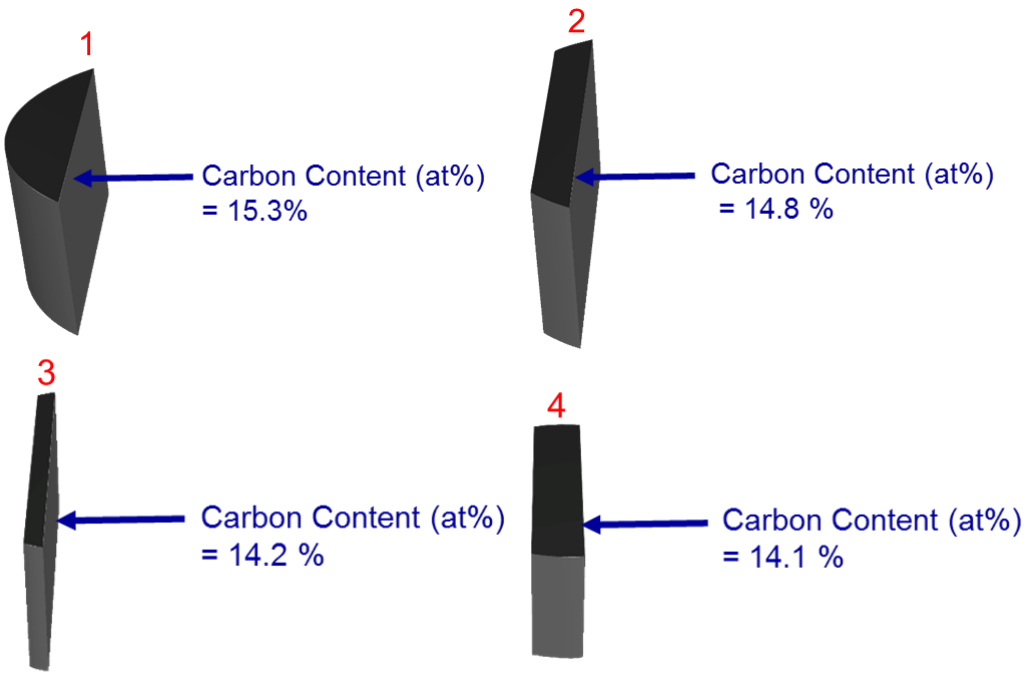

Figure 66. Variation in the carbon concentration from cut 1 to cut 4 in a sample that has an expected carbon content of 14 at%.

In order to evaluate the compositional variation across cut 4, XRD was performed at regular intervals and the corresponding lattice parameters and B:C ratios were evaluated using Aselage's data as shown in Figure 67. The literature data served as a reference point and provided insight into the compositional variations across the sample[13]. Due to the large scan area of the x-ray diffractometer and presence of overlap regions during scanning, Raman spectra were acquired from both the cross-sectional faces with the aim of achieving better spectral resolution due to its significantly lower spot size. The Raman spectra attained at regular intervals from the edge towards the center, exhibited variations in the peak positions and intensities. Beyond 6 mm from the edge, the spectra remained qualitatively unchanged, indicating the central region consisted of boron carbide with constant stoichiometries (Figure 68). Owing to the presence of consistent B:C ratios in the central region, the inhomogeneous regions of the samples were cut at 6 mm from the edges.

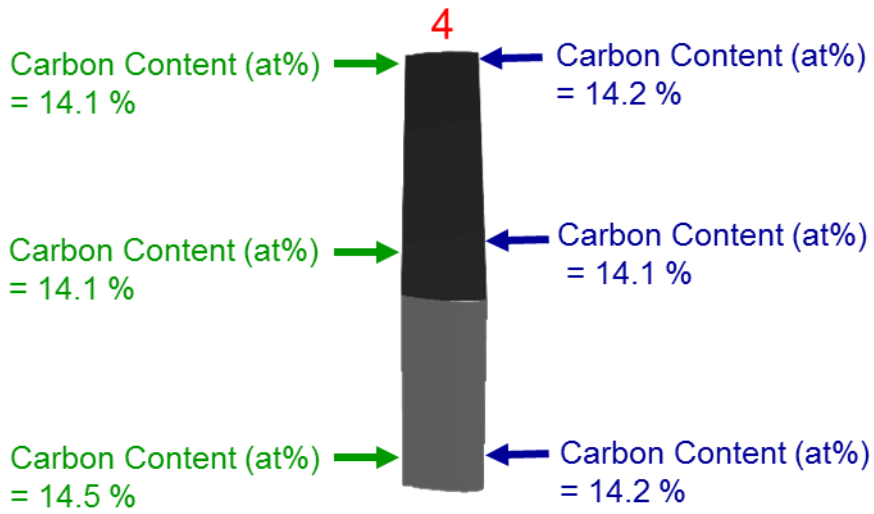

Figure 67. Carbon content on both the cross sectional faces of cut 4 from X-ray diffraction.

These samples were then crushed using a diamond embedded motor, pestle and hammer. The crushed powders were washed using the cleaning procedure (**Sections 3.2.5**) to remove iron contaminants entering the system during crushing. X-ray diffraction data from the crushed powders was collected using a Panalytical X'Pert system utilizing conditions similar to those detailed in **Sections 3.2.1**. The crushed powders were mixed with methanol to form a slurry and this then formed a thin layer of powder on the zero background silicon wafer XRD holder. A line position NIST silicon standard (SRM 640e) for powder diffraction was mixed with the crushed powders during sample preparation. Phase analysis and lattice parameter refinement was conducted using MDI Jade version 9.0

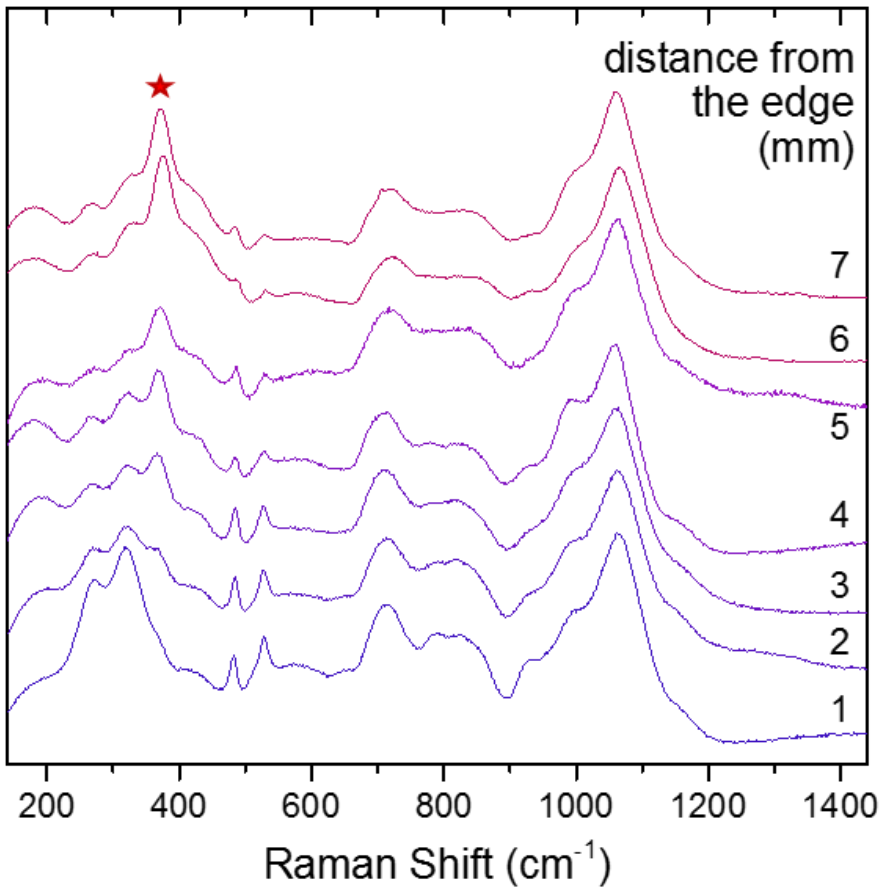

Figure 68. Raman spectra variations at regular intervals from the edge towards the center across the right cross sectional face.

with a hybrid whole pattern fit/least squares refinement. The lattice parameters were calculated to average precisions of +/- 0.0003 angstroms. Sample compositions were then assessed using various chemical techniques. A LECO CS230 was used to obtain the total carbon present in the boron carbide samples. Oxygen and nitrogen analysis was performed using a LECO TC600 instrument. Boron titration was conducted using ASTM C791-04. This method involved mannitol titration after fusing the boron carbide, Na_2CO_3 and KNO_3 in a platinum crucible. For further details about the boron, carbon and oxygen/nitrogen methods used, please refer to **Section 3.2.4.1**, **Section 3.2.4.2** and **Section 3.2.4.3**, respectively.

5.2.3 Polishing

Cut 3 was mounted in an epoxy with a Buehler Simplimet 100 mounting machine and the surface of cut 3 facing cut 4 was polished as previously mentioned (Figure 69 (a)). Polishing was performed using a Buehler Ecomet 250 polisher with Automet 250 powder

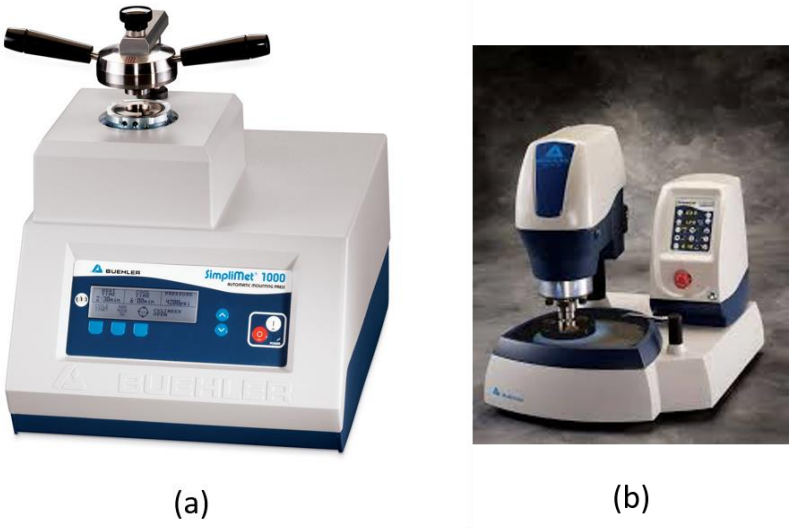

Figure 69. (a) Buehler Simplimet 100 mounting machine. (b) Buehler Ecomet 250 polisher with Automet 250 powder heads.

heads (Figure 69 (b)). The first step in the polishing procedure involved using the 125 µm diamond embedded pad to remove excess epoxy from the surface of the sample. The next steps involved using the 70 and 45 um pads to remove pullouts occurring during the polishing procedure. Fine polishing was then conducted using the 9, 6, 1, and 0.25 µm cloth pad with the appropriate diamond suspensions. Table 30 provides specific details of the polishing procedure employed.

Table 30. Polishing cycle used for the boron carbide samples

Size of Polishing Pad (µm)	PAD Type	Cycle-Time (min)	Rotation & Speed	Pressure (lbs per sample)
125	Embedded	4x10	Contra - 180	5
70	Embedded	3x10	Contra - 180	5
45	Embedded	3x10	Contra - 150	5
15	Embedded	2x10	Contra - 150	5
9	Suspension	2x6	Contra - 150	4
6	Suspension	4x6	Contra - 120	4
1	Suspension	3x6	Same - 120	4
0.25	Suspension	3x6	Same - 100	4

5.2.4 Nanoindentation

Nano-indentation was performed using a NanoTest Vantage nanoindenter manufactured by Micro Materials as shown in Figure 70. The polished sample was mounted on the stub (Figure 71) using a small quantity of adhesive and left in the instrument enclosure for 20 minutes for it to thermally stabilize. The temperature inside the nanoindenter enclosure was maintained at ~25°C as higher or lower temperatures could

affect the hardness results. The indenter area function was calibrated with fused silica following the approach detailed by Oliver and Pharr[141].

Figure 70. NanoTest Vantage nanoindenter manufactured by Micro Materials.

Figure 71. Sample stub for mounting the polished sample.

The indenter used for calibration and subsequent indentation was a Berkovich diamond tip which is a three-sided pyramidal indenter commonly used to measure nanoindentation hardness and modulus. Select samples of boron carbide from the compositional range were chosen for nanoindentation. The applied loads ranged from 50 – 500 mN and 20 indents were made at each load. A limit stop load of 0.15 mN, indenter contact velocity of 0.5 µm/s, initial load of 0.05 mN and loading/unloading rate of 2.5 mN/s were used. The indents were separated by a distance of 20 µm to prevent interaction between cracks generated from the indents which could potentially affect the hardness values. The major advantage of nanoindentation over regular microhardness is the relatively small size of the indents. Specific locations within the samples for analysis were picked away from the pores, thus preventing porosity from affecting the hardness results. Once indentation was completed, the load vs displacement curves and optical images of the indents were critically analyzed and those indents hitting pores were disregarded from analysis.

Load displacement curves can be used to evaluate the hardness where the indenter displacement is continuously monitored as load is being applied to an indenter in contact with a specimen (Figure 72)[141]. The load displacement relationship for simple punch geometries can be written as[141]:

$$P = \mathrm{A}\,(\mathrm{h} - \mathrm{h}_f)^m \tag{24}$$

Where P is the indenter load, h-h_f is the elastic displacement of the indenter and A and m are constants.

Oliver and Pharr[141] suggested an analysis technique which accounted for the curvature in the unloading data and provided a physically justifiable procedure for

evaluating the contact depth and the indenter shape function to establish the contact area at peak load. The slope of the unloading curve provides a measure for the elastic modulus.

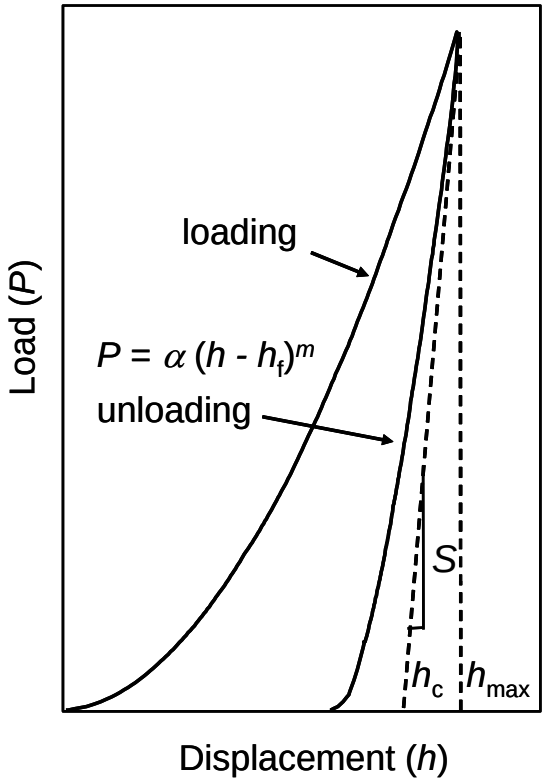

Figure 72. Load vs displacement curves monitored by the nanoindentation system[141].

The area of contact at peak load is determined by the geometry of the indenter and depth of contact. The geometry of the indenter is given by the cross-sectional area of the indenter to the distance from its tip and the projected area at maximum load is given by:

$$A = F(h_c) \quad (25)$$

Where F is the functional form evaluated before experiments are carried out.

The area of the contact is calculated based on the indenter displacement and indenter geometry. Hardness is then defined as the maximum applied load divided by the contact area at maximum load. However, the hardness measurements using the load displacement curve are highly dependent on the applicability of the model proposed by Oliver and Pharr[141]. Instead, conventional hardness was obtained from the ratio of the

maximum load applied to the area of the residual imprint determined using scanning electron microscopy. Furthermore the nanoindentations hardness number was calculated from the results of the Berkovich hardness using the relationship detailed below:

$$H = 1.1\ HB \tag{26}$$

Where H is the true hardnes and HB is the Berkovich hardness number.

5.2.5 Scanning Electron Microscopy

The SEM micrographs of the indents were taken using a Zeiss Σigma Field Emission Scanning Electron Microscope (Figure 73) with inlens (IL) and secondary electron (SE) detectors. The conditions utilized included a voltage of 5 kV, working distance of 2-5 mm, aperture of 30 µm and magnifications of 18 k, 25 k, 30 k, 45 k, 50 k and 75 k. Samples were prepared using an aluminum scanning electron microscopy (SEM) stud with a 1/2" slotted head and a 1/8" pin from Ted Pella Inc. This was covered with carbon tape to prevent charging of the sample.

Figure 73. Zeiss Σigma Field Emission Scanning Electron Microscope.

5.3 Results and Discussion

5.3.1 Structural Properties

5.3.1.1 Phase Identification

In the past, the sensitivity of XRD patterns of boron carbide were compromised because of its low atomic number and transparency. However, recent advancements with regards to equipment and detectors have led to significant enhancements in the resolution and intensities achievable. Applying the conditions detailed in **Section 5.2.2**, sufficient resolution and peak intensity (250 – 500 k) was achieved which permitted detection of traces phases. The phase identification and the corresponding quantitative analysis on the ST-HD20 boron carbide yielded a major phase of boron carbide and a secondary phase of

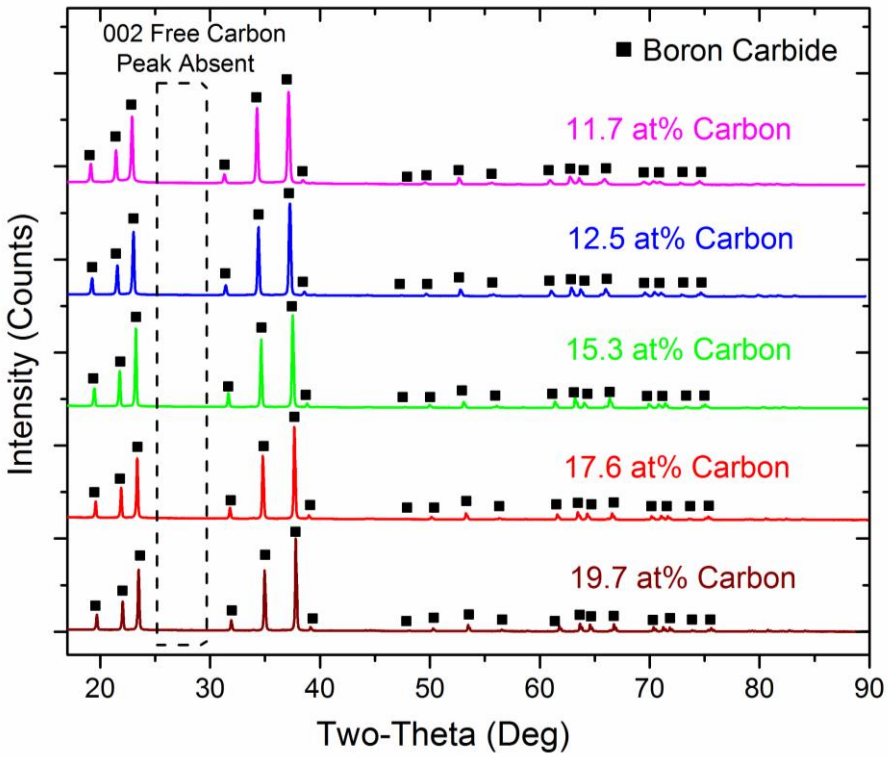

Figure 74. X-ray diffraction patterns of selected boron carbide samples across the solubility range showing the absence of free carbon and presence of phase pure boron carbide.

free carbon as discussed in **Section 3.3.1.** PDF cards for different polytypes of boron carbide were utilized during phase identification to determine the best fit for the primary phase. Based on the results from chemical analysis and x-ray diffraction, the stoichiometry of the boron carbide was estimated at ~B_4C. Figure 74 shows the XRD patterns and phase identification of select boron carbide samples made across the solubility range. Indexing of the peaks was conducted using similar reflections to Table 6. There was an absence of secondary (002) free carbon peaks at 2θ values of ~26.6°. This indicated that there was no graphite infiltration from the graphite punches and the amorphous boron added during densification completely reacted with the free carbon in the original powder. Additionally, no evidence of the free carbon peak was observed in the sample with a carbon concentration of 19.7 at% demonstrating that the solid solution solubility range of boron carbide could possibly extend beyond 18.8 at% carbon ($B_{4.3}C$) proposed by Schwetz[9] and Werheit[142]. According to Werheit, it was suggested that the chemical compound B_4C did not exist when prepared by high temperature methods such as hot pressing or melting at temperatures exceeding ~2027°C. But direct observations of the phase identification of the prepared samples near B_4C dispute this claim. Boron nitride contaminants were also not observed in the XRD patterns allowing us to believe that the boron nitride plates used for the isolation chamber did not infiltrate into the consolidated tile. Metallic impurities were not detected within the detection limits of XRD demonstrating the formation of phase pure boron carbide samples within the homogeneity range. Hence the washing procedure employed serves as an effective tool for cleaning the crushed powder from contaminants entering the system during crushing. Any trace contaminants present in the crushed powder

could only be present at ppm levels which would not be sufficient enough to cause deviation in the lattice parameters.

There was a systematic shift of the maximum intensity (021) boron carbide peaks towards lower 2θ values as seen in Figure 75. This provides visual evidence of the increase in the lattice parameters due to the addition of boron into the boron carbide crystal structure resulting in the formation of boron rich boron carbide at a specific stoichiometry. The boron carbide diffraction profile exhibited symmetric peaks without the presence of peak splitting. This signified that the boron carbide formed consisted of a single phase of boron carbide rather than multiple phases with differing stoichiometries.

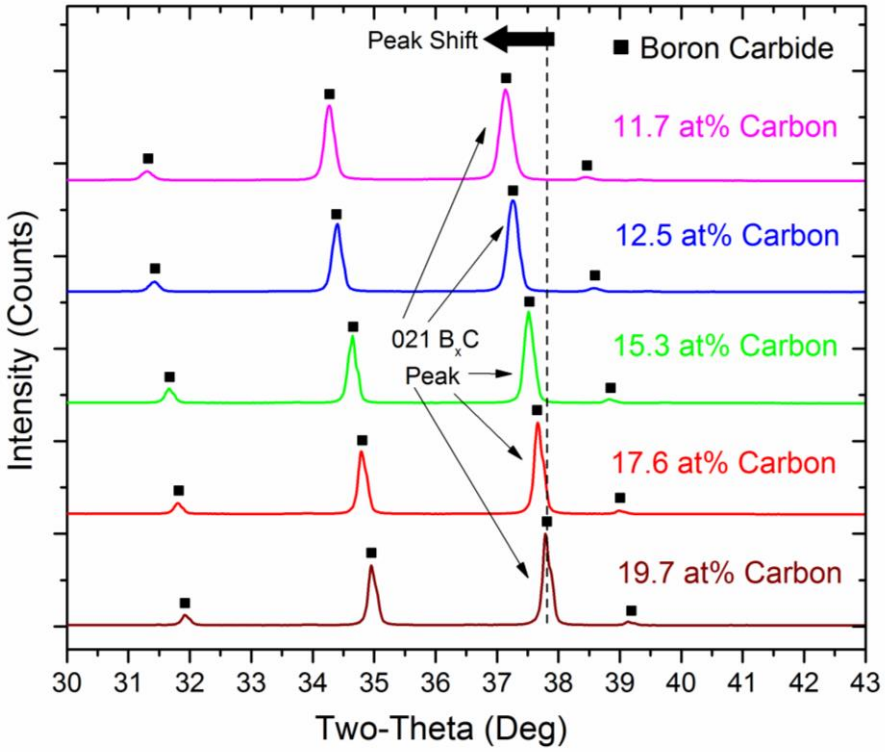

Figure 75. Shift in the (021) boron carbide peak towards lower 2θ values indicating an increase in the lattice parameters.

5.3.1.2 Lattice Parameters vs Carbon Concentration

The XRD patterns possessed a sufficient signal to noise ratio for lattice parameter estimation using Rietveld Refinement. Owing to the use of the NIST line position standard (640 (e)), the presence of systematic errors in the diffraction patterns was eliminated. The results of the hexagonal lattice parameters, unit cell volumes and the corresponding carbon contents are listed in Table 31. The bound carbon contents were determined after calculation of the boron carbide stoichiometry based on the chemical techniques described in the **Section 5.2.2**. In total, 17 samples were prepared at varying B:C ratios and characterized using the developed techniques. The standard deviations of the unit cell parameters and volume results are also reported in Table 31. The variation of the hexagonal lattice parameters and unit cell volume as a function of the bound carbon contents are plotted in Figure 76 (a), (b) and (c). The lattice constants and the unit cell volume increase linearly from ~20 at% to 13.3 at% carbon. This was in agreement with previously developed relationships of the lattice parameters and the carbon concentrations[13, 33, 96]. The results below ~13.3 at% carbon exhibit a linear dependence on the carbon concentration. But, beyond this critical composition, the lattice constants and the unit cell volume show a further increase in their absolute values at decreasing B:C ratios, albeit with a different slope. Previously published lattice parameter calibration curves showed that the lattice parameters were linearly dependent on the carbon content and c_H remained constant beyond 13.3 at% carbon. But the results reported in this paper exhibit a different trend when compared to previously reported lattice constant-carbon concentration relationships[13, 33, 96]. Due to the certainty associated with the analysis and the care taken in utilizing homogenous powders for analysis, sufficient confidence is affiliated with these results. The effect of

Table 31. Hexagonal lattice parameters, unit cell volumes and carbon concentrations of the synthesized boron carbide samples.

a_H (Å)	c_H (Å)	Volume$_H$ (Å^3)	Carbon Concentration (at%) from Chemical Analysis	Stoichiometry of Analyzed Samples
5.5993 ± 9.00E^{-5}	12.0738 ± 2.05E^{-4}	327.82 ± 9.30E^{-3}	19.7	4.09
5.6016 ± 1.10E^{-4}	12.0854 ± 2.57E^{-4}	328.41 ± 1.15E^{-2}	19.1	4.24
5.5998 ± 1.60E^{-4}	12.0814 ± 3.80E^{-4}	328.09 ± 1.68E^{-2}	18.8	4.32
5.6056 ± 9.40E^{-5}	12.1030 ± 2.20E^{-4}	329.35 ± 9.84E^{-3}	17.8	4.62
5.6062 ± 8.40E^{-5}	12.1082 ± 2.00E^{-4}	329.58 ± 8.85E^{-3}	17.6	4.68
5.6136 ± 9.60E^{-5}	12.1208 ± 2.30E^{-}4	330.78 ± 1.02E^{-2}	16.7	4.99
5.6191 ± 1.99E^{-4}	12.1473 ± 2.63E^{-4}	332.16 ± 1.81E^{-2}	15.3	5.54
5.6211 ± 1.05E^{-4}	12.1457 ± 2.45E^{-4}	332.35 ± 1.10E^{-2}	14.9	5.71
5.6252 ± 1.98E^{-4}	12.1542 ± 4.55E^{-4}	333.07 ± 2.07E^{-2}	14.5	5.90
5.6259 ± 2.29E^{-4}	12.1570 ± 5.15E^{-4}	333.23 ± 2.31E^{-2}	14.4	5.94
5.6223 ± 2.29E^{-4}	12.1469 ± 5.26E^{-4}	332.52 ± 2.40E^{-2}	14.4	5.94
5.6332 ± 2.20E^{-4}	12.1696 ± 5.09E^{-4}	334.44 ± 2.32E^{-2}	12.6	6.94
5.6336 ± 1.37E^{-4}	12.1730 ± 3.25E^{-4}	334.58 ± 1.46E^{-2}	12.5	7.00
5.6344 ± 1.50E^{-4}	12.1669 ± 3.53E^{-4}	334.51 ± 1.59E^{-2}	12.4	7.06
5.6329 ± 2.48E^{-4}	12.1760 ± 5.77E^{-4}	334.58 ± 2.62E^{-2}	11.7	7.55
5.6363 ± 2.79E^{-4}	12.1816 ± 7.18E^{-4}	335.14 ± 3.07E^{-2}	9.9	9.10
5.6377 ± 4.65E^{-4}	12.1733 ± 1.12E^{-3}	335.08 ± 4.98E^{-2}	9.6	9.42

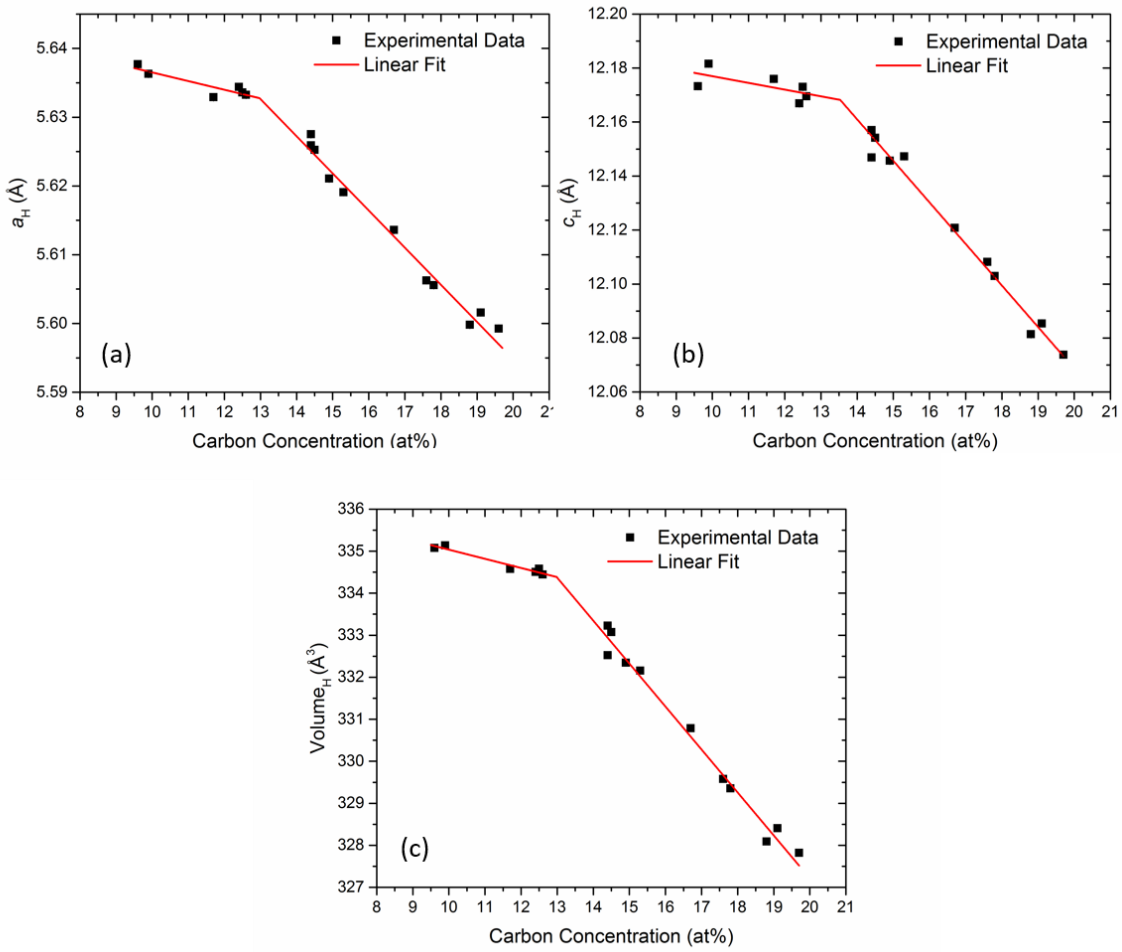

Figure 76. Dependence of the Hexagonal lattice parameters and unit cell volume on the carbon concentration. (a) a_H lattice parameter (Å), (b) c_H lattice parameter (Å) and (c) Unit cell volume (Å^3).

systematic errors and presence of impurities was also negated by utilizing the silicon standard and cleaning procedure respectively. The standard deviations of the lattice parameters and the scatter associated with this experimental data provide additional evidence of the general trend in the lattice parameter and carbon concentration relationships. This change in the slope at ~13.3 at% carbon was indicative of the distinct mechanism of substitution occurring on either side of $B_{6.5}C$. The steeper gradients of the c_H lattice parameter as compared to the a_H lattice parameter is indicative of the non-uniform increase of the volume of the unit cell along the c-axis from 20 at% to 13.3 at% carbon. But from 13.3 at% carbon to 9.6 at% carbon, the gradient of the lattice parameters are relatively similar. This is demonstrative of the uniform increase in the volume of the unit cell along the *a* and *c* axis providing further insight regarding the substitution mechanisms occurring at varying stoichiometries. The *a* lattice parameter shows an increase of ~0.04 Å from the carbon rich end of the phase diagram towards the boron rich solubility limit. Similarly, the c lattice parameter increased by 0.26 Å and volume by 7.46 $Å^3$, across the single phase solubility range of boron carbide. The lattice parameter and volume data were fitted using linear regression to evaluate the best fit possible using the available data points. Due to the discontinuity in the data either side of $B_{13}C_2$, the results were fitted with two distinct curves to account for the change in the slope at ~13.3 at% carbon. Using the developed relation of the a_H lattice parameter and carbon concentration, the stoichiometry of the ED-102 reference sample was determined from the lattice parameters as shown in Table 32. There was agreement between the calculated and reference stoichiometry which signified that the developed lattice parameter carbon concentration relationship could be

used to evaluate the stoichiometry of unknown samples with a high degree of accuracy. Additionally, the a_H lattice parameter proves to be more precise as compared to c_H.

Table 32. Comparison of the calculated and referenced values of the stoichiometry of the ED-102 sample produced by ESK.

Powder #	Powder Company	*a*(Å)	*c*(Å)	Carbon Content (at%) Based on *a*	Calculated Stoichiometry	Reference Stoichiometry
ED-102	ESK	5.6006	12.0742	19.1	$B_{4.22}C$	$B_{4.23}C$

As discussed earlier, phase pure boron carbide was observed in samples beyond 18.8 at% carbon ($B_{4.3}C$) offering confirmation that the solubility limit of boron carbide extended past the carbon contents proposed by Schwetz[9] and Werheit[142]. These observations were further confirmed from the lattice parameter results. From 18.8 at% to ~20 at% carbon, a_H and c_H decreased and constant values were not attained. However, the precise value of the carbon rich solubility is not known but based on these results it can be estimated to be ~20 at% carbon or B_4C. Additional work will be done in the future to ascertain the single phase solubility limit on the carbon rich side by making a series of samples from 19.5 to 22 at% carbon.

5.3.1.3 Raman Spectra Variations

The typical Raman spectra of the synthesized boron carbide samples with varying B:C ratios are shown in Figure 77. It must be noted that although the spectra shown in Figure 77 are the most representative for a particular sample, small variations in peak positions and relative peak intensities were observed when spectra were acquired from different areas on each sample. To incorporate these point-to-point variations in the

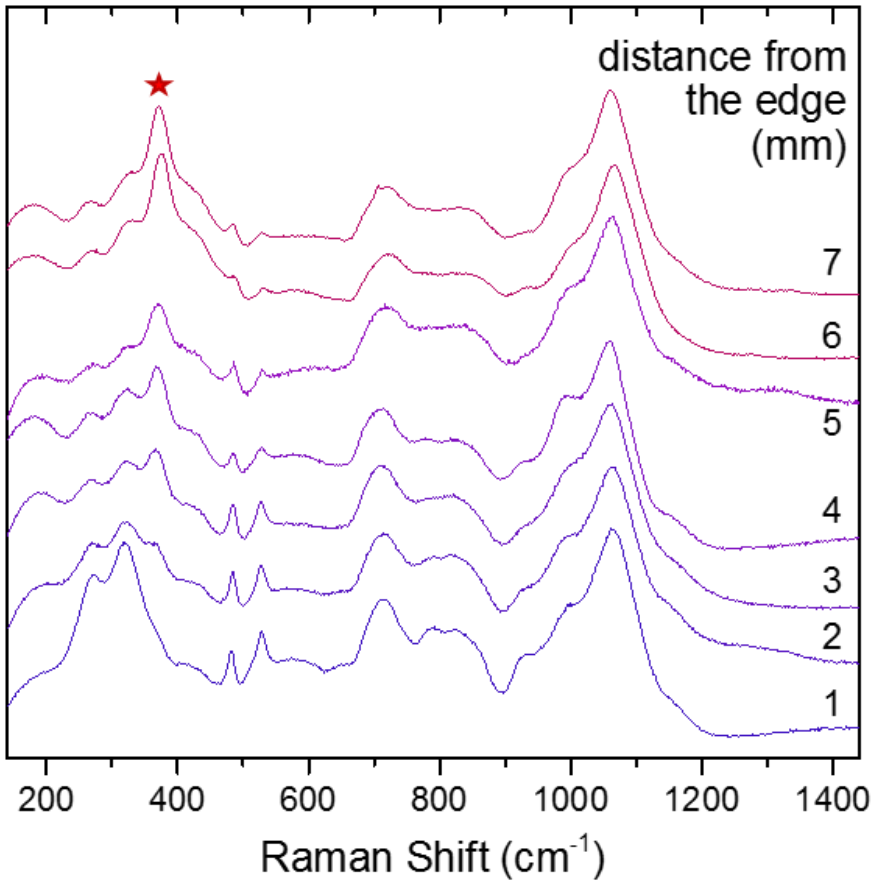

Figure 77. The most representative Raman spectra for boron carbide samples of varying stoichiometries. The 375 cm^{-1} band that appears only in the most boron-rich samples is marked by a star.

analysis, the acquired Raman spectra were deconvolved using the Levenberg–Marquardt algorithm[143]. The curve fitted data were interpreted statistically assuming normal distributions.

It was established that changing stoichiometry had several effects on the Raman spectra of boron carbide. In particular, the position of the major icosahedral mode at 1088 cm^{-1} (the icosahedral breathing mode, IBM) was found to shift towards lower frequencies with increasing boron content (Figure 78 (b)). Similar downshift was also observed for the 530 cm^{-1} band (Figure 78 (d)). Conversely, a narrow band at 485 cm^{-1} was found to shift

to higher frequencies with increasing boron content (Figure 78 (c)). This observation suggests the different nature of the latter two bands. Indeed, since the 530 cm^{-1} band has been attributed to atomic displacements within the icosahedron[110], it is expected to downshift for higher boron concentrations, similar to the IBM, due to the growing size of the icosahedra leading to softening of the intericosahedral bonds. The band at 485 cm^{-1}, on the other hand, has been assigned to vibrations among the atoms in the CBC chain[100, 110], and its upshift would indicate stronger inter-chain bonding at higher boron concentrations.

The dependency in the frequency position of the above bands on stoichiometry becomes much less pronounced for carbon concentrations below ~13.5 at.% (Figure 78). Conversely, as evident from Figure 77, a new sharp band at 375 cm^{-1} appears in the Raman spectra of the most boron-rich samples. The intensity of this band normalized with respect to the band at 320 cm^{-1} is shown in Figure 78 (a). In the literature, the 320 cm^{-1} band has been assigned to disorder-induced acoustic phonons[110]. As follows from the examination of Figure 78 (a), starting with carbon concentrations of ~13.5 at.%, the intensity of the 375 cm^{-1} band shows gradual increase towards most boron-rich stoichiometries. Further, this increase in the intensity appears to follow a linear relation, suggesting a connection with the structural changes as boron atoms start substituting carbon in the chain units. This observation is in agreement with the structural model that assumes formation of B_{12}(B-B) units at higher boron concentrations[104, 144]. Indeed, the bond length for the two-atomic B-B chain would constitute 1.92 Å for the 13.3 at.% C composition. This is the longest bond available among the possible atomic configurations in boron carbide, and the corresponding vibrational mode is expected to have a low frequency. In a similarly bonded

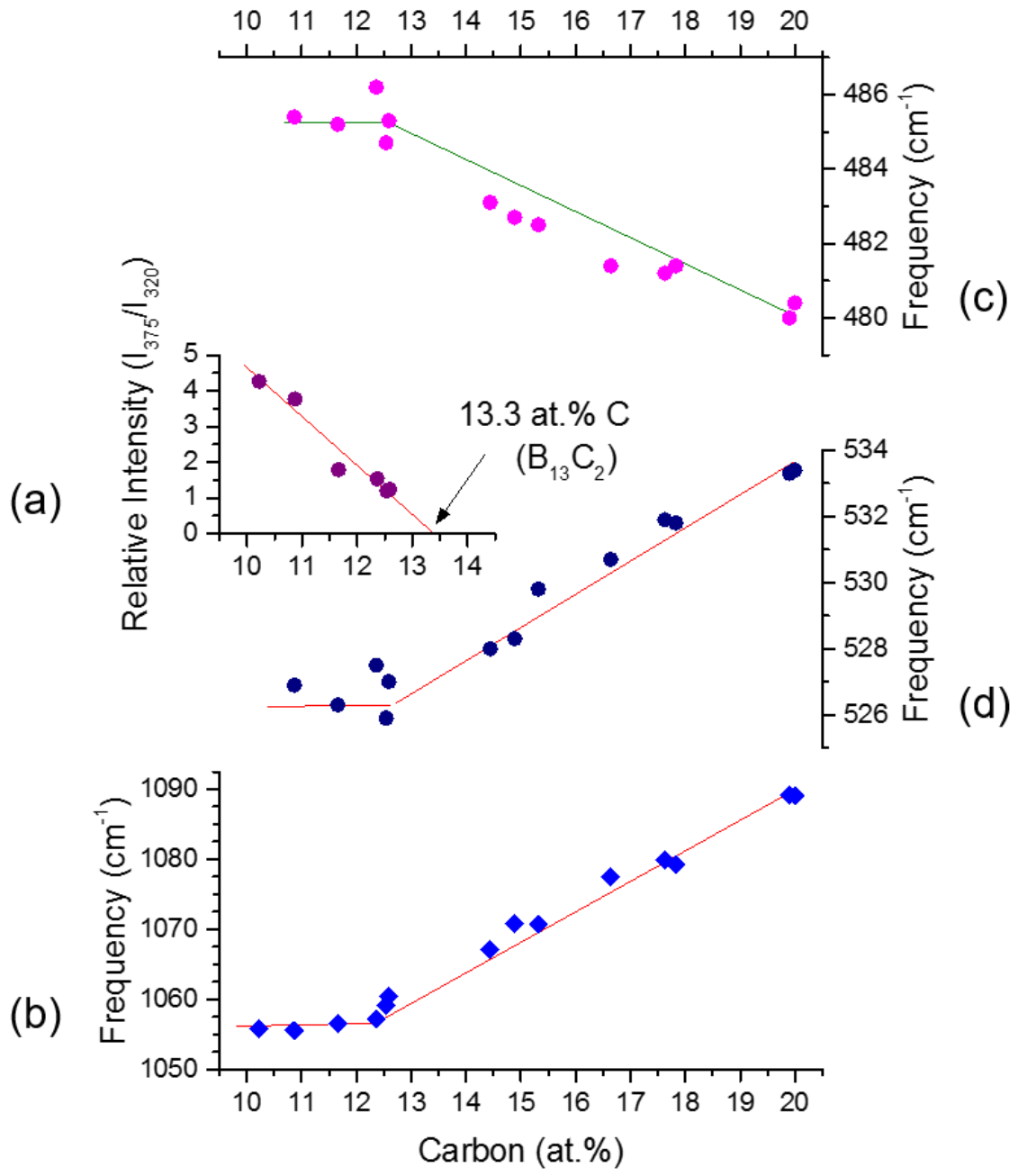

Figure 78. (a) Intensity of the 375 cm^{-1} band normalized to the intensity of the 320 cm^{-1} band, as a function of bound carbon concentaration in boron carbide. Frequency position dependence on bound carbon content for (b) the 1090 cm^{-1} band, (c) the 480 cm^{-1} band, and (d) the 530 cm^{-1} band. Lines serve as guides to the eye.

SiB_3 structure, the Raman band corresponding to stretching vibration of the two-atomic Si-Si units is found at ~400 cm^{-1}, bearing close resemblance to the 375 cm^{-1} band observed in boron-rich boron carbide.

The sharpness of the two Raman bands around 500 cm^{-1}, together with the mutual convergence of their frequencies for the more boron-rich compositions, offer a convenient and instrument-independent tool for measuring the boron carbide stoichiometry based on the Raman spectra. This is illustrated in Figure 79, where the frequency separation between the bands at 485 and 530 cm^{-1} is plotted as a function of the bound carbon concentration in boron carbide. Assuming linear relationship for separation dependence on stoichiometry, the bound carbon concentration can be reliably deduced for an arbitrary sample in the range of ~13.5 to 20 at.% C. As the separation data show no variation for carbon concentrations below ~13 at.% C, the intensity of the 375 cm^{-1} band (Figure 78 (a)) may be used in this range as stoichiometry indicator.

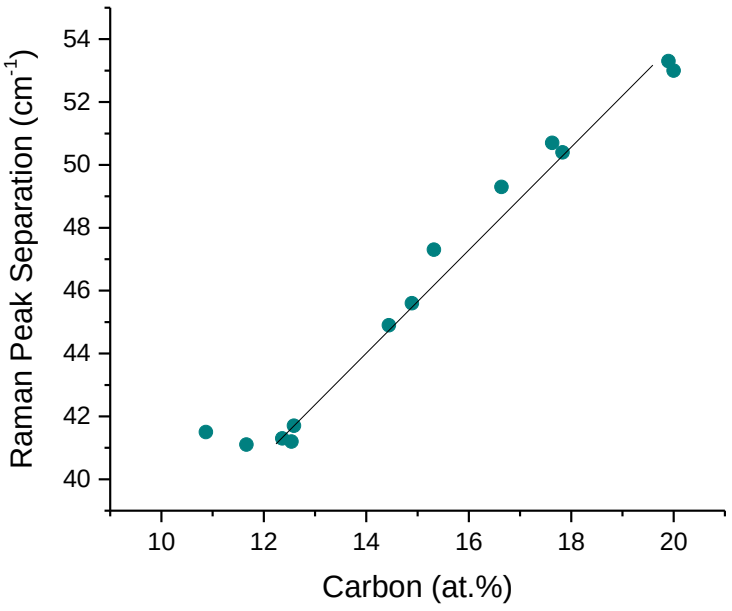

Figure 79. Frequency separation between the 485 and 530 cm^{-1} Raman bands, as a function of bound carbon concentration in boron carbide. Line serves as guide to the eye.

5.3.1.4 Proposed Structural Model

From the XRD and Raman results, an attempt was made to rationalize the changes seen in the lattice parameters as a function of the carbon concentration through the proposal of a simplified structural model. The addition of boron atoms into the boron carbide crystal structure affects the interatomic separations between B1-B1 (equatorial), B1-B2 (diagonal), B1-B2' (diagonal), B2-B2" (polar triangle), B2-B2"' (intericosahedra) and B1-C lattice positions (B-C icosahedra to chain bond). The interatomic separations at varying stoichiometries compiled by Aselage are depicted in Figure 80[12, 13, 145, 146]. The inter and intraicosahedral bonds increase in length with the decrease in the carbon concentration. The largest increase in the bond lengths was observed in the intericosahedral B2-B2"' and B1-B2' bond which resulted in the greater increase of c_H as compared to a_H towards the

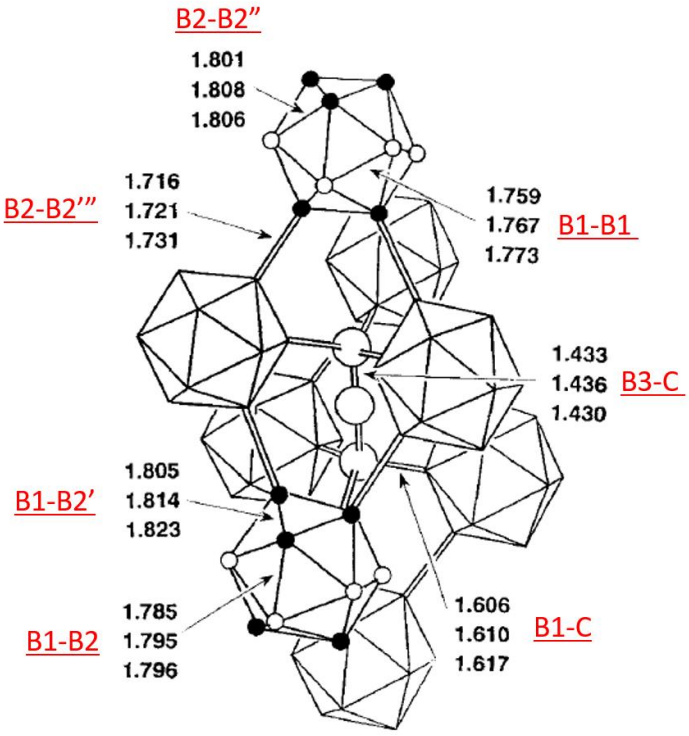

Figure 80. Interatomic separations (Å) based on single crystal studies conducted by Aselage et al.[13, 146], Kirfel et al.[12], and Morosin et al.[145]. Top: 20 at% C, Middle: 16 at% C and Bottom: 13.3 at% C. (Image reproduced from Ref 14.)

boron rich solubility range. The interatomic separation between the carbon and boron atoms in the 3 atom chain (C-B3) remained relatively constant from 20 at% to 13.3 at%.

Larson performed crystal structure refinements on boron carbide at 20 at% carbon. The results were compared with those by Yakel[15] and Kirfel et al.[12] to ascertain the effect of stoichiometry on the bond lengths as shown in Table 33. An increase in most of the bond lengths was observed from 20 at% to 13.3 at% which was in agreement with the results in Figure 80. As discussed previously, at the carbon rich limit of the solubility range, it is widely accepted that the $B_{11}C$ (C-B-C) structure is the preferred atomic configuration. The increase in the lattice constants and volume from 20 at% - 13.3 at% carbon can be attributed to the replacement of the shorter intericosahedral C-B bonds by longer B-B bonds. This is a direct consequence of the preferential substitution of boron atoms in the icosahedra resulting in an increase in the B_{12} cages which leads to expansion of the icosahedra and increase in the lattice parameters. The largest increase in the bond length was observed in the B2-B2”’ intericosahedral bond providing further evidence of the preferential substitution of boron atoms for carbon atoms occurring within the icosahedra.

Table 33. Bond Lengths as a function of carbon concentration[12, 15, 20]

Bond	~9 at% Carbon	~13.3 at% Carbon	~20 at% Carbon
B1-B1	1.781	1.773	1.762
B1-B2	1.803	1.797	1.786
B1-B2’	1.805	1.806	1.800
B2-B2”	1.822	1.821	1.807
B2-B2”’	1.744	1.732	1.719
B1-C	1.632	1.617	1.606
C-B3	1.438	1.429	1.431

From 13.3 at% - ~9 at% carbon, B2-B2”’, B1-C, B1-B1 and C-B3 bonds show an increase in the length. The largest growth in the bond length was observed in the B1-C separation. This can be explained by the change in the mechanism of boron substitution beyond 13.3 at% carbon. The 3-atom C-B-C chains are replaced by shorter B-B chains as discussed in **Section 5.3.1.3**. Although the B-B chains are shorter as compared to equivalent C-B-C bonds, there is still an overall increase in the lattice parameters owing to the increase in B1-B1, B2-B2”’ and B1-C bonds. Therefore, this expansion of the unit cell occurs with a decreased slope as compared to the region between 13.3 at% carbon and 20 at% carbon.

Over the solid solution homogeneity range, various structural configurations have been identified; B_{12} icosahedra, $B_{11}C$ icosahedra with the C atom accommodated in one of the 6 polar sites, C-B-C chains, C-B-B chains and B□B (□ - vacancy)[142]. However, it appears plausible that boron carbide cannot be described by a single unit cell at any

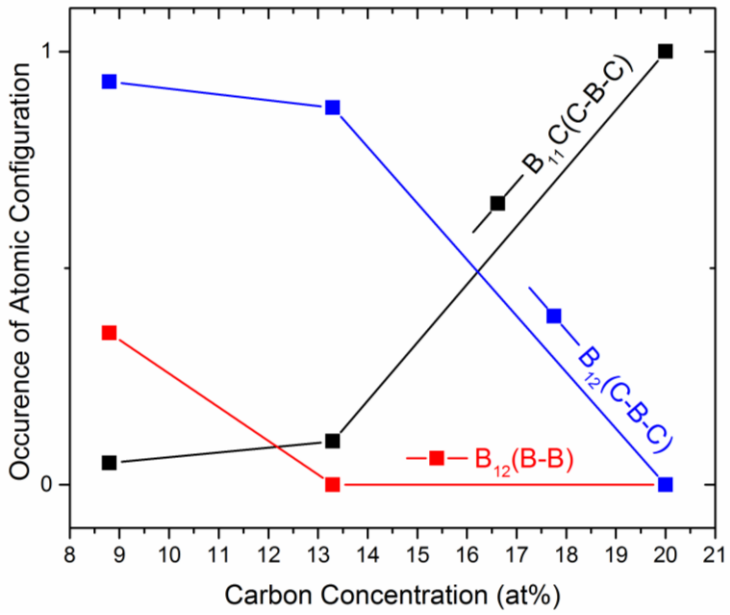

Figure 81. Concentration of the structural units of boron carbide across the solubility range. $B_{11}C$(C-B-C)-Black, B_{12}(C-B-C)-Blue and B_{12}(B-B)-Red. Y axis has arbitrary units.

stoichiometry. We propose that boron carbide consists of a 12-atom icosahedral cage and chain units with different atomic configurations, to accommodate particular B:C ratios. The simplified structural model proposed as part of this work is shown in Figure 81 and the corresponding structural units are depicted in Figure 82.

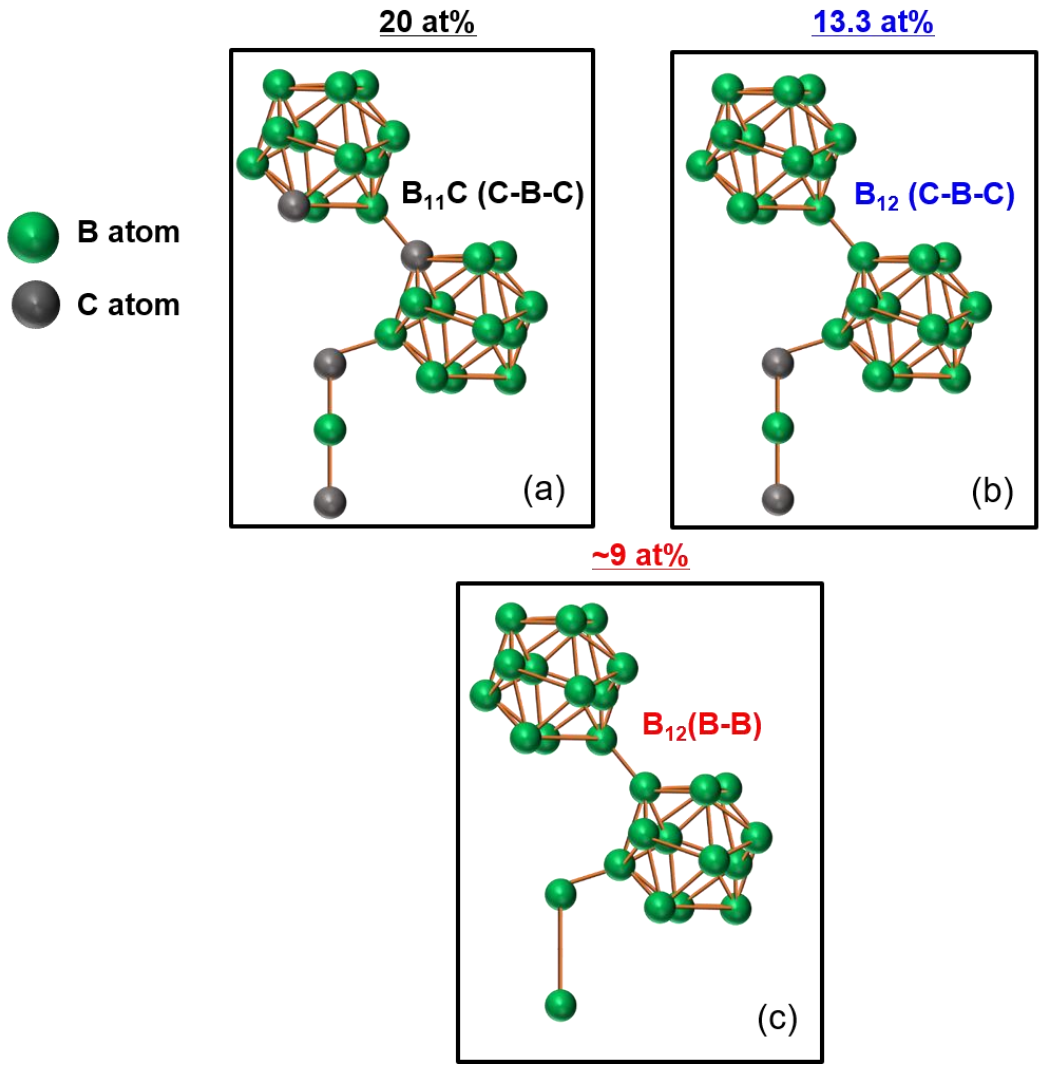

Figure 82. Atomic configurations of boron carbide at (a) 20 at%, (b) 13.3 at% and (c) ~9 at% carbon.

At a carbon concentration of 20 at%, the unit cell of boron carbide consists of a $B_{11}C$(C-B-C) type structure (Figure 82 (a)). However, a report by Kuhlmann et al.[6, 27, 140] also suggests that the structure is not completely uniform and may contain minor portions

of C-B-B chains. But, it is generally accepted that at a carbon content of 20 at%, $B_{11}C$(C-B-C) is the true representation of the B_4C stoichiometry[6, 28, 147]. From 20 at% -13.3 at% carbon, the structure of boron carbide is disordered. As the carbon concentration decreases, boron atoms preferentially substitute for carbon atoms in the icosahedral cage. This continues until most of the carbon atoms are removed from the icosahedra. The B_{12}(C-B-C) configuration in the material increases and at 13.3 at% carbon, boron carbide consists of predominantly B_{12}(C-B-C) units (Figure 82 (b)) with the remaining amount comprising of $B_{11}C$(C-B-C) structures. Similar conclusions were also drawn by Saal et al. through quantum simulations using an ab initio approach[28]. Beyond 13.3 at% carbon, further replacement of the carbon atoms in the $B_{11}C$ icosahedra is accompanied by the formation of B-B bonds resulting in B_{12}(B-B) structures (Figure 82 (c)). Consequently, towards the boron rich solubility limit, the structural model was comprised of primarily B_{12}(C-B-C) and B_{12}(B-B). Moreover, trace amounts of $B_{11}C$(C-B-C) and $B_{11}C$(B-B) units may also be present with complete depletion of these $B_{11}C$ structural units occurring at the boron rich limit of ~9 at% carbon. The formation of B-B was corroborated by the Raman spectra variations. These results were commensurate with single crystal XRD studies performed by Sologub et al.[148] where the boron carbide crystal with a nominal $B_{6.5}C$ stoichiometry was found to contain B_{12} (96%), B_{11} (4%) icosahedra and C-B-C (87%) and B-B (13%) chains.

This proposed atomic configurations was deduced based on lattice parameter and Raman results in addition to previously published work. In order to confirm these observations, single crystal diffraction will need to be performed to identify the location of the boron and carbon atoms.

5.3.2 Mechanical Properties

5.3.2.1 Hardness vs Stoichiometry

Nanoindentation on the boron carbide samples was performed to determine the effect of stoichiometry on hardness. Since, the density of the consolidated materials ranged from 94-96% using the Archimedes method, indents were placed away from the pores to minimize the effect of porosity on the hardness value. However, despite careful positioning of the indents, microporosity and pores beneath the sample surfaces resulted in skewed hardness values. The results from these indents were discarded owing to the bias in the analysis after examining the load displacement curves and the SEM micrographs post indentation. Figure 83 provides an illustration of an indented area considered to determine the hardness of the densified material. All the boron carbide samples exhibited radial cracking from the tips of the indenter surface.

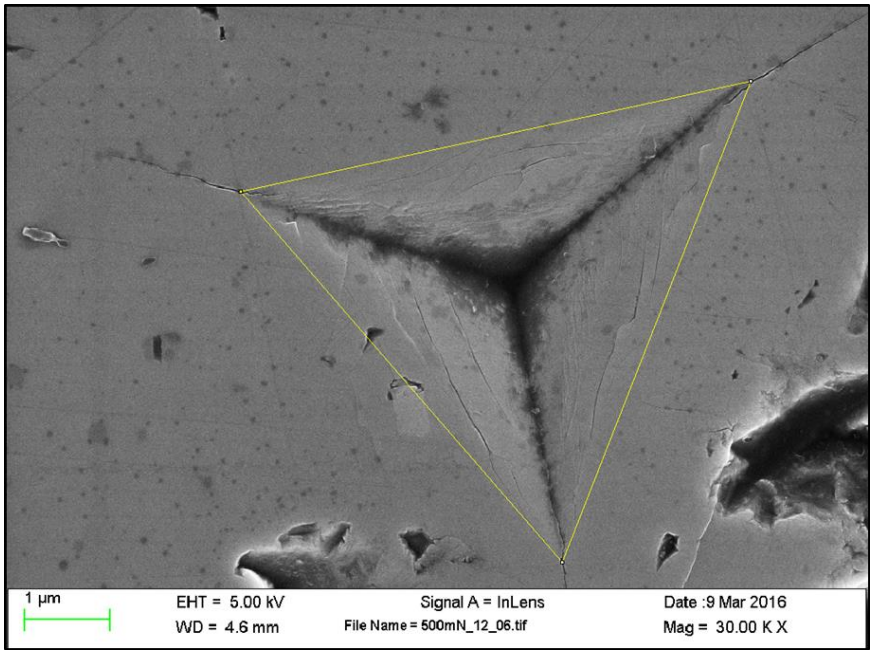

Figure 83. SEM micrograph showing the area of the 500 mN indent in the sample with a carbon concentration of 12.6 at% carbon.

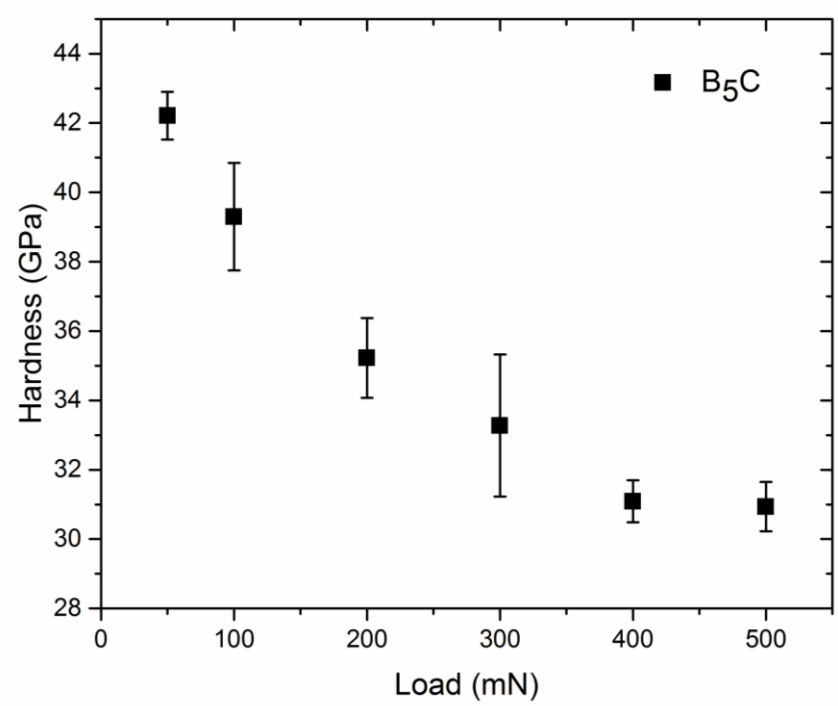

Figure 84. Hardness vs Load curves of the sample with a carbon concentration of 16.4 at% (B_5C).

The results of the hardness vs load curves for the B_5C (16.8 at% carbon) sample are shown in Figure 84. An indentation size effect was observed with an increase in the load[149]. The maximum hardness value of 42.2 GPa was attained at a load of 50 mN. As expected, with an increase in the load from 50 mN to 400 mN, there was a drop in the hardness. Beyond 400 mN the hardness values remained relatively constant. The 14.9, 12.6 and 9.6 at% carbon samples exhibited similar behavior as a function of the carbon concentration. Figure 85 shows the effect of the stoichiometry on the hardness values at constant loads of 50 mN, 300 mN and 500 mN. With an increase in the B:C ratio there is a drop in the hardness values of boron carbide. A consistent drop in the hardness was reported across all loads.

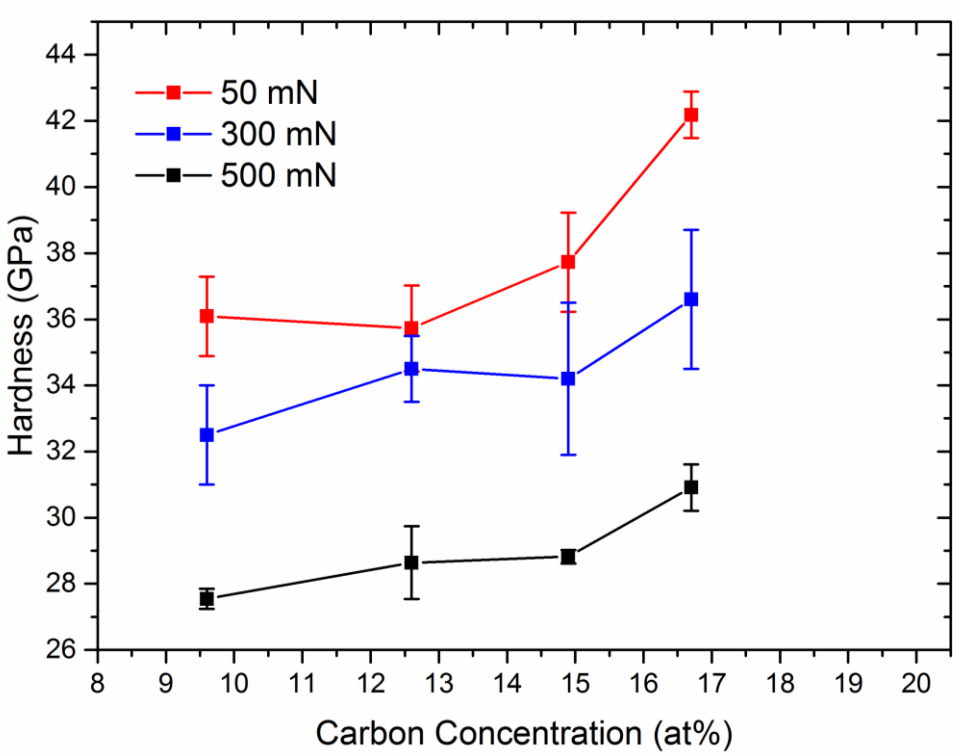

Figure 85. Effect of stoichiometry on the hardness of boron carbide at constant loads.

The mechanical properties of boron carbide are affected by atomic bonding, iconicity and bond covalence and electron density in inter-atomic regions[6, 150, 151]. Higher stiffness and hardness result from increased inter-atomic electron density and localized covalent bonds. From Figure 80 and Table 33, it is discernable that the shortest bond length was seen in the C-B3 (intrachain) bonds. This was followed by the B1-C (B-C icosahedra to chain bond), B2-B2''' (intericosahedra) and intraicosahedral bonds. The interatomic separation is directly proportional to the bond strength which in turn varies inversely with the mechanical properties, particularly hardness of boron carbide. The drop in the hardness of boron carbide at higher B:C ratios can be explained in terms of the bond length, iconicity and inter-atomic electron density. The lattice parameter data insinuates that the volume of the unit cell and bond lengths increase towards the boron rich solubility range. This creates

lower inter-atomic electron density and decreased bond strength. The softer interatomic bonds make the 12 atom icosahedra more compressible leading to a reduction in the hardness at a higher stoichiometry. The hardness results are in alignment with Nihara et al.[56] data which also show a reduction in the hardness with an increase in the B:C ratio. Density Functional Theory (DFT) calculations on $B_{11}C$ icosahedra and C-B-C chain performed by Guo et al.[151] show increased theoretical hardness and reduced bond length as compared to results on a B_{12} icosahedra and C-B-C chain conducted by Gao et al.[152] which were commensurate with the hardness observations as part of this work. These results are also contradictory to a recent theoretical report by Taylor et al.[81] where an increase of 10 GPa was predicted for the shear strength at boron rich configurations.

5.3.2.2 Amorphization

The Raman spectra on the pristine regions of the boron carbide samples extend from 200 to 1600 cm^{-1} which was in accordance with the typical Raman spectra of boron carbide as illustrated in Figure 86 (a), (b), (c) and (d). However, the Raman spectra obtained from the centers of the 500 mN indents were different and the presence of peaks at 1330 cm^{-1}, 1520 cm^{-1} and 1810 cm^{-1} was observed. These bands are different as compared to the band frequencies, band widths and relative intensities of the D and G graphitic peaks. These bands in the literature were attributed to amorphization of boron carbide[6, 77]. Hence, indentation induced amorphization was observed at all stoichiometries. Moreover, Raman mapping also revealed that the amorphous boron carbide phase was contained within the indentation contact area as depicted in Figure 87.

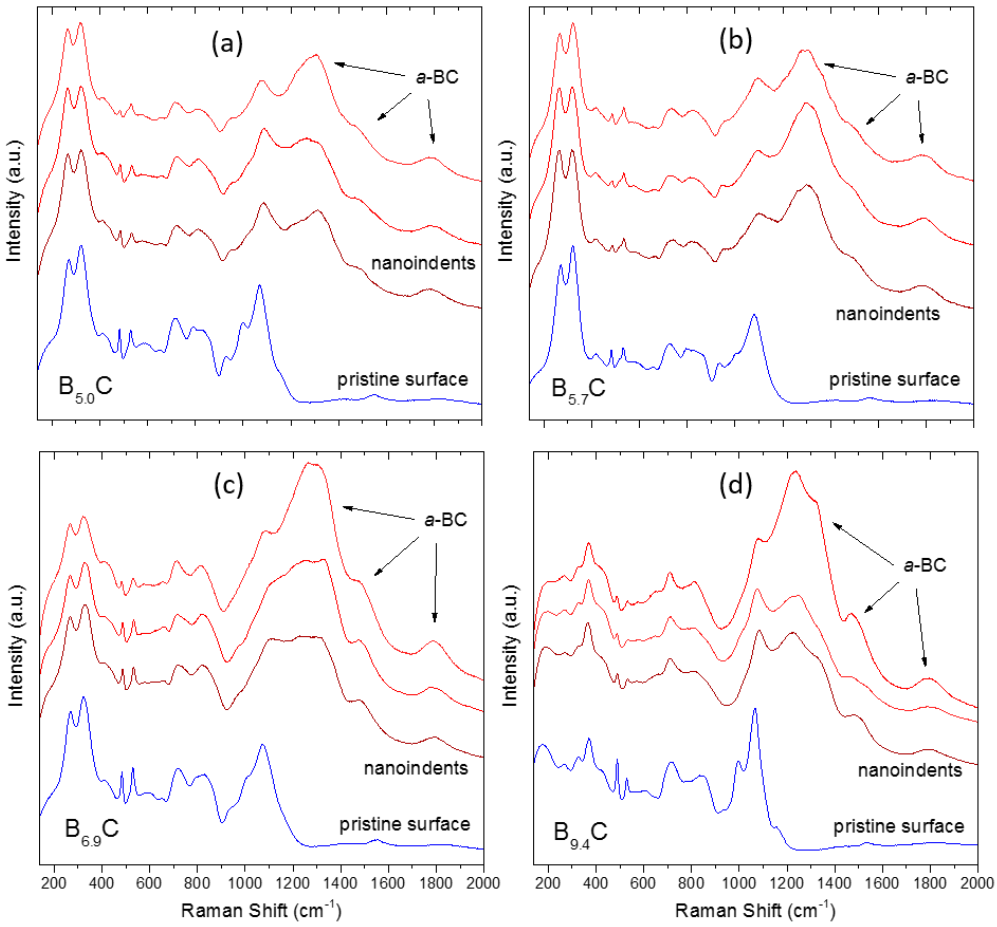

Figure 86. Raman spectra acquired from the pristine regions and center of the 500 mN indents showing the development of amorphous boron carbide in samples at (a) B_5C (16.7 at% carbon) (b) $B_{5.7}C$ (14.9 at% carbon) (c) $B_{6.9}C$ (12.6 at% carbon) (d) $B_{9.4}C$ (9.6 at% carbon)

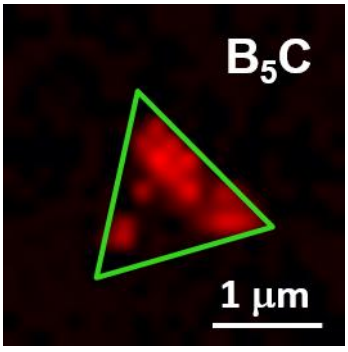

Figure 87. Raman mapping of the 500 mN indent showing the amorphous boron carbide phase contained within the indentation contact area.

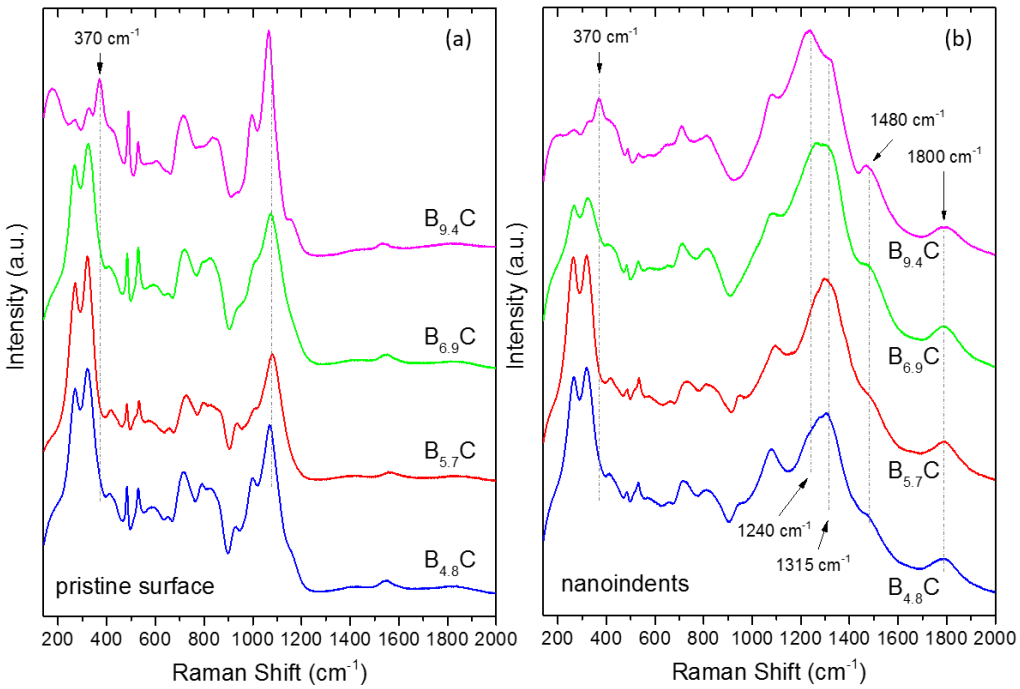

Figure 88. (a) Raman spectra from pristine regions of boron carbide samples at varying stoichiometries. (b) Variation in the Raman spectra from the centers of the 500 mN indents showing the splitting of the amorphous peak at ~1300 cm^{-1}.

Figure 88 shows the effect of stoichiometry on the amorphous boron carbide phase. With an increase in the B:C ratio, splitting of the broad feature at ~ 1300 cm^{-1} was observed which suggests a shift in the short range order of the amorphous phase. The indentation induced amorphized material in more boron rich samples appeared to have a lower density. As mentioned previously, at higher B:C ratios, there is a mixture of different polytypes of boron carbide with varying atoms present in the unit cell. The deformation of these structures could result in the formation of two distinct forms of amorphous boron carbide. The possibility of the existence of two differing forms of boron carbide have also been reported by Ivashchenko et al.[153] where amorphous boron carbide was predicted to contain disordered icosahedra connected by B-C and C-C networks as well as an a-120 configuration with a less random network.

The precise mechanism governing the amorphization behavior is not clear despite extensive experimental and theoretical efforts. Varying theories have been proposed where amorphization could be a consequence of changes in the C-B-C chains[80] or collapse of the B_{12}(C-C-C) structure[154]. Another theory proposed by Qi et al.[155] intimate the shear-induced amorphous band formation through breakage of the B-C intericosahedral B-C bonds. Taylor et al. performed density functional theory calculations (DFT) to investigate the effect of stoichiometry on the mechanical properties of icosahedral boron carbide under loading[81]. The results of Taylor's work suggest that bending of the 3-atom chain is responsible for failure in boron carbide and the yield strength of the B_{12}(C-B-C) under a shear strain is twice that of other structures. This alluded to B_{12}(C-B-C) being the most stable structure under shear loading. However, the present work has shown a drop in the hardness as a function of stoichiometry because of increased interatomic separation. Hence, the B_{12}(C-B-C) structure which occurs at boron rich compositions may not have a higher strength. Indentation induced amorphization was also observed across the entire solubility range. Hence failure in boron carbide may be governed not by amorphization but by another mechanism such as softer interatomic bonds at increased B:C ratios.

5.4 Summary

In this objective, investigations of the variations in the structural and mechanical properties of boron carbide have been conducted. A modified method was developed for the synthesis of high purity and varying chemistry consolidated boron carbide through the use of a BN isolation chamber which permitted minimal graphite diffusion from the surrounding die and plates. Careful analysis of the hot pressed tiles ensured the calculated stoichiometry of the resultant materials was precise and accurate.

From phase identification, lattice parameter and Raman spectroscopy results, conclusions can be made regarding the carbon rich solubility range. The solubility range on the carbon rich side extends beyond 18.8 at% carbon proposed by Schwetz et.al[9]. Certainly, stoichiometries lower than $B_{4.3}C$ (18.8 at% carbon) can exist if synthesized using preparation methods below 2300 K. However, the precise value of the carbon rich solubility limit is still not known. Additional samples will have to be synthesized at small increments from ~19.5 at% carbon to 22 at% carbon to examine the carbon rich limiting composition.

A new lattice parameter-carbon concentration calibration curve was also developed which shows the dependence of the unit cell constants on the stoichiometry. This lattice parameter calibration curve provides a convenient and nondestructive method to evaluate the stoichiometry of unknown boron carbide samples with a relatively high degree of accuracy. Utilizing the information gained from the variations in the lattice parameters and Raman spectra as a function of the stoichiometry a simplified structural model was proposed that considers the preferential substitution of boron and carbon atoms across the solubility range. A change in the slope of the lattice parameter data was observed at ~13.3 at% carbon denoting the change in the mechanism of substitution of boron and carbon atoms at the critical composition of 13.3 at% carbon or stoichiometry of $B_{13}C_2$. At the carbon solubility limit of boron carbide, the preferred atomic configuration if $B_{11}C$(C-B-C). From 20 at% - 13.3 at% carbon, boron atoms substitute in the icosahedral cage resulting in the formation of B_{12}(C-B-C) structures. At ~ 13.3 at% carbon, formation of B-B bonds initiate and the B_{12}(B-B) units increase in number towards the boron rich solubility limit.

The hardness of boron carbide decreased towards the boron rich solubility limit. This was attributed to the reduced inter-atomic density and increased bond length at higher stoichiometries which makes the icosahedra more compressible under high strain rates. These results were in contradiction to those proposed by Taylor et al.[81] where B_{12}(C-B-C) was assumed to have higher hardness. Amorphization of boron carbide was also observed at all stoichiometries and from reduced hardness results, failure of boron carbide may not be governed by amorphization but by another mechanism such as softer interatomic bonds at increased B:C ratios. Finally, synthesizing boron carbide samples near 20 at% carbon could be desirable for improved performance under high strain rate conditions

6 Applicability of Developed Techniques

6.1 Introduction

Over the course of this thesis, novel methods have been developed to characterize boron carbide and an improved understanding of the structural and mechanical properties across the solubility range has been established. The impact of a projectile into a target results in the activation of failure mechanisms originating from defects, including plasticity, phase transformations and fracture[156]. Extending the developed characterization techniques to understand the crystal structure response of boron carbide subjected to extreme dynamic conditions would pave the way to the advancement of the performance of commercial armor grade boron carbide. In particular, this objective focuses on understanding the effect of stress and strain rates on the crystal structure of boron carbide during static and dynamic loading conditions. Additionally, the stress and strain rates experienced by the impacted consolidated ceramic will be linked to the particle size and the effect of these stresses on the defect population and chemistry will also be explored. Investigations of the possible changes in the stoichiometry and phase transformations conducted on the fragments could provide insight into the possible deformation modes. Connecting these results to the failure mechanisms could help explain the factors that affect ballistic performance. The characterization tools utilized to achieve this objective include XRD, Raman spectroscopy and SEM.

6.2 Experimental Procedure

6.2.1 Compression Experiments

Quasi-static and dynamic uniaxial and biaxial confined compression experiments were performed on a hot-pressed boron carbide plate manufactured by CoorsTek (Vista, CA) and the impact of the projectile was conducted in the hot pressing direction. The hot-pressed plate had a Young's Modulus of 430 GPa, density of 2490 kg/m^3 and a Poisson's ratio of 0.16 as provided by the manufacturer. Cuboidal specimens were used for static and dynamic loading experiments. Quasi-static experiments were performed using a MTS servo-hydraulic test machine at a nominal strain rate of 10^{-3} s^{-1}. Dynamic compression experiments were performed at Johns Hopkins University (JHU) using a Kolsky bar apparatus (Figure 89) at rates of 500 s^{-1}. The Kolsky bar apparatus consists of a striker projectile, and incident and transmitted bars made of C-350 steel[157]. Biaxial compression tests were conducted at a confining pressure of 500 MPa using the schematic shown in Figure 90. For further details regarding the Kolsky bar setup refer to Hogan et al.[157] and Kimberley et al.[158].

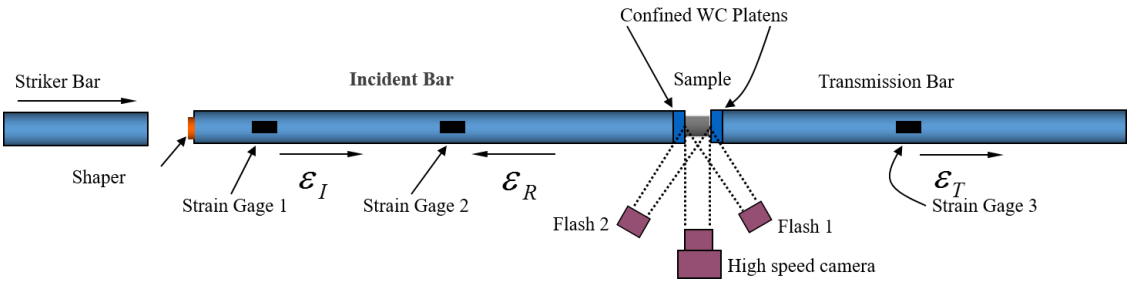

Figure 89.Schematic of Kolsky bar apparatus used at Johns Hopkins University[157].

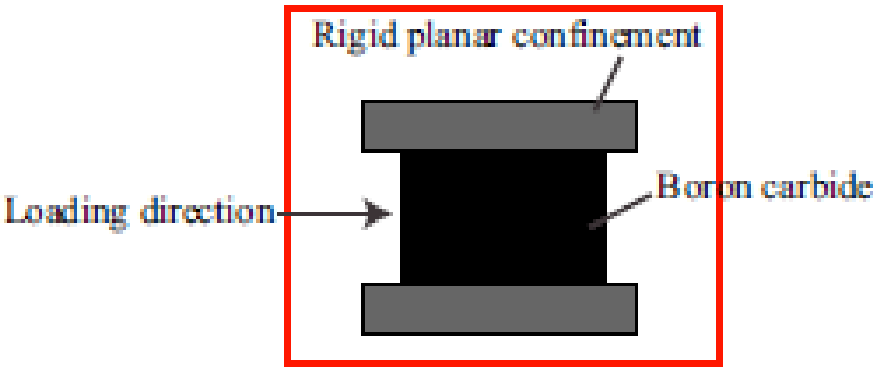

Figure 90. Schematic of biaxial confinement setup[157].

6.2.2 Sample Preparation and Characterization of Fragments

The fragments from the static and dynamic loading tests were collected and sieved through different mesh sizes. The fragments were separated into >710 μm, >250 μm and >45 μm fragments. Sample preparation of the fragments proved very challenging owing to the nature of the fragments. Traditional methods involving dispersion with methanol could not be employed. Instead, an alternate method was used which involved the use of hair spray which served as a viscid medium and enabled the fragments to remain within the cavity of the zero background holder as shown in Figure 91. A NIST silicon standard (NIST-640 (e)) was also used to minimize specimen displacement errors during sample preparation and to account for peaks shifts occurring as a result of possible misalignment of the XRD diffractometer. To ensure the fragments were in alignment with the upper surface of the silicon wafer, a glass slide was utilized to flatten the mixture of silicon and boron carbide fragments. XRD scans were taken using a Panalytical X'Pert system using similar conditions to those detailed in **Section 3.2.1**.

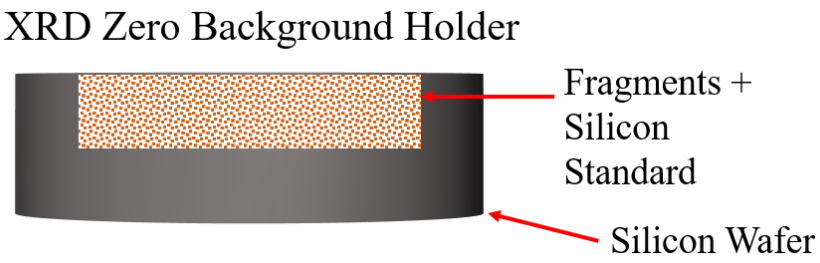

Figure 91. Schematic of the XRD zero background sample holder consisting of boron carbide fragments and a NIST silicon line position standard.

A Renishaw InVia Raman microspectrometer equipped with a 633 nm laser and a 50x objective lens was used for Raman analysis of fracture surface. The spatial dimensions of the analyzed volume at each position of the laser probe were ~2 µm laterally and ~1 µm axially. Raman measurements were done at ambient conditions. For Raman imaging, sets of Raman spectra were collected over the selected areas with a 1 µm step size. Peak deconvolution was performed using the Renishaw Wire 3.2 software and Raman maps created based on the intensity of the peaks corresponding to the phase of interest. Lastly, SEM/EDS analysis on the fragments was performed using a Zeiss Sigma field emission SEM. The fragments were mounted on an aluminum stud with a 1/2" slotted head and a 1/8" pin from Ted Pella Inc. The analysis was conducted at an excitation voltage of 5 KV and working distance of 8.5 mm with the help of the secondary electron detector.

6.3 Results and Discussion

6.3.1 Baseline Boron Carbide Tile

Phase analysis and quantitative analysis on the commercial hot pressed boron carbide armor plate yielded a major phase of boron carbide and minor phases of graphite, boron nitride and aluminum nitride. Figure 92 shows the schematic of the hot pressed boron carbide tile. The carbon inclusions present in the tile consisted of circular graphitic discs

with a flake like geometry. During hot pressing, graphitic inclusions preferentially orientate. This results in the major axis of the carbon inclusions having a perpendicular orientation to the hot pressing direction. The anisotropy of the graphite inclusions is clearly discernable from Figure 93. The intensity of the 002 carbon peak in the XRD pattern is significantly higher in the hot pressing direction as compared to the in plane directions.

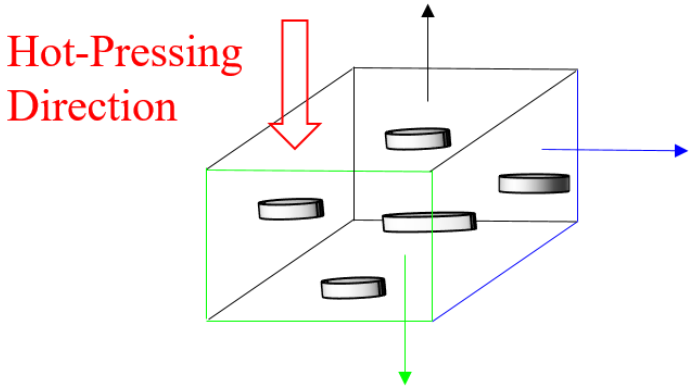

Figure 92. Schematic of hot pressed PAD-tile 8 manufactured by CoorsTek.

To quantify the secondary phases and average the anisotropy of graphite, the tile was crushed and XRD was performed on randomly orientated particles to attain a true reflection of the quantity of the secondary precipitates. The weight percentages of the graphite, AlN and BN were estimated at 1.05 ± 0.07, 0.25 ± 0.07 and 0.55 ± 0.07 wt%, respectively. Rietveld refinement and whole pattern fitting were also utilized to determine the lattice parameters of the boron carbide tile. The lattice parameters were consistent across all the cross sectional faces. The average values of the *a* and *c* lattice parameters were 5.5991 Å and 12.0777 Å respectively. The lattice parameter and carbon concentration relationship developed as part of this work was used to obtain the stoichiometry. The boron was estimated to be 80.7 ± 0.1 at% and carbon 19.3 ± 0.1 at% with a stoichiometry of $B_{4.18}C$.

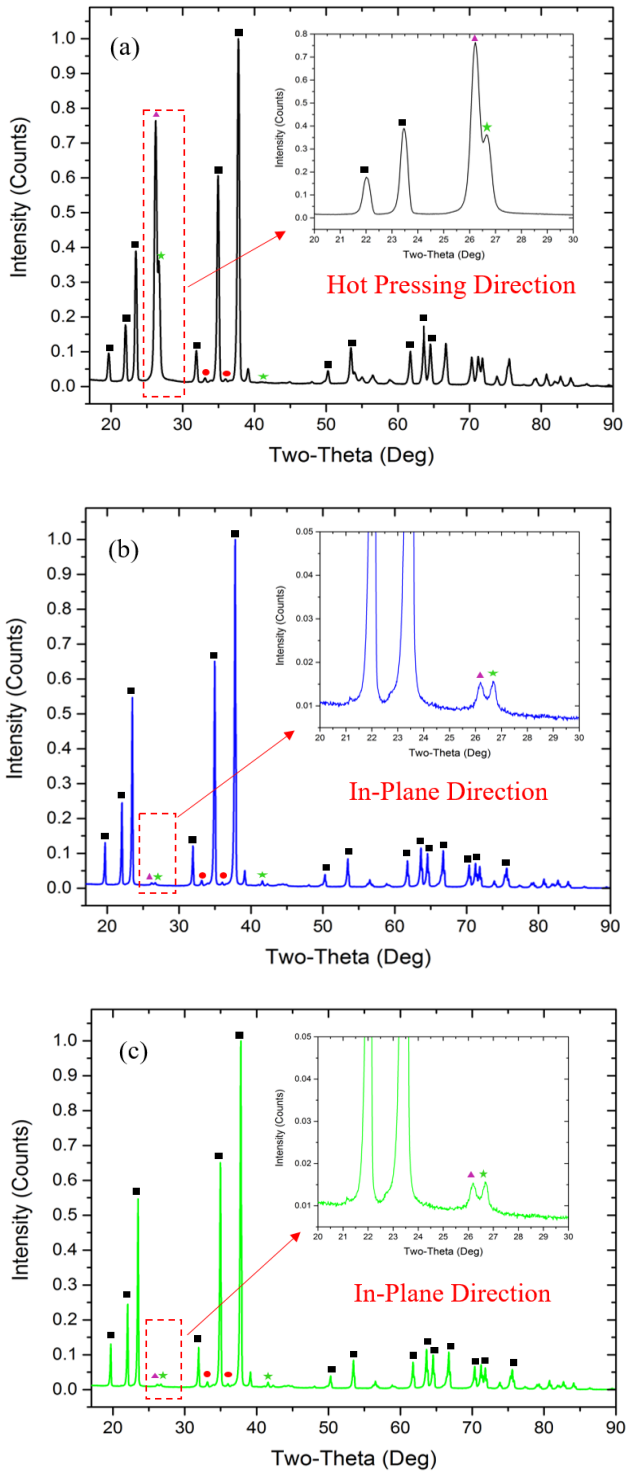

Figure 93. Phase identification of the original tile. (a) XRD pattern taken in the hot pressed showing preferred orientation of the 002 carbon peak. (b) and (c) XRD pattern taken in the in plane direction showing the reduced intensity of the 002 carbon peak. Here, ■: Boron Carbide, ▲: Graphite, ★: Boron Nitride and ●: Aluminum Nitride.

Electron energy loss spectroscopy (EELS) was also used to evaluate the stoichiometry of the boron carbide grain before impact[159]. This work was done at Johns Hopkins using a Phillips CM420 and CM300FEG TEM. EELS spectra were acquired from multiple grains and the stoichiometry was calculated by integrating the background corrected K-edges of boron and carbon as depicted in Figure 94. Boron was estimated at 79.3 ± 1.9 at% and carbon at 20.7 ± 1.9 at% which was in good agreement with the results from XRD. TEM observations also revealed the grains were equiaxed and only a few defects were present. Carbon inclusions were typically accompanied by mircocracks in adjacent boron carbide grains and these microcracks could be introduced during sample preparation. The secondary precipitates of AlN and BN were micrometers to submicrometer in size, however nanoprecipitaes of AlN were also observed. For a further detailed discussion of the microstructural characterization of the commercial hot pressed tile, refer to the paper by Kelvin et al.[159]

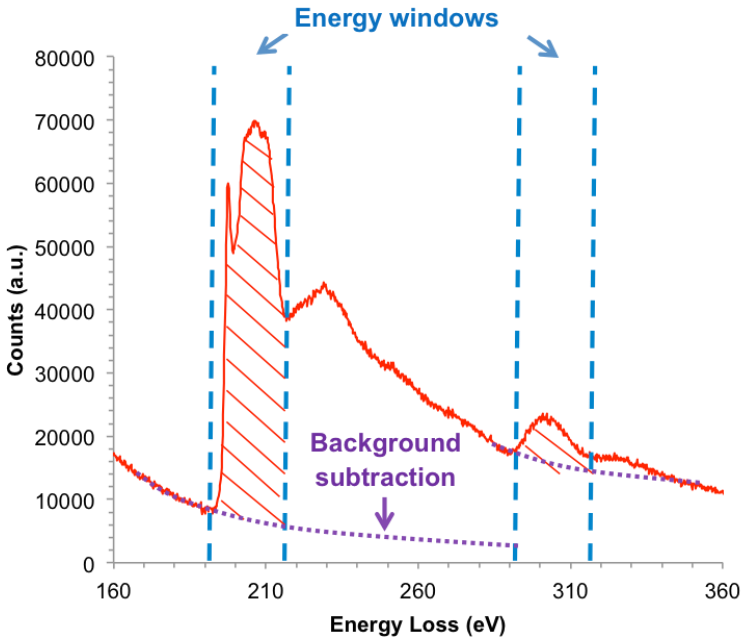

Figure 94. Electron energy loss spectrum of the boron carbide matrix[159].

6.3.2 Characterization of Fragmented Material

Phase identification of the fragments showed no signs of phase transformations occurring within the detectability limits of the XRD. Lattice parameter results of the uniaxial, biaxial and quasi-static fragments revealed that the lattice parameters of the >710 µm fragments had smaller values than those of the original unimpacted tile. Furthermore, decrease in the particle size of the fragments from >710 µm to >250 µm and >45 µm resulted in an decrease in the corresponding lattice parameters as depicted in Figure 95 and Figure 96. The >710 µm and >250 µm fragments showed significantly lower lattice parameter values than the original tile, while the >45 µm results were comparable. These variations in the unit cell constants of the fragments could only occur because of two phenomena: 1) decrease in the B:C ratio post fragmentation; 2) reduction in the lattice parameter values owing to the presence of residual strain. Investigation of the underlying reason for the changes seen in the lattice parameters was carried out by performing combustion tests to evaluate the total carbon concentration and examining the lattice parameters pre and post crushing. LECO combustions tests on the >710 µm uniaxial fragments provided total carbon contents of 22.27 wt% and 22.31 wt% pre and post crushing respectively. This indicates that the change in the unit cell constants were not a result of a decreased B:C ratio. Similar observations were made in the >250 µm and >45 µm uniaxial, biaxial and quasi-static fragments. Additionally, the lattice parameters post crushing were similar to the original tile as illustrated in Figure 97 and Figure 98. Based on these results, it is discernable that the difference in the unit cell constants of the fragments were a direct consequence of the presence of residual strain.

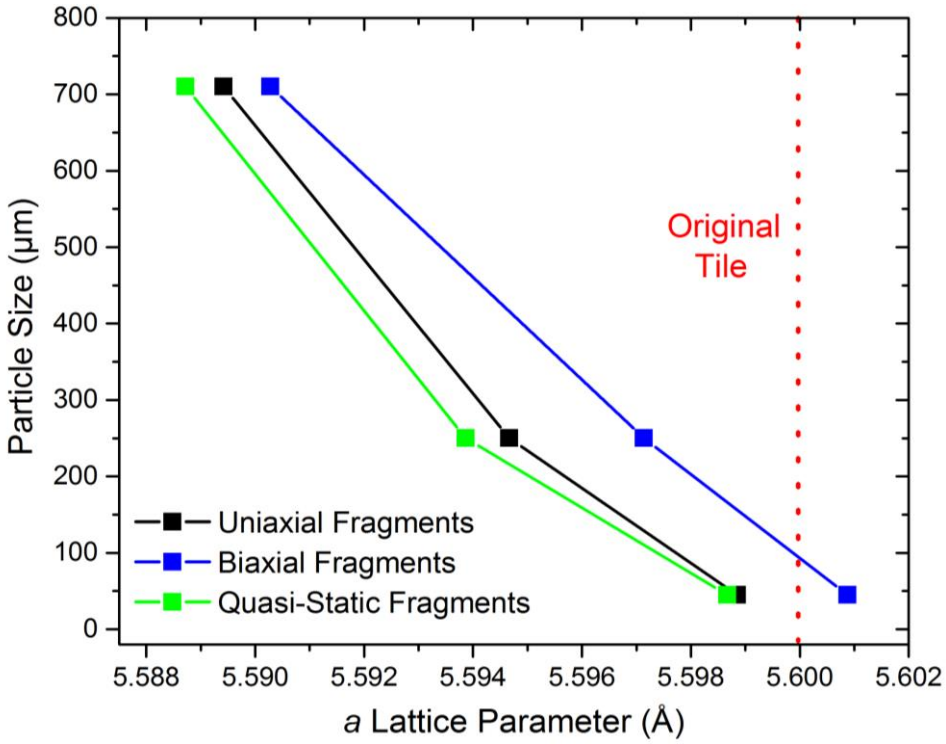

Figure 95. Variation of the *a* (Å) lattice parameter with the fragment size before crushing.

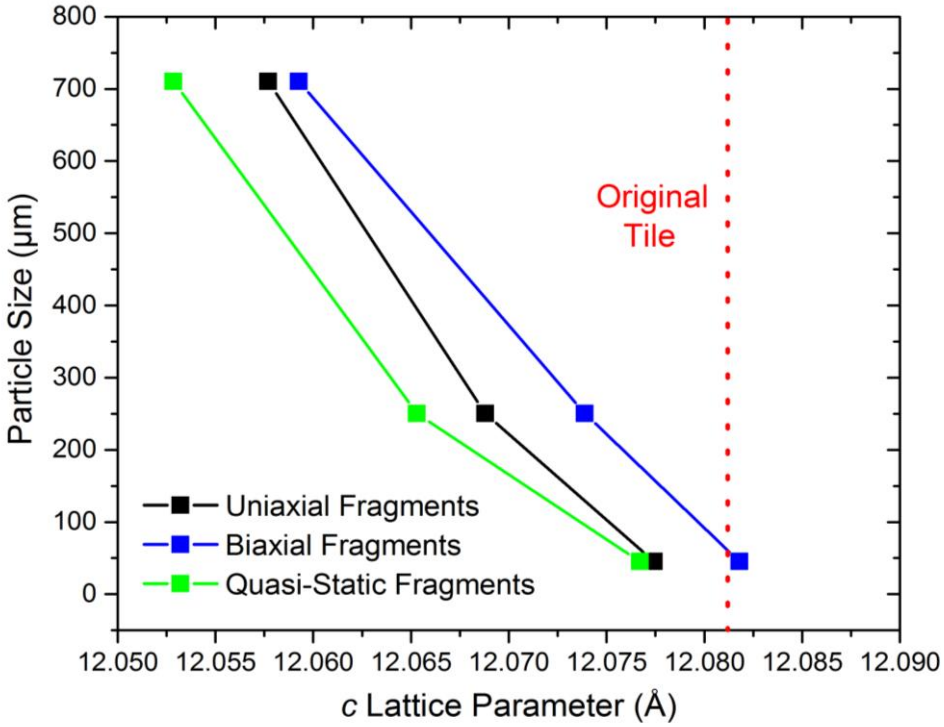

Figure 96. Variation of the *c* (Å) lattice parameter with the fragment size before crushing.

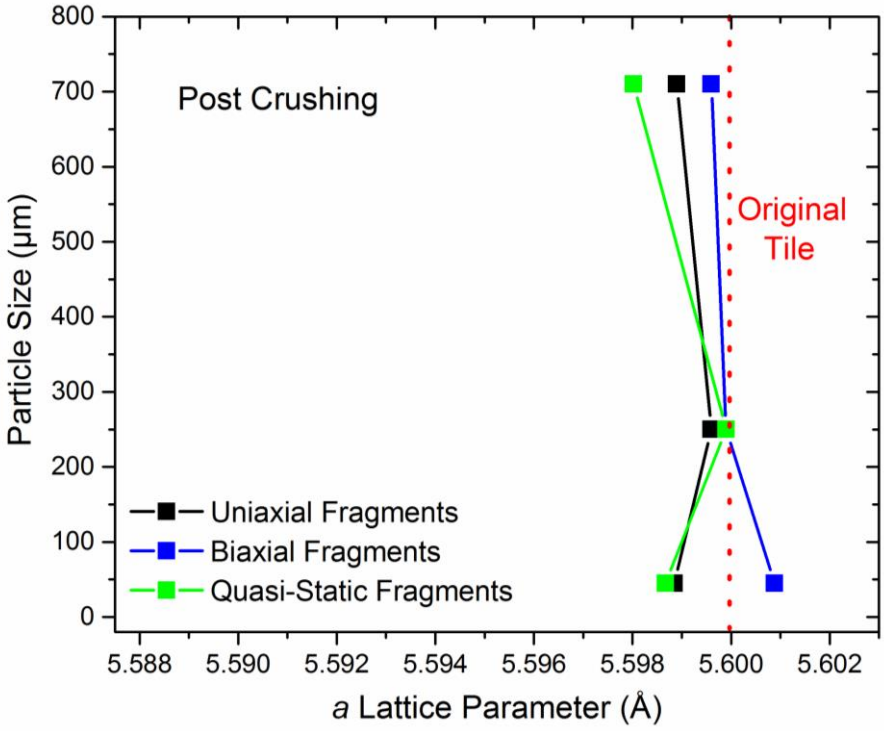

Figure 97. Variation of the *a* (Å) lattice parameter with the fragment size after crushing.

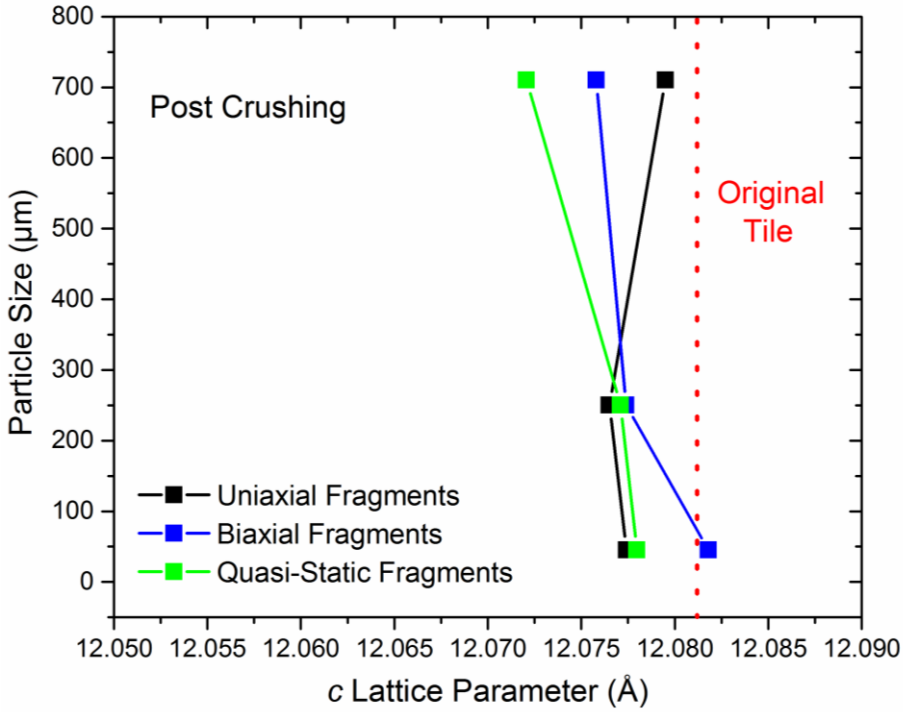

Figure 98. Variation of the *c* (Å) lattice parameter with the fragment size after crushing.

The resultant volumetric residual strain in the fragments was calculated from the change in the volume of the unit cell before and after compression tests using the formula below:

$$\varepsilon_V = \frac{V_B - V_A}{V_B} \quad (27)$$

Where, V_B= Volume of hexagonal unit cell of boron carbide before compression tests

V_A= Volume of hexagonal unit cell of boron carbide after compression tests

ε_V = Residual volumetric strain

From the results in Figure 99, larger fragments showed the presence of a higher residual volumetric strain as compared to smaller fragments. As the fragment size decreased, residual strain was alleviated as a result of crack propagation from the graphitic inclusions and increased surface area of the fragments. The >45 µm fragments exhibited a marginal value of the residual volumetric strain. Based on these observations, it can be concluded that the boron carbide was subjected to hydrostatic compression which results in a shrinkage of the unit cell. This could lead to a deduction of the presence of elastic strain resulting in the distortion of the lattice. The largest distortion of the lattice occurs in the larger fragments. Furthermore, hydrostatic compression is the root cause for the shrinkage in the crystal lattice of boron carbide as illustrated in Figure 100. Preliminary conclusions have been made based on the XRD results, however, the precise mechanism explaining these observations has not completely been understood. Further work needs to be done to link these observations to the performance of boron carbide under extreme dynamic conditions.

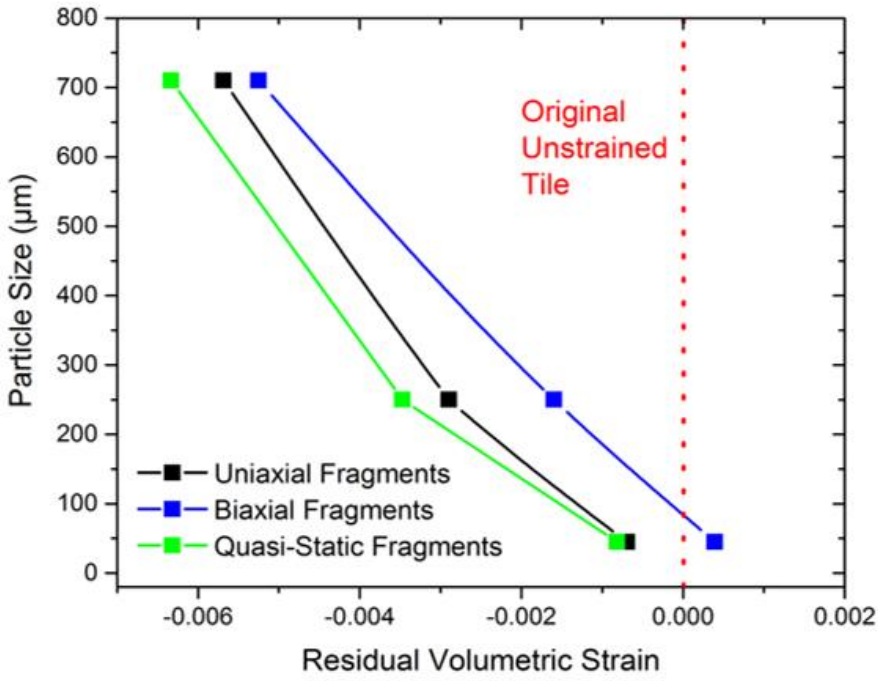

Figure 99. Variation of the fragment size and the residual volumetric strain from compression experiments.after crushing.

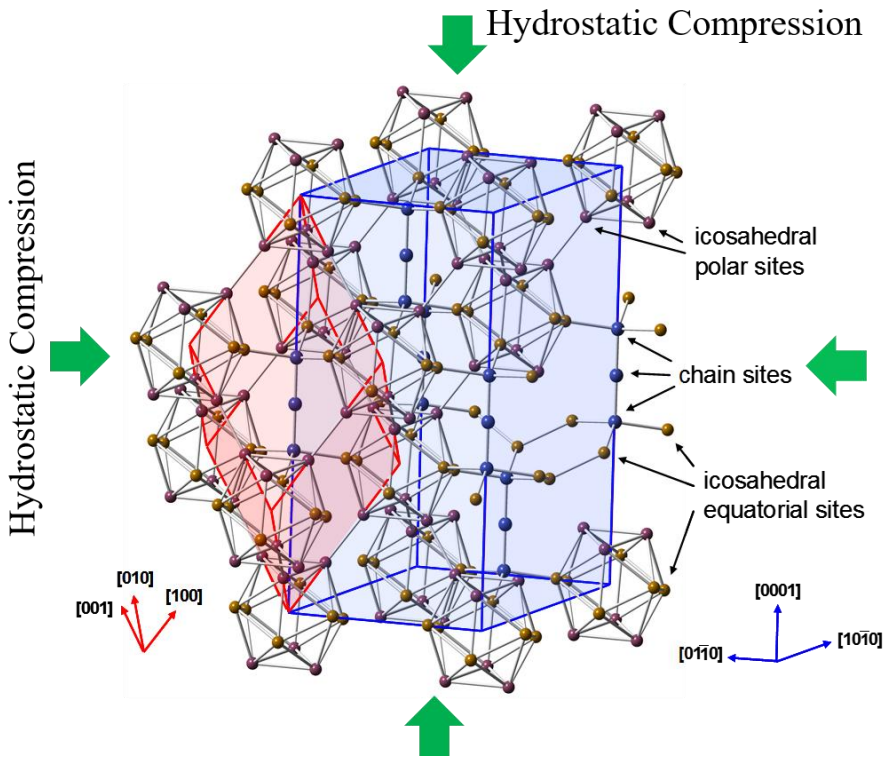

Figure 100. Hydrostatic compression of the boron carbide unit cell.

6.3.3 Raman Mapping

Raman spectroscopy was also performed on the fragmented material to explore evidence of amorphization. Figure 101 shows Raman mapping of the fragments obtained from uniaxial, biaxial and quasi-static compression tests. Carbon defects (red), boron nitride (cyan) and amorphized (blue) phases were mapped on the fracture surfaces. Carbonaceous defects were typically present on the fracture surfaces of the impacted material. Amorphous boron carbide zones were also observed especially in the biaxial and quasi-static fragments. But these amorphous zones were not a result of stress induced amorphization that characteristically appears in boron carbide subjected to high strain rate impact tests. These were a direct consequence of shear as a result of surface grinding of the original hot pressed tile. Further, the presence of organic impurities was also seen in the boron carbide fragments. These impurities were due to the backing material (Styrofoam) used to collect the fragments during Kolsky bar tests.

Figure 102 (a) and (c) are the representative Raman spectra and the corresponding optical images from the locations from which the Raman spectra were acquired. Only Raman bands linked to boron carbide were observed from Raman analysis on the ground surfaces. However, focusing the beam on the fracture surfaces of the fragments (Figure 102 (b) and (d)) resulted in the formation of peaks corresponding to carbonecous defects and boron nitride. This provided further evidence of the important role carbon defects play in the failure of boron carbide during extreme dynamic conditions. Hence minimizing these defects could theoretically improve the performance of consolidated boron carbide under static and dynamic loading conditions.

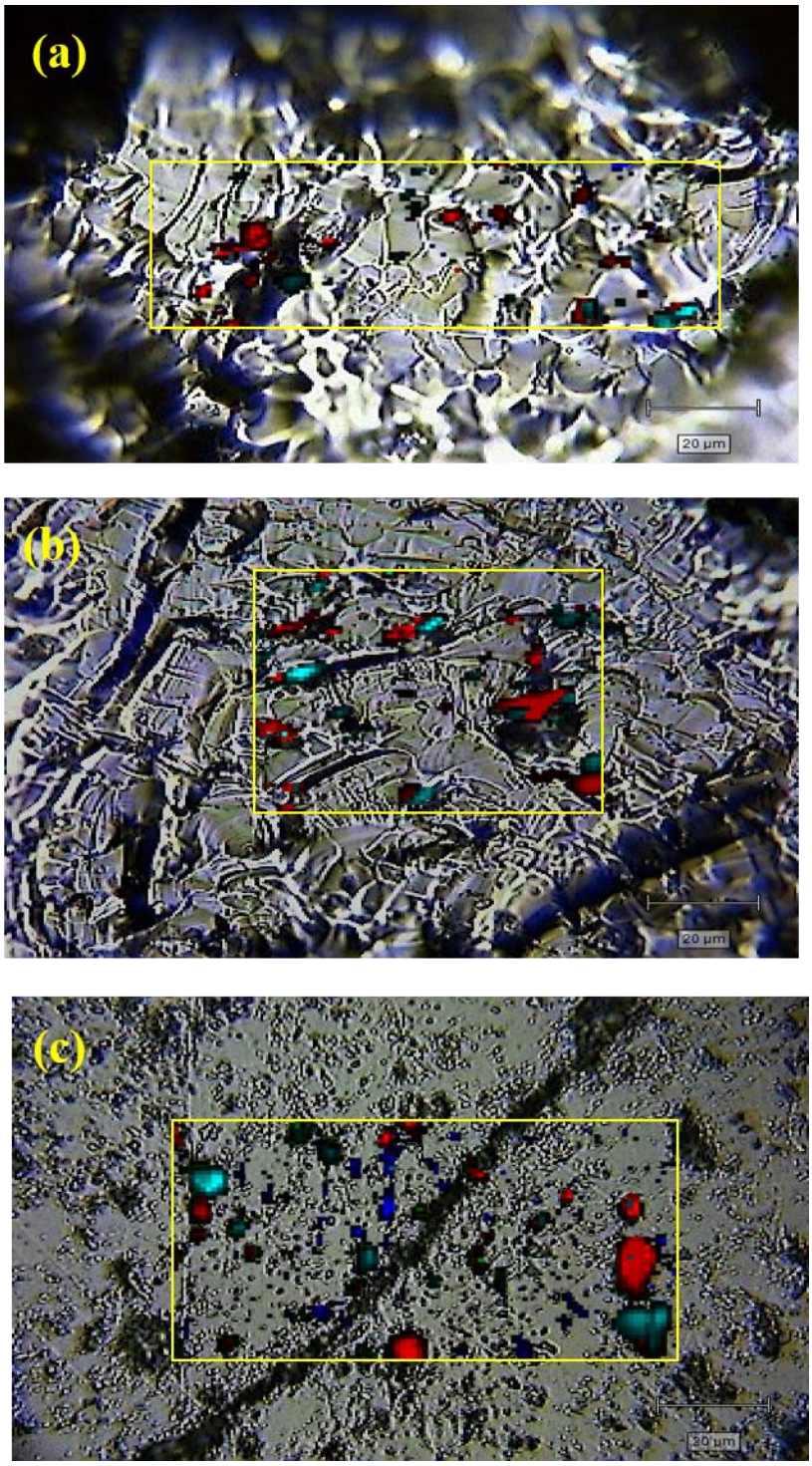

Figure 101. Raman maps showing the presence of graphitic carbon (red), h-BN (cyan), amorphous boron carbide (blue) and organic impurities (green) in the a) uniaxial, b) biaxial and c) quasi-static fragments.

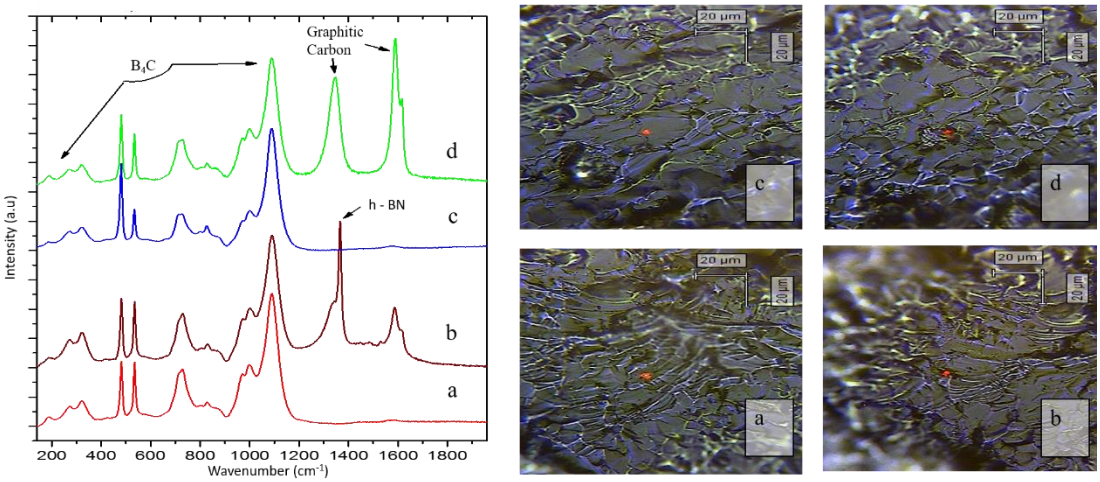

Figure 102. Typical Raman spectra from the ground (a and c) and fracture surfaces (b and d) of the fragments subjected to high strain rate compression tests.

6.3.4 SEM/EDS Mapping

SEM micrographs and EDS maps on the ground surfaces showed the carbon inclusions were present as graphitic sheets on the surface of boron carbide as shown in Figure 103 (a) and (b). The typical fracture surfaces of the fragments collected after compression tests are shown in Figure 103 (c) and (d). Generally, transgranular cleavage was the primary crack propagation mode[160]. Crack initiation occurs from carbon inclusions with the fracture surfaces showing predominantly carbon rich areas. Characteristically, flaky carbonaceous inclusions cause crack deflection with the crack propagating from one carbon inclusion to another through the boron carbide grains. Similar observations for the same material under analogous loading conditions were made by Farbaniec et al[160]. Figure 104 shows a fractured boron nitride grain with an aluminum nitride grain boundary. These observations agreed with the results from Raman spectroscopy and indicated that graphite was not the sole actor in the failure of boron carbide. Boron nitride and aluminum nitride were also responsible for failed ballistic response in commercial grade consolidated boron carbide.

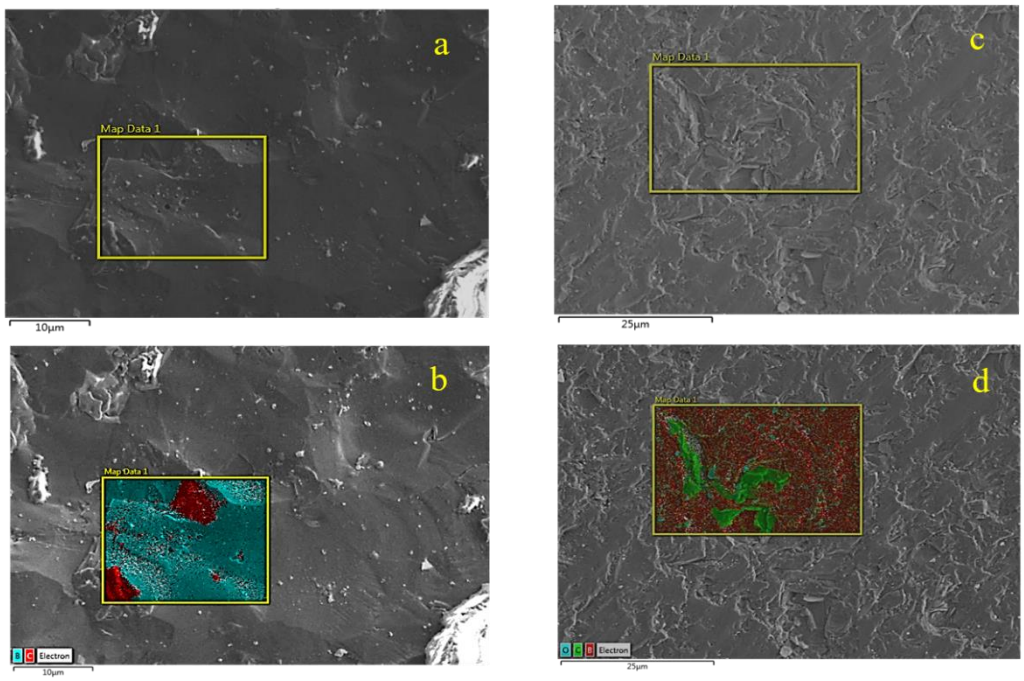

Figure 103. SEM micrograph and EDS maps showing, (a) and (b): Presence of graphitic sheets on the surface of the boron carbide and (c) and (d): Carbon rich fracture surfaces.

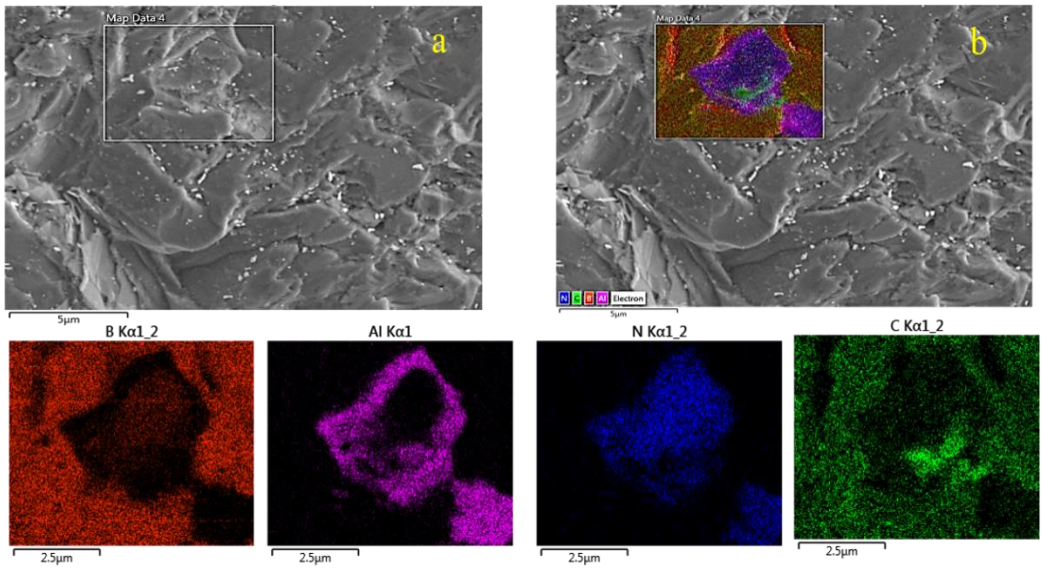

Figure 104 (a) SEM micrograph showing the fracture surfaces in boron nitride grains. (b) Elemental mapping of the fracture surfaces in the boron nitride grains.

6.4 Summary

In this section, the developed chemical and analytical techniques were applied to investigate the crystal structure response of boron carbide following high strain rate compression tests. Fragments with the largest particle size contained the highest residual volumetric strain and as the fragments decreased in size, the strain was relieved through crack propagation and increase in the surface area of the fragments. The precise mechanisms resulting in these observations were not completely understood and this work will be done in the future.

Failure of boron carbide is dependent on the defect population (carbonaceous inclusions) and the defect spacing. Crack propagation typically originated from the carbon inclusions. Moreover, the observed fracture surfaces from Raman and SEM mapping were commensurate with each other showing that the fracture surfaces were carbon rich indicating the role played by free carbon in the failure of boron carbide. Additionally, the presence of boron nitride and aluminum nitride also affected the performance of boron carbide as was observed in the Raman map. Further studies will have to be conducted to understand how these observations translate to the performance of boron carbide.

7 Conclusions

The objective of this thesis was to develop an improved methodology for the chemical and structural characterization of boron carbide. Utilizing the developed techniques, an improved understanding of the variations in the structural and mechanical properties across the solubility range was gleaned. The work done as part of the thesis can be used to establish the preferred composition and purity of boron carbide for extreme dynamic conditions which would then aid in controlling dynamic failure processes to improve the performance of boron carbide.

Currently used analytical and chemical techniques were assessed to determine the sources of inaccuracies associated with the determination of the boron carbide stoichiometry. Currently available Powder Diffraction Files (PDF) cannot be exclusively used to detect the precise stoichiometry owing to the inconsistencies with previously developed analysis techniques and earlier misconceptions regarding the absence of a wide homogeneity range of boron carbide. Boron carbide powders should be thoroughly cleaned before analysis using the cleaning procedure highlighted in **Section 3.2.5** to prevent surface oxides altering the stoichiometric results.

Critical examination of existing characterization techniques indicated the method employed to calculate the free carbon concentration provided the largest source of error. In lieu of these inspections, a method known as the modified spiking technique was introduced for the determination of the free carbon concentration in boron carbide. This method showed an increased reliability as compared to previously used analytical techniques. This method can be employed for free carbon determination, irrespective of

the nature of carbon present in the boron carbide. Additional testing against a reference boron carbide powder revealed results which were commensurate with the reported values.

An improved dependence of the lattice parameters on the carbon concentration was also presented through the synthesis and characterization of high purity and varying chemistry boron carbide. As the carbon concentration was decreased, the unit cell volume of boron carbide increased and a change in the slope was observed at ~13.3 at% carbon. The observed trend in the lattice parameter data was explained through the proposal of a simplified structural model. From 20 at% - 13.3 at% carbon, preferential substitution of boron for carbon atoms occurs in the icosahedra resulting in the formation of a B_{12}(C-B-C) structure from $B_{11}C$(C-B-C). The B_{12}(C-B-C) configuration had increased bond lengths and interatomic separations leading to an expansion of the unit cell. Additional boron enrichment caused the formation of B_{12}(B-B) units which grew in number towards the boron rich solubility range.

The developed lattice parameter calibration curve also provides a convenient and non-destructive method to calculate the stoichiometry of boron carbide. From the results of phase identification, lattice parameters and Raman spectroscopy, knowledge of the single phase solubility range has also been garnered. It has been shown that the carbon rich limit of boron carbide could extend beyond 18.8 at% carbon or a stoichiometry of $B_{4.3}C$. Although the precise value of this limit was not discerned, preliminary estimation pointed to a limiting stoichiometry of B_4C or 20 at% carbon.

Hardness measurements as a function of stoichiometry also uncovered decreased hardness values with an increase in the B:C ratio. These results were attributed to reduced interatomic separation and increased bond length leading to a weaker unit cell.

Amorphization of boron carbide was also seen on all the indented boron carbide samples. From the lattice parameter, hardness and amorphization data, there is a possibility that failure in boron carbide may be a consequence of another mechanism such as softer bonds at higher B:C ratios. These results indicate synthesizing boron carbide with modified microstructures at stoichiometries close to 20 at% carbon may be the way forward to attain improved ballistic performance.

Finally, the work done as part of this thesis is essential as the lattice parameters-carbon concentration relationship, atomic configurations at different stoichiometries, single phase solubility limits and effect of stoichiometry on mechanical properties have been the consideration of significant debate in the boron carbide community. The atomic configuration and positions of the boron and carbon atoms play a key role in the structure of the boron carbide phases. Depending on the atomic structure, boron carbide exhibits different mechanical properties. Hence by understanding how the atomic configuration changes as a function of the stoichiometry, boron carbide with a preferred atomic configuration and consequently properties can be synthesized to attain improved performance under extreme dynamic conditions.

8 Recommendations for Future Work

Based on the results from this thesis, there are still areas in the research on boron carbide that have not been completely understood and could be explored further. The precise carbon and boron rich solubility limit can be determined by synthesizing a series of samples at regular intervals across both the solubility limits of B and C. These materials can then be analyzed using the developed characterization procedures and techniques

detailed in this work. These results could potentially shed some light on the single phase solubility range of boron carbide.

The simplified structural model proposed in this work has been based on deductions from the lattice parameter and Raman spectroscopy results. To confirm the proposed atomic model, single crystal X-ray refinement should be performed on boron carbide samples with varying stoichiometries to discern the boron and carbon atomic positions.

Finally, consolidated boron carbide can be synthesized with reduced porosity by increasing the temperatures and pressures used during hot pressing. Further, utilization of a BN sleeve during densification would ensure no graphite contamination occurs from the graphite dies. These samples can then be tested using high strain rate experiments to discern the ballistic response of boron carbide at varying stoichiometries.

9 References

1. F. Thévenot, "Boron carbide - A comprehensive review," *J. Eur. Ceram. Soc.,* 6 205-25 (1990).
2. R.R.Ridgway, *J.Am.Electrochem.Soc,* 66 (1934).
3. G. N. Samsonov, N. N. Zhuravlev, and I. G. Amnuel, "Physicochemical properties of boron-carbon alloys," *Fiz. Met. Metalloved.,* 3[2] 309-13 (1956).
4. N. N. Zhuravlev, G. Makarenko, and G. N. Samsonov, *Izv. Akad. Nauk SSSR, OTN,* 1 133 (1961).
5. G. S. Zhdanov and N. G. Sevastyanov, "Crystal structure of boron carbide (B_4C)," *Dokl. Akad. Nauk SSSR,* 32 832 (1941).
6. V. Domnich, S. Reynaud, R. A. Haber, and M. Chhowalla, "Boron carbide: Structure, properties, and stability under stress," *J. Am. Ceram. Soc.,* 94[11] 3605-28 (2011).
7. F. Thévenot, "Boron carbide - A comprehensive review," pp. 2.1-2.25. in Properties of Ceramics, Vol. 2**.** *Euro-ceramics 1, Proc. 1st Eur. Ceram. Soc. Conf.* Edited by G. de With, R. A. Terpstra, and R. Metselaar. Elsevier Appl. Sci., London and New York, 1989.
8. M. Beauvy, "Stoichiometric limits of carbon-rich boron carbide phases," *J. Less-Common Met.,* 90[2] 169-75 (1983).
9. K. A. Schwetz and P. Karduck, "Investigations in the boron-carbon system with the aid of electron probe microanalysis," pp. 405-13. in Boron-Rich Solids**.** Edited by D. Emin, T. Aselage, C. L. Beckel, A. C. Switendick, and B. Morosin. American Institute of Physics, New York, 1991.
10. V. I. Matkovich, "Extension of the boron-carbon homogeneity range," *J. Less-Common Met.,* 47 39 (1976).
11. D. M. Bylander, L. Kleinman, and S. B. Lee, "Self-consistent calculations of the energy bands and bonding properties of $B_{12}C_3$," *Phys. Rev. B,* 42[2] 1394-403 (1990).
12. A. Kirfel, A. Gupta, and G. Will, "The nature of the chemical bonding in boron carbide, $B_{13}C_2$. I. Structure refinement," *Acta Cryst. B,* 35 1052 (1979).
13. T. L. Aselage and R. G. Tissot, "Lattice constants of boron carbide," *J. Am. Ceram. Soc.,* 75[8] 2207-12 (1992).
14. L. J. A. E.L. Venturini, D. Emin and C. Wood, "Electronic Spin Resonance Study of Hot-Pressed Boron Carbide," pp. 292-304. in Boron Rich Solids, AIP Conference Proceedings, Vol. 140. Edited by T. A. D.Emin, C.L Beckel, I.A. Howard and C.Wood. American Institute of Physics, New York, 1986.
15. H. L. Yakel, "The crystal structure of a boron-rich boron carbide," *Acta Cryst. B,* 31 1797-806 (1975).
16. D.W.Bullet, "Boron Rich Solids," *Proceedings of an International Conference on the Physics and Chemistry of Boron and Boron-Rich Borides* (1985).
17. C. Wood and D. Emin, "Conduction mechanism in boron carbide," *Phys. Rev. B,* 29[8] 4582-87 (1984).
18. M. Van Schilfgaarde and W. A. Harrison, "Electronic structure of boron," *J. Phys. Chem. Solids,* 46[9] 1093-100 (1985).
19. D. Emin, "Structure and single-phase regime of boron carbides," *Physical Review B,* 38[9] 6041 (1988).

20. A. C. Larson, "Comments concerning the crystal structure of B_4C," pp. 109-13. in Boron-Rich Solids**.** *AIP Conf. Proc.* Edited by D. Emin, T. Aselage, C. L. Beckel, I. A. Howard, and C. Wood. American Institute of Physics, New York, 1986.
21. B. Morosin, A. W. Mullendore, D. Emin, and G. A. Slack, "Rhombohedral crystal structure of compounds containing boron-rich icosahedra," pp. 70-86. in Boron-Rich Solids**.** *AIP Conf. Proc.* Edited by D. Emin, T. Aselage, C. L. Beckel, I. A. Howard, and C. Wood. American Institute of Physics, New York, 1986.
22. T. L. Aselage and D. Emin, "Structural model of the boron carbide solid solution," pp. 177-85. in Boron-Rich Solids**.** *AIP Conf. Proc.* Edited by D. Emin, T. Aselage, C. L. Beckel, A. C. Switendick, and B. Morosin. American Institute of Physics, New York, 1991.
23. K. A. Schwetz and A. Lipp, "Boron carbide, boron nitride, and metal borides," pp. 265. in Ullmann's Encyclopedia of Industrial Chemistry, Vol. 4A**.** Verlag Chemie, Weinheim, 1985.
24. T.Aselage and D.Emin, "Structural Model of the Boron Carbide Solid Solution," pp. 177-85. in Structure. American Institute of Physics, AIP Conference Proceedings, Albuquerque, New Mexico, 1990.
25. K. A. Schwetz and P. Karduck, "Investigations in the boron-carbon system with the aid of electron probe microanalysis," *J. Less-Common Met.,* 175[1] 1-11 (1991).
26. H. Werheit, "On excitons and other gap states in boron carbide," *J. Phys.: Condens. Mat.,* 18[47] 10655-62 (2006).
27. U. Kuhlmann and H. Werheit, "On the microstructure of boron carbide," *Solid State Commun.,* 83[11] 849-52 (1992).
28. J. E. Saal, S. Shang, and Z. K. Liu, "The structural evolution of boron carbide via ab initio calculations," *Appl. Phys. Lett.,* 91[23] 231915 (2007).
29. R. P. Elliott, "The boron-carbon system," pp. 50. in. Armour Research Foundation of Illinois Institute of Technology, Chicago, IL, 1961.
30. R. Dolloff, "Air Force Report." in. WADD, Tech. Rep. 60-143, 1960.
31. H. K. Clark and J. L. Hoard, "The crystal structure of boron carbide," *J. Am. Chem. Soc.,* 65 2115-19 (1943).
32. G. Will and K. H. Kossobutzki, "X-ray diffraction analysis of $B_{50}C_2$ and $B_{50}N_2$ crystallizing in the "tetragonal" boron lattices," *J. Less-Common Met.,* 47 33-38 (1976).
33. M. Bouchacourt and F. Thévenot, "Analytical investigations in the BC system," *J. Less-Common Met.,* 82 219-26 (1981).
34. M. Bouchacourt and F. Thévenot, "The melting of boron carbide and the homogeneity range of the boron carbide phase," *J. Less-Common Met.,* 67 327-31 (1979).
35. L. B. Ekbom and C. O. Amundin, "Microstructural evaluations of sintered boron carbides with different compositions," pp. 237-43. in Science of Ceramics, Vol. 11**.** Edited by R. Carlsson and S. Karlsson. Swedish Ceramic Society, Stockholm, 1981.
36. F.Wolher and H. S. C. Deville, *Annales de chimie et de physique*, 52[3] 63 (1958).
37. G. Will and K. H. Kossobutzki, "An x-ray structure analysis of boron carbide, $B_{13}C_2$," *J. Less-Common Met.,* 44 87 (1976).
38. G. Will, A. Kirfel, and A. Gupta, "Is the concept of boron icosahedra in boron carbide correct?," *J. Less-Common Met.,* 67 13-18 (1979).

39. F.W.Glaser, D.Moskowitz, and B.Post, *J.Appl.Phys*, 24[6] (1953).
40. M. Bouchacourt and F. Thévenot, "Etudes sur le carbure de bore. I. Métallographie et microdureté Knoop du carbure de bore," *J. Less-Common Met.*, 59 119-30 (1978).
41. A. Vogt and F. Schroll, "Electrothermic production of boron carbide." in. Google Patents, 1939.
42. W. S. Wilson and P. J. Guichelaar, "Electric Arc Furnace Processes," pp. 131-36. in Carbide, Nitride and Boride Materials Synthesis and Processing**.** Springer, 1997.
43. A. K. Suri, C. Subramanian, J. K. Sonber, and T. Murthy, "Synthesis and consolidation of boron carbide: a review," *Int. Mater. Rev.*, 55[1] 4-40 (2010).
44. W. Yang, L. Zhang, L. Cheng, Y. Liu, and W. Zhang, "Preparation and Comparision of Two Typical CVD Films from CH4 and C3H6 as Carbon Resources," *Ceramic Materials and Components for Energy and Environmental Applications: Ceramic Transactions*, 210 47 (2010).
45. R. Riedel and I.-W. Chen, "Ceramics Science and Technology, Materials and Properties," Vol. 2. John Wiley & Sons, (2011).
46. A. Lipp, "Boron carbide: Production, properties, application," *Tech. Rundsch.*, 58[7] 1-47 (1966).
47. H. Salimijazi, T. Coyle, J. Mostaghimi, and L. Leblanc, "Characterization of Vacuum Plasma Sprayed Boron Carbide," *Thermal Spray* (2004).
48. O. Conde, A. Silvestre, and J. Oliveira, "Influence of carbon content on the crystallographic structure of boron carbide films," *Surface and Coatings Technology*, 125[1] 141-46 (2000).
49. D. W. Maiorano, "The evolution and implication of boron carbide microstructural variations and transformations during powder processing." in. Rutgers University-Graduate School-New Brunswick, 2011.
50. B. Champagne and R. Angers, "Mechanical Properties of Hot-Pressed B-B4C Materials," *Journal of the American Ceramic Society*, 62[3-4] 149-53 (1979).
51. M. Beauvy, "Properties mechaniques du carbide de bore'Fritte'," *Rev. Int. Hautes* (1982).
52. A. Osipov, I. Ostapenko, V. Slezov, R. Tarasov, V. Podtykan, and N. Kartsev, "Effect of porosity and grain size on the mechanical properties of hot-pressed boron carbide," *Soviet Powder Metallurgy and Metal Ceramics*, 21[1] 55-58 (1982).
53. H. Lee and R. F. Speyer, "Hardness and Fracture Toughness of Pressureless-Sintered Boron Carbide (B4C)," *Journal of the American Ceramic Society*, 85[5] 1291-93 (2002).
54. Kieffer-Benesovsky, *Hartsoffe*, 42 (1963).
55. R. D. Allen, "The solid solution series boron - boron carbide," *J. Am. Chem. Soc.*, 75 3582 (1953).
56. K. Niihara, A. Nakahira, and T. Hirai, "The effect of stoichiometry on mechanical properties of boron carbide," *J. Am. Ceram. Soc.*, 67[1] C13-C14 (1984).
57. M. Chheda, J. Shih, C. Gump, and A. Weimer, "Synthesis and processing of boron-rich boron carbide." in. Ceradyne Inc., Costa Mesa, CA, 2008.
58. K. J. McClellan, F. Chu, J. M. Roper, and I. Shindo, "Room temperature single crystal elastic constants of boron carbide," *J. Mater. Sci.*, 36[14] 3403-07 (2001).
59. J. H. Gieske, T. L. Aselage, and D. Emin, "Elastic properties of boron carbides," pp. 376-79. in Boron-Rich Solids**.** *AIP Conf. Proc.* Edited by D. Emin, T. Aselage, C.

L. Beckel, A. C. Switendick, and B. Morosin. American Institute of Physics, New York, 1991.
60. M. H. Manghnani, Y. Wang, F. Li, P. Zinin, and W. Rafaniello, "Elastic and vibrational properties of B_4C to 21 GPa," pp. 945-48. in Science and Technology of High Pressure**.** Edited by M. H. Manghnani, W. J. Nellis, and M. F. Nicol. Universities Press, Hyderabad, India, 2000.
61. R. J. Nelmes, J. S. Loveday, R. M. Wilson, W. G. Marshall, J. M. Besson, S. Klotz, G. Hamel, T. L. Aselage, and S. Hull, "Observation of inverted-molecular compression in boron carbide," *Phys. Rev. Lett.*, 74[12] 2268-71 (1995).
62. R. Vojtovich, "Oxidation of carbides and nitrides," (1981).
63. L. M. Litz and R. Mercuri, "Oxidation of Boron Carbide by Air, Water, and Air-Water Mixtures at Elevated Temperatures," *Journal of the Electrochemical Society*, 110[8] 921-25 (1963).
64. M. Steinbrück, A. Meier, U. Stegmaier, and L. Steinbock, "Experiments on the oxidation of boron carbide at high temperatures," Vol. 6979. FZKA, (2004).
65. M. L. Wilkins, "Third progress report of light armor program." in. Lawrence Livermore National Laboratory, University of California, CA, 1968.
66. M. V. Demirbas, "Microstructure-property relationship in silicon carbide armor ceramics," (2008).
67. M. Chen, J. W. McCauley, and K. J. Hemker, "Shock-induced localized amorphization in boron carbide," *Science*, 299 1563-66 (2003).
68. J. W. Mccauley, "Summary of hugoniot elastic limit findings," (2005).
69. T. J. Vogler, W. D. Reinhart, and L. C. Chhabildas, "Dynamic behavior of boron carbide," *J. Appl. Phys.*, 95[8] 4173-83 (2004).
70. R. G. McQueen, S. P. Marsh, J. W. Taylor, J. N. Fritz, and W. J. Carter, "The equation of state of solids from shock wave studies," pp. 239-417. in High-Velocity Wave Phenomena**.** Edited by R. Kinslow. Academic Press, New York, 1970.
71. M. N. Pavlovskii, "Shock compressibility of six very hard substances," *Sov. Phys. Solid State*, 12 1736-37 (1971).
72. W. H. Gust, A. C. Holt, and E. B. Royce, "Dynamic yield, compressional, and elastic parameters for several lightweight intermetallic compounds," *J. Appl. Phys.*, 44[2] 550-60 (1973).
73. D. E. Grady, "Analysis of shock and high-rate data for ceramics: Equation of state properties and fragmentation in the ballistic environment." in. Applied Research Associates, Inc., Albuquerque, NM, 2009.
74. D. E. Grady, "Analysis of shock and high-rate data for ceramics: Application to boron carbide and silicon carbide." in. Applied Research Associates, Inc., Albuquerque, NM, 2002.
75. D. E. Grady, "Shock-wave strength properties of boron carbide and silicon carbide," *J. Phys. IV*, 4 385-91 (1994).
76. Y. Zhang, T. Mashimo, Y. Uemura, M. Uchino, M. Kodama, K. Shibata, K. Fukuoka, M. Kikuchi, T. Kobayashi, and T. Sekine, "Shock compression behaviors of boron carbide (B_4C)," *J. Appl. Phys.*, 100[11] 113536 (2006).
77. D. Ge, V. Domnich, T. Juliano, E. A. Stach, and Y. Gogotsi, "Structural damage in boron carbide under contact loading," *Acta Mater.*, 52[13] 3921-27 (2004).

78. J. Hay, "Introduction to instrumented indentation testing," *Experimental Techniques*, 33[6] 66-72 (2009).
79. V. Domnich, Y. Gogotsi, M. Trenary, and T. Tanaka, "Nanoindentation and Raman spectroscopy studies of boron carbide single crystals," *Appl. Phys. Lett.*, 81[20] 3783-85 (2002).
80. X. Q. Yan, W. J. Li, T. Goto, and M. W. Chen, "Raman spectroscopy of pressure-induced amorphous boron carbide," *Appl. Phys. Lett.*, 88 131905 (2006).
81. D. Taylor, E., J. McCauley, W., and T. W. Wright, "The effects of stoichiometry on the mechanical properties of icosahedral boron carbide under loading," *J. Phys.: Condens. Mat.*, 24[50] 505402 (2012).
82. H. Werheit, H. Binnenbruck, and A. Hausen, "Optical properties of boron carbide and comparison with b-rhombohedral boron," *Phys. Status Solidi B*, 47 153-58 (1971).
83. J. Lagrenaudie, "A study of the properties of boron," *J. Phys.-Paris*, 14 14-18 (1953).
84. M. Yamazaki, "Electronic band structure of boron carbide," *The Journal of Chemical Physics*, 27[3] 746-51 (1957).
85. H. Dekura, K. Shirai, and A. Yanase, "Metallicity of boron carbides at high pressure " *J. Phys.: Conf.Ser.*, 215 012117 (2010).
86. H. Rietveld, "A profile refinement method for nuclear and magnetic structures," *Journal of applied Crystallography*, 2[2] 65-71 (1969).
87. R. Jenkins, "An introduction to X-ray powder diffractometry." Philips Gloeilampenfabrieken, (1970).
88. L. McCusker, R. Von Dreele, D. Cox, D. Louër, and P. Scardi, "Rietveld refinement guidelines," *Journal of Applied Crystallography*, 32[1] 36-50 (1999).
89. G. Will, "Powder diffraction: The Rietveld method and the two stage method to determine and refine crystal structures from powder diffraction data." Springer Science & Business Media, (2006).
90. S. K. Chatterjee, "X-ray diffraction: Its theory and applications." PHI Learning Pvt. Ltd., (2010).
91. P. Thompson, D. Cox, and J. Hastings, "Rietveld refinement of Debye–Scherrer synchrotron X-ray data from Al2O3," *Journal of Applied Crystallography*, 20[2] 79-83 (1987).
92. "Standard Test Methods for Chemical, Mass Spectrometric, and Spectrochemical Analysis of Nuclear-Grade Boron Carbide." in. ASTM International, 2012.
93. LECO, "Carbon Determinator - C/S 230," pp. 7.1-7.3. in., 2008.
94. LECO, "Oxygen/Nitrogen Determinator - TC 600," 7.1-7.3 (2008).
95. K. Y. Xie, M. F. Toksoy, K. Kuwelkar, B. Zhang, J. A. Krogstad, R. A. Haber, and K. J. Hemker, "Effect of alumina on the structure and mechanical properties of spark plasma sintered boron carbide," *Journal of the American Ceramic Society*, 97[11] 3710-18 (2014).
96. D. Gosset and M. Colin, "Boron carbides of various compositions: an improved method for x-ray characterization," *J. Nucl. Mater.*, 183 161-73 (1991).
97. M. Bouchacourt and F. Thévenot, "The properties and structure of the boron carbide phase," *J. Less-Common Met.*, 82 227-35 (1981).
98. T. L. Aselage, D. R. Tallant, J. Gieske, S. Van Deusen, and R. Tissot, "Preparation and properties of icosahedral borides," pp. 97-111. in The Physics and Chemistry of Carbides, Nitrides and Borides**.** Springer, 1990.

99. H.E.Robson. in, Vol. PHD. University of Kansas, 1959.
100. D. R. Tallant, T. L. Aselage, A. N. Campbell, and D. Emin, "Boron carbide structure by Raman spectroscopy," *Phys. Rev. B,* 40[8] 5649-56 (1989).
101. U. Kuhlmann and H. Werheit, "Raman effect of boron carbide ($B_{4.3}C$ to $B_{10.37}C$)," *J. Alloy. Compd.,* 205 87-91 (1994).
102. T. L. Aselage, D. R. Tallant, and D. Emin, "Isotope dependencies of Raman spectra of $B_{12}As_2$, $B_{12}P_2$, $B_{12}O_2$, and $B_{12+x}C_{3-x}$: Bonding of intericosahedral chains," *Phys. Rev. B,* 56[6] 3122-29 (1997).
103. F. Demangeot, P. Puech, V. Paillard, V. Domnich, and Y. G. Gogotsi, "Spatial distribution of strain and phases in Si nano-indentation analysed by Raman mapping," pp. 777-82. in Gettering and Defect Engineering in Semiconductor Technology, Vol. 82-84**.** *Solid State Phenomena.* Edited by V. Raineri, F. Priolo, M. Kittler, and H. Richter. Trans Tech Publications Ltd, Zurich-Uetikon, 2002.
104. H. Werheit, H. W. Rotter, F. D. Meyer, H. Hillebrecht, S. O. Shalamberidze, T. G. Abzianidze, and G. G. Esadze, "FT-Raman spectra of isotope-enriched boron carbide," *J. Solid State Chem.,* 177 569-74 (2004).
105. D. R. Tallant, T. L. Aselage, and D. Emin, "Structure of icosahedral borides by Raman spectroscopy," pp. 301-11. in Boron-Rich Solids**.** *AIP Conf. Proc.* Edited by D. Emin, T. Aselage, C. L. Beckel, A. C. Switendick, and B. Morosin. American Institute of Physics, New York, 1991.
106. H. Werheit, U. Kuhlmann, M. Laux, and R. Telle, "Solid solutions of silicon in boron-carbide-type crystals," *J. Alloys Compd.,* 209 181-87 (1994).
107. R. Schmechel and H. Werheit, "Correlation between structural defects and electronic properties of icosahedral boron-rich solids," *J. Phys.: Condens. Mat.,* 11 6803-13 (1999).
108. H. Werheit, A. Leithe-Jasper, T. Tanaka, H. Rotter, and K. Schwetz, "Some properties of single-crystal boron carbide," *Journal of Solid State Chemistry,* 177[2] 575-79 (2004).
109. R. Lazzari, N. Vast, J. M. Besson, S. Baroni, and A. Dal Corso, "Atomic structure and vibrational properties of icosahedral B_4C boron carbide," *Phys. Rev. Lett.,* 83[16] 3230-33 (1999).
110. N. Vast, R. Lazzari, J. M. Besson, S. Baroni, and A. Dal Corso, "Atomic structure and vibrational properties of icosahedral α-boron and B_4C boron carbide," *Comp. Mater. Sci.,* 17 127-32 (2000).
111. A. C. Ferrari and J. Robertson, "Interpretation of the Raman spectra of disordered and amorphous carbon," *Phys. Rev. B,* 61[20] 14095-107 (2000).
112. F. Tuinstra and J. L. Koenig, "Raman spectrum of graphite," *J. Chem. Phys.,* 53 1126-30 (1970).
113. U. Kuhlmann and H. Werheit, "Improved Raman effect studies on boron carbide ($B_{4.3}C$)," *Phys. Status Solidi B,* 175 85-92 (1993).
114. V. Domnich, D. W. Maiorano, R. A. Haber, and J. W. McCauley, "Raman spectroscopy and X-ray diffraction studies of boron carbide with variable stoichiometries," pp. in preparation. in., 2011.
115. A. Alizadeh, E. Taheri-Nassaj, and N. Ehsani, "Synthesis of boron carbide powder by a carbothermic reduction method," *J. Eur. Ceram. Soc.,* 24[10–11] 3227-34 (2004).

116. K. A. Schwetz and J. Hassler, "A wet chemical method for the determination of free carbon in boron carbide, silicon carbide and mixtures thereof," *J. Less-Common Met.*, 117[1–2] 7-15 (1986).
117. M. Beauvy and R. Angers, "Method for the determination of free graphite in boron carbide," *J. Less-Common Met.*, 80[2] 227-33 (1981).
118. P. Walker, J. Rakszawsiki, and A. Amington, "Distinguishing between graphitic and amorphous carbon," *ASTM Bulletin*, 208 52-54 (1955).
119. C. Houska and B. Warren, "X-Ray Study of the Graphitization of Carbon Black," *Journal of Applied Physics*, 25[12] 1503-09 (1954).
120. J. Zhao, L. Yang, F. Li, R. Yu, and C. Jin, "Structural evolution in the graphitization process of activated carbon by high-pressure sintering," *Carbon*, 47[3] 744-51 (2009).
121. H. Takagi, K. Maruyama, N. Yoshizawa, Y. Yamada, and Y. Sato, "XRD analysis of carbon stacking structure in coal during heat treatment," *Fuel*, 83[17] 2427-33 (2004).
122. B. K. Saikia, R. K. Boruah, and P. K. Gogoi, "A X-ray diffraction analysis on graphene layers of Assam coal," *Journal of chemical sciences*, 121[1] 103-06 (2009).
123. Z. Q. Li, C. J. Lu, Z. P. Xia, Y. Zhou, and Z. Luo, "X-ray diffraction patterns of graphite and turbostratic carbon," *Carbon*, 45[8] 1686-95 (2007).
124. A. Austin and W. Hedden, "Graphitization processes in cokes and carbon blacks," *Industrial & Engineering Chemistry*, 46[7] 1520-24 (1954).
125. H. Pinnick, "X-Ray Diffraction of Heat-Treated Carbon Blacks," *The Journal of Chemical Physics*, 20[4] 756-57 (1952).
126. L. E. Alexander and E. C. Sommer, "Systematic analysis of carbon black structures," *The Journal of Physical Chemistry*, 60[12] 1646-49 (1956).
127. K. Norrish and R. M. Taylor, "Quantitative analysis by X-ray diffraction," *Clay Miner. Bull*, 5[28] 98-109 (1962).
128. B. D. Cullity and J. W. Weymouth, "Elements of X-ray Diffraction," *American Journal of Physics*, 25[6] 394-95 (1957).
129. H. Lipson and A. Stokes, "The structure of graphite," pp. 101-05 in Proceedings of the Royal Society of London A: Mathematical, Physical and Engineering Sciences. Vol. 181.
130. J. Méring and J. Maire, "Aspects structuraux de la graphitation," *Les Carbones, Le Groupe Français dÉtude des Carbones*, 1 129-75 (1965).
131. J. Maire and J. Mering, "Graphitization of soft carbons," *Chemistry and physics of carbon*, 6 125-90 (1970).
132. L. Zou, B. Huang, Y. Huang, Q. Huang, and C. a. Wang, "An investigation of heterogeneity of the degree of graphitization in carbon–carbon composites," *Materials Chemistry and Physics*, 82[3] 654-62 (2003).
133. H. Gavin, "The Levenberg-Marquardt method for nonlinear least squares curve-fitting problems." in., 2011.
134. R. Couture, "Intelligent Interpolation for Background Subtration-A Hybrid Approach For Trace-Element Analysis," (2001).

135. P. S. Prevéy, "X-ray diffraction characterization of crystallinity and phase composition in plasma-sprayed hydroxyapatite coatings," *Journal of Thermal Spray Technology*, 9[3] 369-76 (2000).
136. H. Shi, J. Reimers, and J. Dahn, "Structure-refinement program for disordered carbons," *Journal of applied crystallography*, 26[6] 827-36 (1993).
137. G. Will and K. Kossobutzki, "An X-ray diffraction analysis of boron carbide, B 13 C 2," *Journal of the Less Common Metals*, 47 43-48 (1976).
138. D. R. Armstrong, J. Balland, P. G. Pukins, and A. Kirfel, "The nature of the chemical bonding in boron barbide. IV. Electronic band structure of boron carbide, $B_{13}C_2$, and three models of the structure $B_{12}C_3$ " *Acta Cryst. B*, 39 324-29 (1983).
139. H. Werheit, T. Au, R. Schmechel, S. O. Shalamberidze, G. I. Kalandadze, and A. M. Eristavi, "IR-active phonons and structure elements of isotope-enriched boron carbide," *J. Solid State Chem.*, 154 79-86 (1999).
140. U. Kuhlmann, H. Werheit, and K. A. Schwetz, "Distribution of carbon atoms on the boron carbide structure elements," *J. Alloy. Compd.*, 189 249-58 (1992).
141. W. C. Oliver and G. M. Pharr, "An improved technique for determining hardness and elastic modulus using load and displacement sensing indentation experiments," *J. Mater. Res.*, 7[6] 1564-83 (1992).
142. H. Werheit, "On microstructure and electronic properties of boron carbide,″ pp. 87-102 in Advances in Ceramic Armor X: A Collection of Papers Presented at the 38th International Conference on Advanced Ceramics and Composites January 27-31, 2014.
143. J. Nocedal and S. Wright, "Numerical optimization.″ Springer Science & Business Media, (2006).
144. K. Kuwelkar, V. Domnich, W. Rafaniello, R. A. Haber, K. Behler, and J. LaSalvia, "Investigation of the Structural Properties of Boron Carbide Across the Solubility Range," *In Preparation* (2016).
145. B. Morosin, T. Aselage, and R. Feigelson, "Crystal structure refinements of rhombohedral symmetry materials containing boron-rich icosahedra,″ pp. 145 in MRS Proceedings. Vol. 97.
146. T. Aselage, S. Van Deusen, and B. Morosin, "Solution growth, structure and composition of boron carbide crystals," *Journal of the Less Common Metals*, 166[1] 29-44 (1990).
147. D. Emin, "Structure and single-phase regime of boron carbides," *Phys. Rev. B*, 38[9] 6041-55 (1988).
148. O. Sologub, Y. Michiue, and T. Mori, "Boron carbide, b13-xc2-y (x= 0.12, y= 0.01)," *Acta Crystallographica Section E: Structure Reports Online*, 68[8] i67-i67 (2012).
149. D. Hallam, A. Heaton, B. James, P. Smith, and J. Yeomans, "The correlation of indentation behaviour with ballistic performance for spark plasma sintered armour ceramics," *Journal of the European Ceramic Society*, 35[8] 2243-52 (2015).
150. S. Aydin and M. Simsek, "Hypothetically superhard boron carbide structures with a B11C icosahedron and three-atom chain," *Phys. Status Solidi B*, 246[1] 62-70 (2009).
151. X. J. Guo, J. L. He, Z. Y. Liu, Y. J. Tian, J. Sun, and H. T. Wang, "Bond ionicities and hardness of $B_{13}C_2$-like structured B_yX crystals (X=C,N,O,P,As)," *Phys. Rev. B*, 73[10] 104115 (2006).

152. F. Gao, L. Hou, and Y. He, "Origin of superhardness in icosahedral B_{12} materials," *J. Phys. Chem. B*, 108[35] 13069-73 (2004).
153. V. I. Ivashchenko, V. I. Shevchenko, and P. E. A. Turchi, "First-principles study of the atomic and electronic structures of crystalline and amorphous B_4C," *Phys. Rev. B*, 80[23] 235208 (2009).
154. G. Fanchini, J. W. McCauley, and M. Chhowalla, "Behavior of disordered boron carbide under stress," *Phys. Rev. Lett.*, 97[3] 035502 (2006).
155. Q. An, W. A. Goddard III, and T. Cheng, "Atomistic explanation of shear-induced amorphous band formation in boron carbide," *Physical review letters*, 113[9] 095501 (2014).
156. J. D. Hogan, D. Mallick, V. Domnich, K. Kuwelkar, J. W. McCauley, L. Farbaniec, and K. T. Ramesh, "Fragmentation of an Advanced Ceramic under Ballistic Impact:Mechanisms and Microstructure." in., 2016.
157. J. D. Hogan, L. Farbaniec, M. Shaeffer, and K. Ramesh, "The Effects of Microstructure and Confinement on the Compressive Fragmentation of an Advanced Ceramic," *Journal of the American Ceramic Society* (2014).
158. J. Kimberley, K. Ramesh, and N. Daphalapurkar, "A scaling law for the dynamic strength of brittle solids," *Acta Materialia*, 61[9] 3509-21 (2013).
159. K. Y. Xie, K. Kuwelkar, R. A. Haber, J. C. LaSalvia, and K. J. Hemker, "Microstructural Characterization of a Commercial Hot-pressed Boron Carbide Armor Plate," *Journal of the American Ceramic Society* (2016).
160. L. Farbaniec, J. Hogan, and K. Ramesh, "Micromechanisms associated with the dynamic compressive failure of hot-pressed boron carbide," *Scripta Materialia*, 106 52-56 (2015).